The optical modelling and design of Fabry Perot Interferometer sensors for ultrasound detection

Harikrishn Varu

UCL

A dissertation submitted in fulfilment of the requirements for the degree of

Doctor of Philosophy

at

University College London

Department of Medical Physics and Bioengineering

April 2014

Official declaration

I, Harikrishn Varu confirm that the work presented in this thesis is my own. Where information has been derived from other sources, I confirm this has been indicated in the thesis.

Abstract

The work in this thesis documents the optical modelling and design of Fabry Perot Interferometer (FPI) sensors for the detection of ultrasonic waves.

The ultrasonic waves modulate the optical phase of the beam through a change in the cavity spacing of the FPI sensor. The optical sensitivity is defined as the change in the reflected light per unit change in the cavity thickness.

An optical model to simulate Interferometer Transfer Functions (ITFs) for a Gaussian beam propagating in a Fabry Perot Interferometer is implemented. An understanding of the Gaussian beam phase propagation in a Fabry Perot Interferometer is presented to help in explaining the shape of ITFs simulated. The model is experimentally validated.

The model is applied as a design tool for the purpose of optimising FPI sensors. This is achieved by choosing the beam radii, mirror reflectivities and cavity spacing's which lead to high optical sensitivity. A FPI sensor with high optical sensitivity and pressure linearity is achieved. A high pressure linearity can be achieved by creating a highly asymmetric ITF, by a combination of a highly diverging beam and aperturing the reflected beam.

The understanding presented in this work helps in designing optimised FPI sensors for ultrasound detection, as well as in providing a general understanding of the effects of Gaussian beams or other types of divergent beams illuminating FPIs.

Acknowledgements

I would like to acknowledge and thank my principal supervisor, Prof. Paul Beard (UCL) for his great amount of support and advice while undertaking this work. I would also like to acknowledge my secondary supervisor, Dr. Ben Cox (UCL) for his support and advice on many aspects of the modelling. Also I would like to acknowledge Dr. Edward Zhang (UCL) for his help in setting up and advising on various aspects of the experimental work for this project.

Table of Contents

Chapter 1 Introduction 1
1.1 Motivation 1
1.2 Aims and objectives 2
1.3 Thesis structure 3
Chapter 2 Methods of detecting ultrasound and photoacoustic waves 4
2.1 Methods of ultrasound detection 4
2.1.1 Piezoelectric ultrasound detectors 4
2.1.2 CMUTs as ultrasound detectors 6
2.1.3 Optical detection of ultrasonic waves 7
2.1.4 Sensitivity of an optical FPI sensor 10
2.2 Photoacoustic imaging and detection with optical FPI sensors 14
2.2.1 Basic theory of the photoacoustic effect 14
2.2.1 Wavelength dependence absorption 15
2.2.2 Application of the Fabry Perot Interferometer in photoacoustic imaging 16
2.3 Design and manufacture of FPI sensors 18
2.3.1 FPI sensor schematic and fabrication 18
2.3.2 Properties of the spacer layer and mirrors 19
2.4 Summary 21
2.4.1 The FPI sensor for medical ultrasound detection 21
2.4.2 Alternative applications of the Fabry Perot Interferometer 21
Chapter 3 The Airy function description of a ITF for a Fabry Perot Interferometer 23
3.1 Fabry Perot theory 23
3.1.1 Airy function 24
3.1.2 Measures of quality of a Fabry Perot Interferometer 28
3.2 Relationship of Airy function with phase and sensitivity definition 30
3.2.1 ITF variation with various phase parameters 30

3.2.2 Expressions for optical sensitivity 32

Chapter 4 Model implementation for a planar and wedged Fabry Perot Interferometer ... 34

4.1 Modelling of Gaussian beam illumination of a FPI 34

4.2 Planar FPI illuminated with a Gaussian beam 35

4.2.1 Gaussian beams of the TE_{00} mode 35

4.2.2 Model of Gaussian beam illuminating a planar Fabry Perot Interferometer 39

4.2.3 Numerical model implementation 40

4.2.4 Computational implementation 43

4.3 Evaluation of the planar FPI model 49

4.4 Model for a Gaussian beam illuminating a wedged FPI 52

4.4.4 Model of Gaussian beam illuminating a wedged Fabry Perot Interferometer ... 52

4.4.5 Numerical model implementation 53

4.4.6 Computational implementation 55

4.5 Evaluation of the wedged FPI model 56

4.6 Model summary 59

Chapter 5 Numerically simulated and experimental ITF_λs of a planar FPI, with interpretation of the ITF_λ shapes 61

5.1 Experimental method 61

5.1.1 Experimental schematic and arrangement 61

5.1.2 Fabry Perot Etalons 68

5.2 Experimental results 70

5.2.1 Comparison of Interferometer Transfer functions (ITF_λs) 70

5.2.2 Comparison of finesse and visibility results 73

5.3 Explanation of asymmetry in ITF_λs for a Gaussian beam illumination 76

5.3.1 Explanation of the shape of ITF_λs for a non-diverging beam 76

5.3.2 Explanation of the shape of ITF_λs for a Gaussian beam 79

5.3.3 Effect of the Gaussian beam phase characteristics on the experimental ITF_λ 95

5.3.4 Effect of phase on visibility 95
5.4 Summary of experimental validation of the planar FPI model 96
Chapter 6 Numerically simulated ITF$_\lambda$s for a wedged FPI, with interpretation of the ITF$_\lambda$ shapes 99
6.1 Results of numerical simulations of a wedged FPI 99
6.1.1 Effect of a wedged FPI on the shape of ITF$_\lambda$s 99
6.1.2 Variation in asymmetry with wedge angle α in a wedged FPI 101
6.1.3 Visibility variation with a wedged FPI 102
6.2 Comparison of finesse and visibility results 104
6.2.1 Finesse variation with beam radius 104
6.2.2 Visibility variation with beam radius 105
6.3 Explanation of the shapes of ITF$_\lambda$ for a wedged FPI 106
6.3.1 Phase progression in a wedged FPI 106
6.4 Summary of ITF$_\lambda$s in a wedged FPI 113
6.5 Experimental method for measuring surface change 114
6.5.1 Measuring non-uniform cavity thicknesses 114
6.5.2 Experimental arrangement for measuring surface non-uniformity 116
6.6 Non-uniformity of spacer layers in FPI sensors 117
6.6.1 Non-uniformity measurements of FPI sensors 117
6.6.2 Effect of non-uniformity of FPI sensors 121
Chapter 7 Defining metrics for characterising the performance of FPI sensors 122
7.1 Defining the optical sensitivity for FPI sensors 122
7.1.1 Definition of optical sensitivity 123
7.1.2 Optimum bias wavelengths according to the optical sensitivity definition 127
7.1.3 Experimental determination of optimum bias wavelength 131
7.2 Noise characteristics of telecomm C+L band (1510-1620nm) laser systems 134
7.2.1 Noise variation with power 134

7.2.2 Noise variation in a Fabry Perot etalon....141
7.3 Summary....143
Chapter 8 Designing optimised Fabry Perot Interferometer sensors....144
8.1 Characterising the FPI sensor performance for various optical parameters....144
8.1.1 Effect of beam divergence and mirror reflectivity on the ITF$_\lambda$....144
8.1.2 Finesse and visibility variation with beam radius....146
8.2 Variation in optical sensitivity by spatial filtering....152
8.2.1 Spatial filtering by a disc aperture....152
8.2.2 Spatial filtering by a ring based aperture....154
8.3 Choice of optimum mirror reflectivities for optimum FPI performance....156
8.3.1 Optimum mirror reflectivities with a non-diverging beam....156
8.3.2 Optimum mirror reflectivities for Gaussian beams....157
8.3.3 Optimum mirror reflectivities for spatially filtered ITF$_\lambda$s and non-linear noise response....164
8.3.4 Choosing the optimum mirror reflectivities....167
8.4 Designing optimum FPI sensors....168
8.4.1 Designing FPI sensors for various applications....168
8.4.2 Effect of surface non-uniformity on optical sensitivity for FPI sensors....172
8.5 Pressure linearity of FPI sensors....175
8.5.1 Calculating the maximum linear pressure amplitude....175
8.5.2 Pressure linearity in asymmetric ITF$_\lambda$s....178
8.5.3 Designing FPIs with high pressure linearity....180
8.5.4 Relating linearity of dl to dλ....180
8.6 Developing the model as a design software tool....182
8.7 Design summary....183
Chapter 9 Modelling alternative Fabry Perot type resonators....185
9.1 FPIs at the tip of fibre GRIN lenses....185

9.1.1 Phase analysis of Gaussian beams along the optic axis 186
9.1.2 Model and experimental arrangement of FPIs being off focus 188
9.1.3 Modelled and experimental results of off-focus FPIs 190
9.2 Hemi-spherical Fabry Perot Interferometer 193
9.2.1 Geometry of Fabry Perot Interferometer 193
9.2.2 Calculation of optimum beam radius 194
9.3 Future directions for modelling high finesse FPI type resonators 199
Chapter 10 Conclusions 201
10.1 Achievements 201
10.2 Novel features 202
10.3 Conclusions 203
10.3.1 Understanding of ITF_λ shapes 203
10.3.2 Optical Fabry Perot Interferometer sensor design 203
10.4 Future directions 204
Appendix A Explicit code for planar and wedged model 206
References 212

Table of definitions

FPI	Fabry Perot Interferometer
ITF	Interferometer Transfer Function
ITF_{φ}	Phase Interferometer Transfer Function
ITF_{λ}	Wavelength Interferometer Transfer Function
ITF_{l}	Cavity Thickness Interferometer Transfer Function
ITF_{n}	Refractive index Interferometer Transfer Function
$dR/d\varphi$	Derivative of the phase ITF_{φ}
$dR/d\lambda$	Derivative of the wavelength ITF_{λ}
$dR/d\lambda_{long}$	Maximum derivative of wavelength ITF_{λ} at long wavelength of reflectivity peak
$dR/d\lambda_{short}$	Maximum derivative of wavelength ITF_{λ} at short wavelength of reflectivity peak
dR/dl	Derivative of cavity thickness ITF_{l}
PA	Photoacoustic
λ_{bias}	Wavelength corresponding to the maximum or minimum of $dR/d\lambda$, of the ITF_{λ}
reflectivity peak	The position around the ITF where the resonance occurs for reflection mode
reflectance minima	The point at which resonance occurs in a ITF for reflection mode

Chapter 1 Introduction

The thesis is written to fulfil the requirements of the degree of Doctor of Philosophy at University College London. The work presented in this thesis was carried out in the Department of Medical Physics and Bioengineering. The thesis details the optical modelling of Fabry Perot Interferometer (FPI) sensors for detecting ultrasonic waves. This modelling work can then lead to the improved design of FPI sensors for better optical performance. This opening chapter gives the motivation for undertaking this work, as well as briefly describing the structure of the thesis.

1.1 Motivation

The conventional method of ultrasound detection is through the use of piezoelectric transducers. The limitations with piezoelectric transducers such as PZT is acoustic impedance mismatch and non-uniform frequency response when in contact with biological tissue and water, although PVDF overcome these problems they suffer from lower sensitivity. Another limitation arises when high frequency (ten to hundreds of MHz) directivity is required, therefore detector sizes much smaller than the acoustic wavelength are needed, which reduces the sensitivity of the piezoelectric detectors [1]. An alternative to piezoelectric is optical sensors.

The main advantage of using optical sensors is the higher sensitivity achieved with small element sizes in comparison to piezoelectric sensors, particularly so for high frequency ultrasound. Additional advantages of optical sensors are that they do not suffer from electromagnetic interference as piezoelectric do, and if building an array of optical sensors they do not require extensive electrical wiring for each array. One method of optical detection of ultrasound is by interferometry. A Fabry Perot Interferometer (FPI) is one such device that detects ultrasonic waves by the incident acoustic pressure wave causing an optical phase modulation. Other optical devices for detecting ultrasonic waves are Fibre Bragg Gratings (FBG). This thesis deals with improving the performance of the Fabry Perot Interferometer sensor, particularly applied to the field of photoacoustic imaging. One of the reasons for improving the performance of the FPI sensor is to detect smaller pressure amplitude waves.

Other reasons are to increase the pressure linearity to detect a wider range of pressure amplitudes.

A certain type of FPI sensor which has been presented by Beard et al is a polymer based optical FPI sensor [2]. This sensor has been shown to provide wide acoustic bandwidth, with a uniform frequency response with detector element volumes being on the order of tens of microns such that the sensor is considered omnidirectional and has high frequency bandwidth. The current finesses achieved have been ~50, with minimum detectable pressures of 0.21 kPa. To improve the detection sensitivity for photoacoustic imaging, one can increase the mirror reflectivities of the Fabry Perot Interferometer (FPI). However this would cause the beam interrogating the FPI sensor to start diffracting within the FPI, leading to a loss in sensitivity. Therefore a study on the optimum parameters needed to obtain high detection sensitivity is required. Also a study on how one can optimise pressure linearity is important in applications such as ultrasound metrology.

1.2 Aims and objectives

The aim of the work described in this thesis is to design optimum FPI sensors with high optical sensitivity and in certain cases high pressure linearity. To achieve this aim several objectives have been identified that need to be achieved. These are outlined below:-

- Develop and implement a numerical model for a planar and wedged FPI illuminated by Gaussian beams of the TE_{00} mode.
- Undertake an experimental validation of the model, to satisfy that the model simulates ITFs one would encounter experimentally.
- Develop an understanding of how the shape of the ITF is affected by the variation in the optical parameters chosen.
- Develop a set of metrics that characterise the performance of the sensor, in order to choose the optimum parameters for beam radius, mirror reflectivities, level of beam aperturing and other such parameters.
- Design and develop optimised FPI sensors that have optimum sensitivity and pressure linearity.

This thesis presents the work to meet these objectives.

1.3 Thesis structure

Chapter 2 describes the traditional methods of ultrasound detection, as well as discussing optical sensors and their detection mechanisms. The current setup for a specific type of Fabry Perot Interferometer sensor used for photoacoustic imaging is presented. Chapter 3 presents the analytical model of a Fabry Perot Interferometer for a non-diverging beam. Chapter 4 presents the development of a planar and wedged FPI illuminated by a Gaussian beam, as well as the numerical evaluation of the model. Chapter 5 describes the experimental arrangement and the comparison of the results between model and experiment. It also presents an explanation of the shape of ITFs. Chapter 6 presents the results of the simulation of ITFs for a wedged FPI illuminated by a Gaussian beam. It also extends the explanation of the shape of the ITF in Chapter 5 to explain the ITFs for a wedged FPI. Chapter 7 defines how to bias the FPI sensor, based on the definition of optical sensitivity. Also a noise analysis of the system is presented which is important in defining the metrics. Chapter 8 uses the understanding gained in chapters 5 and 6, as well as chapter 7 to optimise the FPI sensor to obtain the highest optical sensitivity and pressure linearity. Chapter 9 presents how to design FPI sensors that can overcome the limitations posed by planar FPIs. Chapter 10 summarises and concludes the work presented in this thesis.

Chapter 2 Methods of detecting ultrasound and photoacoustic waves

This chapter describes the various types of ultrasound detectors, such as piezoelectric devices and their limitations in terms of acoustic impedance, non-uniform frequency response as well as reduction in sensitivity with small element sizes. Certain types of optical sensors are advantageous in the detection of ultrasound with small element sizes. The type of ultrasound concentrated on is medical ultrasound applications (5 MHz to 100 MHz), especially in regards to the field of photoacoustic imaging. This chapter also provides a brief overview of biomedical photoacoustics and how the optical FPI sensor is designed for this application. This chapter does not go into the details of various sources of ultrasound and applications of ultrasound.

2.1 Methods of ultrasound detection

2.1.1 Piezoelectric ultrasound detectors

Traditional ultrasound detectors are made using piezoelectric materials [1]. The piezoelectric effect is an electro-mechanical effect which occurs in crystalline materials such as quartz, Rochelle salt or piezoelectric ceramics such as Lead-Zirconate-Titonate (PZT), and Lithium Niobate ($LiNO_3$) which is also optically transparent. As a mechanical deformation is applied to the piezoelectric material, this results in a change in the AC (alternating current) voltage across the material. Conversely if the applied voltage varies across the material, this leads to a mechanical contraction or expansion forming an ultrasound wave. This change in the voltage is because of dipole moments forming a charge distribution in the crystals. An incident pressure wave alters the charge distribution leading to a change in the voltage across the material. The detection sensitivity of incident ultrasound waves is affected by the acoustic impedance mismatch between the medium and the piezoelectric detector. This is because of acoustic reflections between the boundary of the medium and detector due to the acoustic impedance mismatch. The characteristic acoustic impedance of piezoelectric materials is dependent on the density of the material ρ, and the speed of the acoustic wave in the material.

Table 1 shows some properties of various piezoelectric materials, as well as properties of various human tissues. Materials such as PZT have high sensitivity but suffer from acoustic impedance mismatch with water and human tissue. The piezoelectric polymer material polyvinylidene diflouride (PVDF) has a closer acoustic impedance matching to water and various other human tissues, resulting in a uniform frequency response, as the amplitude of the acoustic reflections is less, resulting in reduced resonances in the detector at certain frequencies. The disadvantage of PVDFs is that they suffer from reduced sensitivity [3].

Material	**Sound velocity (longitudinal) (m/s)**	**Density ρ_0 (g/cm^3)**	**Characteristic acoustic impedance z_0 (10^6 $kgm^{-2}s^{-1}$)**
Quartz (x-cut)	5700	2.65	15.3
Lead zirconate titanate (PZT-5A)	4350	7.75	33.7
Lead Metaniobate	3330	6.0	20.5
Polyvinylidene fluoride (PVDF)	2200	1.78	4.2
Water	1	1480	1.48
Blood	1.055	1575	1.66
Fat	0.95	1450	1.38
Bone axial (longitudinal waves)	1.9	2800	5.32

Table 1 Properties of Piezoelectric materials and various tissues

Other limitations of piezoelectric materials are their susceptibility to electromagnetic interference as well as reduced sensitivity with smaller element sizes. The transducer constant S defined as the applied force to the voltage, is a measure of its sensitivity,

$$S = \frac{eA}{d} \qquad 2.1$$

where *e* is the electron charge, *A* is the surface area and *d* the thickness of the transducer respectively [1]. The transducer constant S is a measure of its sensitivity. Equation 2.1 shows that a smaller detector area *A* results in a smaller sensitivity. This is because the total electric potential across the surface area of the transducer is reduced with smaller element sizes. Small element sizes are needed when the detector needs to omnidirectional, as well as improving the spatial resolution of the acoustic wave front that is to be measured.

2.1.2 CMUTs as ultrasound detectors

An alternative to piezoelectric materials as ultrasound detectors and transmitters are capacitive micro-machined ultrasound transducers (CMUTS). The mechanism of operation is the creation of a potential between two charged plates. As an ultrasonic wave impinges on the CMUTs the electric field between the charged plates is altered, hence the voltage across the two plates is altered forming the basis of the signal [4], [5]. For transmitting ultrasound, the voltage applied across the CMUT is varied, resulting in a deflection of one of the plates, as the other is fixed. This deflection causes a change in the surrounding pressure forming an acoustic wave which propagates through the surrounding medium. They have been applied in the field of photoacoustic imaging [6], although like certain piezoelectric detectors, are not transparent. This is a problem when the acoustic waves needs to be detected on the same side as the optical illumination of the tissue (Reflection mode imaging) for generating photoacoustic waves. Reflection mode imaging is required for imaging blood vessels or other superficial structures close to the surface of the skin. Therefore CMUTs are used in transmission mode photoacoustic imaging, where they are placed on the opposite side of the excitation light with the tissue sample in between. This results in an experimental arrangement which may be far from ideal particularly for certain clinical applications.

2.1.3 Optical detection of ultrasonic waves

Ultrasound detectors based on optical methods have been extensively studied for various applications. This thesis considers an optical sensor based on interferometric methods, hence the two main types of optical interferometric sensors are reviewed in this section. The fundamental principle relies on measuring the change in the optical phase modulation of the detected light via the change in the measured intensity. This sub-section details the Fibre Bragg Gratings (FBG) and Fabry Perot Interferometer (FPI) sensors for ultrasound detection.

2.1.3.1 Fibre Bragg gratings (FBG)

Optical fibre Bragg gratings have been utilised for detecting pressure and strain variations [7], [8], as well as in underwater acoustics [9]. The ultrasonic waves impinging on the FBGs causes a change in the density of the optical fibre gratings by inducing a strain. This density change is converted to a change in the refractive index which causes a change in the optical path difference of the light, leading to a change in the intensity of the transmitted and reflected light from the optical fibre.

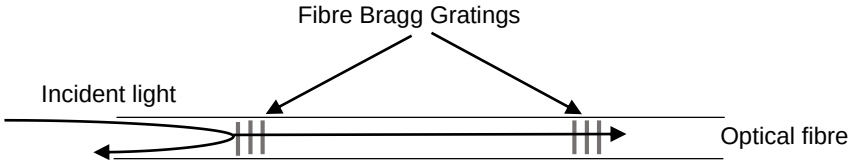

Figure 2-1 Diagram of a optical Fibre Bragg Grating

Figure 2-1 shows a schematic of an inline optical Fibre Bragg grating. The reflected wavelength (Bragg wavelength) is defined as,

$$\lambda_B = 2n_e\Lambda \tag{2.2}$$

where λ_B is the Bragg wavelength, n_e the effective refractive index and Λ the period of the grating. The bandwidth $\Delta\lambda$ of the grating is defined as,

$$\Delta\lambda = \left(\frac{2\delta n_0 \eta}{\pi}\right)\lambda_B \tag{2.3}$$

where δn_0 is the variation in the refractive index, and η is the fraction of power in the fibre core. Therefore a change in the refractive index by the induction of strain will change the

bandwidth of light reflected or transmitted through the fibre. The sensitivity is defined as the change in the refractive index d*n* per unit of strain dε ($dn/d\varepsilon$). The Fibre Bragg gratings have been utilised as an array of sensors for sensing acoustic waves [10], [11], [12] and vibrations with applications as diverse as monitoring the vibration and strain on aircraft wing structures [13] to real time monitoring of buildings and other such structures [14], [15], [16]. In medical applications it has found use in the monitoring of ultrasound doses delivered to tissue samples, particularly that of high frequency ultrasound (HIFU) [17], [18], [19] with minimum detectable pressure levels of 0.52 kPa in ultrasound frequency range of 10 MHz to 20 MHz when in the form of a optical hydrophone. Wang et al [20] have presented a FBG at the tip of optical fibre to measure HIFU doses with minimum detectable pressure of 10.4 kPa, and acoustic sensitivities of 31.3 mV/MPa. The FBGs have higher sensitivity than a conventional PVDF hydrophone [21]. These type of sensors are also beneficial in bio-mechanical studies in-vivo to characterise the forces in various animal tissues [22]

2.1.3.2 Fabry Perot Interferometers (FPI)

Another method of optical detection of ultrasonic waves is by the use of Fabry Perot Interferometers(FPI) [23], [24], [25], [26]. These are in the form of optical polymer FPI sensors [27], [28], and fibre optic hydrophones [29] at the tip of optical fibres with frequency ranges down to 100 kHz to 500 kHz being detected [30], by use of an absorbing acoustic waveguide in front of the acoustic source. This thesis details the optical modelling of Fabry Perot Interferometer sensors to improve their performance. The method of detection of ultrasound by FPIs is as follows:- As the acoustic waves impinge on the FPI sensor it causes a change in the cavity thickness. This change in cavity thickness leads to change in the optical phase of the beam, leading to a change in the reflected or transmitted light from the FPI[8], when at the maximum slope of the ITF.

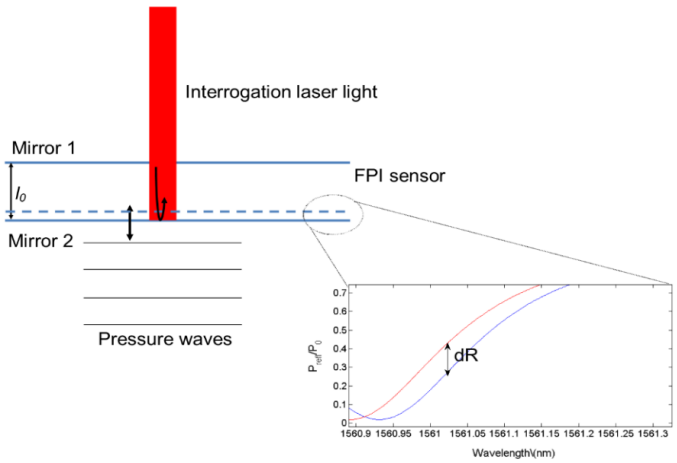

Figure 2-2 Mechanism of detecting acoustic waves, as the pressure contracts the thickness of the cavity changes which alters the power of the reflected light

Figure 2-2 shows the mechanism for the detection of acoustic waves. As the pressure wave impacts with the FPI sensor, it causes a change in the cavity thickness. As a consequence the incident light interrogating the FPI undergoes a change in phase, leading to a change in the reflected light. The FPI sensor has been a promising application in photoacoustic imaging. The work in this thesis will primarily focus on the scale of FPI sensors used for photoacoustic (PA) imaging [27], [32]. The ultrasound frequencies usually encountered in photoacoustic imaging is in the tens of MHz regime [33], with minimum detectable pressures of 0.2 kPa, which is slightly better than the FBG sensors at 0.52 kPa. The acoustic wavelengths are in the range of sub-millimetres to a millimetre. The cavity thicknesses of typical FPI sensors are on the scale of tens of microns, ranging from 10 μm to 80 μm. This is much smaller than the acoustic wavelengths. The optical FPI sensor allows for uniform frequency response of 39 MHz at -3dB with detector elements on the size of a few tens of microns. The broadband nature allows the FPI sensor to measure down to low frequencies of hundreds of kHz, compared to traditional piezoelectric detectors which are highly resonant when damped.

2.1.4 Sensitivity of an optical FPI sensor

2.1.4.1 *Biasing the FPI sensor*

The FPI sensor is biased at the maximum slope of the reflectivity or transmission peak of the ITF [34]. The ITF and definition of optical sensitivity is derived from the simple Airy model. However in high finesse FPI structures where the mirror reflectivities are greater than 90%, the effect of beam divergence and non-uniformities will cause the ITF to depart from that of the ideal Airy function.

2.1.4.2 *Defining the optical phase sensitivity*

The optical sensitivity or optical phase sensitivity as it is sometimes termed is defined by the change in the reflected light for a small change in the phase. The round trip phase of the light for a non-diverging beam in the cavity is expressed as,

$$\varphi = \frac{4\pi n l}{\lambda} \tag{2.4}$$

where l is the cavity spacing, n the refractive index and λ the wavelength. The phase is related to the phase ITF_{φ} by the Airy function R as,

$$R = \frac{F \sin(\frac{\varphi}{2})^2}{1 + F \sin(\frac{\varphi}{2})^2} \tag{2.5}$$

where F is the coefficient of finesse. Therefore a maximum change in the reflected light dR occurs at maximum of the derivative of Eqn. 2.5 with respect to the phase φ. This is termed the optical sensitivity S_0, and defined as,

$$S_0 = \frac{dR}{d\varphi} \tag{2.6}$$

A high optical sensitivity is achieved when a small modulation in phase dφ produces the largest change in the reflected light dR. For a non-diverging beam this can be achieved by increasing the mirror reflectivities to make the slope of the reflectivity peak sharper.

2.1.4.3 *Defining the acoustic sensitivity*

The acoustic sensitivity in FPI sensors is defined as the modulation of the optical phase by a pressure d*p*. To achieve a modulation dφ for a given pressure change d*p*, the expression for the acoustic sensitivity S_A is,

$$\frac{d\varphi}{dp} = \frac{\partial\varphi}{\partial l}\frac{\partial l}{\partial p} + \frac{\partial\varphi}{\partial n}\frac{\partial n}{\partial p} \tag{2.7}$$

Substituting Eqn. 2.4 for φ into Eqn. 2.7 leads to the expression,

$$\frac{d\varphi}{dp} = \frac{4\pi n}{\lambda}\frac{\partial l}{\partial p} + \frac{4\pi l}{\lambda}\frac{\partial n}{\partial p} \tag{2.8}$$

It is assumed the ratio Δ*n*/*n* is much less than the ratio of Δ*l*/*l* expressed as,

$$\frac{\Delta n}{n} \ll \frac{\Delta l}{l} \tag{2.9}$$

It was found that the refractive index variation with pressure was negligible by Cox. B who found that Δ*nl*/*n*Δ*l* was found to be 0.001 in the range of frequencies, cavity spacings and material properties typically associated with the FPI sensor for PA imaging [33]. For acoustic detection, the modulation of the cavity spacing is the main source of the phase change. The change in the cavity spacing d*l* per unit of pressure d*p* is expressed as,

$$\frac{dl}{dp} = \frac{l}{E} \tag{2.10}$$

which is obtained by rearranging the expression for Young's modulus E in terms of d*l*/d*p*. The product of the change in cavity thickness d*l* per unit pressure d*p* expressed in Eqn. 2.10 with Eqn. 2.8 results in the following expression,

$$S_A = \frac{d\varphi}{dp} = \frac{4\pi n}{\lambda}\frac{l}{E} \tag{2.11}$$

which is the definition of acoustic sensitivity of FPI sensors. This suggests that for increasing *l* and a small Young's modulus E, the acoustic sensitivity increases.

2.1.4.4 *Sensitivity definition for a FPI sensor*

The product of the optical sensitivity S_0 defined in Eqn. 2.6 with the acoustic sensitivity definition S_A in Eqn. 2.11 defines the overall sensitivity S. The sensitivity is therefore expressed as,

$$S = \frac{dR}{dp} = \frac{dR}{d\varphi}\frac{d\varphi}{dp}$$
$$S = \frac{dR}{d\varphi}\frac{4\pi n}{\lambda}\frac{l}{E} \tag{2.12}$$

The acoustic sensitivity has certain requirements in terms of choice of cavity thickness for large acoustic bandwidth. Also the spacer material forming the FPI cavity has certain mechanical and optical properties. To increase the sensitivity, therefore requires building FPI sensors with higher optical sensitivities. To design FPI sensors with higher optical sensitivity could be achieved by increasing the mirror reflectivities. However the scale of the beam radius used is a few tens of microns, and where the diffraction free range is comparable or less than the distance propagated on a round trip in the cavity. Therefore the beam would diverge in the cavity and cause a departure in the ITF from the ideal Airy function. This is because of the divergent walk-off of the beam. Therefore an implementation of a model to simulate Gaussian beam propagation in a FPI is required. This will aid in the optimum choice of beam radius, mirror reflectivities and choice of other optical parameters to achieve high optical sensitivity. Modelling work by Guo. D [35] focussed on Fabry Perot diaphragm

structures to detect pressure waves. This was done for low finesse cavity thickness ITF_ls by a pressure wave with a 1 mm beam waist. This was so reasonable sensitivity and pressure linearity can be achieved. For these parameters it can be approximated as a plane wave beam incident on FPI sensor. Wilkinson et al [36] also modelled a low finesse ITF_ls for a FPI on the tip of an optical fibre for the purpose of pressure measurements. The model was combined with the effect of the fibre coupling of the reflected light from the FPI. A study implementing a numerical model to analyse the effect of wavelength ITF_λs for high finesse FPIs (R>90%, these mirror reflectivities will give higher optical sensitivities) to choose the optimum parameters that give the highest optical sensitivity as well as provide a large pressure linearity has not been undertaken. This thesis undertakes this work to develop FPI sensors that can provide high optical sensitivity, but also provide high pressure linearity, with particular focus on the polymer FPI sensors for photoacoustic imaging.

2.2 Photoacoustic imaging and detection with optical FPI sensors

The FPI sensor is applied in the detection of photoacoustic waves. The scale of the cavity thickness and beam radius is chosen based on the acoustic wavelengths encountered in photoacoustic imaging. This section provides a brief overview of biomedical photoacoustics. This is important in designing FPI sensors for photoacoustic imaging as is detailed in section 2.3.

2.2.1 Basic theory of the photoacoustic effect

The photoacoustic effect was first realised in 1880 by Alexandar Graham Bell, from the observation of sound created by light [37] in various materials. Photoacoustic imaging (PA imaging) is based on the same principle, where a nanosecond pulse of laser light irradiates a biological tissue surface. The light propagates into the tissue, where it is scattered and absorbed by certain molecules termed chromophores. These chromophores have wavelength dependence absorption and scattering [38]. The absorbed laser light by the molecules results in a temperature rise at constant volume. This temperature rise leads to an increase in the ambient pressure through increasing vibrations, forming an acoustic wave that travel to the surface of the tissue [39], [40]. The acoustic wave is then detected by an array of ultrasound detectors. Figure 2-3 shows the photoacoustic effect in tissue structures and the application of free space optical FPI sensor to detect the ultrasound wave. The detected acoustic waves are in the region of MHz frequencies in the ultrasound regime [41]. The pressures usually generated in PA are in the region of a few kPa to 100 kPa.

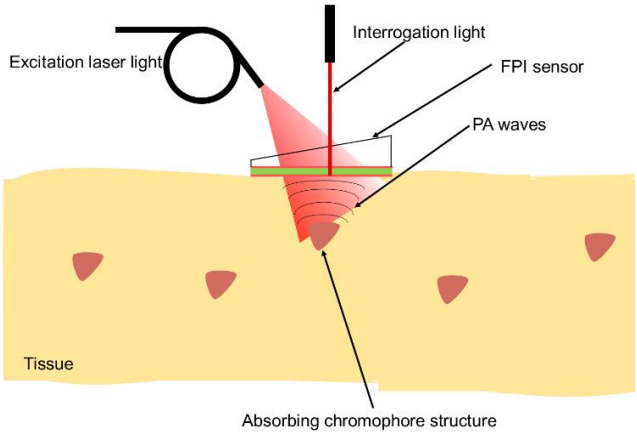

Figure 2-3 Diagram showing the photoacoustic effect, with laser light irradiating the tissue causing certain absorbing chromophores to give rise to a pressure change that creates an acoustic wave detected by the optical FPI sensor at the surface

The speed of ultrasound close to the surface of the skin in human tissue varies from 1450 ms^{-1} in fat to 1570 ms^{-1} in blood and 2800 ms^{-1} in bone. For ultrasound frequencies of tens to hundreds of MHz, the acoustic wavelength is a tenth of a millimetre. This is important in choosing the cavity thickness of FPI sensors to obtain a broadband ultrasound sensor. The cavity thickness of typical FPI sensors are in the region of a few tens of microns, which is a thousandth of the acoustic wavelength, therefore the FPI senor can be considered acoustically transparent.

2.2.1 Wavelength dependence absorption

The wavelength dependence of the absorbing chromophores is important in the design of optical FPI sensors, as will be explained in section 2.3. As PA imaging is absorption based it can be used to resolve the tissue and chromophore composition [42], as different chromophore will absorb a greater amount of light at certain wavelengths [43]. Figure 2-4 shows the spectral dependence of the absorption coefficient μ_a for oxy- and deoxy-haemoglobin.

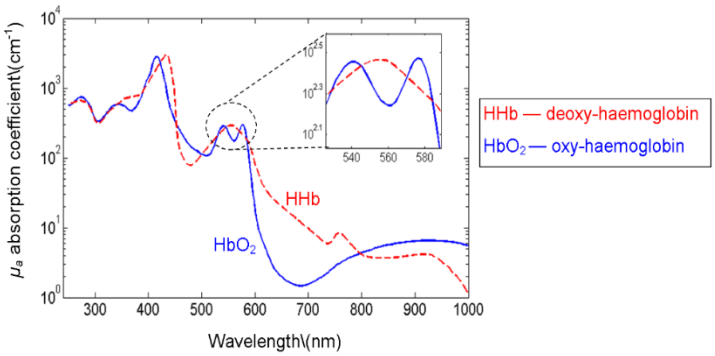

Figure 2-4 Spectral dependence of μ_a (absorption coefficient) for HHb (deoxy-haemoglobin) [dashed red line], and HbO_2 (oxy-haemoglobin) [solid blue line]
(http://omlc.ogi.edu/spectra/hemoglobin/summary.html)

There are two absorption peaks for the Haemoglobin chromophores, one at around 390-400 nm, while the second one is between 530-590 nm. The difference in the absorption coefficient between these two wavelength ranges are a factor 10. In PA imaging when using the FPI sensor, both haemoglobin chromophores can be excited at a wavelength of 390 nm or 580 nm. There are many other chromophores, which are highly absorbing at certain wavelengths allowing PA imaging to distinguish between specific chromophore structures in the tissue [44].

2.2.2 Application of the Fabry Perot Interferometer in photoacoustic imaging

The Fabry Perot Interferometer (FPI) sensor is applied in the detection of ultrasonic waves generated by the photoacoustic process. The FPI sensor is transparent at optical wavelengths to allow the excitation light through into the tissue, whereas conventional piezoelectric transducer arrays are at a disadvantage as the experimental system needs to be modified to allow the light to illuminate the tissue. The Fabry Perot Interferometer sensor presented by Beard et al [27] allows the photoacoustic imaging of blood vessels and superficial structures close to the surface of the tissue, whereas with piezoelectric sensors, the imaging would have to be done in transmission mode where the ultrasound wave would have to pass through the tissue. This transmission of the ultrasound wave through tissue would cause it to be attenuated leading to a reduced signal amplitude. This is a problem when imaging soft tissue and superficial structures close to the surface of the skin. There has been literature on overcoming these problems with an annular ring or spherical array with the excitation light delivered through the centre [45], [46], or creating a probe where the photoacoustic waves are reflected onto the ultrasound detector [47]. This is less than ideal as the illuminated features would be out of the field of view of the ultrasound detector in comparison to an optically transparent detector. Therefore the optical Fabry Perot Interferometer addresses this problem, where a single beam can be scanned across the Fabry Perot Interferometer sensor, allowing it to acquire signals sequentially across the area of the sensor. This data is then used to reconstruct the wavefront of the incident ultrasonic wave [48]. The spatial resolution of the wavefront is on the order of a few tens of microns.

The work in this thesis aims to primarily improve the detection sensitivity of the Fabry Perot Interferometer for photoacoustic imaging. This is so that the signal to noise ratio improves thus being able to detect smaller pressure amplitudes. This would benefit the field of photoacoustics as high frequency ultrasound wave components which are highly attenuated, can be detected helping to improve the image reconstruction. The FPI sensor can also be useful in the field of ultrasonic measurements. Certain examples of ultrasonic measurements are in the field of High Frequency Ultrasound (HIFU) used in monitoring the ultrasound dose delivered during medical treatments [49], [50], [51]. The Fabry Perot Interferometer has potential applications in this field as it can be fabricated on the tip of optical fibres to monitor the dose in-vivo [52], [53]. Yang et al [54] reported the integration of photoacoustics with HIFU to treat solid tumours. This was achieved using a single US transducer with a central frequency of 5 MHz to detect photoacoustic waves from the tissue and transmit HIFU fields

to the target. The Fabry Perot Interferometer sensor for PA imaging could play a role in the real time acquisition of photoacoustic images of the target of interest, to monitor the effect of the HIFU field [55]. The FPI sensor can also be utilised in ultrasound metrology [56], where optical schlieren techniques [57] are being used to image acoustic beams with features as small as a few tens of microns at frequencies of greater than 110 MHz [58]. The FPI can image such acoustic beams as the element sizes are on the order of a few tens of microns.

The FPI sensor has also been used to monitor the effectiveness of various medical treatments [59], by combining photoacoustic imaging with other optical imaging modalities such as Optical Coherence Tomography (OCT) [60]. The Fabry Perot Interferometer can also be used in thermo-acoustic imaging (TA imaging), where the tissue is heated by microwaves [61], [62], [63]. The microwaves excite features deeper in the tissue, up to a few centimetres. The detected acoustic signals would have a very low amplitude due to the attenuation of the ultrasound by the tissue material, hence an improvement in the signal to noise ratio of the FPI sensor would make it available for use in thermo-acoustic imaging. The following section describes the current design of the FPI sensor and how it is manufactured.

2.3 Design and manufacture of FPI sensors

This section describes the design of the optical FPI sensor applied for photoacoustic imaging. This section details the fabrication of the FPI sensor, taking into account the optical design consideration which arises from the understanding of the photoacoustic process.

2.3.1 FPI sensor schematic and fabrication

The optical FPI sensor consists of two mirror coating which are separated by a spacer layer composed of Parylene-C. The FPI sensor is built on an optically transparent Perspex substrate, as shown in Figure 2-5 below.

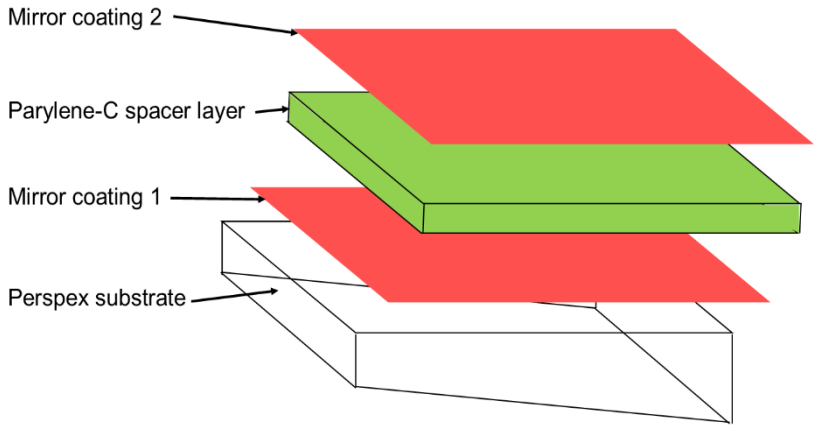

Figure 2-5 Design schematic of the FPI sensor, which is built on a optically transparent perspex substrate

The substrate is wedged to prevent parasitic interference due to the Fresnel reflection coefficients formed by the refractive index mismatch between the perspex and surrounding medium [27]. The dielectric mirrors are composed of quarter wavelength stacks of low and high refractive index material. The first mirror (coating 1) is deposited directly onto the substrate via a vacuum sputtering mechanism. The spacer layer between the mirrors is then deposited onto the first coating. The usually cavity thicknesses formed are typically on the order of a few tens of microns. This is so that a wide acoustic bandwidth is achievable, as the acoustic waves are on the scale of sub-millimetres to a millimetre. The spacer layer material is composed of a polymer that is Parylene-C, which is in a pellet type form and is heated forming a gas, and is then deposited in vacuum onto the sensor, via a chemical vapour deposition method [64], [65], [66]. The second mirror coating (coating 2) is then deposited onto the Parylene-C. Then finally a thin film of Parylene-C is coated onto the sensor to protect it from water ingress and abrasion, which is not shown in Figure 2-5.

2.3.2 Properties of the spacer layer and mirrors

2.3.2.1 *Properties of the spacer layer*

Listed below in the table are some properties of the Parylene-C material[1],

Properties	**Parylene-C properties**
Young's modulus, E	2.9 GPa
Index of Refraction	1.639
Water absorption (% after 24 hrs)	<0.1
Specific Heat (@ 20 ^{0}C) (J/g*K)	0.712
Linear coefficient of thermal expansion at 25 ^{0}C (ppm)	35

Table 2 Various properties of Parylene-C

The Parylene-C has very low absorption at optical NIR (Near Infra-red) wavelengths, which makes it a useful material to use in the sensor. A pressure amplitude of a few kPa creates a change of a few nanometres in the spacer layer which is significant to measure a detected change in the reflected light, as the Young's modulus is 2.9 GPa which is a factor of 10^6 greater than the pressures detected.

[1] Speciality Coating Systems, Properties of Parylene. *Data Sheet*.

2.3.2.2 *Dielectric mirror properties*

The dielectric mirrors on either side of the spacer layer forms the resonant cavity, with a cavity thickness of *l*. The dielectrics mirrors have very low power absorption, such that the relationship between the transmitted power T and reflected power R is as follows

$$1 = R + T \qquad 2.13$$

and where the effects of absorption have been ignored. Figure 2-6 shows the transmission spectrum of the dielectric mirrors.

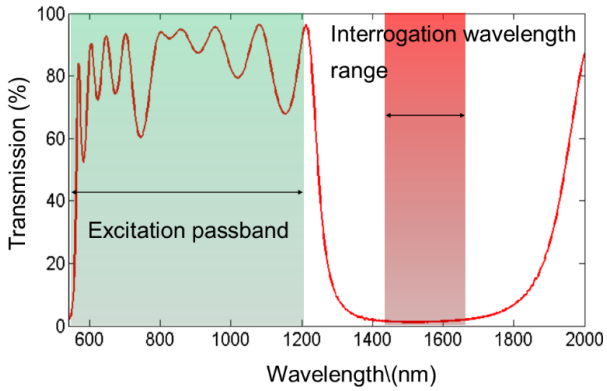

Figure 2-6 Transmission spectrum of the dielectric mirrors forming the Fabry Perot Interferometer sensor

The mirrors are highly transmissive between 580 and 1200 nm, which forms the excitation pass band. This is because the absorption coefficient of most chromophores are high in this region as shown in Figure 2-4 for haemoglobin, therefore the higher the transmission the greater the light power transmitted into the tissue, to generate photoacoustic waves. This is therefore advantageous over traditional piezoelectric ultrasound detectors because of its optical transparency at these wavelengths. Therefore it allows backward mode imaging, where the signal is detected on the incident side of illumination, and is useful for imaging features close to the surface of the tissue. Between 1500 nm and 1650 nm the transmission is low, hence high reflectivities. At these wavelength corresponding to the telecoms bandwidth the optical FPI sensors is interrogated with robust and low cost semiconductor diode lasers with a wide wavelength tuning range. Increasing the mirror reflectivities at these wavelengths would lead to increased optical sensitivity for a non-diverging beam. However for small

beams comparable to the cavity thickness, this would cause the beam to diffract and have an effect on the optical sensitivity.

2.4 Summary

2.4.1 The FPI sensor for medical ultrasound detection

This chapter has described the various methods of ultrasound detection and some of its limitations. Optical sensors based on Fabry Perot Interferometry can overcome some of these limitations. One such application of the FPI is in photoacoustic imaging. Section 2.2 and section 2.3 described the photoacoustic effect and the current setup of the FPI sensor for PA imaging, and can be applied for clinical photoacoustic imaging [67]. This requires high sensitivity and wide acoustic bandwidth, and which is robust for clinical and biomedical imaging scenarios, which the Fabry Perot Interferometer can address. The work in this thesis models the optical FPI characteristics with the aim of improving the design of the sensors for wide variety of applications in the field of medical ultrasound. This will be achieved by improving the optical sensitivity such that ultrasound waves from deeper within the tissue can be detected, as well as imaging the acoustic wavefront with better spatial resolution and sensitivity, by using smaller beam radii which defines the element size of the detector.

2.4.2 Alternative applications of the Fabry Perot Interferometer

The work undertaken in this thesis can also contribute to the general development of Fabry Perot Interferometers in a wide variety of applications. As well as ultrasound detection, the Fabry Perot is also applied in vibrational detection [68] and strain measurements [26] to measure the magnitude of vibrations in industrial machinery, as well as in aeronautical design. The Fabry Perot Interferometer has found applications in temperature sensing [69], [70], [71], [72], as well as in humidity sensing [73]. In temperature sensing the cavity is changed by a heating effect of the cavity spacer layer, which in turn changes the phase of the beam in the cavity [74]. Also in certain applications in chemical analysis, the optical Fabry Perot Interferometer sensor is used to measure the chemical composition of the liquid material between the cavity by a change in its refractive index [75], [76]. Therefore the understanding of the parameters which affect the detection sensitivity in this work can also be applied in developing better Fabry Perot Interferometer sensors in other applications.

The Fabry Perot also has applications in wavelength division multiplexing, where the signal at the end of the optical transmission line is spectrally filtered, such that higher rates of data can be passed over the transmission line [77], [78]. The Fabry Perot is also applied in controlling the laser linewidth and the spectral filtering of laser light [79], [80] as well as in the formation of laser cavities with a gain medium [81]. The FPI is also useful in the study of Brillouin scattering [82]. An understanding of how to better control the shape of the ITF can benefit the development of Fabry Perot Interferometers for better linewidth control as well as having the ability to control the spectral output of the laser, which the work in this thesis would provide. This section has described some of the wider applications of the Fabry Perot Interferometer. The work in this thesis can help to develop a method for improving the design of FPIs for a wide range of applications.

Chapter 3 The Airy function description of a ITF for a Fabry Perot Interferometer

The Fabry Perot Interferometer was first proposed by Charles Fabry and Alfred Perot for resolving the wavelength spectrum of light [83]. The first section within this chapter, section 3.1 describes the physics of Fabry Perot Interferometry and presents a derivation to the Airy function, which describes the power vs. phase relationship, which has a series of resonance peaks spaced 2π apart. The theory of the Fabry Perot Interferometer assumes a plane wave beam, with perfectly parallel mirrors. Section 3.2 describes the relationship of ITFs between different parameters.

3.1 Fabry Perot theory

A Fabry Perot Interferometer consists of two thin partially reflecting and transmitting mirrors. The structure of a planar Fabry Perot Interferometer (FPI) is a sandwich like structure as shown in Figure 3-1, where the spacing between the two mirrors is l_0, with the medium between the two mirrors having a refractive index n_c, which is different to the refractive index of the surrounding medium n_s. The Fabry Perot Interferometer is an interferometer based on amplitude division of the electromagnetic waves [84]. The incident beam is partially reflected of the incident mirror of illumination which has amplitude reflection coefficient r_1. The transmitted beam into the cavity is reflected and transmitted on each incidence with the mirrors. A complete round trip by the beam occurs when the electric field is incident on the internal surface of mirror 1 with amplitude coefficient r_1' after propagating a distance of twice the mirror spacing $2l_0$. This results in interference of the reflected fields $E_{r,2}$, $E_{r,3}$, $E_{r,4}$, which are transmitted from the cavity, with that of the electric field $E_{r,1}$.

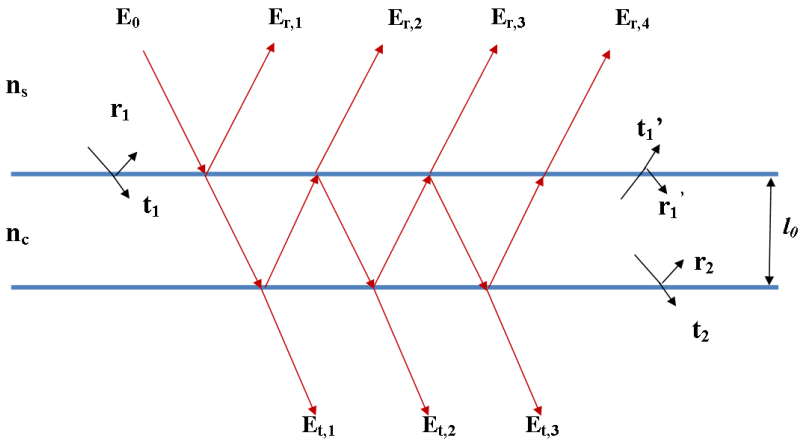

Figure 3-1 Fabry Perot Interferometer with amplitude mirror reflection coefficients of r_1 and r_1' for mirror 1 and r_2 for mirror 2. The transmission amplitude coefficients are t_1 and t_2 for mirror 1 and mirror 2 respectively, with transmission t_1' at mirror 1 from within the cavity.

3.1.1 Airy function

The electric field E which is incident on the FPI, is described by the phase and initial amplitude E_0. The electric field in the following analysis assumes a plane wave, non-diverging beam. The summation of the total electric fields transmitted from the cavity at mirror 1 leads to interference with the field reflected of the incident mirror. As the phase of the electric field is varied in the cavity, the electric field destructively interferes with the electric field reflected of the first mirror. This leads to the Interferometer Transfer Function ITF_φ in terms of phase φ. The transmission mode ITF is the compliment of the reflection mode ITF_φ, assuming there is no absorption present in the FPI. Therefore the electric fields for the first three round trips in reflection mode and in general for the m^{th} round trip are expressed in Eqn. 3.1,

$$
\begin{aligned}
E_1 &= {t_1}^2 r_2 \mathrm{e}^{-\mathrm{i}(\mathrm{k}2l-2\pi\mathrm{ft})} E_0 \\
E_2 &= {t_1}^2 {r_2}^2 r_1' \mathrm{e}^{-\mathrm{i}(\mathrm{k}4l-2\pi\mathrm{ft})} E_0 \\
E_3 &= {t_1}^2 {r_2}^3 {r_1}'^2 \mathrm{e}^{-\mathrm{i}(\mathrm{k}6l-2\pi\mathrm{ft})} E_0 \\
&\ldots. \\
&\ldots. \\
E_m &= {t_1}^2 {r_2}^m {r_1}'^{(m-1)} \mathrm{e}^{-\mathrm{i}(\mathrm{k}2ml-2\pi\mathrm{ft})} E_0
\end{aligned}
\qquad 3.1
$$

where the amplitude transmission coefficient for the incident mirror is t_1, and where r_1' and t_1' is the amplitude reflection and transmission coefficient respectively of mirror 1 inside the cavity. Mirror 2 has amplitude reflection and transmission coefficients r_2 and t_2 respectively. The distance propagated on a complete round trip is 2ml, where m is the round trip number, and the factor of 2 arises due to the beam having to undergo twice the cavity spacing *l* to return to mirror 1. The summation of the electric fields which have undergone m number of round trips with the electric field reflected of the first mirror is shown in Eqn. 3.2,

$$E_{total} = r_1 E_0 e^{i(kz-2\pi ft)} + \sum_{m=0}^{\infty} t_1 t_1{}' r_1{}'^{(m-1)} r_2^m E_0 e^{i(k2ml-2\pi ft)} \qquad 3.2$$

where r_1 is the amplitude reflection coefficient at the first mirror. The reflection and transmission coefficients are less than 1; therefore the beam loses amplitude on each incidence with the mirrors. The summation of the electric field which have undergone m number of round trips in the cavity converges to zero when the electric fields have undergone a significant amount of round transits in the cavity. When both mirror reflectivity amplitude are equivalent, that is $r=r_1=r_2$, and $r<1$ and $t<1$ the electric field summation is a geometric series and Eqn. 3.2 reduces to,

$$E_{total} = \left(re^{i(kz-2\pi ft)} + \frac{1}{1-t^2 re^{i(kz-2\pi ft)}} \right) E_0 \qquad 3.3$$

The intensity is the time average of the square of the electric field, as expressed in Eqn. 3.4. This leads to the ITF_λ which is the total reflected power from the incident mirror of illumination, which changes as the wavelength is varied, leading to reflectivity peaks. The analytical solution for the total reflected power can be obtained by using the expression for E_{total} in Eqn. 3.3 and multiplying by its complex conjugate.

$$I_{total} \propto \frac{< {E_{total}}^2 >}{2} \tag{3.4}$$

The analytical expression (Airy function) for the reflected light power from the Fabry Perot Interferometer for a non-diverging beam is presented in Eqn. 3.6. P_{refl} is the total reflected power as a function of phase φ. F is the coefficient of finesse, defined in Eqn. 3.5 which is used as a measure of the broadness of the peaks. R is the power reflection coefficient which is related to the amplitude reflection coefficient by $R=r^2$ for normal incidence of the beam on the mirrors.

$$F = \frac{4R}{(1-R)^2} \tag{3.5}$$

$$P_{ref} = \frac{F \sin(\frac{\varphi}{2})^2}{1 + F \sin(\frac{\varphi}{2})^2} \tag{3.6}$$

The phase φ is defined Eqn. 3.7, where *nl* is the optical path length, n_c is the refractive index of the cavity, *l* is the physical path length and λ is the wavelength.

$$\varphi = \frac{4\pi n_c l}{\lambda} \tag{3.7}$$

The phase difference between each round trip is therefore constant. The phase in the Airy function in Eqn. 3.6 leads to reflectance minima's at particular values of phase

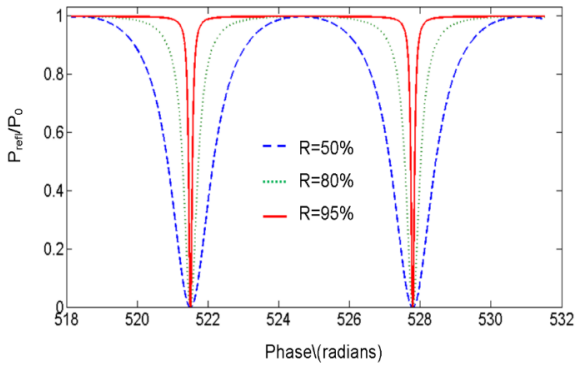

Figure 3-2 Transfer function (P_{refl} vs. φ) for mirror reflectivities of 50% , 80% and 95 %

Figure 3-2 shows the phase Interferometer Transfer Functions ITF_{φ} for mirror reflectivities of R=50%, R=80% and R=95%. As the mirror reflectivities increase the reflectivity peaks become narrower. This is because the ability of the FPI cavity to retain energy is greater as the mirror reflectivity is increased. As R increases F increases resulting in a narrow reflectivity peak. The reflected power is a maximum when the criterion for constructive interference is $\sin^2(\frac{\varphi}{2})=1$, therefore $\varphi=(2p+1)\pi$, where p is an integer, resulting in the relation in Eqn. 3.8,

$$\frac{p\lambda}{4} = nl \qquad 3.8$$

Similarly for destructive interference where $\varphi=2\pi p$ results in the expression in Eqn. 3.9, with p=1, 2, 4, 6…m.

$$\frac{p\lambda}{2} = nl \qquad 3.9$$

Assuming the refractive index n_c as 1, the wavelength has to be a multiples of a quarter of the optical thickness for constructive interference. For destructive interference the wavelength has to be multiples of half the optical thickness, so that the phase difference is π between the field reflected of the incident mirror and the electric fields which have undergone a number of round transits in the cavity.

3.1.2 Measures of quality of a Fabry Perot Interferometer

3.1.2.1 Finesse

A measure of the quality of the resonance of the interferometer is given by the finesse. This is defined as the ratio of the Free Spectral Range (FSR) to the Full Width at Half Maximum (FWHM), and is expressed in Eqn. 3.10.

$$\mathfrak{F} = \frac{FSR}{FWHM} \tag{3.10}$$

The free spectral range defined in terms of wavelength is derived by equating the difference in phase between successive reflectance minima's which is 2π, with that for the derivative of the phase with respect to wavelength and rearranging to get it in terms of $d\lambda$. Equation 3.11 expresses the final form,

$$FSR_{\lambda} = \frac{{\lambda_0}^2}{2nl} \tag{3.11}$$

where λ_0 is the wavelength corresponding to the first reflectance minima, and *nl* is the optical thickness. This expression shows that the FSR_{λ} decreases with increasing cavity thickness, due to the inverse relationship. The FSR in terms of phase will always be 2π.

3.1.2.2 Q-factor of optical resonators

Another measure of the performance of the Fabry Perot Interferometer is the Q-factor, which is defined as the ratio of the energy loss per round trip to the initial energy stored in the cavity. The definition of the Q-factor for a Fabry Perot Interferometer is defined as,

$$Q = \frac{4\pi l}{\lambda_0 \kappa} \tag{3.12}$$

Where l is the cavity spacing of the Fabry Perot Interferometer, λ_0 is the wavelength at resonance and κ the fractional power loss per round trip

3.1.2.3 Visibility

Another variable which is important to consider is the visibility, which is in effect a measure of the depth of the reflectivity peaks in the transfer function. The visibility is defined in Eqn. 3.13:-

$$V = \frac{P_{max} - P_{min}}{P_{max} + P_{min}} \tag{3.13}$$

P_{max} is the maximum reflected power in reflection mode and P_{min} is the reflected power at the reflectance minimum of the reflection mode ITF. For a non-diverging (collimated) beam, the visibility is 1.

3.2 Relationship of Airy function with phase and sensitivity definition

The phase expressed in Eqn. 3.7 showed it is proportional to cavity spacing *l*, and the refractive index n_c. Therefore as these parameters increase, the phase increases proportionally. The wavelength λ is inversely proportionally to the phase, therefore the phase ITF_φ is the inversion of the wavelength ITF_λ. This is important as this thesis deals with wavelength ITF_λs.

3.2.1 ITF variation with various phase parameters

There is an inverse relationship of phase with wavelength, as expressed in Eqn. 3.7. Therefore the smaller phase values correspond to long wavelengths and the higher phase values correspond to shorter wavelengths, where Figure 3-3 shows the inverse relationship of phase with wavelength.

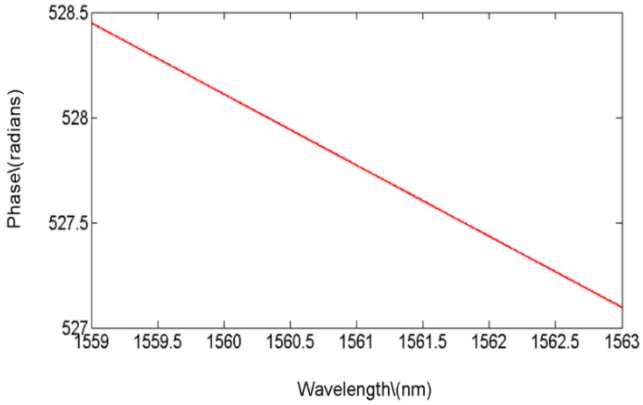

Figure 3-3 Relationship of phase with wavlength

Therefore the derivative of the ITF_λ in wavelength space would have the maximum sensitivity at long wavelengths as shown in Figure 3-4.

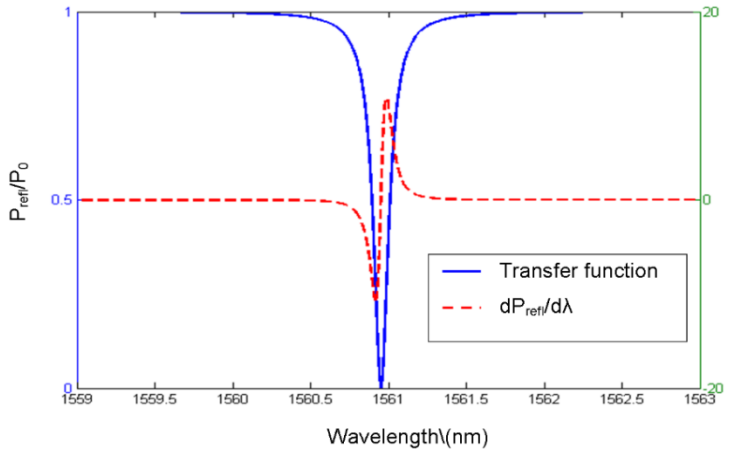

Figure 3-4 Graph of ITF_λ against wavelength λ, and dR/dλ against wavelength λ

Figure 3-5 shows the Airy function and the derivative of the normalised reflected power R with phase (dR/dφ), and the corresponding value for dR/dλ on dR/dφ. As can be seen the maximum of dR/dλ corresponds to the minimum of dR/dφ. This analysis is based on the Airy function description for non-diverging beams. The optical beam used to interrogate the FPI sensors are Gaussian beams described by the TE_{00} mode, which are divergent and can affect the instrumental finesse of the FPI.

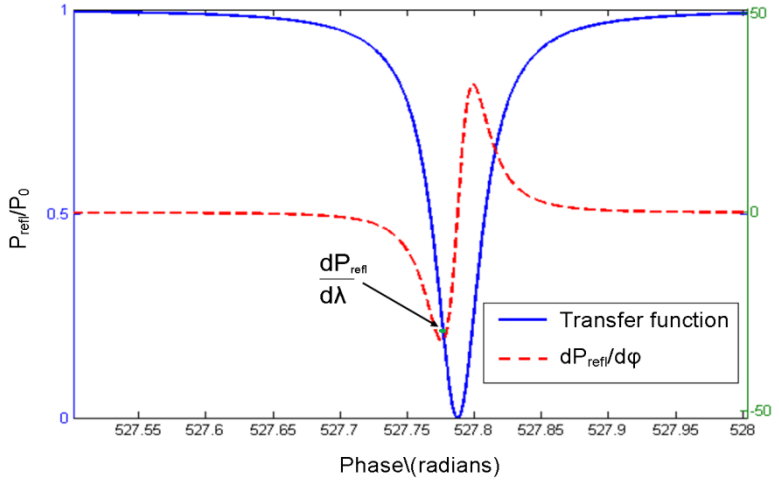

Figure 3-5 Graph of Airy function and dR/dφ as a function of phase and maximum of dR/dλ, for 95% mirror reflectivities.

3.2.2 Expressions for optical sensitivity

This section presents the explicit expression of optical sensitivity based on the Airy function. The Airy function varies with phase, and the derivative defines the optical phase sensitivity,

$$\frac{dR}{d\phi} = \frac{F\sin\left(\frac{\phi}{2}\right)\cos\left(\frac{\phi}{2}\right)}{1+F\sin^2\left(\frac{\phi}{2}\right)} - \frac{F\sin^3\left(\frac{\phi}{2}\right)\cos\left(\frac{\phi}{2}\right)}{\left(1+F\sin^2\left(\frac{\phi}{2}\right)\right)^2} \tag{3.14}$$

Equation 3.14 is the explicit expression for the optical phase sensitivity based on the Airy function. The maximum and minimums of the expression correspond to the point on the ITF_{φ} where the maximum modulation in light occurs for $d\varphi$. However for ultrasound sensing the cavity thickness is being modulated, therefore the optical sensitivity can be defined as,

$$\frac{dR}{dl} = \left[\frac{F\sin\left(\frac{\phi}{2}\right)\cos\left(\frac{\phi}{2}\right)}{1+F\sin^2\left(\frac{\phi}{2}\right)} - \frac{F\sin^3\left(\frac{\phi}{2}\right)\cos\left(\frac{\phi}{2}\right)}{\left(1+F\sin^2\left(\frac{\phi}{2}\right)\right)^2}\right]\frac{4\pi n}{\lambda} \tag{3.15}$$

For the derivative of the wavelength ITF_{λ} which is used to find the optimum wavelength to interrogate the FPI sensor, it is defined as,

$$\frac{dR}{d\lambda} = \left[\frac{F\sin\left(\frac{\phi}{2}\right)\cos\left(\frac{\phi}{2}\right)}{1+F\sin^2\left(\frac{\phi}{2}\right)} - \frac{F\sin^3\left(\frac{\phi}{2}\right)\cos\left(\frac{\phi}{2}\right)}{\left(1+F\sin^2\left(\frac{\phi}{2}\right)\right)^2}\right]\frac{4\pi nl}{\lambda^2} \tag{3.16}$$

Equation 3.15 and Eqn. 3.16 show that at resonance modes corresponding to longer wavelengths, the optical sensitivity decreases. For the FPI sensors in photoacoustic imaging, the wavelengths at which the FPI sensor is interrogated is at the telecoms bandwidth due to the design of the dielectric mirrors. If one were to bias at optical wavelengths, it would result in a low finesse FPI.

Chapter 4 Model implementation for a planar and wedged Fabry Perot Interferometer

This chapter presents an implementation of a model of Gaussian beams illuminating FPIs to simulate wavelength ITF_{λ}s in reflection mode. The model draws upon the work of others who have implemented models of Gaussian beams illuminating a FPI for studying various aspects of Fabry Perot Interferometry such as how the transmitted intensity through the FPI or the finesse varies for certain optical parameters such as beam radius, cavity spacing, or mirror reflectivities. Section 4.2 presents a model for a planar FPI and section 4.4 presents the model for a wedged FPI. Both model implementations are numerically evaluated in sections 4.3 and 4.5.

4.1 Modelling of Gaussian beam illumination of a FPI

One of the most common types of model implemented is that by Safia. A.H [85], which is a mode coupling setup. The model involved sampling the electric field of a Gaussian beam at certain intervals along the optic axis corresponding to the distance propagated by a round trip in the cavity. The beam radius used in the model was on the scale of a few millimetres, and mirror reflectivities R ranged from 0.1 to 0.95. The model was applied to study the reduction in the transmitted beam from the FPI. Other models such as Wilkinson's to model low finesse FPI's was based on the same principle but modified to study the reflected power from the FPI couple back into a fibre as the cavity spacing was varied. Lee. J.Y [86] et al employed a variant of the model by Safia, which involved the Fourier transform of the electric field into the *k*-space domain and considered the components along the optic axis and along the spatial plane individually. Presented was the shift in the transmission of the frequency ITF as the beam radius increases. Moreno. F attempted to obtain analytical equations for Gaussian beams with low divergence (<1 mrad) in FPI's with mirror reflecitivities of 0.7 to 0.8, although broke down for $R \geq 0.9$. Alternative methods of modelling Gaussian beams in Fabry Perot Interferometers is by using Jones matrices [87] or extended Jones matrices, this is particularly useful for polarisation effects in the cavity however the most common method of modelling Gaussian beam illumination of FPIs is by the use of the mode coupling theory.

This thesis implements a model based on that by Safia to simulate wavelength ITF$_\lambda$s for a Gaussian beam illuminating a Fabry Perot Interferometer where the beam radius and cavity spacing is in the range of 10 μm to 50 μm with mirror reflectivities in the region of 90% to 99%. The model is setup such that various geometrical apertures can be applied on the reflected beam to study the effect on the shape of the ITF, as well as analysing the shape of the ITFs using the model. The reason for incorporating the effect of geometrical apertures is to study the performance of FPIs for various scenarios such as at the tip of optical fibres, where a Gaussian weighted disc aperture is required.

4.2 Planar FPI illuminated with a Gaussian beam

Chapter 3 described the Airy function description of the ITF for a non-diverging beam. However in reality the output of laser beams, and the focussing of those laser beams is described by Gaussian beams. The most common type of Gaussian beam is of the TE_{00} mode. This section describes the physical nature of Gaussian beams which describes a realistic laser beam found in most laser systems.

4.2.1 Gaussian beams of the TE_{00} mode

A Gaussian beam of the TE_{00} mode is one in which the phase and amplitude vary in the plane normal to the optic axis [84]. As the beam is circularly symmetric about the optic axis, the variation in the amplitude and phase in the plane normal to the optic axis can be described by its radial component ρ. The amplitude follows a bell shape, where the amplitude at the centre of the beam is maximum, and decreases away from the centre with the amplitude profile described mathematically by a Gaussian function. As the wave propagates the amplitude at the centre of the beam decreases, the beam radius also increases. This is due to the spreading (divergence) of the electric fields radially due to diffraction.

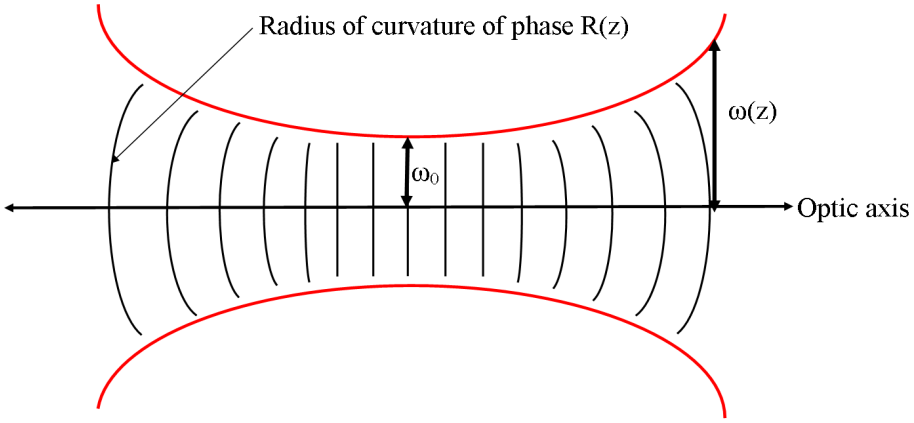

Figure 4-1 Gaussian beam divergence with beam width ωo, and radius of curvature R (z) of phase

Figure 4-1 shows the divergence of the Gaussian beam along the optic axis. Where ω_0 is the initial beam radius at the focal plane and ω(z) is the beam after propagating a distance z. The curvature of the wave front is denoted by R(z). The divergence is symmetric around the focal region where the beam radius is the narrowest and the phase is approximated as planar.

A Gaussian beam equation describes the phase and amplitude of a laser beam across the radial plane to a good approximation. The most fundamental Gaussian beam considered in the study of the interaction of laser beams with Fabry Perot interferometers are of the TE_{00} mode which are solutions to the paraxial wave equations used to describe single mode cavity lasers. Although there exists higher modes which are described by Hermite-Gaussian modes or Laguerre-Gaussian modes, they are neglected in this study.

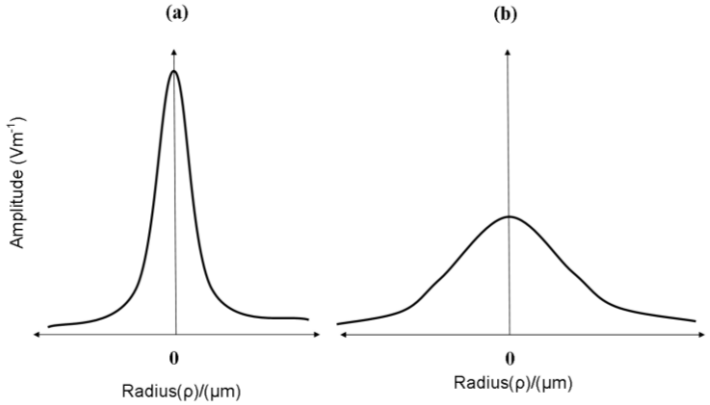

Figure 4-2 Amplitude profile of Gaussian beam at an initial beam width, (b) Amplitude profile after a distance z after the beam has diverged

The beam radius is defined as the radius of the beam at which the amplitude has fallen to 1/e of the maximum amplitude from that at the centre of the beam. For a small beam radius the electric field distribution in the radial direction will diffract to a greater extent and over a much shorter distance, compared to that of a larger initial beam radius. The relationship of amplitude with radius is shown in Figure 4-2. The equation for the electric field describing the amplitude and phase is approximated by a Gaussian function with the phase and amplitude terms dependent on the radial coordinate ρ. The expression for the phase and amplitude profile of a Gaussian beam is expressed in Eqn. 4.1.

$$E(\rho,z) = \frac{\omega_0}{\omega(z)} e^{-\frac{\rho^2}{\omega^2(z)}} e^{\frac{ik\rho^2}{2R(z)}} e^{-i\,tan^{-1}(\frac{z}{z_0})} e^{i(kz-\omega t)} \qquad 4.1$$

Where ω_0 is the beam radius at the focal plane of the beam, and $\omega(z)$ the beam radius after the beam has propagated a distance z. The expression for the initial beam radius ω_0 is given in Eqn. 4.2

$$\omega_0 = \sqrt{\frac{\lambda z_0}{\pi}} \qquad 4.2$$

Where λ is the wavelength and z_0 the Rayleigh range, which is the distance from the initial beam radius to where the phase is approximated as planar. The expression for the beam radius after propagating a distance z is expressed in Eqn. 4.3.

$$\omega^2(z) = \omega_0^2\left(1 + \left(\frac{z}{z_0}\right)^2\right) \tag{4.3}$$

The radius of curvature R(z) expression in Eqn. 4.1, describes the curvature of the phase as the beam propagates along the optic axis z and is expressed in Eqn. 4.4.

$$R(z) = z(1 + (\frac{z_0}{z})^2) \tag{4.4}$$

The radius of curvature in the far field increases with z, so the phase difference across the beam radially increases with z.

The Gouy phase is represented by the tan inverse function in the phase term in Eqn. 4.1 and explicitly expressed in Eqn. 4.5. It represents the effect the curvature of the wave front has on the phase as the beam propagates along the optic axis.

$$\Theta = tan^{-1}\left(\frac{z}{z_0}\right) \tag{4.5}$$

The Gouy phase asymptotically tends to maximum of π/2 radians in the far field, as the beam propagates away from the Rayleigh range. The phase change between the far field distance z_f and the equivalent distance $-z_f$ in the negative direction along the optic axis, has a phase change of π radians. The Gouy phase therefore expresses phase lag due to the radius of curvature of the wave front as the beam propagates along the optic axis. This in effect means a reduction in the magnitude of the wave vector k_z along the optic axis z. A mathematical proof using Fourier transforms was shown by Winful [88]. This was due to the wave vector across the optic axis being a component of a wave vector expressing a diffractive ray. As the

diffraction increases k_z decreases to a asymptote, while k_x increases, and was shown using a geometrical proof combined with a Fourier integral of the wave vector.

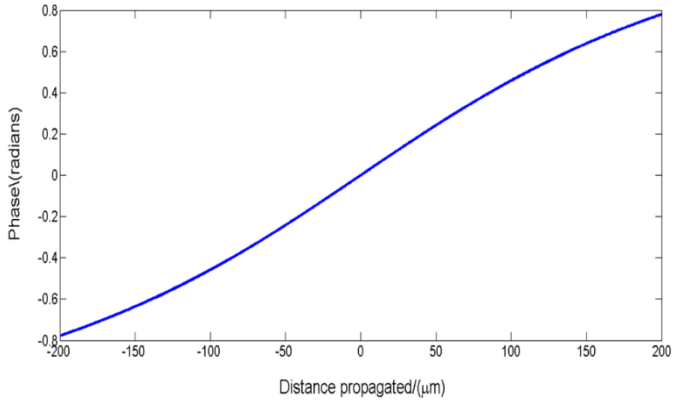

Figure 4-3 Graph of Gouy phase increase as the beam propagates away from the focal point at z= 0 μm and diverges in the far field at z= 200 μm

4.2.2 Model of Gaussian beam illuminating a planar Fabry Perot Interferometer

The model for a planar Fabry Perot Interferometer illuminated by a Gaussian beam is described in this section. The model is constructed by summing the electric field propagated after a number of complete round trips in the Fabry Perot cavity. The Fabry Perot Interferometer (FPI) is shown in Figure 4-4. It is comprised of two mirrors, mirror 1 and mirror 2 with amplitude reflection coefficients and phase change r_1, θ_1 and r_2, θ_2 respectively. The spacing between the two mirrors is *l*, and the refractive index of the medium between the mirrors is n_c. The refractive index of the medium surrounding the FPI is n_s.

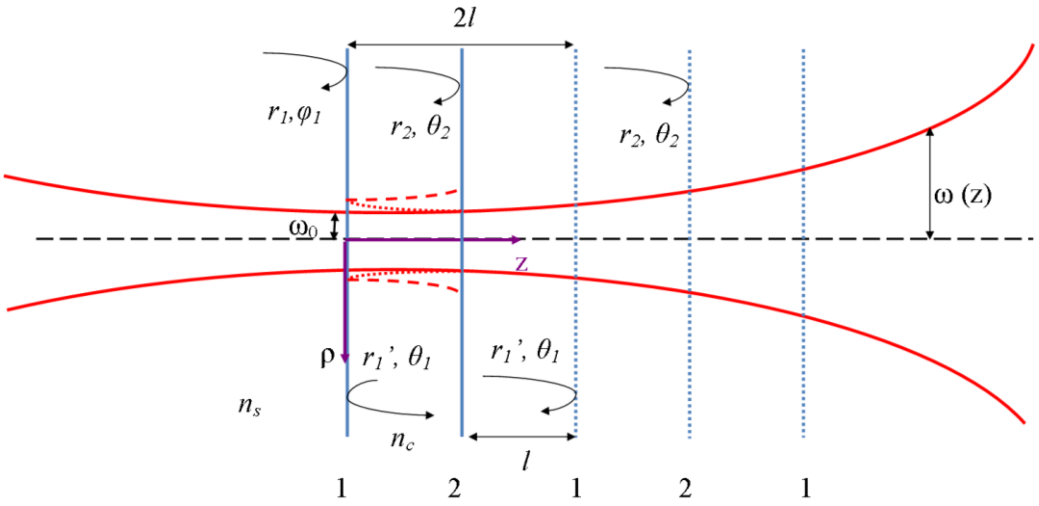

Figure 4-4 Gaussian beam propagation through a FPI with cavity spacing l extended along the optic axis z, with r_1, r_2 and θ_1, θ_2 the amplitude reflection coefficients and phase change respectively of mirror 1 and mirror 2 within the cavity, and φ_1 the phase change on reflection from mirror 1

The propagation of a Gaussian beam in a plane parallel FPI, where the mirrors are parallel to each other and normal to the optic axis is shown in Figure 4-5, as well as in Figure 4-4. The beam diverges as it propagates within the FPI. Figure 4-4 shows the propagation within the cavity unfolded along the optic axis, where the beam waist ω_0 is incident at mirror 1.

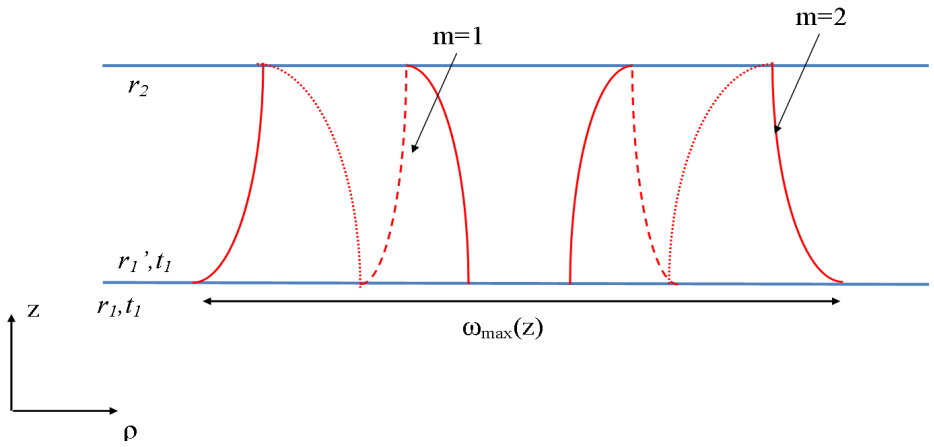

Figure 4-5 Diagram of Gaussian beam diverging within a Fabry Perot Interferometer

4.2.3 Numerical model implementation

This section presents a numerical model that simulates ITFs when the FPI is illuminated by a Gaussian beam. This is achieved by summing the reflected field contributions for each round trip in the cavity at mirror 1. The electric field expression $E_m(\rho,2ml)$ after undergoing a round trip in the cavity and passing through mirror 1, with radial dependence ρ is expressed in Eqn. (4.6),

$$E_m(\rho, 2ml) = a_m E_{G,m}(\rho, 2ml) e^{-i(k2ml-\omega t)} E_0 \qquad 4.6$$

where a_m represents the complex amplitude coefficients of the mirrors, $E_{G,m}$ describes the amplitude and phase characteristics of the Gaussian beam. The distance propagated along the optic axis after the m^{th} round trip is $2ml$ ($z=2ml$). The wave vector is k ($k=2\pi n_c/\lambda$), and λ is the wavelength, ω is the angular frequency. E_0 is the amplitude of the initial electric field. The $E_{G,m}$ term modifies the characteristics of a plane wave beam with that of a Gaussian beam of the TE_{00} mode, as it propagates along the optic axis z and along the radial plane ρ. The beam is radially symmetric for the TE_{00} mode, which is advantageous during the model implementation stage in sub-section 4.2.4. The amplitude coefficient of the mirrors a_m reduces the amplitude of the initial electric field E_0, as well as altering the phase on

subsequent round trips. The amplitude coefficients due to the mirrors for the first three round trips and in general for the m[th] round trip are expressed in Eqn. 4.7

$$
\begin{aligned}
a_1 &= {t_1}^2 r_2 e^{i\theta_2} e^{i\theta_{t_1}} e^{i\theta_{t_1}'} \\
a_2 &= {t_1}^2 {r_2}^2 r_1' e^{i\theta_1} e^{i2\theta_2} e^{i\theta_{t_1}} e^{i\theta_{t_1}'} \\
a_3 &= {t_1}^2 {r_2}^3 {r_1'}^2 e^{i2\theta_1} e^{i3\theta_2} e^{i\theta_{t_1}} e^{i\theta_{t_1}'} \\
&\ldots. \\
&\ldots. \\
a_m &= {t_1}^2 {r_2}^m {r_1'}^{(m-1)} e^{i(m-1)\theta_1} e^{-im\theta_2} e^{i\theta_{t_1}} e^{i\theta_{t_1}'}
\end{aligned}
\qquad 4.7
$$

where the transmission amplitude coefficient of mirror 1 when the beam is transmitted into the cavity is denoted by t_1, with phase change on transmission of θ_t. When the beam is transmitted from the cavity the phase change on transmission is $\theta_{t1'}$, θ_1 and θ_2 are the phase change on reflection with mirror 1 and mirror 2 respectively. The equation for the electric field for a Gaussian beam of TE_{00} mode is stated in Eqn. 4.8,

$$E_G(\rho, z) = \frac{\omega_0}{\omega(z)} e^{-\frac{\rho^2}{\omega^2(z)}} e^{-\frac{ik\rho^2}{2R(z)}} e^{-ikz} e^{i\Theta} e^{-\alpha(z+\frac{k\rho^2}{2R(z)k_\rho})} E_0 \qquad 4.8$$

where the beam radius at the focus of the beam is given by ω_0 (radius where amplitude falls to 1/e relative to the centre of the beam), and $\omega(z)$ is the beam radius after propagating a distance z, and is expressed in Eqn. 4.11. The Gouy phase Θ inherent in Gaussian beams is expressed by the inverse tan term in Eqn. 4.9. R(z) is the radius of curvature of the wave front which is expressed in Eqn. 4.10. The Rayleigh range z_0 is the distance over which the wave front of the beam is non-diverging. The decay of the electric field amplitude as the beam propagates in an absorbing medium is described by the fifth exponential term in Eqn. 4.8, where α is the amplitude decay per unit distance, and where the second term in the amplitude decay exponent describes the additional distance traversed by diverging electric fields and k_ρ is the component of the wave vector along the radial direction.

$$\Theta = tan^{-1}\left(\frac{z}{z_0}\right) \qquad 4.9$$

$$R(z) = z\left(1 + \frac{{z_0}^2}{z^2}\right) \tag{4.10}$$

$$\omega(z) = \omega_0\sqrt{1 + \left(\frac{z^2}{{z_0}^2}\right)} \tag{4.11}$$

The Gaussian beam term $E_{G,m}$ describing the electric field propagation in a FPI for the first three round trips and the general mth round trip within the cavity is expressed as,

$$E_{G,1}(\rho, 2l) = \frac{\omega_0}{\omega(2l)} e^{-\frac{\rho^2}{\omega^2(2l)}} e^{\frac{ik\rho^2}{2R(2l)}} e^{-i\Theta_1} e^{-\alpha(2l + \frac{k\rho^2}{2R(2l)k_\rho})}$$

$$E_{G,2}(\rho, 4l) = \frac{\omega_0}{\omega(4l)} e^{-\frac{\rho^2}{\omega^2(4l)}} e^{\frac{ik\rho^2}{2R(4l)}} e^{-i\Theta_2} e^{-\alpha(4l + \frac{k\rho^2}{2R(4l)k_\rho})}$$

$$E_{G,3}(\rho, 6l) = \frac{\omega_0}{\omega(6l)} e^{-\frac{\rho^2}{\omega^2(6l)}} e^{\frac{ik\rho^2}{2R(6l)}} e^{-i\Theta_3} e^{-\alpha(6l + \frac{k\rho^2}{2R(6l)k_\rho})}$$

. . . 4.12

. . .

$$E_{G,m}(\rho, 2ml) = \frac{\omega_0}{\omega(2ml)} e^{-\frac{\rho^2}{\omega^2(2ml)}} e^{\frac{ik\rho^2}{2R(2ml)}} e^{-i\Theta_m} e^{-\alpha(2ml + \frac{k\rho^2}{2R(2ml)k_\rho})}$$

The expression for the total electric field reflected from the FPI is the sum of the electric fields transmitted from the cavity at mirror 1. The total electric field transmitted from the cavity at mirror 1 is given by the summation of Eqn. 4.6 with round trip number m, where $E_{G,m}$ is given by the general expression in Eqn. 4.12, and a_m given by the general expression in Eqn. 4.7. Therefore the total electric field E_{total} is given by,

$$E_{total}(\rho, \lambda) = E_f + \sum_{m=1}^{\infty} {t_1}^2 {r_2}^m {r_1'}^{((m-1))} \frac{\omega_0}{\omega(2ml)} e^{-\frac{\rho^2}{\omega^2(2ml)}} e^{\frac{ik\rho^2}{2R(2ml)}} e^{-i\Theta_m} e^{i\left(k2ml + \left((m-1)\theta_1 + m\theta_2 + \theta_{t_1} + \theta_{t_1'}\right) - \omega t\right)} e^{-\alpha\left(2ml + \frac{k\rho^2}{2R(2ml)k_\rho}\right)} E_0 \tag{4.13}$$

where E_f is the field reflected from the first mirror expressed in Eqn. 4.14,

$$E_f = r_1 e^{-\frac{\rho^2}{\omega_0{}^2}} e^{\frac{ik_s\rho^2}{2R(0)}} E_0 e^{i(k_s 0+\omega t+\varphi_1)} \quad 4.14$$

φ_1 is the phase change on reflection with mirror 1, and $z = 0$. The wave vector k_s ($k_s = 2\pi n_s/\lambda$) denotes the wave vector when the beam is in the surrounding medium of the FPI. Equation 4.13 expresses the summation of the total reflected electric field. The wavelength Interferometer Transfer function (ITF_λ) is the total power reflected as a function of wavelength, and is expressed in Eqn. 4.15. The total electric field is integrated over the area of the reflected beam by taking rings of radii $2\pi\rho$ with ring width $d\rho$,

$$P_{refl}(\lambda) = \int_0^\infty (E_{total}(\rho,\lambda)E_{total}(\rho,\lambda)^*)2\pi\rho\, d\rho \quad 4.15$$

The explicit expressions in Eqn. 4.13, 4.14 and 4.15 form the model, and is implemented as a numerical model in Matlab. The next section describes the implementation of the model.

4.2.4 Computational implementation

4.2.4.1 Discretisation of variables and coding structure

The model was numerically implemented in MATLAB. The continuous variables ρ and λ are discretized,

$$\rho_j = j\Delta\rho$$
$$\lambda_j = j\Delta\lambda \quad 4.16$$

where j=0,1,2,3,….J, and $\Delta\rho$ and $\Delta\lambda$ are the discrete spacing intervals of the radial component and wavelength respectively. The integration of the total reflected intensity expressed in Eqn. 4.15 was performed using the Trapezoidal method, and is given by;

$$P_{refl}(\lambda) = \sum_{j=0}^{J} (E_{total}(j\Delta\rho, \lambda) E_{total}(j\Delta\rho, \lambda)^{*})\ 2\pi j\Delta\rho\ \Delta\rho \qquad 4.17$$

where J is the maximum index number of the radius array. The reflected intensity was summed by taking rings of radii ρ and thickness Δρ to a maximum radius of J= $\omega(2m_{max}l)/\Delta\rho$, due to the symmetric nature of the Gaussian beam. $\omega(2m_{max}l)$ is the beam radius after the beam has propagated such that the amplitude falls to a negligible level, which is presented in sub-section 4.2.4.2. The round trip number m_{max} is the maximum number of round trips the electric field at mirror 1 is summed up to. The electric field after m_{max} number of round trips would have fallen to a level, such that further round transits by the beam do not significantly contribute to the total reflected electric field.

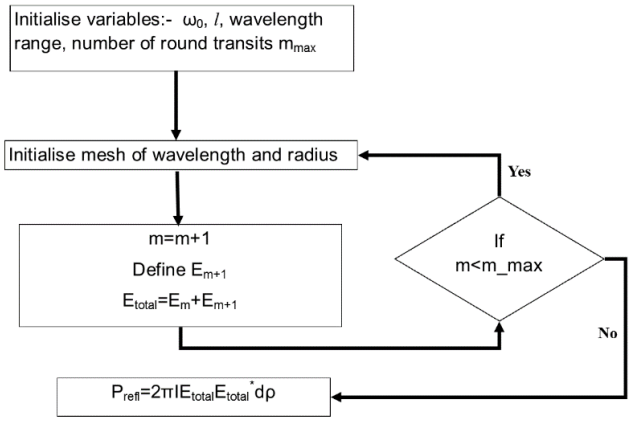

Figure 4-6 Flow diagram depicting the flow structure of the code to simulate the ITF$_\lambda$ for a Gaussian beam in a planar Fabry Perot

The structure of the code is represented by a flow diagram, as shown in in Figure 4-6, and the explicit code is shown in Appendix B. The code lets users input variables for mirror reflectivities (R_1, R_2), cavity thickness (l), beam radius (ω_0) and the wavelength range (λ). The electric fields that have undergone the m^{th} round trip were summed to the electric field for the previous round trip in the loop. The wavelength sampling size can be set by the user in the model.

4.2.4.2 Summation limits for number of round transits by electric field

The number of round transits traversed by the beam in a Fabry Perot Interferometer for a non-diverging beam assumes an infinite number of round trips forming a geometric series, with the amplitude coefficients being less than 1. Numerically summing the electric field to infinity is impossible; as well as the ability to form an analytical expression due to the additional phase components, which have a non-linear variation with the number of round trips m. Therefore an understanding of the number of round transits that should be computed for a Fabry Perot Interferometer with specific mirror reflectivities is useful. The number of round trips computed for the ITF due to a Gaussian beam to converge to that of a non-diverging beam is considered. Taking the reflection and transmission amplitude coefficients and plotting the decrease in amplitude on each round trip m for a non-diverging beam, the number of round trips to consider can then be chosen by selecting the round trip number where the change in amplitude coefficient is not considerable.

$$a_m = {t_1}^2 {r_1}^{(m-1)} {r_2}^m \quad 4.18$$

Equation 4.18 expresses the amplitude coefficient for each round trip m for the reflected beam, where t_1 is the amplitude transmission coefficient for the incident mirror and r_1 is the amplitude reflection coefficient for the incident mirror. The amplitude coefficient for the second mirror is denoted by r_2. The incident electric field amplitude E_0 of the beam is 1. This is used to calculate the amplitude decrease for subsequent round trips shown in Figure 4-7.

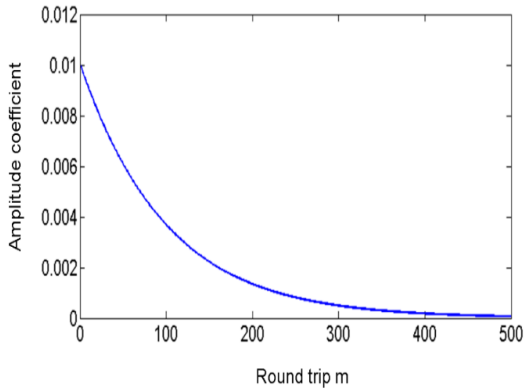

Figure 4-7 Graph of electric field amplitude with round trip number m, for power reflection coefficient R=99% for both mirrors

Figure 4-7 suggests the number of round trips when the electric field starts to asymptote to zero is 500. Also the change in the electric field amplitude with round trip is significantly small, where it is reduced by a factor of 10^2 relative to the first round trip (~0.01). This analysis was for mirror reflectivities of R=99%, and a non-diverging beam. For mirror reflectivities lower than R=99%, this leads to computing the electric field for more round trips than is necessary, leading to inefficient use of CPU memory and computing time to perform the electric field calculations. To calculate the necessary number of round trips for different mirror reflectivities, Safia showed that the maximum number of round trips m_{max} is twice the value of finesse when the FPI is illuminated by a non-diverging beam [85], [89]. This was shown by the differences in the numerical simulation of the transmitted beam for various values of m_{max}. The number of round trips is related to the finesse, therefore the higher the finesse the greater the number of round trips. A reasonable approach to calculating the number of round trips is $m_{max} = 2F$. To evaluate that the maximum number of round trips

m_{max} is twice the value of finesse and to calculate the error between the wavelength ITF_λs, a variety of ITF_λs for various m_{max} values were simulated to see the differences in their shape.

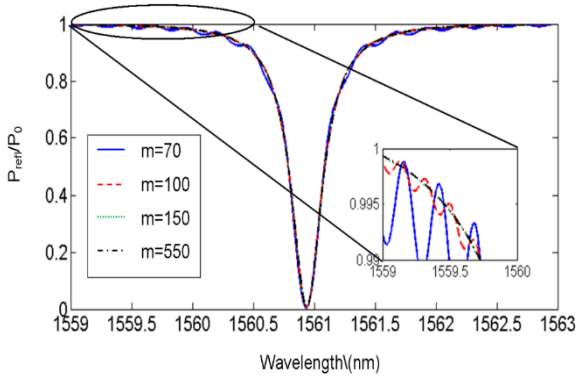

Figure 4-8 Graph of ITF_λs for a 40 µm cavity thickness with beam radius of ω_0=50 µm for mirror reflectivities of R=95% with m_{max}=70, 100,150 and 550

Figure 4-8 shows simulated wavelength Interferometer Transfer functions (ITF_λs) for a 40 µm cavity thickness with a 50 µm beam radius approximating to an Airy function. The finesse of the ITF_λ for an non-diverging beam was computed to be 65. The ITF_λ for m_{max}=70 results in oscillations rather than a smooth ITF_λ. The same effect also occurs for the ITF_λ where m_{max}=100 but is more subdued, as shown by the enlargement of the ITF_λ over a narrow wavelength range in Figure 4-8. The ITF_λ when the number of round trips are m_{max}=150 and m_{max}=550 overlap with a smooth profile. The average difference between the normalized ITF_λs for the two m_{max} values of 150 and 550 was 0.00148% which is assumed negligible. This was also repeated for a high finesse FPI (R=98%), a non-diverging beam with the round trip number being m_{max}=320 and m_{max}=550, with a difference of 0.0078%. These changes in the ITF are less than 1%, showing that increasing the round trip number further than this has no specific advantage. This shows that $m_{max} \geq 2F$ is a practical relationship to determine the finite number of round trips to sum the electric field to. The run time of the model to simulate a ITF is around a minute.

4.2.4.3 Radial sampling interval

The radial interval $\Delta\rho$ at which the electric field is sampled between radial points needs to have sufficient samples while not leading to under sampling or over sampling. To check the optimum radial sample, $\Delta\rho$ was varied to see how much the ITF_λ varied.

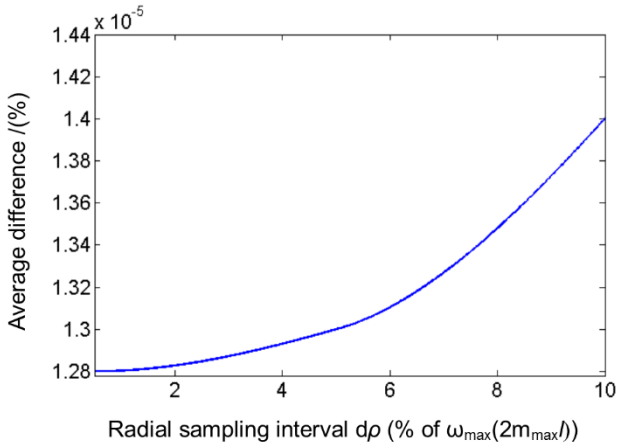

Figure 4-9 Difference in the wavelength ITF_λ as the radial element size $\Delta\rho$ is varied, for a FPI with mirror reflectivities of 98% and cavity thickness of 40 µm and beam radius of 200 µm,

Figure 4-9 shows the change in the wavelength ITF_λ as the radial element size $\Delta\rho$ is increased from being less than 1% of the total reflected beam radius $\omega(2m_{max}l)$ to 10%. As the radial element size increases, the difference in the ITF_λ increases. The difference is measured by taking the average of the absolute difference between each point in the ITF_λ. The average differences increases as the radial sampling size increases. The change in the ITF_λ is significantly smaller compared to the effect on the ITF_λ from the difference in the number of round trips. For smaller beam waists, the sampling was set to 0.5% of the total reflected beam to achieve similar sampling rates as that for larger beam waists. Therefore for this study the radial sampling $\Delta\rho$ was chosen to be between 0.5% to 1% of the $\omega(2m_{max}l)$, as the change in the ITF_λ with changing radial element $\Delta\rho$ below 1% is constant as shown in Figure 4-9.

4.3 Evaluation of the planar FPI model

The characteristics of the model is evaluated by two methods, one of which is to analyse the electric field distribution at mirror 1 after each round trip. This is achieved by a series of plots of the intensity of the individual electric field after a number of complete round trips. Figure 4-10 shows the radial intensity of the beam for a 10 μm beam radius, after individual complete round trips in the cavity from m=1 to m=9, shown from top left to bottom right respectively. This is to show that the beam waist after propagating a round trip increases by the right amount. As expected, as the beam propagates the beam radius expands, as shown by the intensity plots and the beam radius ω(z) along the optic axis at the bottom of the figure. The reflected power is given by the scale on the right hand side of each plot. The power both at the centre and radially across the beam drops, due to the divergence and the reflection and transmission coefficients of the mirrors.

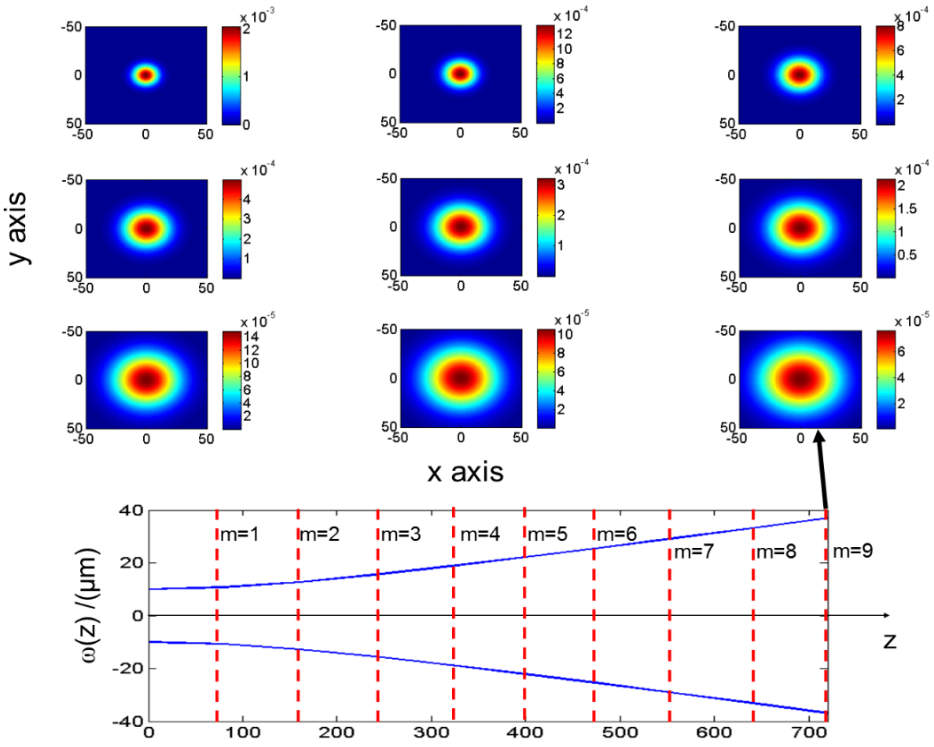

Figure 4-10 Plots of reflected intensity from mirror 1 as the beam has completed a round trip in the cavity for a 10 μm beam radius, with the beam radius along the optic axis shown at the bottom of the figure

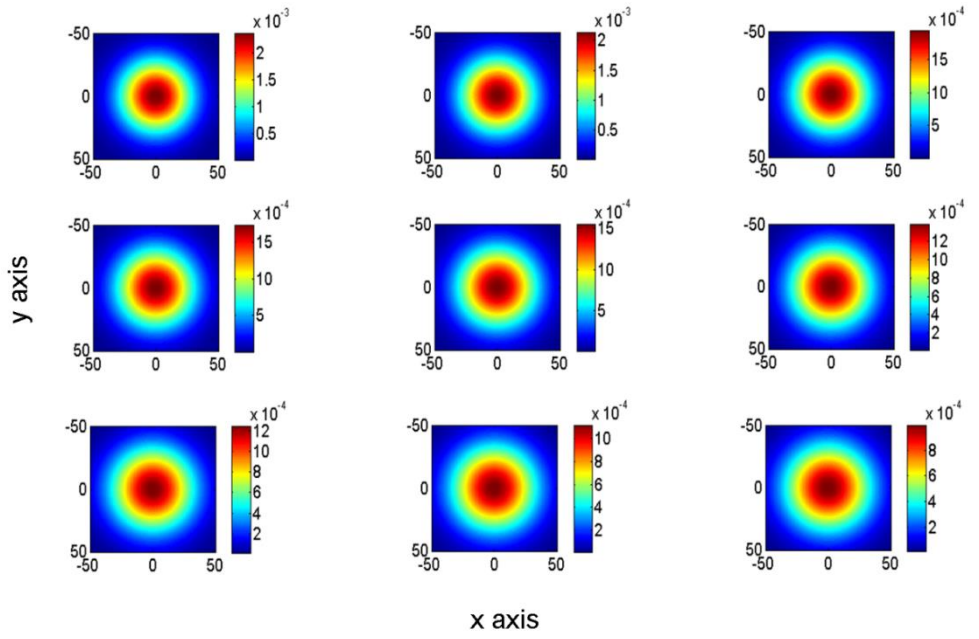

Figure 4-11 Plots of reflected intensity from mirror 1 as the beam has completed a round trip in the cavity for a 40 µm beam radius

Figure 4-11 shows the reflected intensity plots for a 40 µm beam radius for 9 complete round trips from m=1 at the top left to m=9 at the bottom right. The beam radius on each round trip is constant, as the beam is less divergent. The order of magnitude drop in power from m=1 to m=9 is less than that for a 10 µm beam radius. This is expected as the Rayleigh range for the 40 µm beam radius is longer; therefore the rate at which the amplitude decreases along the optic axis is much less than that for a 10 µm beam radius.

The second method to evaluate the model is to compare the ITF_λs between a non-diverging beam and a Gaussian beam with a large beam radius such that its divergence is negligible. In the evaluation of the model, at large beam radii where the beam can be approximated as a non-diverging beam, the characteristics would follow similar trends to the Airy function. This is done by comparing the wavelength ITF_λ simulated by the model for a large Gaussian beam radius with an Airy function. The large Gaussian beam radius approximates to a non-diverging beam, while the Airy function is formed from Eqn. 3.6. Figure 4-12 shows the wavelength ITF_λ for a collimated beam and a Gaussian beam with a 1000 µm beam radius. The average difference between the ITF_λs is 1.801×10^{-3} %.

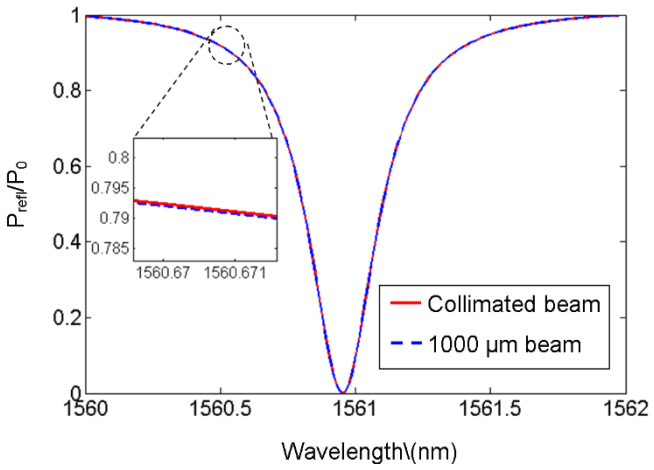

Figure 4-12 ITF for a collimated beam and a Gaussian beam with a beam radius of 1000 µm,in a FPI with mirror reflectivities of R=98% and cavity thickness of 40 µm

This numerically evaluates the model for simulating the propagation of a Gaussian beam in a planar FPI cavity. At large beam radii it approximates to that of a non-diverging beam. Also evaluated was the beam expansion on each round trip in the cavity for a highly diverging beam. These are characteristics expected of a Gaussian beam from conceptualisation.

4.4 Model for a Gaussian beam illuminating a wedged FPI

To model Fabry Perot Interferometer (FPI) sensor with typical characteristics encountered experimentally, it is useful to include cavity thickness non-uniformities. Gaussian beams illuminating a wedged FPI have been modelled for the purpose of analysing the transmitted beam through the FPI by Xia [90] and Liu. M [91]. Meyer studied the effect of fringe formation in FPI's with a wedge [92]. In relation to the FPI sensors, the beam dimension is on the micron scale, while the surface non-uniformities of the FPI sensor vary on the scale of millimetres. Therefore to a first approximation, the change in cavity spacing can be treated as linear across the dimension of the beam. Therefore a wedged FPI can approximate to the characteristics of a non-uniform FPI sensor.

4.4.4 Model of Gaussian beam illuminating a wedged Fabry Perot Interferometer

This section describes the model for a wedged Fabry Perot Interferometer illuminated with a Gaussian beam. Section 4.2 described the setup of a planar FPI model. The setup for a planar FPI propagated a Gaussian beam in free space, with mirrors spaced equally apart at a distance l which are normal to the optic axis, at which the electric field is sampled at every other mirror plane. In a wedged FPI, mirror 2 is at an angle α to the x-axis as shown in Figure 4-13, with a Gaussian beam of the TE_{00} mode propagating in free space. Mirror 1 would form an angle 2α after the beam has traversed a round trip, as shown in Figure 4-13. This is the same as unfolding the FPI cavity about the apex of the wedge, which is a length x_α from the mirror intersection. The circular symmetry of the total reflected beam is lost, due to the lateral shift of the beam with each round trip.

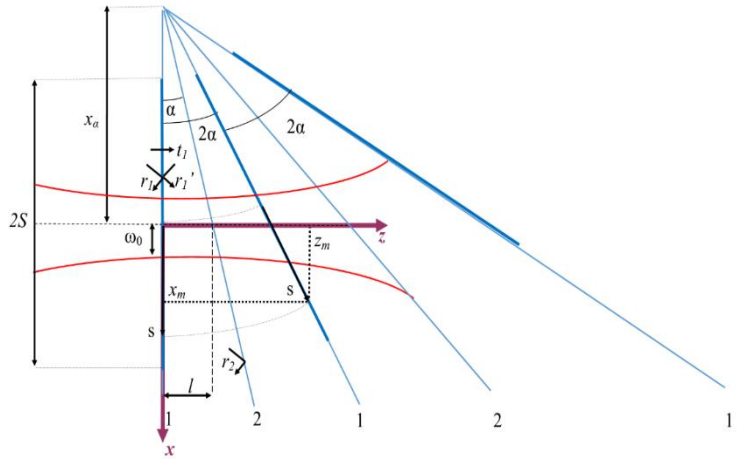

Figure 4-13 Diagram of a Gaussian beam propagating through a wedged FPI with angled planes of 2mα at which the electric field after a round trip is sampled

4.4.5 Numerical model implementation

The model is setup so that the beam propagates in free space along the z-axis (optic axis). The electric field is sampled at planes which are at an angle 2mα to the *x*-axis for each round trip m, as shown in Figure 4-13. The point *s* from the centre of mirror 1 rotated by an angle 2mα, is a position in the coordinate space x-z, with corresponding coordinate points x_m and z_m. Equation. 4.19 describes the corresponding *x* coordinate for the m^{th} round trip,

$$x_m = (x_\alpha + s)\, cos(2m\alpha) - x_\alpha \tag{4.19}$$

where x_α defines the length from the apex of the wedge to the centre of the beam,

$$x_\alpha = \frac{l}{tan(\alpha)} \tag{4.20}$$

The cavity spacing *l* is the distance between the two mirrors at the centre of the beam. The coordinate point z_m for the point *s* on the rotated plane 2mα, corresponding to the m^{th} round trip is expressed as,

$$z_m = (x_\alpha + s)\, sin(2m\alpha) \tag{4.21}$$

The distance propagated by the electric field on each round trip is then z_m. The radial position is a function of x_m for each round trip, and defined as $\rho=\sqrt{(x_m^2+y^2)}$. The model for a Gaussian beam illuminating a wedged FPI is then expressed as,

$$E_{total}(x,y,\lambda) = E_f + \sum_{m=1}^{\infty} t_1{}^2 r_2{}^m r_1{}'^{((m-1))} \frac{\omega_0}{\omega(z_m)} e^{-\frac{\rho^2}{\omega^2(z_m)}} e^{\frac{ik\rho^2}{2R(z_m)}} e^{-i\Theta_m} e^{i(kz_m - 2\pi ft)} e^{i\left(k2ml + \left(m\theta_1 + (m-1)\theta_2 + \theta_{t_1} + \theta_{t_1'}\right) - 2\pi ft\right)} e^{-\alpha\left(2ml + \frac{k\rho^2}{2R(2ml)k_\rho}\right)} E_0 \quad 4.22$$

The radial component ρ_m is modified on each round trip to account for the shift in the beam per round trip due to the wedge. E_f is the field reflected from the incident mirror as expressed in Eqn. 4.14. E_0 is the amplitude of the electric field incident at mirror 1. The total reflected power is therefore;

$$P_{refl}(\lambda) = \int_{x=-\infty}^{\infty} \int_{y=-\infty}^{\infty} (E_{total}(x,y,\lambda) E_{total}(x,y,\lambda)^* \, dxdy \quad 4.23$$

Equation 4.23 expresses the integration of the intensity reflected from the FPI cavity in the *x-y* plane of the incident mirror. Due to the loss in the symmetry of the total reflected beam, the integration is performed along the *x* and *y* directions respectively, rather than a radial integration performed for a planar FPI model. The *x-y* plane is assumed infinite, in that it is much larger than the beam size.

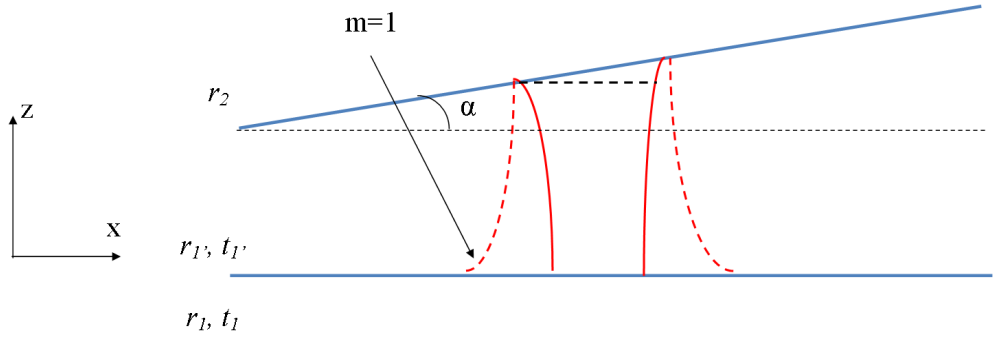

Figure 4-14 Diagram of Gaussian beam diverging within a wedged Fabry Perot Interferometer

Figure 4-14 shows the beam diverging within a wedged FPI. The path length of the electric fields within the beam are altered due to a wedge. This results in a variation in the phase radially across the beam. This shows the beam is no longer symmetric along the radial plane after undergoing m number of round trips.

4.4.6 Computational implementation

The wedged FPI model is coded in Matlab. The criterion for the maximum number of round trips m_{max} to sum the electric field was the same as that for a planar FPI model, as described in section 4.2.4.2. The *x-y* plane is defined in terms of an S-Y matrix from -S to +S and –Y to +Y values, which correspond to a finite size of the FPI. The centre of the beam is at S=0, Y=0.). The point S_m in the x-array corresponding to the point S in the rotated plane, and the distance z_m is expressed as,

$$\begin{aligned} S_{p,m} &= (x_\alpha - S + p\Delta s)\, cos(2m\alpha) - x_\alpha \\ Y &= -Y + q\Delta y \\ z_m &= (x_\alpha - S + j\Delta s)\, sin(2m\alpha) \end{aligned} \qquad 4.24$$

with p=0,1,2,3…P. The value of P is 2S/Δs. The *y*-axis is defined as above where q=0,1,2,3…,Q, where Q=2Y/Δy. The numerical integration of the total unapertured reflected field E_{total} is then given by,

$$P_{refl}(\lambda) = \sum_{p=0}^{P} \sum_{q=0}^{Q} (E_{total}(S,Y,\lambda) E_{total}(S,Y,\lambda)^*)\, \Delta s \Delta y \qquad 4.25$$

Δs and Δy are the sampling intervals in the x and y axis respectively, and set to 1 µm in order to be consistent with the planar FPI model. The size of the S-Y plane was chosen to be S = ±300 µm and Y = ±300 µm, with P=Q., such that the s and y array have the same sampling interval and the 2D X-Y mesh is even. For these dimensions the walk-off of the beam is still within the bounds of the S-Y plane, as the input beam radii are less than 40 µm, and wedge angles of less than 0.5^0 are used. If the beam radius increases greater than 100 µm, then the mesh size increases by an arbitrary chosen value of 4 times the beam radius.

4.5 Evaluation of the wedged FPI model

To evaluate the model of Gaussian beam illuminating a wedged Fabry Perot Interferometer, a similar method to the evaluation of the planar FPI model is used. A series of plots showing the reflected power intensity at mirror 1 is shown for a highly diverging beam and less diverging beam at a wedge angle such that the walk off the beam is seen.

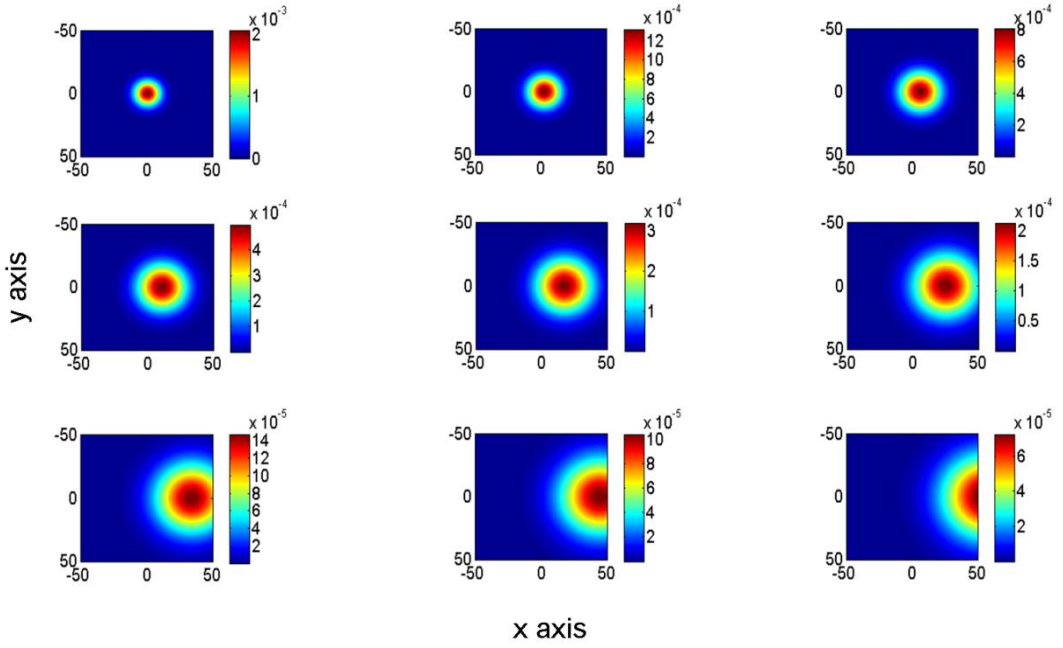

Figure 4-15 Plots of reflected intensity from mirror 1, as the beam has completed a round trip in a wedged FPI cavity for a 10 μm beam radius and a wedge angle of $\alpha=0.5^0$.

Figure 4-15 shows the reflected intensity for a 10 μm beam radius with a wedge angle of $\alpha=0.5^0$. As the number of round trips increase from m=1 (top left) to m=9 (bottom right), the beam shifts towards the right of the figure, while simultaneously the beam size increases. The shift in the beam is due to the walk of the beam at large wedge angles. Also the reflected intensity decreases as the number of round trips increase [93]. For a wedge angle of 0.5^0, the shift in the beam along the x-axis after the first round trip is 0.34 μm, and then increases on subsequent round trips.

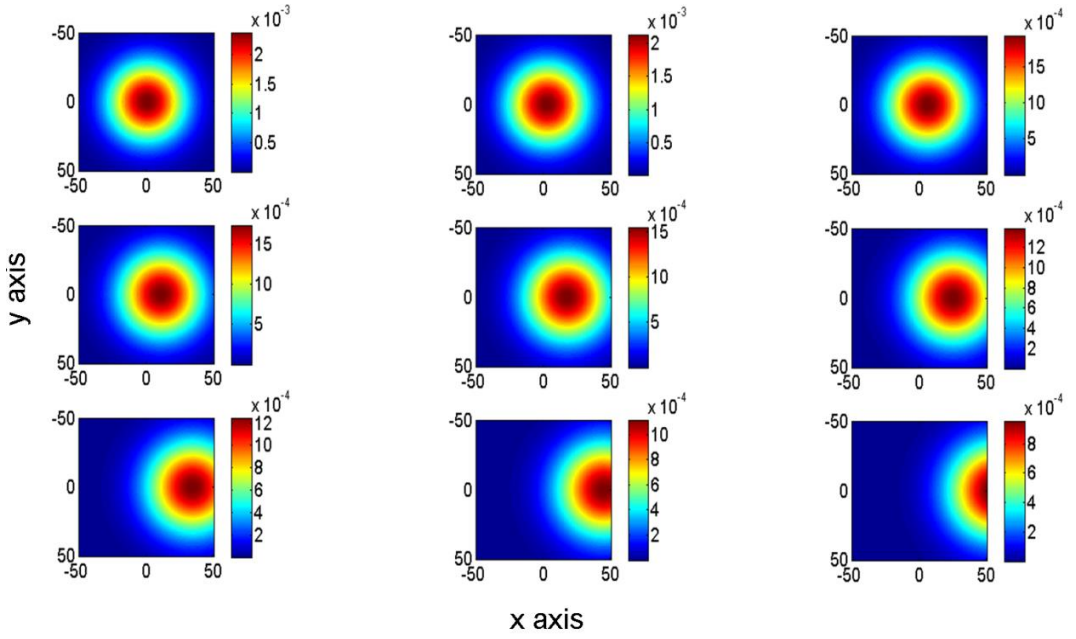

Figure 4-16 Plots of reflected intensity from mirror 1 as the beam has completed a round trip in a wedged FPI cavity for a 40 µm beam radius and a wedge anlge of α=0.5⁰.

Figure 4-16 shows the reflected intensity plots for a 40 µm beam radius, in a FPI with a wedge angle of $\alpha=0.5^0$. As the number of round trips increase from m=1(top left) to m=9(bottom right), the beam shifts to the right of the figure, while the beam size stays constant. A calculation of the shift in the beam per round trip can be considered from the model implementation presented in section 4.4. Taking the length x_α as the position of the centre of the beam for the mth round trip and wrapping it onto mirror 1, the central position of the beam after m round trips can be found. The expression for the shift Δx on each round trip is expressed as,

$$\Delta x = \frac{x_\alpha}{\cos(2m\alpha)} - x_\alpha \qquad 4.26$$

where x_α is the position of the centre of the beam from the apex of the wedge. The cosine term maps to the point x_m at mirror 1 for the mth round trip. Taking the difference from x_α gives the shift Δx on each round trip. Figure 4-17 shows the shift Δx for the centre of the beam on each round trip for a wedge angle of $\alpha = 0.5^0$.

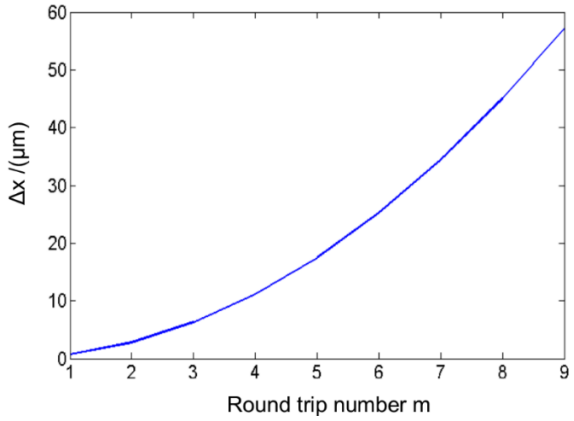

Figure 4-17 Shift along the x-axis for the centre of the beam after each round trip, for a FPI with wedge angle of α= 0.5^0 and cavity spacing of 40 μm

For the first few round trips, the shift in Δx is small. For m=1 the shift in the x-axis 0.698 μm. To compare with a geometric calculation, the expression for the shift in Δx for the first round trip can be expressed as,

$$\Delta x_1 = l_0 \tan(2\alpha) \qquad 4.27$$

Where Δx_1 is the shift in the x-axis for the first round trip, l_0 is the cavity spacing at x_α where the beam is incident, and α is the wedge angle. Taking values of l_0 as 40 μm and α = 0.5^0 the value of Δx_1 is 0.698 μm, agreeing with the expression in Eqn. 4.26. At m=5 the shift is 21 μm, which agrees with the corresponding reflected beam intensities in Figure 4-15 and Figure 4-16 for the fifth round trip. Similarly for m=9 the shift is 57 μm which is also shown Figure 4-15 and Figure 4-16.

The above analysis has shown that the model does indeed follow the conceptual idea of the beam walking off for large wedge angles, for both small and large beam radii. The small beam radius also expands as it propagates in the cavity.

4.6 Model summary

This chapter has presented a model for a Gaussian beam illuminating a planar and wedged FPI. This was setup for a planar FPI by propagating the beam in free space and sampling the electric fields at planes normal to the optic axis, spaced equally apart by 2*l*. The numerical expression for the model was shown in Eqn. 4.13, and where Eqn. 4.15 expressed the total reflected power as a function of wavelength. The wedged model was also setup in a similar way. Instead of sampling planes normal to the optic axis, the electric fields after having gone a round trip are sampled in a plane that is rotated by 2mα to the normal of the optic axis. Equation 4.22 represents the total electric field in a wedged FPI, and where Eqn. 4.23 expresses the total reflected power from the wedged FPI. The model was evaluated by comparing the ITF_λ for a large beam radius with that of a non-diverging beam described by the Airy function, a good comparison was shown. Also for small beam radii, the beam expands radially as it propagates in the FPI, and in a wedged FPI the lateral walk-off of the beam is consistent with the wedge angle modelled. The purpose of setting up these models is to implement them as predictive design tools that can be used to design FPI sensors to obtain the highest optical sensitivity, as well as the optimisation of optical parameters by taking into account the conditions imposed by the experimental system. To achieve this, the next step in the implementation of the model is to experimentally validate the model, by comparing the modelled ITF_λs with experiment for a range of FPI's with different mirror reflectivities and beam radii. Also a comparison of figure of merits such as finesse and visibility, between the model and experiment is needed to compare the trends. The next chapter presents the experimental arrangement for experimentally validating the model, as well as the comparison between model and experiment.

Chapter 5 Numerically simulated and experimental ITF$_\lambda$s of a planar FPI, with interpretation of the ITF$_\lambda$ shapes

This chapter details the experimental arrangement and results for validating the planar FPI model. The experimental wavelength ITF$_\lambda$s are compared with modelled ITF$_\lambda$s. A comparison of the finesse and visibility between the experiment and model is presented. Section 5.1 describes the experimental system, and Section 5.2 presents the results of the experiment and model comparison results. Section 5.3 presents an understanding of the shapes of ITF$_\lambda$s by considering the individual effects of the phase due to a Gaussian beam. The explanation of the shape of the ITF$_\lambda$ is undertaken by decomposition of the electric field for each round trip in a Fabry Perot Interferometer.

5.1 Experimental method

5.1.1 Experimental schematic and arrangement

5.1.1.1 *Experimental schematic*

The experimental arrangement utilised the photoacoustic imaging system, which employs the Fabry Perot Interferometer sensor. Figure 5-1 shows the schematic of the experimental arrangement, with an enlargement of the collimator, showing how the collimator along with the focussing lens L1 adjusts the focussed beam radius in this experiment.

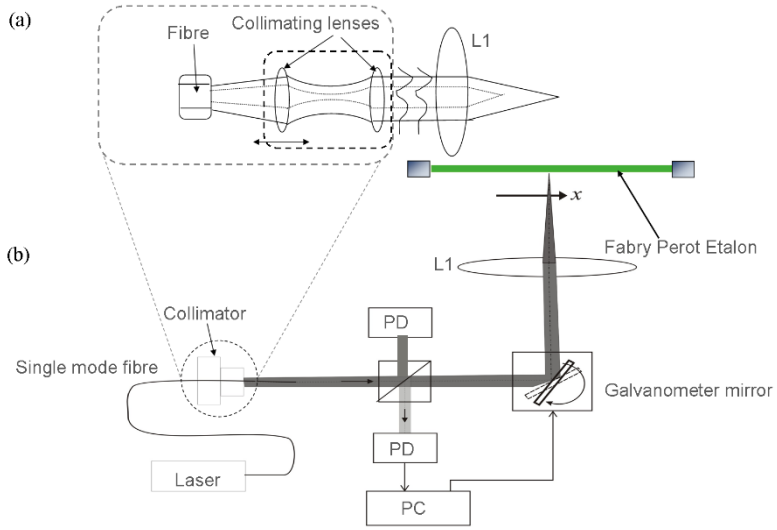

Figure 5-1 Experimental schematic for validation of the model using etalons. The interrogation light is provided by a tuneable laser coupled to a single mode fibre and an adjustable collimator, where the light is then focussed by lens L1. PD is the photodiode to detect the reflected light from the etalon and detecting the output from the collimator

The experimental system consists of an external cavity Santec Laser (TSL 510) with a wavelength tuning range of 1510-1620nm. The output of the laser is coupled into a single mode fibre, which is subsequently connected to an adjustable collimator. The adjustable collimator is used to alter the beam radius incident on the focussing lens L1, thus changing the beam radius at the focus of the beam. The etalon is mounted on a three-axis optical mount to adjust the etalon such that it is the focal plane of the beam and to adjust the angle of the etalon until the beam is normal to the etalon. The galvanometer mirrors are used to align the beam at the centre of the focussing lens L1. The reflected light from the Fabry Perot etalon is then deflected onto a photodiode (PD) via a beam splitter to detect the reflected light received. The same photodiode is used before the experiments to measure the output light from the collimator, and to compare with the reflected light from the etalon to correct for any wavelength dependent attenuation from the experimental system. This is done by normalising the reflected power from the etalon with output power from the laser. It was found that the wavelength dependent attenuation is negligible over a wavelength range of 1500 nm to 1560 nm.

5.1.1.2 *Adjusting the incident beam radius through the adjustable collimator*

This section aims to explain qualitatively of the principal of how the beam radius incident on the FPI is adjusted in the experimental setup. The adjustable collimator alters the radius of the beam incident on lens L_1 shown in Figure 5-1. The change in the incident beam radius on lens L_1 causes a change in the beam radius incident at the Fabry Perot etalon. The collimator consists of a pair of lenses $L_{C,1}$ and $L_{C,2}$ to collimate the output light from the single mode fibre. The maximum collimated beam diameter is achieved when the distance between the lenses is $2F_C$.

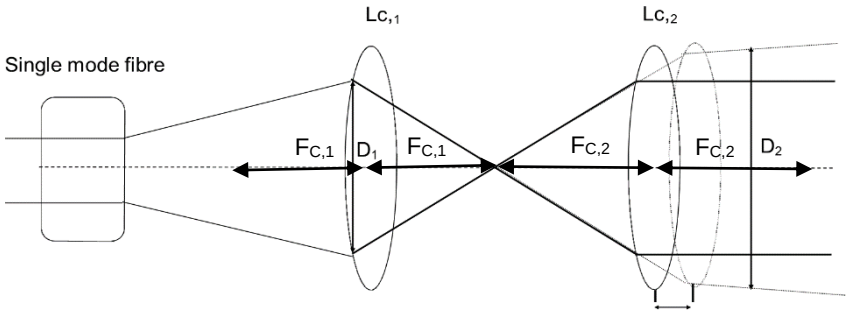

Figure 5-2 Diagram of a collimator, where $L_{C,1}$ and $L_{C,2}$ are the two lenses which form the collimator, with focal lengths $F_{C,1}$ and $F_{C,2}$ with the back focal length and front focal length being the same

Figure 5-2 shows a schematic of an adjustable collimator, where the lens $L_{C,2}$ can be adjusted along the optic axis to show the principle of collimation. The collimator when connected to the single mode fibre delivers the interrogation light to the FPI sensor. The incident beam diameter at the lens $L_{C,1}$ is focussed and then incident on lens $L_{C,2}$. The output beam diameter of the collimator is changed by adjusting the lens $L_{C,2}$ along the optic axis, such that the beam diameter at the lens $L_{C,2}$ is changed, as shown in Figure 5-2. This results in a change in the output beam diameter at lens $L_{C,2}$ by having output beam that is divergent. The expression for the divergence angle at $z>>z_0$ is expressed in Eqn. 5.1 , where z_0 is the Rayleigh range,

$$\theta = \frac{4\lambda}{2\pi\omega_0} \tag{5.1}$$

and ω_0 is the beam radius, λ is the wavelength. The f-number of the lens is the incident diameter D of the incident beam over the focal length F of the lens expressed as,

$$\theta = \frac{D}{F} \tag{5.2}$$

Equating Eqn. 5.1 with Eqn.5.2 by assuming the divergence angle is small, to rearrange in terms of $2\omega_0$ results in the expression for the beam radius at the focus as,

$$2\omega_0 = \left(\frac{4\lambda}{\pi}\right)\left(\frac{F}{D}\right) \tag{5.3}$$

This assumption holds in the case of an incident beam that is collimated and the beam is focussed at the focal plane of the lens.

5.1.1.3 *Photodiode characteristics – power linearity*

The characterisation of the photodiode is helps to understand how the wavelength Interferometer Transfer Function (ITF_λ) changes with the reflected power as wavelength is varied. A large area (2mmx2mm) InGaAs photodiode was used in the experimental arrangement to ensure that all the light is collected onto the detector, such that there is no aperturing effect. This is done by focusing the reflected light from the etalon onto a photodiode area of a few tens of microns by a focussing mirror. The calibration of the photodiode involved increasing the output power from the laser and measuring the change in voltage, rather than current. This is because the photocurrent generated by the photodiode passes through a trans impedance amplifier and feedback resistor to the scope, therefore to obtain a linear measurement power change requires the voltage to be measured. The direct output power of the laser was measured using a power meter (Newport Dual channel 2832-C) while the voltage was measured by the photodiode, as the output power from the laser was increased. The power was measured at a wavelength of 1550 nm.

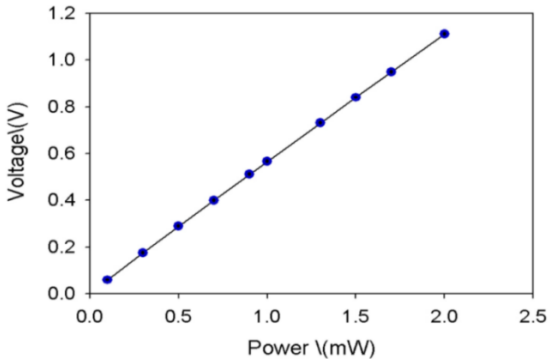

Figure 5-3 Graph of Voltage variation with output power of the laser (Santec TSL-510)

The voltage increases linearly as the output power increases, shown by Figure 5-3. The voltage change with power (dV/dP) is 0.5 V/mW. For the power range recorded, the voltage increases with increasing power, where a change of 1V is due to a change of 2 mW of the reflected power. The power incident on the etalons in this experiment had laser output power levels between 1 mW and 2 mW.

5.1.1.4 *Photodiode characteristics – spectral response*

The spectral response of the photodiode also has to be taken into account when making measurements of ITF$_\lambda$s. The photodiode used was a Thorlabs InGaAs calibrated to NIST (National Institute of Standards) traceable standards.

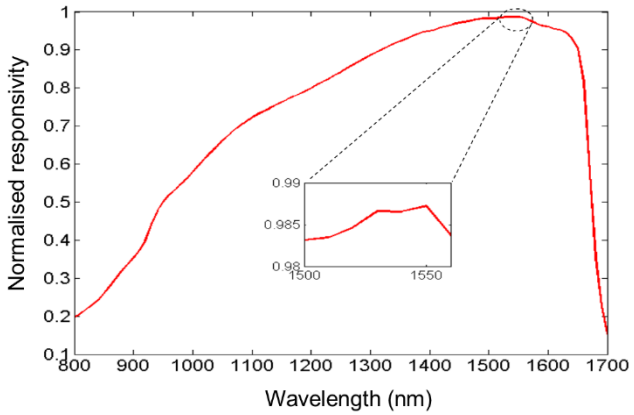

Figure 5-4 Responsivity vs. wavelength for Thorlabs InGaAs photodiode

Figure 5-4 shows the responsivity of the InGaAs photodiode as a function of the wavelength from 800 nm to 1750 nm. The responsivity is defined as the ratio of the photocurrent I_g due to incident light falling on the detector to the incident power P_i,

$$R(\lambda) = \frac{I_g(\lambda)}{P_i} \qquad 5.4$$

The responsivity as function of wavelength around 1550 nm is roughly flat as seen in Figure 5-4, where a difference of less than 1% was found between 1500 and 1570 nm. This wavelength range was investigated as the reflectivity of the etalon mirrors are designed at 1550 nm. Also for this study the wavelength range used will be in the region of 1550 nm to 1560 nm. Therefore over this wavelength range the spectral dependence of the photodiode response can be neglected. Equation 5.5 expresses the normalisation of the ITF_λ from the measured voltages $V_i(\lambda)$ due to the output light of the laser P_0 and $V_{refl}(\lambda)$ which is the voltage due to the reflected light from the etalon,

$$\frac{P_{refl}}{P_0} = \frac{V_{refl}(\lambda)}{V_i(\lambda)} \qquad 5.5$$

5.1.1.5 *Optical Alignment of the Fabry Perot etalon at the beam waist*

The beam waist needs to be incident at the first mirror of the Fabry Perot etalon. This is because the model assumes that the beam waist is incident at mirror 1 of the FPI. To make sure that the beam waist is at normal incidence to the first mirror of the etalon, the etalon is translated along the optic axis and rotated around the *x-y* plane, by using the three axis mount. To determine when the incident mirror of the etalon is aligned normally at the beam waist, the beam is scanned across a 10 mm by 10 mm area. The etalon is adjusted along the optic axis as well as the *x-y* plane until the voltage measured by the photodiode is a maximum. This is done by use of a Lab View VI program used to align the FPI sensors for PA imaging at the focal waist of the beam.

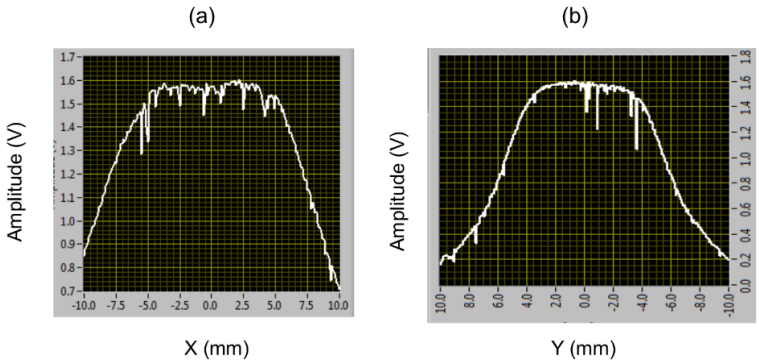

Figure 5-5 Measured voltage (from LabView program) in the x and y planes as the beam is scanned across the FPI sensor when the etalon is at the beam focus and at normal incidence to the beam

Figure 5-5 shows when the maximum voltage is measured as the etalon is adjusted along the optic axis. A flat line of roughly 5 mm across the surface of the etalon in both the x and y planes is shown in Figure 5-5, is achieved such that the beam is normal to the etalon. This is done by rotating the etalon in the *x* and *y* plane. If the beam was not normal, then the beam will be reflected at an angle and not trace the same path back to the beam splitter, where it is then deflected onto the photodiode.

5.1.1.6 *Measuring the beam radius of the focussed beam*

The diameter of the focussed beam is measured using a beam profiler (DataRay Beam – R2 DD) for the purpose of inputting the correct beam radius in to the model. The beam profiler is placed on the optical mount for the etalon. The mount is then adjusted along the optic axis until the smallest beam diameter is measured, corresponding to the beam waist.

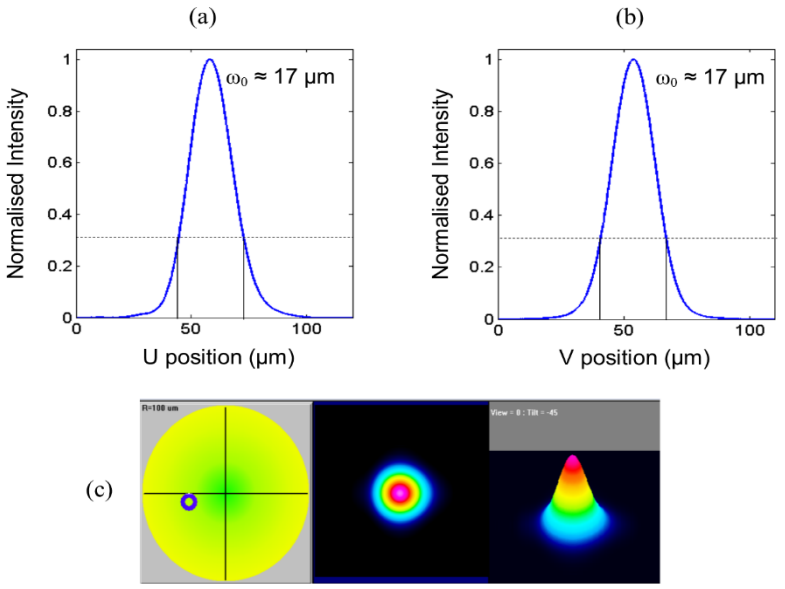

Figure 5-6 Beam profile along the U and V axis with a beam diameter of 34 µm, as well as (c) 3D rendering and position of the beam relative to the centre of the calibrated detection area on the beam profile

Figure 5-6 shows a beam profile for 34 µm beam diameter along two planes which are normal to each other. A 3D representation of the beam is shown of the beam.

5.1.2 Fabry Perot Etalons

The experimental validation of the model requires a Fabry Perot etalon with well-known surface non-uniformity and mirror reflectivities R, where the mirror reflectivities of the first and second mirror R_1 and R_2 respectively are the same. Two solid fused silica Fabry Perot etalons of thickness 200 µm were used, one with mirror reflectivities being R=95% and the second etalon having mirror reflectivities of R=98%, where the mirror reflectivity is specified at 1550 nm. The mirror reflectivities are known to a precision of 1%. The variation in cavity thickness is λ/100 per cm^2 at 1550nm. The etalon can then be approximated as planar across the surface of the etalon illuminated by the beam, since the radii of the latter are in the range of 15 µm to 80 µm in this study.

5.1.2.1 *Mirror transmission spectrum*

The mirror coatings of the two etalons are formed using dielectric materials, built up layer by layer using an epitaxial method. The transmission spectrum is related to the reflectivity spectrum by T=1-R, where T and R are the power transmission and reflection coefficients, and ignoring absorption.

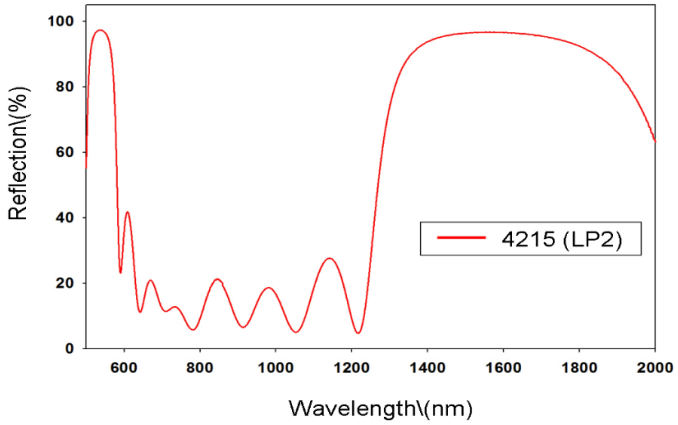

Figure 5-7 Reflection spectrum for 95% mirror coatings for both mirror coatings

Figure 5-7 shows the reflection spectrum for the etalon with 95% mirror reflectivity. Both mirrors have the same reflection spectrum compared to the etalon with 98% mirror reflectivity. Figure 5-8 shows the reflection spectrum for the etalon for 98% mirror reflectivities at λ=1550 nm. In the region of 1510-1700 nm the reflectivity is high at around 98%. As can be seen in Figure 5-8, the coating of the second mirror (6688) has been shifted to longer wavelengths relative to the first mirror coating (6738). At 1550 nm a difference of less than 0.2% in the reflectivity is found between the mirrors.

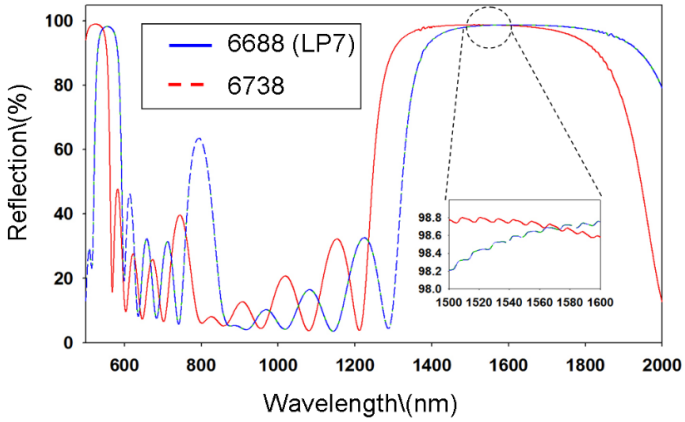

Figure 5-8 Reflection spectrum for the etalon with R=98%, with 6738 and 6688 referring to the first and second mirror coating respectively

5.1.2.2 *Etalon cavity spacer thickness*

The cavity of the Fabry Perot etalon was composed of fused silica (n=1.44) and was around 200 μm thick. The Free spectral range FSR_λ in wavelength space is defined in Eqn. 5.6,

$$FSR_\lambda = \frac{{\lambda_0}^2}{2nl} \tag{5.6}$$

where λ_0 is the wavelength corresponding to the reflectance minima, and *nl* is the optical thickness. The refractive index is *n* and the physical thickness is *l*. The FSR_λ is determined by acquiring a wavelength ITF_λ across two reflectivity peaks and measuring the wavelength difference between the two peaks. The larger the physical thickness the smaller the wavelength separation between reflectivity peaks. The advantage of having reflectivity peaks closely spaced together in wavelength space is that the wavelength tuning range needed to find two consecutive reflectivity peaks is narrow. Therefore the chances of finding a reflectivity peak close 1550 nm is much higher compared to smaller cavity spacings of 10 μm to 40 μm.

5.2 Experimental results

This section details the comparison between experimental and modelled ITFλs for the planar FPI model. The finesse and visibility are also compared between the model and experiment for the two Fabry Perot etalons with mirror reflectivities of 95% and 98%.

5.2.1 Comparison of Interferometer Transfer functions (ITF_λs)

This section compares the experimental wavelength Interferometer Transfer Function (ITF_λ) with the modelled ITF_λ. The input parameters for the model such as beam radius, mirror reflectivities and cavity spacing are experimentally determined as described in the previous sections. The beam radius is measured by the beam profiler, while the input mirror reflectivities are those specified by the manufacturer at the corresponding wavelength used to

obtain an ITF$_\lambda$. The absorption by the spacer layer was ignored as the spacer layer is composed of fused silica (n=1.44). A small phase offset was introduced in the model to align the ITF$_\lambda$ reflectance minima.

5.2.1.1 *ITF$_\lambda$ comparison for FPI of R=95% mirror reflectivities*

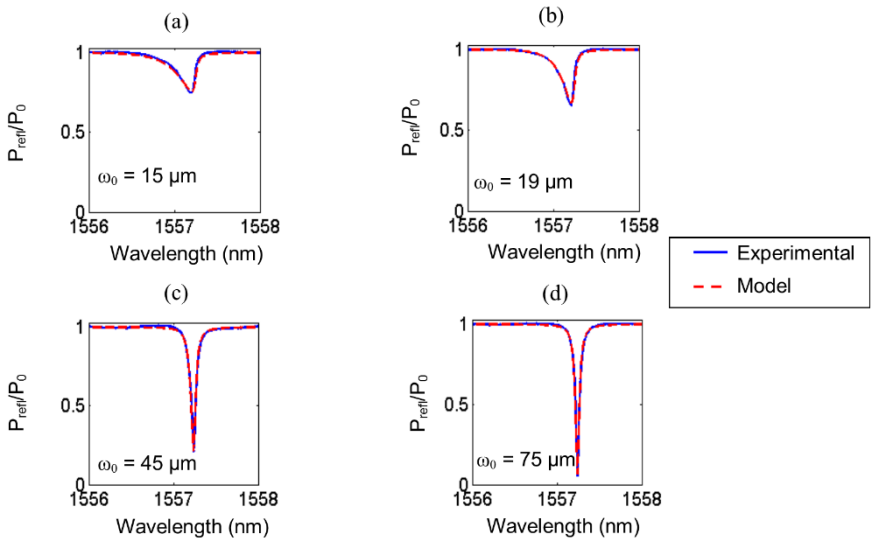

Figure 5-9 Experimental and modelled ITF$_\lambda$s for beam radii (a) ω_0 = 15 µm, (b) ω_0 = 19 µm, (c) ω_0 = 45 µm and (d) ω_0 = 75 µm for a cavity thickness of 190 µm (n=1.44). The mirror reflectivities were R=95%

Figure 5-9 shows the wavelength ITF$_\lambda$s for various beam radii, with mirror reflectivity of 95%, and cavity thickness of 190 μm. The simulated and experimental ITF$_\lambda$s are in close agreement for all beam radii. Figure 5-9 (a) shows the ITF$_\lambda$ for a 15 µm beam radius (ω_0), the ITF$_\lambda$ exhibits asymmetry characterised by a shallow slope (dR/dλ) in the reflectivity peak at short wavelengths, and relatively steeper slope at longer wavelengths. The reflectance minimum is 0.75 therefore the visibility is 0.15, which is much less than the ideal visibility of 1 for a non-diverging beam. Figure 5-9 (b)-(d) show ITF$_\lambda$s for beam radii of 19 µm, 45 µm and 75 µm respectively. As the beam radius increases the asymmetry decreases and the visibility increases. This is because as the beam radius increases it becomes less divergent, approximating closer to a non-diverging beam.

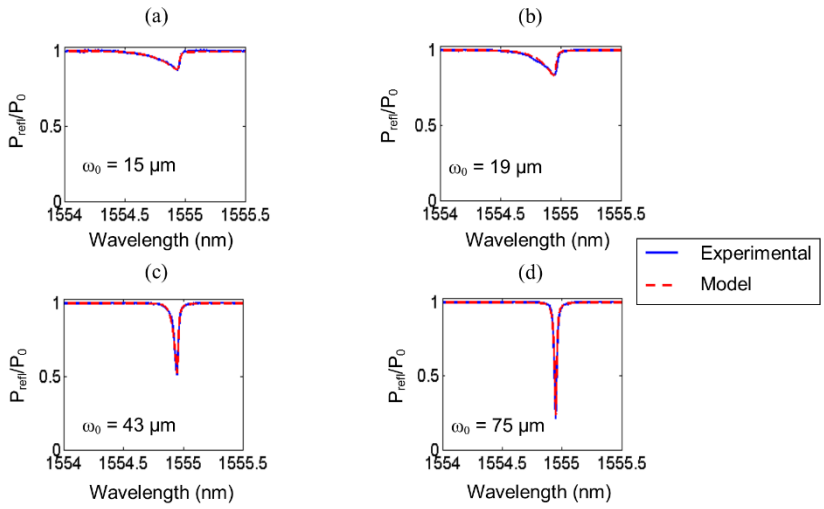

Figure 5-10 Experimental and modelled ITF$_\lambda$s for beam radii (a) ω_0 = 15 µm, (b) ω_0 = 19 µm, (c) ω_0 =43 µm and (d) ω_0 = 75 µm with cavity thickness of 193 µm and fused silica (n=1.44), for mirror reflectivity of R=98%

Figure 5-10(a) shows the ITF$_\lambda$ for a 15 µm beam radius incident on an etalon with R=98% and cavity thickness of 193 μm. The asymmetry of the ITF$_\lambda$ at small beam radii is greater compared to that for R=95%, shown in Figure 5-9 (a). The visibility is also much less. This is also the same for a beam radius of 19 µm. Figure 5-10 (b)-(d) shows ITFλs for beam radii of 19 µm, 45 µm and 75 µm respectively. The general trend of asymmetry reducing as beam radius increases is the same as that shown for the etalon with R=95%. Although in general the visibility is much less for all beam radii for the etalon with R=98%.

5.2.2 Comparison of finesse and visibility results

This section presents the comparison between the experimentally determined finesse and visibility with the modelled finesse and visibility as the beam radius varies.

5.2.2.1 *Finesse and visibility calculation*

The finesse calculated in both the model and experimental result is defined as the ratio of the Free Spectral Range (FSR) over the Full Width at Half Maximum (FWHM) in wavelength space, as defined in Eqn.5.7. The FWHM in both the model and experimental results is determined from the width of the reflectivity peak at the halfway value

$$F = \frac{FSR_\lambda}{FWHM_\lambda} \tag{5.7}$$

The reflectivity finesse F_R for a non-diverging beam is stated as,

$$F_R = \frac{\pi\sqrt{\mathcal{F}}}{2} = \frac{\pi\sqrt{R}}{(1-R)} \tag{5.8}$$

which is the maximum achievable finesse for a specific mirror reflectivity R, where $\mathcal{F}$ is the coefficient of finesse. The visibility is given by the difference between the normalised maximum R_{max} and normalised reflectance minima R_{min}, divided by the summation of the two values. The expression for visibility is expressed in Eqn. 5.9 below,

$$V = \frac{R_{max} - R_{min}}{R_{max} + R_{min}} \tag{5.9}$$

Therefore from the experimental and modelled ITF_λs shown in Figure 5-9 and Figure 5-10, the finesse and visibility would increase as the beam radius increases.

5.2.2.2 *Finesse and visibility for different beam radii*

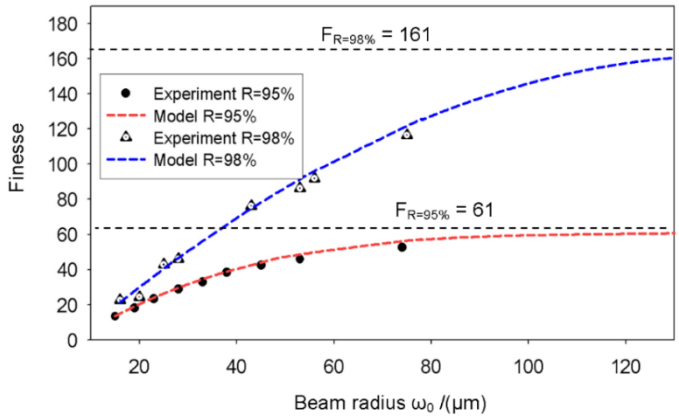

Figure 5-11 Finesse variation with beam radius for both the model and experimental results, for 95% and 98% Fabry Perot etalons with cavity spacing *l* = 190 μm, where $F_{R=98\%}$ = 220 and $F_{R=95\%}$ = 90 are the finesses due to a collimated beam for R=98% and R=95% respectively.

Figure 5-11 shows the relationship between finesse versus beam radius for both the model and experimental data of both etalons. The cavity thickness of the Fabry Perot is 190 μm for R=95% and 193 μm for R=98%. Figure 5-11 shows that as the beam radius increases the finesse increases. There is good agreement between the model and experiment for both etalons with mirror reflectivities of R=95% and R=98%. The finesse for the etalon with mirror reflectivities of R=98% is higher compared to the finesse obtained when the mirror reflectivities are R=95%. As the beam radius is increased, the finesse tends to limiting values corresponding to the finesse for a non-diverging beam. These are F=161 for R=98.07% and F=61 for R=95% which are calculated using Eqn. 5.8. For R=95%, the beam radius at which the finesse reaches a maximum value is at 75 μm, in comparison the beam radius for the etalon with R=98% is 130 μm.

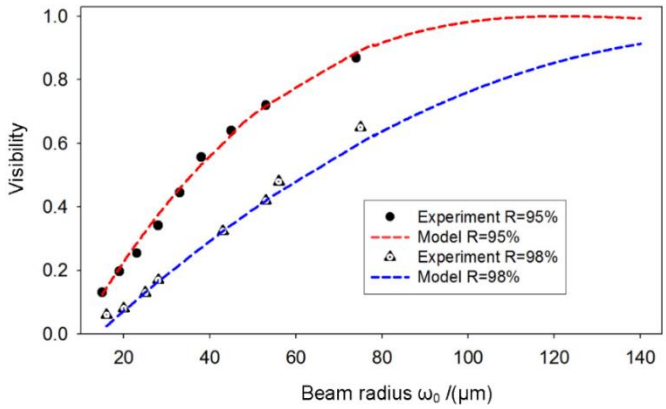

Figure 5-12 Visibility variation with beam radius for both the model and experimental results, for the 95% and 98% Fabry Perot etalon with cavity spacing *l* = 190 μm and *l* = 193 μm respectively

Figure 5-12 shows the visibility variation with beam radius for both Fabry Perot etalons. The visibility increases as beam radius increases for both etalons. It is a similar trend to finesse versus beam radius. As the beam radius increases, the visibility tends to a limiting value of 1. The experimental results also follow the modelled trend with good agreement. The visibility for all beam radii is higher for the etalon with mirror reflectivities of R=95% compared to the etalon with mirror reflectivities of R=98%.

5.2.2.3 *Validity of the model*

The good agreement between experimental and modelled ITF_λs, as well as their finesse and visibility shows the model as a valid tool in the design of optical FPI sensors. The ability to replicate the ITF_λ one would expect from experiment with different optical parameters, verifies in using the model to characterise the performance of the Fabry Perot Interferometer with these range of parameters. As the model being a valid tool, it is also useful to understand the shapes of the ITF_λ for various optical parameters. This will further help in designing optimised FPI sensors. The next section aims to explain the cause of asymmetry exhibited for when the etalon is illuminated with small beam radii.

5.3 Explanation of asymmetry in ITF$_\lambda$s for a Gaussian beam illumination

The experimental results and those simulated by the model for a Gaussian beam propagating in a Fabry Perot Interferometer (FPI), show an asymmetric reflectivity peak for highly divergent beams. This suggests there is a link between the divergence and the asymmetry. It is important to understand the behaviour exhibited by the ITF$_\lambda$ when the FPI is illuminated by diverging beams, as it could give clues on how to design FPI sensors with small beam radii. Asymmetric ITF$_\lambda$s have been shown in the modelling of Fabry Perot Interferometers by others such Lee. J[1] for frequency space ITFs in transmission mode. It was noted that the transmission peak reduces and shifts towards longer frequencies for smaller beam radii, with an attempt at an analytical expression for this transmission peak shift involving the Gouy phase. Others such as La Penna. P. [94] showed asymmetric cavity thickness ITFs also in transmission mode. There has not been an attempt at understanding the shape of the ITFs through the phase characteristics of the Gaussian beam. This section will aim to explain the cause of the asymmetry by considering the individual components of the phase propagation of a Gaussian beam. Initially the shape of ITF$_\lambda$s for a non-diverging beam is explained. This explanation is then extended to Gaussian beams. This is done by aperturing the Gaussian beam with a disc at the centre so that the divergent parts of the beam are neglected, as presented in subsection 5.3.2.1. Then a ring based aperture is considered for understanding the effects of the divergent part of the beam on the asymmetric shape of the ITF$_\lambda$, which is presented in section 5.3.2.4.

5.3.1 Explanation of the shape of ITF$_\lambda$s for a non-diverging beam

This section explains the shape of ITF$_\lambda$s for a non-diverging beam, by decomposing the electric field into individual round trips. The phase difference between each round trip for a non-diverging beam is inversely proportional to the wavelength, as expressed below

$$\varphi = \frac{4\pi nl}{\lambda} \tag{5.10}$$

where n is the refractive index, l the physical cavity thickness and λ the wavelength. As wavelength increases the phase decreases. At longer wavelengths the change in the phase is

smaller. This therefore induces a small asymmetry in the ITF_λ reflectivity peak even for a non-diverging beam. The asymmetry is characterised by a shallow slope at long wavelengths and a sharper slope at short wavelengths. This is a very small asymmetry where the difference in the slope between each side is 0.0091%. Figure 5-13 shows the ITF_λ for a non-diverging beam showing a slight a difference in the magnitude of the slope, where at longer wavelengths the maximum of the slope is slightly lower than the maximum at the shorter wavelengths.

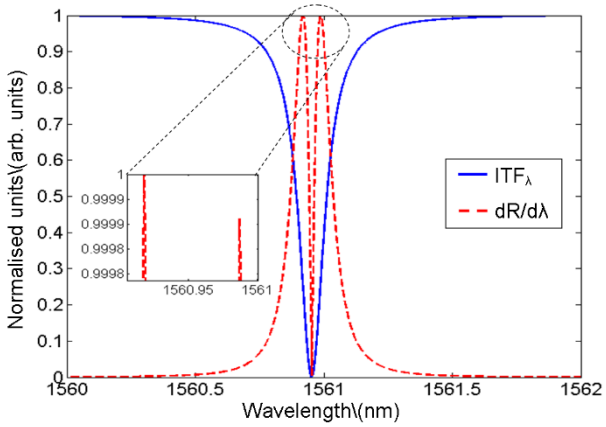

Figure 5-13 ITF_λ for a non-dverging beam illuminating a FPI with R=98% and l = 40 µm, with the derivative dR/dλ

As shown in Figure 5-9(a) and Figure 5-10(a)-(b), the asymmetry for a highly diverging Gaussian beam is reversed, in that the shallower slope is at shorter wavelengths and the steeper slope is at longer wavelengths. This is because the electric field expression for a Gaussian beam has additional phase terms describing the beam propagation along the optic axis. These additional phase terms are a consequence of the divergent effects of the beam and are responsible for the highly asymmetric nature of the ITF_λ. In a non-diverging beam the round trip phase difference $\Delta\phi_{rt}$ in the cavity has to be 2π for resonance to occur. Equation 5.11 expresses the electric field at mirror 1 for a non-diverging beam, where a_m is the amplitude coefficients, and 2ml is the distance propagated on a round trip,

$$E_m = a_m E_0 e^{-i2kml} \tag{5.11}$$

Figure 5-14(a) shows the electric field magnitude at mirror 1 for the m^{th} round trip, as the wavelength is varied. The electric field magnitude at the minima of the peak is reduced for consecutive round trips. The reflectance minima are all at the same wavelength highlighted

by the dashed line. For this reason the summation of the electric field magnitudes shown in Figure 5-14(b) forms a symmetric resonance peak as expected.

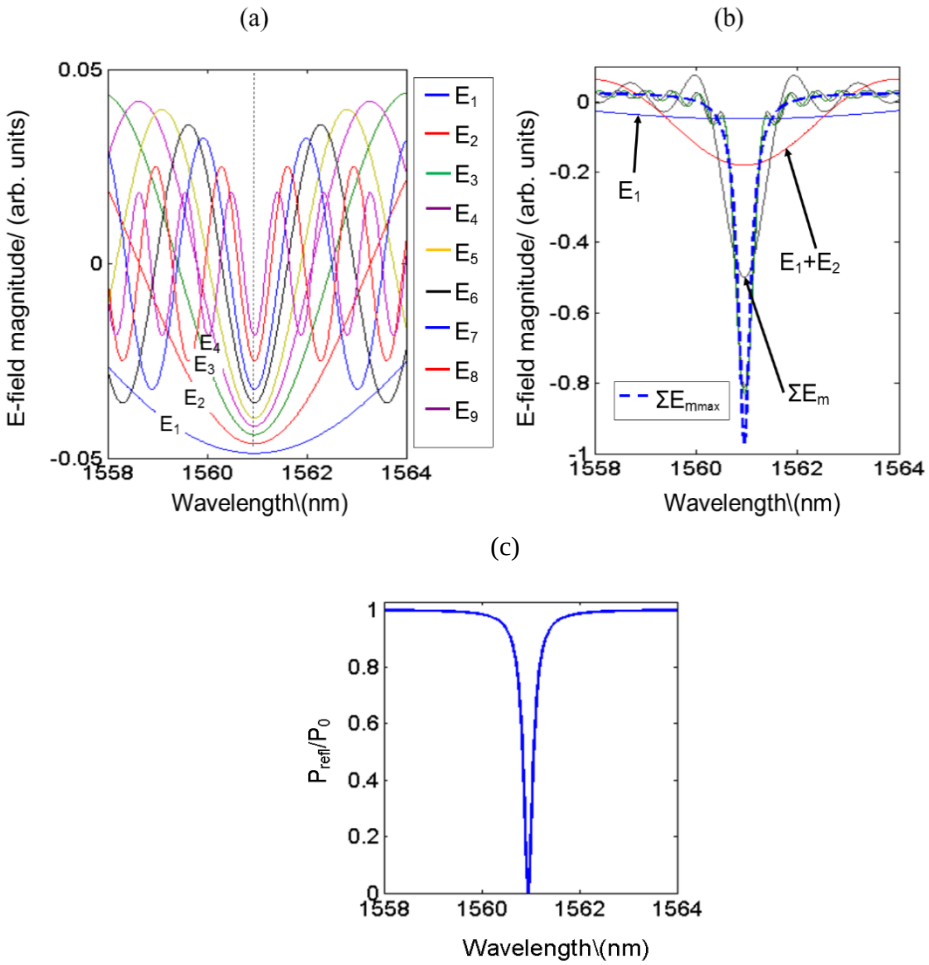

Figure 5-14 Graph of (a) Electric field magnitude at mirror 1 for each round trip, as the wavelength is varied, with the legend shown to the right of the figure and (b) cumulative sum of electric field magnitude after each round trip and (c) ITF_λ for a collimated beam with *l*=40 µm and R=98%

The electric field magnitudes presented in Figure 5-14 and in subsequent analysis is only a function of wavelength, and has ignored the time varying component of the electric field. This is because of the cavity spacing is in the range of a couple of tens of microns, therefore the time variation of the field is on the order of a hundredth of a picometre. This is assumed negligible as no current photo detector can feasibly resolve the electric field variation to this time scale. The electric field magnitude is therefore assumed a snapshot in time.

5.3.2 Explanation of the shape of ITF$_\lambda$s for a Gaussian beam

This section explains the asymmetric shapes of ITF$_\lambda$s for divergent Gaussian beams. In comparison to the non-diverging beam, where the only phase consideration is the path length phase *kz*, a Gaussian beam has additional phase components. Equation 5.12 expresses the electric field for a Gaussian beam after each round trip at mirror 1.

$$E_m = a_m E_0 e^{-i(2kml-\Theta_m+\frac{k\rho^2}{2R_m(2ml)})} \quad 5.12$$

To analyse the effect each individual phase component has on the electric field for each round trip hence on the shape of the ITF$_\lambda$, each component is analysed separately. This is done by only considering the propagation phase *kz* and Gouy phase Θ by setting the radial phase component to zero (ρ=0), this is equivalent to spatially filtering the beam using a disc based aperture. To consider the effect of the radial phase at various radii ρ, a ring aperture is used.

5.3.2.1 *Spatially filtering by applying a disc aperture*

The expression for the electric field magnitude for the mth round trip by a Gaussian beam at mirror 1 is expressed in Eqn. 5.13. This is the equation implemented in the model to simulate Gaussian beams illuminating Fabry Perot Interferometers expressed in Eqn. 4.6 in chapter 4. In the first instance for simplicity, the radial component of phase due to a Gaussian beam is neglected by setting ρ = 0 µm, this effectively apertures the beam such that the divergent parts of the beam are neglected.

$$E_{G,m}(\rho = 0,2ml) = a_m \frac{\omega_0}{\omega(2ml)} e^{-i(2kml-\Theta_m)} \quad 5.13$$

Θ_m is the Gouy phase term. The Gouy phase term manifests itself as a result of the curvature of the wave front of a Gaussian beam. Substituting the expression for the Rayleigh range ($z_0=\pi\omega_0^2/\lambda$) and the distance propagated for the mth round trip ($z=2ml$) into the Gouy phase expression, allows Θ_m to be expressed as follows,

$$\Theta_m = \tan^{-1}\left(\frac{\lambda 2ml}{\pi {\omega_0}^2}\right) \qquad 5.14$$

The Gouy phase evolves with the distance propagated; hence it varies with each round trip of the cavity. This results in a non-constant phase shift on each round trip. The Gouy phase describes the lag in the phase of the wave front as the beam propagates, compared to a non-diverging planar wave front. The phase lag is non-linear as the variation in the radius of curvature of the wave front with propagation distance is non-linear. Figure 5-15(a) shows the phase of the wave front curvature on subsequent round trips reduced by $\Delta\Theta_m$, and this difference varies on each round trip.

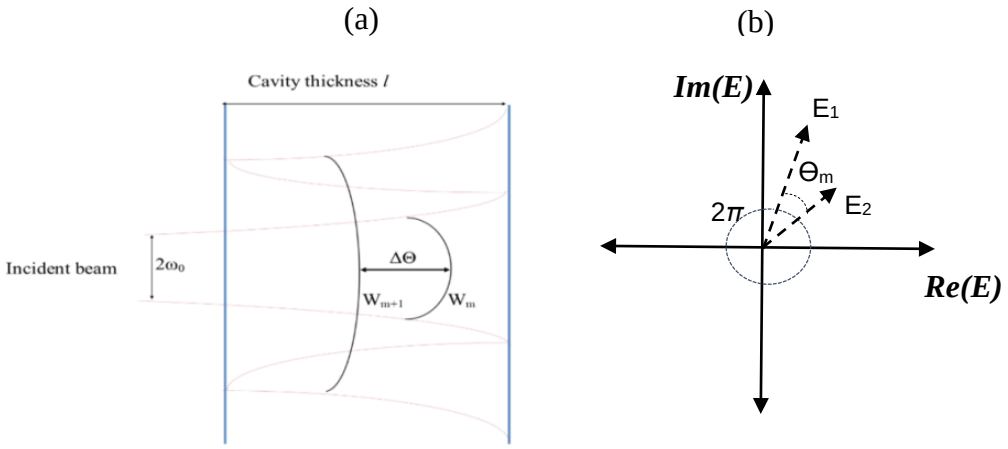

Figure 5-15 (a) Depiction of the lag in the wave front between W_m and for the subsequent round trip W_{m+1} by $\Delta\Theta_m$ due to the Gouy phase and (b) Argand diagram showing the shift in the electric field at resonance between the first two round trips

For a Gaussian beam the addition of the Gouy phase reduces the phase as the beam propagates. This phase reduction is non-linear due to the Gouy phase expression of Eqn. 5.14.

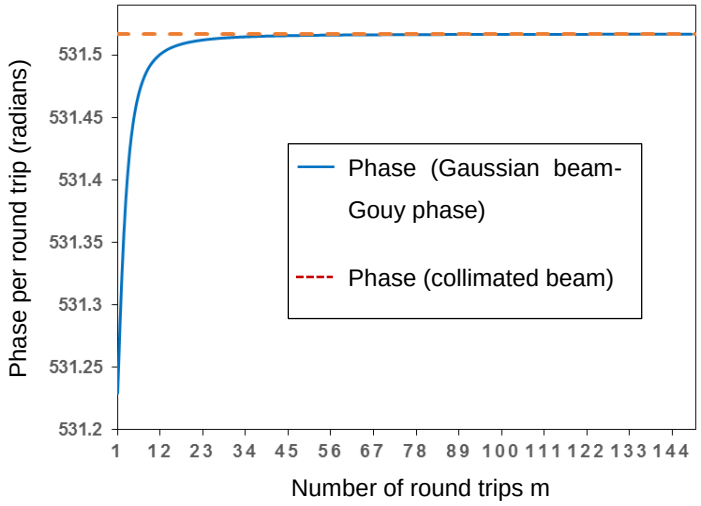

Figure 5-16 Propagation phase *kz* per round trip m, along with the propagation phase for a Gaussian beam with a disc aperture for a 40 µm thick FPI cavity illuminated with a Gaussian beam of 10 µm beam radius

Figure 5-16 shows the phase per round trip for a collimated beam, which is constant ($\varphi=4\pi nl/\lambda$). For a disc aperture applied to a Gaussian beam, as the beam propagates the Gouy phase increases until it tends to a limiting value of $\pi/2$ radians. For larger beam radii the increase in the Gouy phase magnitude per round trip will be smaller as it reaches the limiting value over a much larger propagation distance. The effect of the Gouy phase will be different from that of a constant phase shift induced by transmission or reflection from a mirror. The electric fields for a non-diverging beam at resonance (which has a 2π constant phase shift) would overlap. Figure 5-15(b) shows a Argand diagram of the electric field of a Gaussian beam for the first two round trips at resonance, which are shifted by the Gouy phase. The Gouy phase shifts the electric field phase per round trip. The shift in the electric field phase reduces as the number of round trips increases.

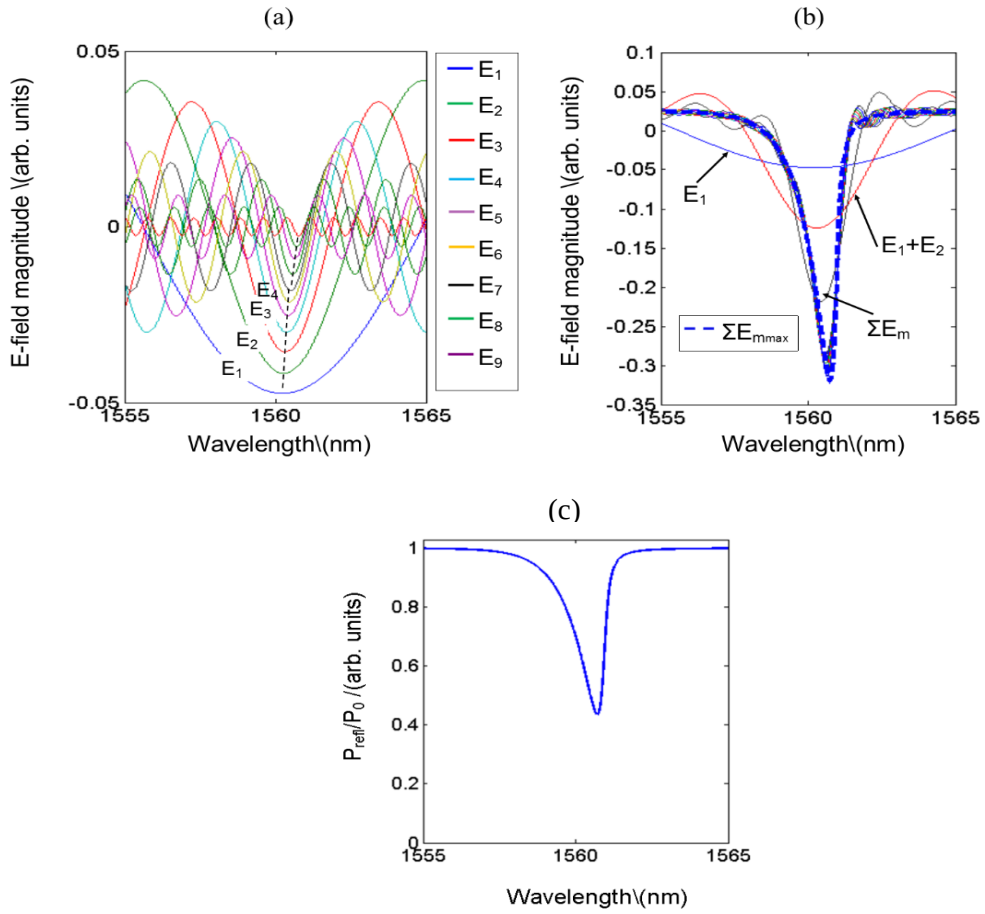

Figure 5-17 Graph of (a) Electric field magnitude at mirror 1 for each round trip, as the wavelength is varied, (b) cumulative sum of electric field magnitude after each round trip at the centre and (c) ITF$_\lambda$ of the beam for a Gaussian beam with beam radius of ω_0 = 10 µm, *l*=40 µm and R=98%

Figure 5-17(a) shows the individual electric field magnitudes for the mth round trip at mirror 1 as the wavelength is varied. The incident Gaussian beam radius is ω_0 = 10 µm, on a FPI with R=98% and a cavity spacing of 40 µm. Note that in contrast to Figure 5-14(a), the electric field minima are not located at the same wavelength as shown by the dashed line in Figure 5-17(a). The electric field for the first round trip is shifted to shorter wavelengths relative to a non-diverging beam due to the reduction in phase by the Gouy phase. The shift in the electric field minima to shorter wavelengths is reduced with increasing m. This is because the change in the magnitude of the Gouy phase becomes much less than the constant round trip phase. The summation of the electric field magnitude for each round trip results in an asymmetric electric field magnitude and ITF$_\lambda$ shown in Figure 5-17(b) and Figure 5-17(c) respectively. As the electric field minima are shifted to longer wavelengths on subsequent round trips, this does not create a strong resonance at the wavelength corresponding to the

reflectance minima of the ITF$_\lambda$. As a result it causes the value at the reflectance minima to be higher compared to that for a non-diverging beam. Therefore the visibility is lower as shown in Figure 5-17(c). This section has provided a simple understanding of the effect of the Gouy phase through decomposing the electric fields and showing the effect of the phase shifts due to a Gaussian beam. However this section considered the effect of the Gaussian beam at the centre, as the radial component was neglected. In the experimental results presented in section 5.2 the beam was unapertured, therefore the component of the radial phase will also have an effect on the ITF$_\lambda$.

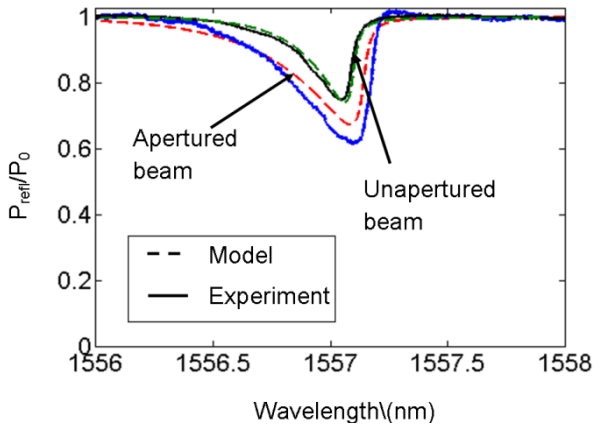

Figure 5-18 Experimental (solid lines) and modelled (dashed lines) ITFλs for a 17 µm beam radius incident on a etalon with R=95% and *l* = 190 µm, showing a difference in the asymmetry between a apertured and unapertured beam

Figure 5-18 shows the difference in the ITF$_\lambda$ between an apertured beam and an unapertured beam for a 17 µm beam radius incident on an etalon with mirror reflectivities of 95% and cavity spacing of 190 µm. There is a difference in the asymmetry and visibility of the ITF$_\lambda$ between the apertured and unapertured beam. Therefore understanding the effect of the radial phase component has on the shape of the ITF$_\lambda$ when the beam is unapertured is presented in the next section. This is done by considering ring apertures with radii ρ, due to the symmetric nature of the Gaussian beam. An experimental study with ring apertures is undertaken and compared with the model. The following subsections presents this work, with subsection 5.3.2.4 explaining the shape of the ITFλs at various radial positions.

5.3.2.2 *Spatially filtering by ring apertures- Experimental arrangement*

Section 5.2.1 presented the ITF$_\lambda$ for when all the light is collected onto the photodiode, with sub-section 5.3.2.1 explaining the shape of asymmetric ITF$_\lambda$s by a considering a disc aperture. The following sub-sections describes the shapes ITF$_\lambda$s for when the beam is apertured with a ring based geometry, by taking rings of radii ρ with ring thickness dρ. This is to consider the effect of the radial divergence on the ITF$_\lambda$. This was achieved experimentally by replacing the photodiode PD2 in the experimental arrangement as shown in Figure 5-1, with a beam profiler (DataRay Beam R2-DD). A 1D profile across the beam was measured as the reflected intensity varied as the wavelength was swept across the tuning range corresponding to a reflectivity peak in the ITF$_\lambda$, as shown in Figure 5-19.

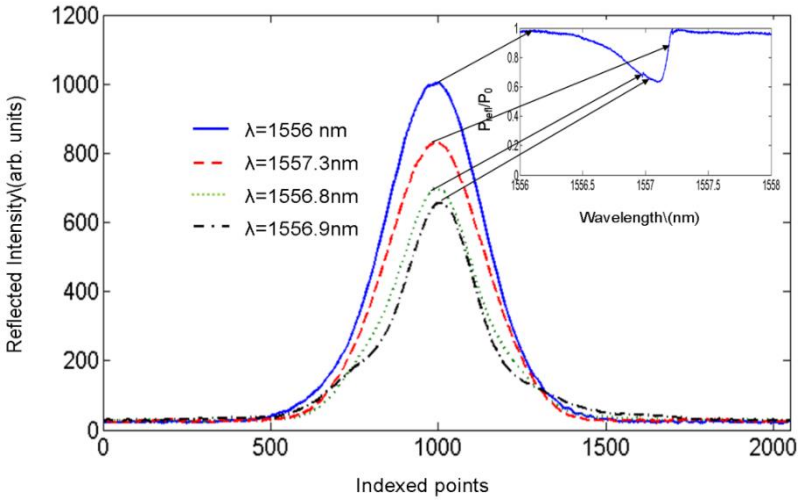

Figure 5-19 Beam profile for various wavelengths, showing the change in the reflected intensity as the wavelength changes

The reflected beam from the Fabry Perot Interferometer was focussed onto the beam profiler using a lens with focal length of 10mm to form a beam diameter ($1/e^2$) of 70 µm. This is so the profile is smooth, leading to a smoother ITF$_\lambda$. If the beam size was larger for the same power, the intensity at each point is much lower; the detector noise would therefore contribute to a less than ideal ITF$_\lambda$. The output power of the interrogation beam was set to 1 mW. The experimental ITF$_\lambda$s are compared with the model in the same manner as for the unapertured case in section 5.2. The reason for taking rings is to increase the detection sensitivity due to the symmetric nature of the TE$_{00}$ Gaussian beam mode. The focussed beam size incident on the etalon was measured using the beam profiler. Beam radii of 17 µm (radius where amplitude falls to 1/e) and 75 µm were measured. A Fabry Perot etalon with mirror reflectivities R=95% and cavity spacing of 190 µm was used. Measurements of ITF$_\lambda$s

at various radial points on the beam were analysed to observe the change in the shape of the ITF_λ. The scale factor between the reflected beams experimentally and in the model was found by taking the ratio of the reflected beam in the model and in the experiment. The measured experimental beam reflected from the etalon was taken as 70 μm due to focussing the beam by a lens. The modelled beam size was calculated in the model by calculating the beam radius at a distance of $2m_{max}l$, such that all of the reflected power from the etalon is taken into account. The scale factor γ between the beam radii is expressed as,

$$\gamma = \frac{\omega_{0,exp}}{\omega_{0,mod}} \tag{5.15}$$

where $\omega_{0,exp}$ is the experimental beam radius and $\omega_{0,mod}$ is the modelled beam radius. The detector ring width in the experiment is known from the slit width of the beam profiler. However due to the profile of a Gaussian beam, the ring width in the model will vary at different radii. Therefore at a radii ρ the ring width $d\rho$ is then defined as,

$$d\rho_{mod} = \frac{\rho d\rho_{exp}}{\gamma} \tag{5.16}$$

where $d\rho_{exp}$ and $d\rho_{mod}$ is the experimental and modelled ring width and ρ is the radii from the centre of the beam. Therefore the modelled ring width increases linearly with the radii ρ from the centre. This is expected as the experimental detector width stays constant, but the modelled ring width increases as more of the power of the beam is concentrated on a smaller area when focussed.

5.3.2.3 *Spatial filtering by ring apertures- Results*

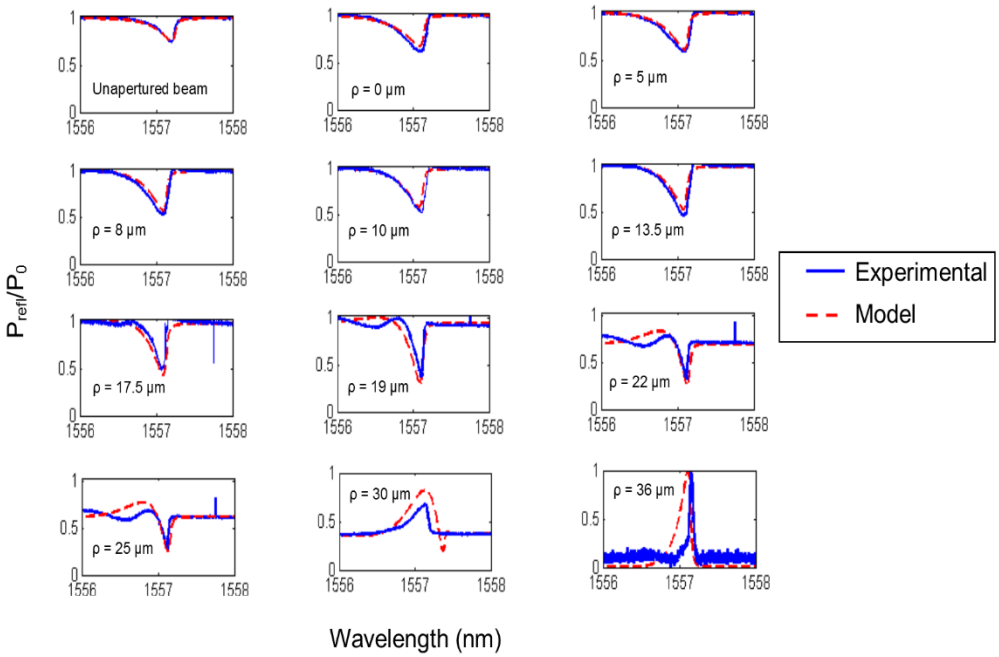

Figure 5-20 Modelled and experimental ITF$_\lambda$s for a incident beam radius of 17 μm on the etalon with a 190 μm cavity spacer with mirror reflectivities of R=95% for ring apertures with radius ρ and experimental ring width of 3 μm. The radii of the rings are from the beam centre to 36 μm away from the centre of the beam

Figure 5-20 shows experimental and modeled ITF$_\lambda$s for spatial filtering of a ω_0 = 17 μm incident beam on the Fabry Perot etalon with R=95%, and cavity thickness of 190 μm. An experimental ring width of 3 μm in the experiment was then used to calculate the ring width in the model. The visibility of the ITF$_\lambda$ increases as the detector moves away from the centre of the beam. The asymmetry decreases as the detector moves away from the centre as shown by the agreement with the model. The fit between the model and experiment becomes less good as the ring radii increases. This is due to the reduction in the power at increasing radii from the centre as a consequence of the Gaussian amplitude profile, resulting in greater uncertainties in the detection at larger ring radii. The general trend of the experimental ITF$_\lambda$s follows the modelled trend. The modelled sensitivities of the change in the ITF$_\lambda$ over a ±1.5 μm difference in the ring radius was calculated. At ring radii close to the centre, the change in the ITF$_\lambda$ was found to be 0.89%. At a radii of ρ = 17 μm the sensitivity of the ITF$_\lambda$ to a change in the ring radius was found to be 5% - 6%. When the ring radius is ρ = 30 μm, the percentage change in the ITF$_\lambda$ was found to be 11% - 12%. This therefore shows that as the ring radius increases the change in the ITF$_\lambda$ becomes greater.

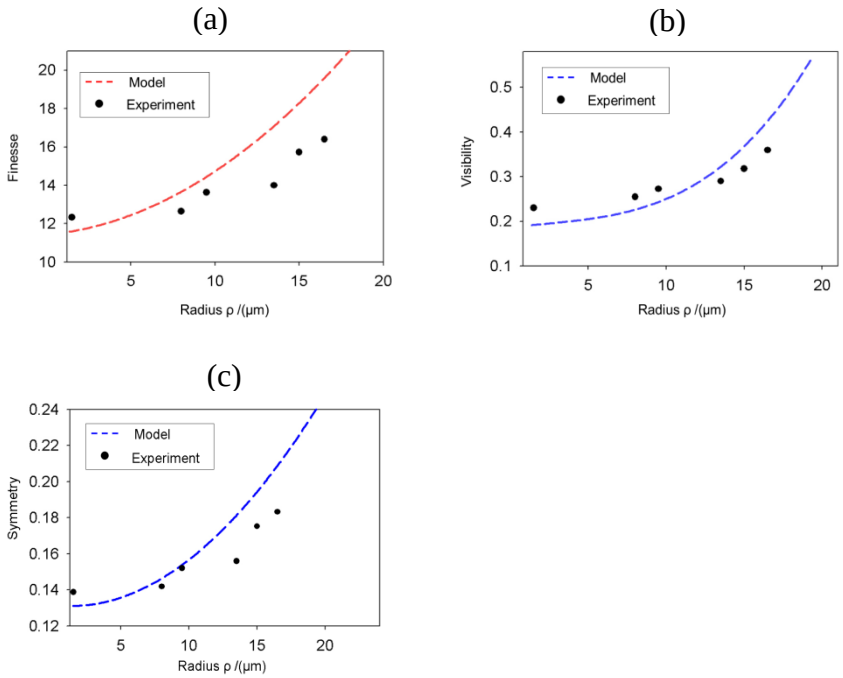

Figure 5-21 Modelled and experimental variation in (a)finesse variation, (b) visibility and (c) asymmetry with radial position from the centre for an incident beam radius of 17 μm in a FPI with R=95% and cavity thickness of 190 μm

Figure 5-21(a) shows the variation in finesse against the radial position from the centre of the beam for both the model and experiment. As the radial position increases the finesse increases. The experimental values also follow a similar trend. Figure 5-21(b) shows the variation in visibility against the radial position from the centre of the beam for both model and experiment. It has a similar trend to the finesse. Another figure of merit is introduced, which is that of the symmetry factor. For this purpose of a wavelength ITF_{λ}, it is defined as the ratio of the maximum derivative at short wavelengths over the maximum derivative at longer wavelengths across a reflectivity peak,

$$S = \frac{\frac{dR}{d\lambda_{short}}}{\frac{dR}{d\lambda_{long}}} \qquad 5.17$$

where S has values between 0 and 1, with values close to 0 being highly asymmetric, and values close to 1 being highly symmetric. Figure 5-21(c) shows the variation in asymmetry against the radial position from the centre of the beam for both the model and experiment. As radial position ρ increases, the asymmetry of the ITF_λ decreases. The experiment follows a similar trend to the model.

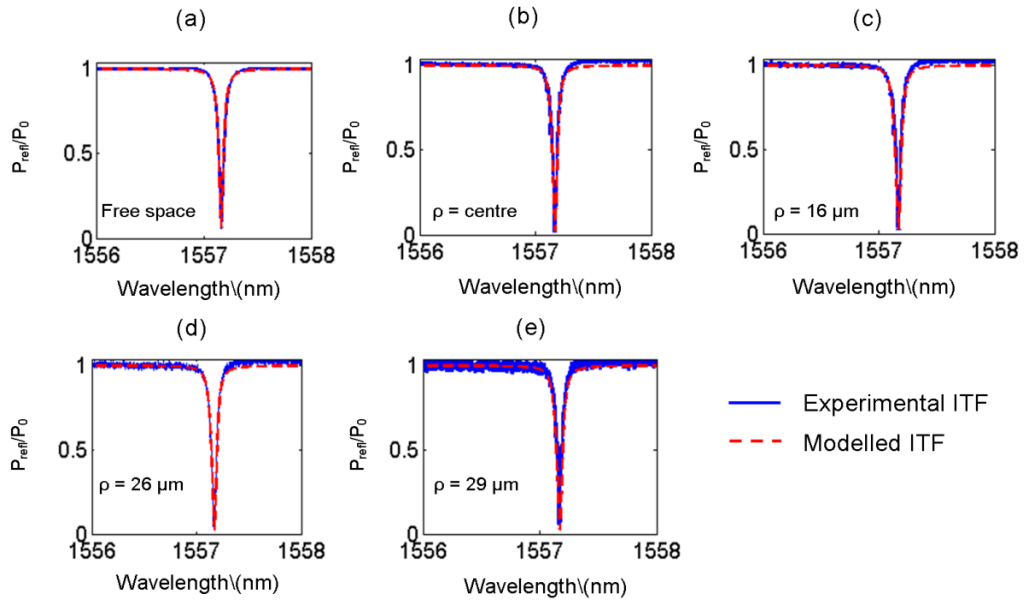

Figure 5-22 Graph of modelled and experimental spatially filtered ITFs for a 75 µm beam size at various radial points from the beam centre with a ring width of 3 µm, (a) Free space beam, (b) beam centre, (c) 16 µm, (d) 26 µm and (e) 29 µm

Figure 5-22 shows the ITF_λs at various radial points away from the centre of the reflected beam from the Fabry Perot etalon, for an incident beam radius of 75 µm and mirror reflectivities of R=95%. Figure 5-22(a) shows the ITF_λ for when all the light is incident on the photodiode. Figure 5-22(b), Figure 5-22(c), Figure 5-22(d) and Figure 5-22(e) show the ITF_λ at various radial points away from the centre of the beam. Compared to the smaller beam radius of 17 µm, there is not much change in the ITF_λ at radii further from the centre of the beam. This is due to the beam approximating closer to a non-diverging beam.

5.3.2.4 *Spatial filtering by ring apertures-Explanation of shape of ITF$_\lambda$s*

This section explains the shapes of the ITF$_\lambda$s at certain radii from the centre of the beam which was presented in the previous subsection. This is to understand the effect the phase due to the divergent parts of the beam has on the shape of the ITF$_\lambda$. The electric fields diverging at an angle to the optic axis undergo an increased path length in the cavity compared to the electric field at the centre of the beam. The phase of the electric field due to a Gaussian beam including the radial phase is expressed in Eqn. 5.18, where ρ is the radial coordinate, $R_m(2ml)$ is the radius of curvature,

$$E_m = a_m E_0 e^{-i(2kml - \Theta_m + \frac{k\rho^2}{2R_m(2ml)})} \quad 5.18$$

The radius of curvature changes with the distance propagated along the optic axis, with the expression for the radius of curvature $R_m(2ml)$ given by,

$$R_m(2ml) = 2ml\left(1 + \frac{{z_0}^2}{(2ml)^2}\right) \quad 5.19$$

where z_0 is the Rayleigh range. In the near field $(2ml<z_0)$ the radius of curvature decreases from an infinite asymptote. The beam in the near field is approximated as collimated and does not diverge; therefore the $z_0/(2ml)^2$ term dominates. The radius of curvature is a minimum at $z=2z_0$. As the distance propagated by the beam increases ($2ml > z_0$), the radius of curvature increases linearly as the $z_0/(2ml)^2$ term becomes negligible. The relationship of the radius of curvature $R(2ml)$ with the distance propagated is shown in Figure 5-23.

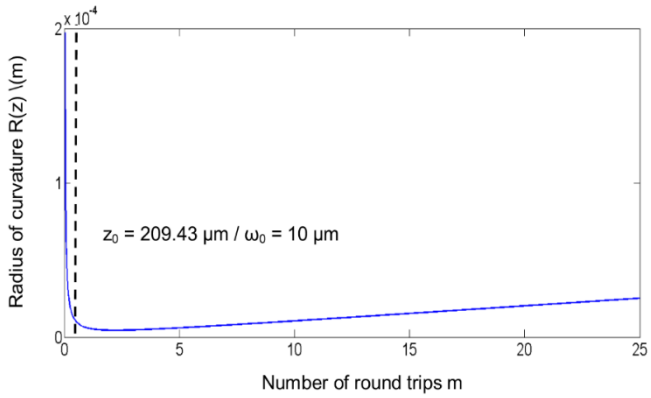

Figure 5-23 Graph of radius curvature R(z) change with number of round trips, for a 10 µm beam radius with a Rayleigh range z_0 of 209.43 µm incident on a FPI with 40 µm cavity thickness and R=95%

The effect of the radial phase term in Eqn. 5.18 is to counter balance the effect of the Gouy phase. Therefore at a radius ρ from the centre of the beam, the phase contribution on each round trip will be less affected by the Gouy phase due to the ρ^2 dependence of the radial phase term.

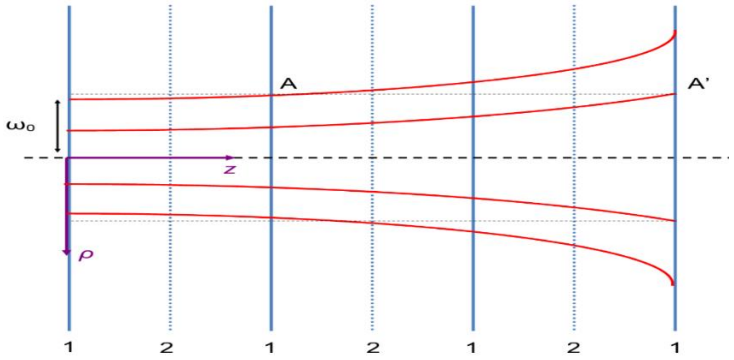

Figure 5-24 Divergence of Gaussian beam with the path length by divergent electric fields increasing on each round trip in the cavity, as shown by the radial point A and correspondin point A' after the beam has propagated a round trips, where 1 and 2 signify mirror 1 and mirror 2 respectively

Figure 5-24 shows the divergence of the Gaussian beam along the optic axis. The electric field at the centre of the beam traverses a constant cavity thickness 2ml on each round trip in the cavity. The electric fields which are divergent have an increase in the path lengths on each complete round trip. The path length propagated by the electric field to point A for the first round trip is greater than the path length propagated by the beam along the optic axis. For the round trip corresponding to m=3, the electric field at the same radial point A now termed A' has propagated a path length that is greater than the previous round trip at A. Therefore at a specific radial point away from the centre of the beam, the additional path

length change alters the radial phase component on each round trip. Therefore the radial phase like Gouy phase, evolves with the path length propagated,

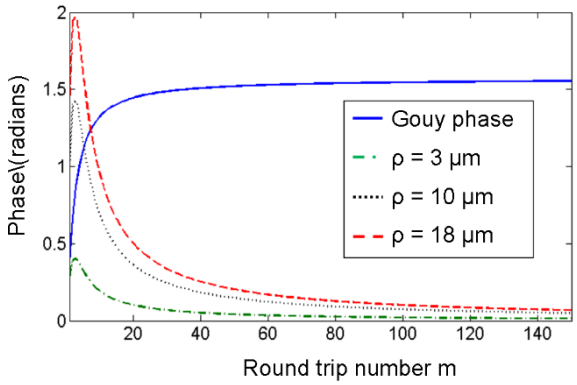

Figure 5-25 Evolution of the Gouy phase and the radial phase due to a Gaussian beam of the TE_{00} mode with a 10 μm beam radius for m=150 round trips in a 40 μm cavity spacer with R=95%,

Figure 5-25 shows the Gouy phase and the radial phase evolution with the number of round trips. The Gouy phase as shown in Figure 4-3 increased with propagation distance to a limiting value of $\pi/2$ radians. For the radial phase expressed in Eqn. 5.18 it increases as the square of the radius ρ, therefore at larger radii the magnitude of the radial phase will be greater. As the distance propagated by the beam increases the radius of curvature increases with a minimum at z_0. Therefore the radial phase has a peak corresponding to the Rayleigh range and then decreases as the distance propagated increases. This is because the radial phase has the Rayleigh range in the denominator as expressed in Eqn. 5.18. The radial phase will therefore reduce the effect of the Gouy phase. At a certain radius ρ the effect of the radial phase will be greater than the effect of the Gouy phase. For greater number of round trips both the effect of the Goy phase and radial phase can be neglected, as the change per round trip is negligible.

Sub-Section 5.3.2.1 described the phase of the Gaussian beam at the centre, and showed for highly diverging beams that the Gouy phase was responsible for the asymmetry seen in the ITF$_\lambda$s. Sub-section 5.3.2.3 showed experimental ITF$_\lambda$s at certain radii from the centre of the beam for a 17 µm beam radius. This section analyses the electric field magnitude of ITF$_\lambda$s at a certain radii away from the centre of the beam and relates it to the phase propagation analysed in the previous section. Equation 5.18 defined the electric field of a Gaussian beam for the mth round trip.

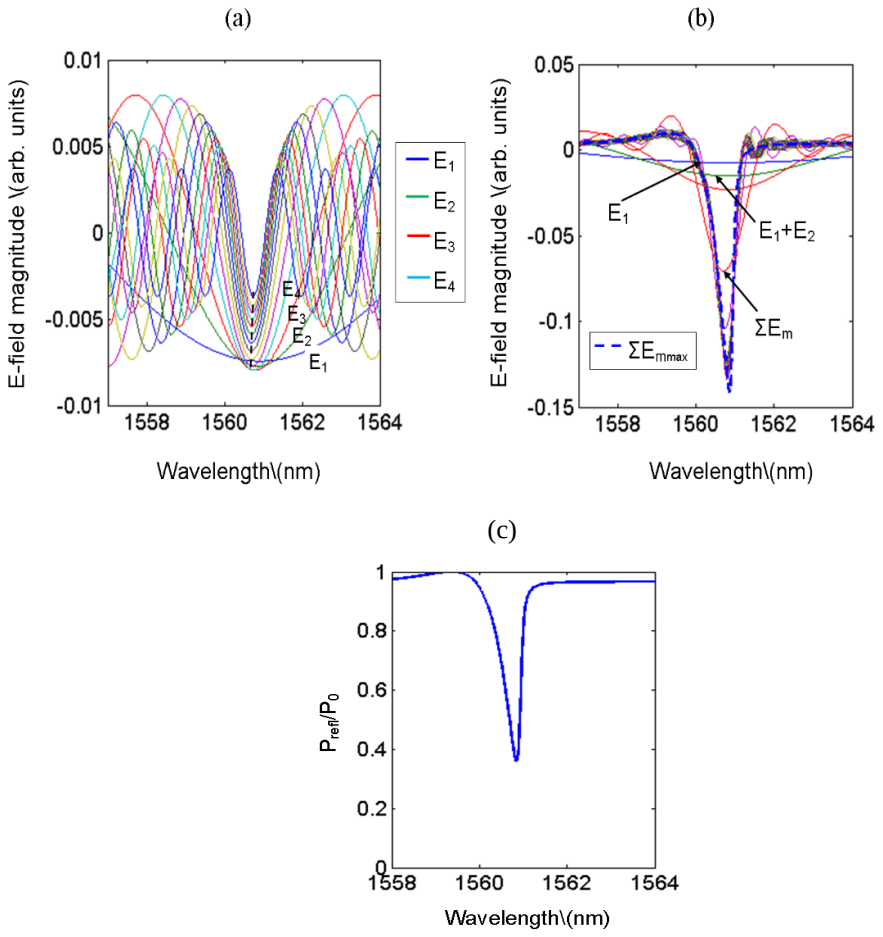

Figure 5-26 Graph of (a) Electric field magnitude at mirror 1 for each round trip, as the wavelength is varied and (b) cumulative sum of electric field magnitude after each round trip (c) ITF$_\lambda$ for a Gaussian beam with beam radius of ω_0= 10 µm, *l*=40 µm, and a ring aperture at a radii of ρ= 12.8 µm with ring width of 3 µm

Figure 5-26(a) shows the individual electric field magnitude at mirror 1 for each round trip at a radial position of 12.8 µm with ring width of 3 µm for an incident beam radius of 10 µm. The FPI has mirror reflectivities R=98% and cavity thickness of 40 µm. As seen in Figure 5-26(a) the electric field magnitude shift on each round trip due to the Gouy phase is reduced compared to Figure 5-17(a), as shown by the dashed lines on the plot. This is because of the

balance between the Gouy phase and radial phase. Figure 5-26(b) shows the cumulative summation of the electric field magnitude on each round trip. This forms a more symmetric reflectivity peak, with the ITF_λ in Figure 5-26(c) showing greater symmetry.

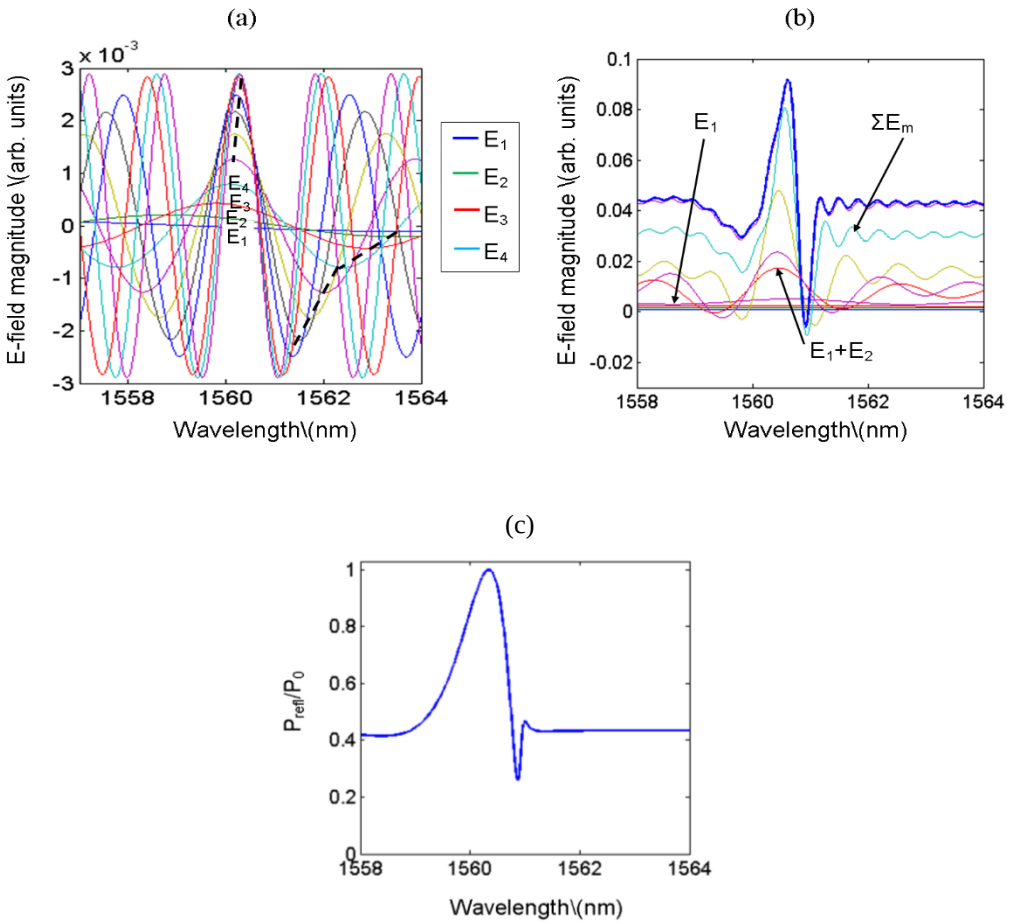

Figure 5-27 Graph of (a) Electric field magnitude at mirror 1 for each round trip, as the wavelength is varied and (b) cumulative sum of electric field magnitude and after each round trip and (c) ITF_λ for a Gaussian beam with beam radius of ω0= 10 µm, *l*=40 µm,and a ring aperture at a radii of ρ= 30 µm with ring width of 3 µm

Figure 5-27(a) shows the individual electric field magnitude per round trip at a radius of 30 µm from the centre of the beam, for the optical parameters described in Figure 5-26. As the radius is far away from the centre of the beam the radial phase component dominates over the Gouy phase, due to the radial phase increasing as the square of the radii ρ. There is an addition to the round trip phase expressed in Eqn. 5.10, by the radial phase. The addition of the radial phase to the round trip phase becomes smaller as the number of round trips increase. The electric field shifts to longer wavelengths due to the addition of the radial phase. Figure 5-27(a) shows the electric field peaks (shown by the black arrows) shifting to

longer wavelengths for each round trip. The electric field minimums shows they are shifting to shorter wavelengths on each round trip. This is because an electric field minima from shorter wavelengths shifts into the respective resonance wavelength range. The electric field amplitude on each round trip is greater, because the electric fields diverging towards the edge of the beam from the centre have greater initial amplitude than the edges of the beam. The cumulative summation of the electric field magnitude in Figure 5-27(b) shows a resonant peak. The total electric field magnitude reflected from the FPI results in an asymmetric transmission peak ITF$_\lambda$, as shown in Figure 5-27(c). This was also shown experimentally in Figure 5-22.

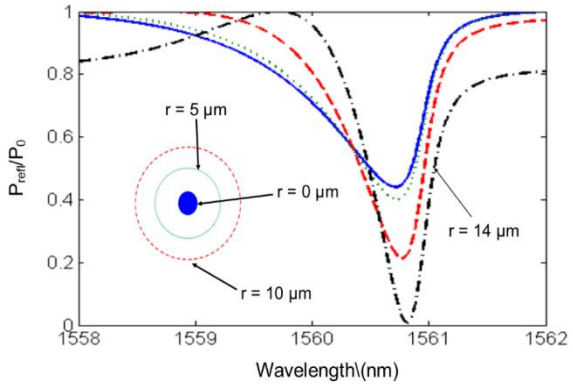

Figure 5-28 Graph showing ITF$_\lambda$s at various radiuses away from the center of the reflected beam radius $\omega_{max}(2m_{max}l)$ for a input beam radius of 10 µm and a cavity thickness of 40 µm, R=98% and refractive index n=1.639. The integration geometry was a ring with a detector width of 1 µm.

Figure 5-28 shows normalized ITF$_\lambda$s obtained by integrating over 1 µm thick rings with ring radii ρ. This is equivalent to spatially filtering the beam. The normalized ITF$_\lambda$s become less asymmetric as the radius from the centre increases. The visibility also increases as the ring radius increases. The asymmetry in a spatially filtered ITF$_\lambda$ at the centre of the beam would be greater than the asymmetry of the unapertured beam. This therefore shows that the Gouy phase causes asymmetry in the ITF$_\lambda$ when the beam is apertured at the centre, but that asymmetry is altered when the beam is unapertured due to the contribution through the summation of ITF$_\lambda$s at each radii ρ with the ITF$_\lambda$ from the centre of the beam.

5.3.3 Effect of the Gaussian beam phase characteristics on the experimental ITF$_\lambda$

The explanation for the asymmetry seen in the experimental ITF$_\lambda$s presented in Figure 5-9 and Figure 5-10 was presented by considering the effect of the individual phase components of a Gaussian beam. This was done by various methods of aperturing the beam, mainly a disc based aperture and ring aperture. It was shown in Figure 5-18 that a disc based aperture produced an asymmetric ITF$_\lambda$ different to that from a unapertured beam. As a result the effect of the radial phase on the ITF$_\lambda$ was considered by taking a ring aperture. This showed that the ITF$_\lambda$ became more symmetric at increasing ring radius. When considering a unapertured beam, the summation of ITF$_\lambda$s across the beam radius alters the asymmetry of ITF$_\lambda$ as well as the visibility. The unapertured ITF$_\lambda$ has reduced asymmetry and lower visibility compared to the ITF$_\lambda$ for a disc based aperture.

5.3.4 Effect of phase on visibility

The shift in the electric field magnitude on each round trip causes the cumulative sum of the electric field magnitude corresponding to the reflectance minima to be higher than if there was no shift on each round trip. This increases the visibility of ITF$_\lambda$s when the FPI is illuminated with a divergent beam. The visibility increases for ITF$_\lambda$s off-centre as the minimums of the electric field minima at resonance are more aligned. This therefore results in a stronger resonance at the wavelength corresponding to the reflectance minima.

5.4 Summary of experimental validation of the planar FPI model

This chapter has described an experimental arrangement for validating the planar FPI model. The focussed beam radius incident at the etalon was varied by using an adjustable collimator. The beam radius was varied between 15 μm and 75 μm. Two etalons with a cavity thickness of 190 μm, and where each etalon had a mirror reflectivity of R=95% and R=98% respectively were used. The ITF_λs between model and experiment were compared for various beam radii for both etalons. There was a good fit between the model and experiment. The general trend of finesse with beam radius, and visibility with beam radius increased to a limiting value. The finesse tended to that of a non-diverging beam, while the visibility tended to 1. The experimental trend also followed this relationship. At small beam radii, where the finesse and visibility is low showed asymmetric ITF_λs, which was due to the Gouy phase evolving with increasing round trip m. Analysing the ITF_λ at a radii ρ showed the asymmetry to decrease and the ITF_λ becoming more symmetric. This was due to the component of phase from the radial divergence counter acting the effect of the Gouy phase. The effect of the various phase components on the electric field magnitude per round trip was presented using an E-field decomposition method, which was related to the shape of the ITF_λ. These results showed that divergence in a FPI when illuminated by a diverging beam radius is advantageous, if a asymmetric ITF_λ is required. A symmetric ITF_λ can be achieved through spatial filtering using a ring based aperture. This analysis was done for a planar FPI, and can be extended to a wedged FPI. The next chapter presents the effect on the ITF_λ for a wedged FPI.

Chapter 6 Numerically simulated ITF_λs for a wedged FPI, with interpretation of the ITF_λ shapes

The FPI sensor will have cavity thickness variations across its area. This is due to the process of depositing the polymer spacer layer onto the first mirror. This non-uniformity needs to be taken into account when considering the design of Fabry Perot Interferometer sensors. The thickness change can be considered linear if the degree of thickness variation is considerably small. The wedged model presented in Chapter 4 is used to simulate ITF_λs when a Gaussian beam is illuminating a wedged FPI. Section 6.1 presents the shape of ITF_λs when a wedge angle is introduced in the FPI. Section 6.2.1 of this chapter presents the effect of a wedge on the finesse and visibility as beam radii increases. Section 6.3 explains the effect of the wedge angle on the ITF_λ. This is done by the use of the electric field magnitude plots for each individual round trip. Section 6.5 and section 6.6 deal with experimentally determining the average non-uniformity present for a range of FPI sensors with different cavity spacings.

6.1 Results of numerical simulations of a wedged FPI

6.1.1 Effect of a wedged FPI on the shape of ITF_λs

This section describes the effect a Gaussian beam of beam radius ω_0 illuminating a wedged FPI has on the shape of the wavelength ITF_λ. This is done by using the model for a Gaussian beam illuminating a wedged FPI. The effect of the wedge is to alter the asymmetry, and for large wedge angles introduce transmission peaks termed sub-resonant peaks. The wedge alters the path length propagated by the electric field across the beam. This modifies the phase across the beam. As a result it would alter the shape of the ITF_λ.

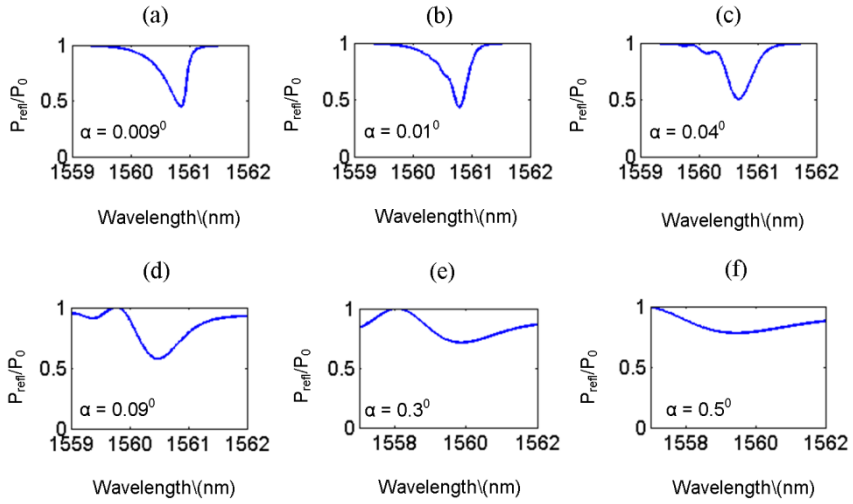

Figure 6-1 Modelled ITF$_\lambda$s for various wedge angles showing the asymmetry variation for a 20 µm beam size and a 40 µm cavity thickness (n=1.639) with R=98%

Figure 6-1 shows the ITF$_\lambda$ reflectivity peak for wedge angles from $\alpha=0.009^0$ to 0.5^0 for a 20 µm beam radius. The asymmetry of the reflectivity peak at small wedge angles is characterized by a shallow slope at short wavelengths and a sharper slope at longer wavelengths ($dR/d\lambda_{short}<dR/d\lambda_{long}$). As the wedge angle increases the asymmetry starts to decrease. Increasing the wedge angle further induces asymmetry but in the reverse direction ($dR/d\lambda_{short}>dR/d\lambda_{long}$). As wedge angle increased further, the asymmetry increases and transmission peaks start appearing in the ITF$_\lambda$. These are termed sub resonant features and are shown in Figure 6-1(d), Figure 6-1(e), and in Figure 6-1(f). These sub resonant features were shown by Meyer. Y.H [92] in a wedged FPI, where the cavity thickness is varied to tune the ITF$_l$s. In this thesis the change in the direction of asymmetry for a wavelength ITF$_\lambda$ with variation in the wedge angle, as well as the growth of the sub resonances is presented. In addition the explanation of the shapes of the ITF$_\lambda$ using the decomposition of the E-field considered in the previous chapter to explain asymmetric ITF$_\lambda$s. For large wedge angles ($>0.5^0$) the reflectivity peak with the sub resonant structures no longer appears. The sub resonances grow with increasing wedge angle, while the asymmetry increases and the normalized reflectance minima increases.

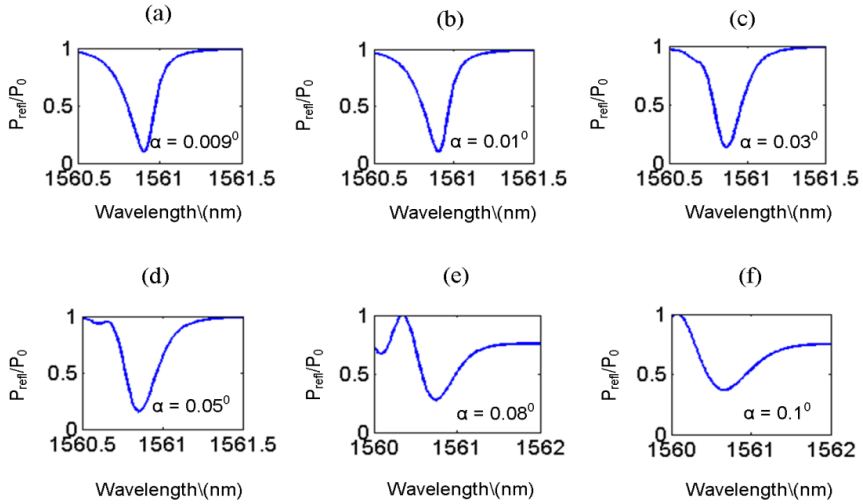

Figure 6-2 ITF$_\lambda$s for various wedge angles for a 40 µm beam radius, with cavity thickness of 40 µm and mirror reflectivities of 98%

Figure 6-2 shows the ITF$_\lambda$s for a 40 µm beam radius as the wedge angle is increased. As shown in Figure 6-2 there is a small asymmetry at small wedge angles. The ITF$_\lambda$ for a wedge angle of ($\alpha = 0.05^0$) shows the asymmetry reverse ($dR/d\lambda_{short} > dR/d\lambda_{long}$). The sub resonant features start appearing at larger wedge angles (0.08^0), with increasing asymmetry.

6.1.2 Variation in asymmetry with wedge angle α in a wedged FPI

In order to illustrate the changes in asymmetry, Figure 6-3 shows the variation in the derivative of the normalized reflected power P_{refl}/P_0 with wavelength ($dR_n\backslash d\lambda$), where $R_n = P_{refl}/P_0$, as the wedge angle is varied for beam radii between 10 µm and 40 µm respectively.

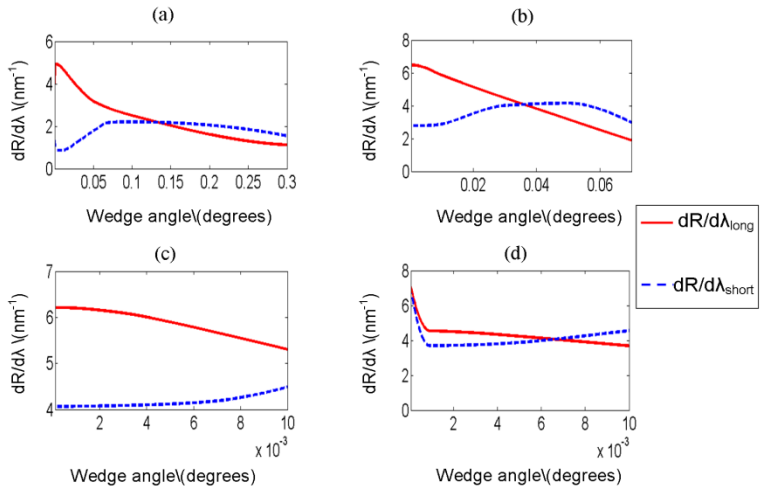

Figure 6-3 Graphs of dR/dλ versus wedge angle for both short and long wavelengths, for a 40 µm cavity thickness and mirror reflectivities of 98%, with beam radiuses of (a) 10 µm, (b) 20 µm, (c) 30 µm and (d) 40 µm

Figure 6-3 shows the variation in dR/dλ for both long and short wavelengths of the reflectivity peak as the wedge angle α is increased. For all beam radii as the wedge angle increases the asymmetry reverses. At larger beam radii of 30 µm and 40 µm, the wedge angle induces an asymmetry and as wedge angle increases the asymmetry reverses. Also for all beam radii at large wedge angles, the ITF_λ shows secondary peaks termed sub-resonant peaks. These grow with the wedge angle until the FPI cavity no longer forms a resonant cavity. The wedge angle at which the ITF_λ becomes symmetric reduces with increasing beam radius. The effect of the wedge in all cases is to alter the asymmetry, but it also reduces the slope of the reflectivity peak for an ITF_λ. The slope is a measure of the optical sensitivity of the FPI sensor. Therefore it is useful to know the cavity spacing non-uniformities in the FPI sensors, which is presented in sub-section 6.5 and sub-section 6.6. This can then feed back into the optimisation of the FPI sensors.

6.1.3 Visibility variation with a wedged FPI

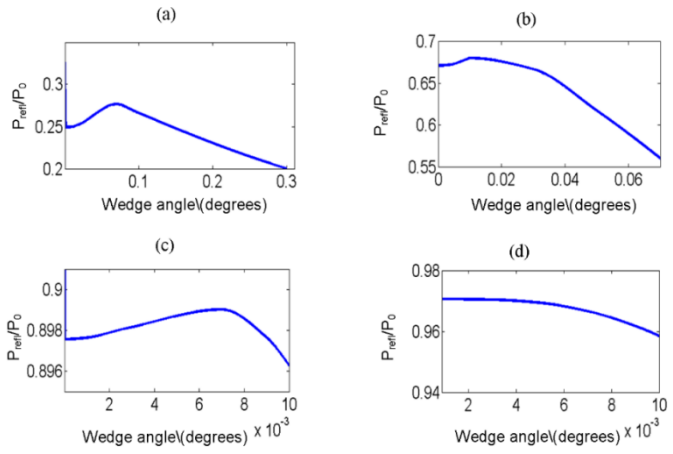

Figure 6-4 Graph of visibility versus wedge angle for (a) 10 µm, (b) 20 µm, (c) 30 µm, (d) 40 µm beam radiuses in a 40 µm cavity thickness, with 95% mirror reflectivities

Figure 6-4 shows the visibility variation with wedge angle α for various beam radii from 10 to 40 µm. The visibility is higher for larger beam radii as the larger beam approximates to a non-diverging beam. The visibility is a maximum for a planar FPI and then falls sharply for small wedge angles before increasing again to a secondary maximum. It then decreases as the wedge angle is increased. For a 40 µm beam radius the visibility falls as the wedge angle increases with no secondary peak as that for smaller beam radii. This shows that when the

FPI has poor cavity thickness uniformity, a combination of wedge angle and beam radius can provide an increase in the visibility, which also corresponds to a symmetric ITF_{λ}.

6.2 Comparison of finesse and visibility results

6.2.1 Finesse variation with beam radius

The relationship between finesse and beam radius (ω_0) is presented for a wedged Fabry Perot Interferometer in this section.

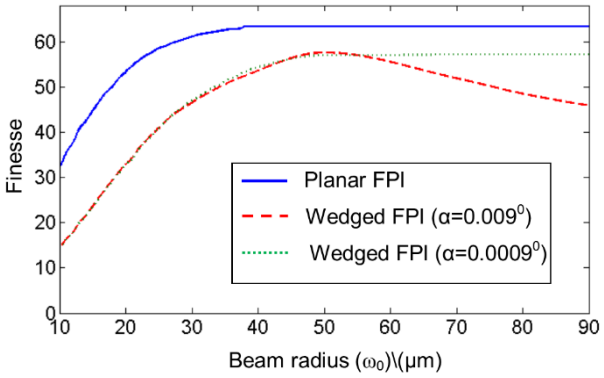

Figure 6-5 Graph of Finesse against beam radius (ω0) for mirror reflectivity of 95% for cavity thickness of 40 μm for a planar FPI, wedged FPIs with wedge angles of α=0.009⁰ and α=0.0009⁰

Figure 6-5 shows the finesse variation with beam radius for a planar FPI and wedged FPIs with mirror reflectivities of 95% and cavity thickness of 40 μm. The wedge angles of the FPI are $\alpha=0.009^0$ and $\alpha=0.0009^0$. The finesse for wedged Fabry Perot Interferometers in general is lower compared to a planar Fabry Perot Interferometer. For small beam radii the difference in finesse between a planar FPI and the wedged FPIs is greatest. As the beam radius increases the difference decreases up to a certain beam radius. The finesse decreases as the beam radius increases for a wedged FPI with $\alpha=0.009^0$, whereas for a planar FPI the finesse tends to a limiting value. For the wedged FPI with $\alpha=0.0009^0$ the finesse is constant until very large beam radii of a few hundred microns (not shown in Figure 6-5), where the finesse starts to decrease. The optimum range of beam radii is between 45 μm to 55 μm for a wedged FPI with $\alpha=0.009^0$. As shown in Figure 6-3 as beam radius increases the wedge angle at which the ITF_λ becomes symmetric and the sub resonances start occurring becomes smaller. Therefore the effect of small non-uniformities is greater for larger beam radii.

6.2.2 Visibility variation with beam radius

Figure 6-6 shows the visibility variation with beam radius (ω_0) between a planar FPI and a wedged FPI. The FPI has a cavity thickness of 40 µm and mirror reflectivities of 95%. The wedge angle of the FPI is $\alpha=0.009^0$. As beam radius increases the visibility increases for both a planar and wedged FPI, although the visibility reduces by 0.09 for a wedged FPI at large beam radii. At large beam radii the visibility tends to 1 for a planar FPI. In the range of beam radius between 32 µm and 38 µm the visibility for both the planar and wedged FPI is the same. Referring to Figure 6-4, as beam radius increases the visibility peaks and starts decreasing at smaller wedge angles.

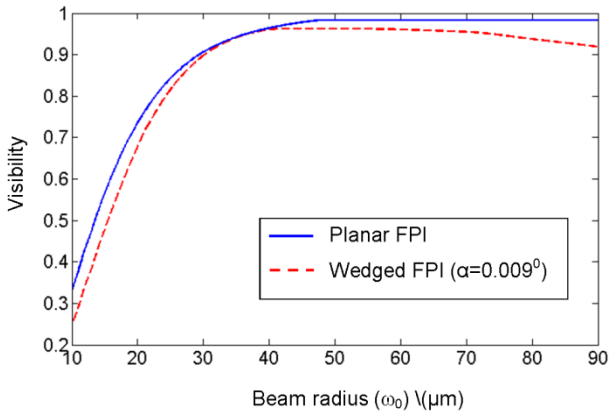

Figure 6-6 Graph of visibility versus beam radius (ω_0) for a cavity thickness of 40 µm and mirror reflectivities of 95%, for a planar FPI, and a wedged FPI ($\alpha=0.009^0$)

This section has shown that for specific wedge angles, a certain range of beam radii can be used to give the highest finesse or visibility. Although these values of finesse will always be lower for a wedged FPI.

6.3 Explanation of the shapes of ITF_λ for a wedged FPI

This section explains the shape of the ITF_λs in a wedged FPI by analysing the phase characteristics of the Gaussian beam propagation per round trip. A similar method as applied for the planar FPI case in section 5.3 chapter 5 to explain the asymmetry is undertaken. The total electric field (as a function of wavelength) reflected from the FPI is decomposed per round trip to observe the effect of the phase shifts on the shape of the ITF_λ.

6.3.1 Phase progression in a wedged FPI

The reversal of asymmetry presented in section 6.1 for a wedged FPI is due to the phase modification caused by the wedge. The effect of the wedge is to alter the path length propagated by the electric fields on each round trip. The electric field defined in Chapter 5, Eqn. 5.18 for a planar FPI, is now defined in a general case for the wedged FPI. Equation 6.1 expresses the electric field magnitude for each complete round trip at mirror 1,

$$E_m(\rho,\lambda) = a_m E_0 e^{-i\left(2kml-\Theta_m+\frac{k\rho^2}{2R_m(2ml)}+k\Delta z_m\right)} \qquad 6.1$$

where Δz_m represents the additional path length on each round trip due to the wedge angle. The initial electric field amplitude is E_0 and is weighted by the amplitude coefficient a_m. Equation 6.2 expresses the difference in the path length traversed by an electric field on the m^{th} round trip,

$$\Delta z_m = (l_{2m+1}(\rho) - l_{2m}(\rho)) \qquad 6.2$$

where 2m+1 is the odd numbered half round trip and 2m the even numbered half round trip propagated on a complete round transit m.

6.3.1.1 *Effect of path length on phase progression in a wedged FPI*

The effect of the alteration in path length due to the wedge angle is to alter the phase of the beam after each complete round trip. This section analyses the change in the path length as the beam propagates within the wedged FPI.

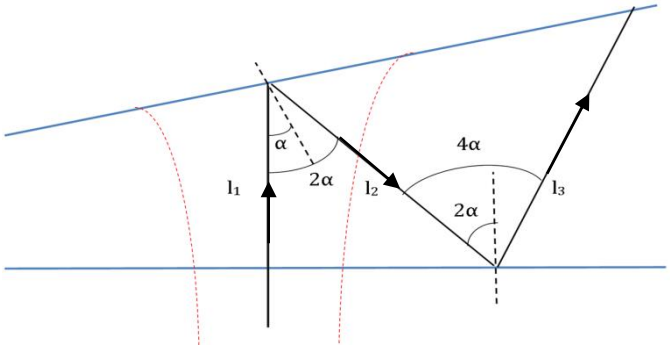

Figure 6-7 Diagram of a wedged FPI with wedge angle α, the path length of a field at the centre of the beam increases on each half round trip

Figure 6-7 shows a wedged Fabry Perot Interferometer (FPI) with wedge angle α. The path length of a field at the centre of the beam is seen to be increasing on each half round trip, due to the wedge causing a slight walk-off in the beam (diagram not to scale). Therefore the path length for the second half round trip l_2 is related to l_1 as expressed in Eqn. 6.3,

$$l_2 = \frac{l_1}{\cos(2\alpha)} \tag{6.3}$$

The path length for l_2 in Eqn. 6.3 follows from simple geometry shown in Figure 6-7, by taking l_1 as the adjacent component of the hypotenuse l_2. Taking right angle triangles of the geometric path lengths, the path length l_3 is related to l_2 by the relation,

$$l_3 = \frac{l_2 \cos(\alpha)}{\cos(3\alpha)} \tag{6.4}$$

Therefore the path length variation for each half round trip p in the cavity can be expressed as,

$$l_p = \frac{l_{p-1}\cos((p-2)\alpha)}{\cos(p\alpha)} \qquad 6.5$$

Equation 6.5 expresses the path length l_p that a field at the centre of the beam would travel on the p^{th} half round trip. The path length l_{p-1} is the propagated path length on the previous half round trip. The divergence in a planar FPI is symmetric. The path taken at the edges of the beam is the same due to the symmetry of the beam. In a wedged FPI this symmetry is broken due to the difference in cavity thickness across the FPI. Figure 6-8 shows the diverging fields in a wedged FPI, the path length of field 1 diverging towards the right hand side of the figure shows an increase in the path length taken on each half round trip. The path length of field 2 which is diverging towards the apex of the wedge, will decrease on each half round trip in the cavity.

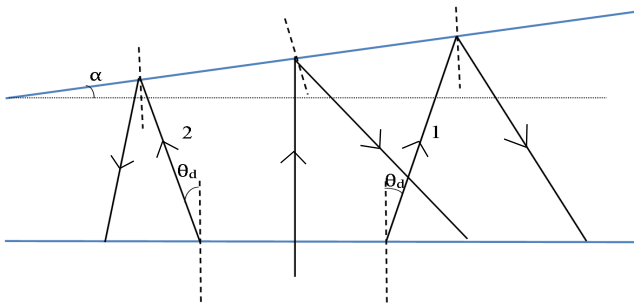

Figure 6-8 Diagram of a wedged FPI with wedge angle α, showing the path length of the diverging fields 1 and 2

The analytical expression for the path length is the same as expressed in Eqn. 6.5, but has the addition of the divergence angle θ_d,

$$l_{p,\theta} = \frac{l_{p-1}\cos(\theta_d + (p-2)\alpha)}{\cos(\theta_d + p\alpha)} \qquad 6.6$$

The fields diverging towards the thin end of the wedge will see a decrease in their path length. This decrease in path length is accounted for by a negative θ_d when propagating towards the apex of the wedge. The expression for the phase due to the additional path length propagated after a complete round trip is the summation of the phase for two half round trips expressed as,

$$k\Delta z_m = k(l_{2m-1} + l_{2m}) \qquad 6.7$$

Where k is the wave vector, and l_{2m-1} is the path length for odd numbered half round trips by the field and l_{2m} is the path length for the even numbered half round trips p.

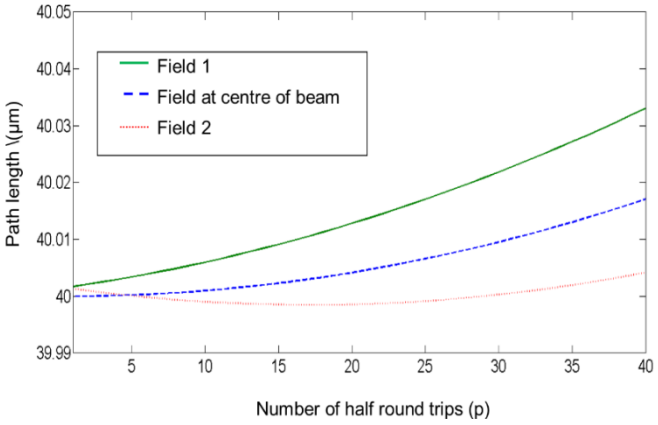

Figure 6-9 Graph showing the path length on each half round trip p for a divergence angle θ_d of 0.5^0 and a wedge angle $\alpha=0.03^0$

Figure 6-9 shows the path lengths for the central field, field 1 and field 2 diverging away from the wedge and diverging towards the wedge respectively. It can be seen that as the number of half round transits increase the path length for field 1 and the central field increase. The path length for field 2 decreases to a minimum as the number of half round trips increase. After reaching the minimum near p=20, the path length starts increasing. This is because after a number of half round trips, the field is incident normal to the mirror resulting in reflection away from the wedge.

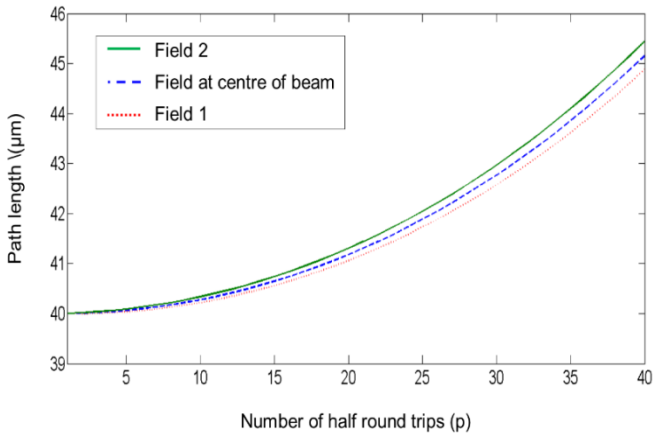

Figure 6-10 Graph showing the path length on each half round trip p for a divergence angle θ_d of 0.5^0 and a wedge angle $\alpha=0.5^0$

Figure 6-10 shows the path lengths for the fields when the wedge angle is the same as the divergence angle of the beam. The path lengths for all the fields increase as the number of half round trips increase. This results in the walk-off of the beam. The path length changes by 5 μm between half round trip numbers 5 and 35. In comparison the path length increase for the smaller wedge angle of 0.03^0 in Figure 6-9 is much less, as it only changes by 0.4 μm. This is due to the reduced walk-off of the beam at smaller wedge angles.

The variation in the path length per round trip causes the phase to be altered to on each round trip, as expressed in Eqn. 6.1 by the $k\Delta z_m$ term. The effect of the Gouy phase and radial phase, which altered the shape of the ITF_λ as shown in section 5.3, chapter 5 for a planar FPI, has an effect on the shape of the ITF_λ for a wedged FPI. The complex interplay between the various phase components for a Gaussian beam illuminating a wedged FPI is explained in the next sub-section.

6.3.1.2 *Electric field magnitude variation for a wedged FPI*

The electric field magnitude for a planar FPI in Chapter 5 presented the effect the phase due to a Gaussian beam had on the electric field magnitude for each round trip. This section presents the effect the combination of the phase due to a Gaussian beam and wedged FPI has on the shape of the ITF_λ on each round trip.

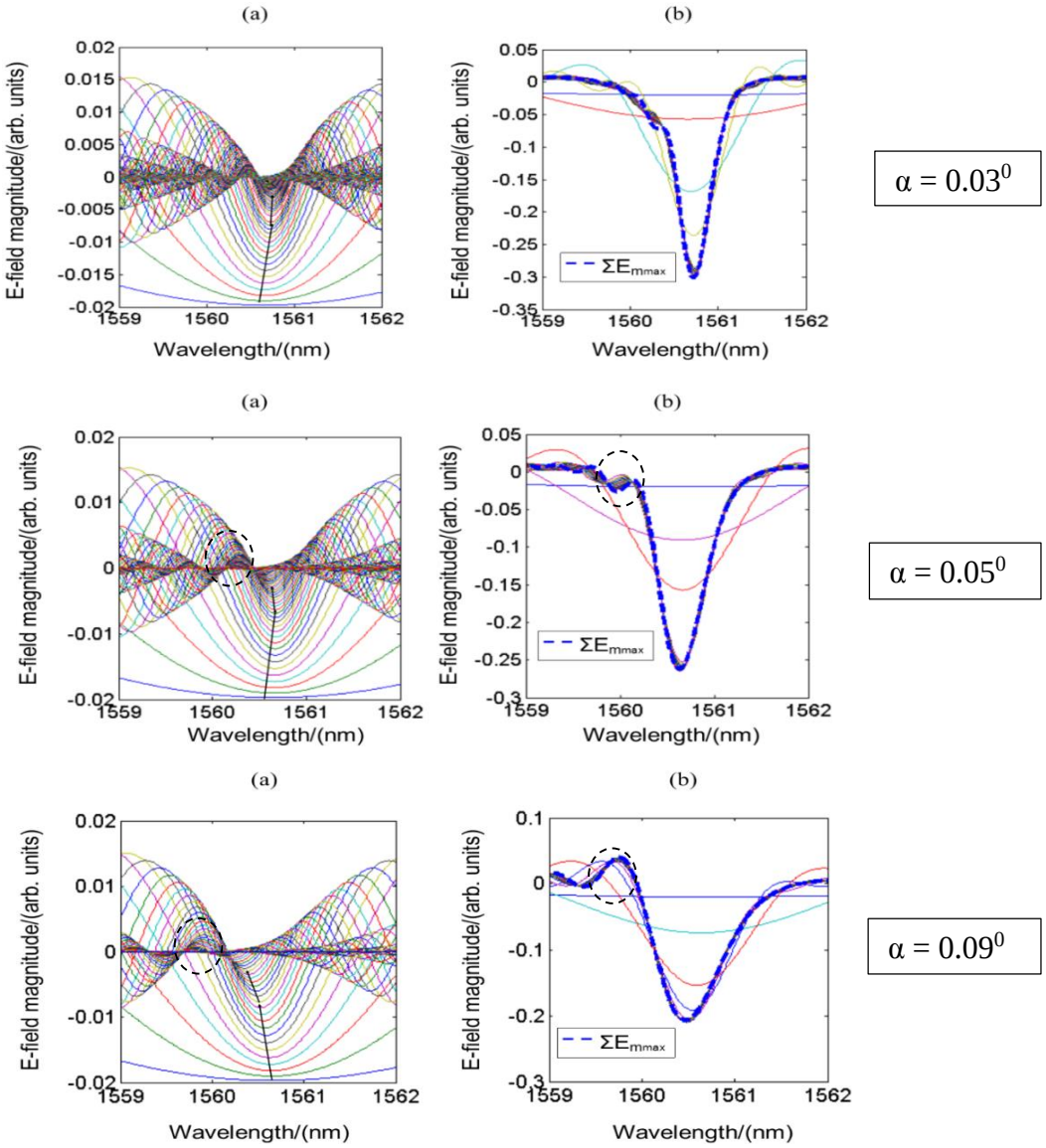

Figure 6-11 Electric field magnitude for (a)each round trip and (b) cumulative sum after m number of round trips at mirror 1. The FPI has mirror reflectivities of 98% and cavity thickness of 40 µm and a 20 µm incident beam radius for FPI's with wedge angles of $\alpha = 0.03^0$, $\alpha = 0.05^0$ and $\alpha = 0.09^0$

Figure 6-11(a) shows the individual electric field magnitude as a function of wavelength for the whole beam for increasing round trips m. This is similar to the analysis shown in section 5.3, chapter 5. Figure 6-11(b) shows the cumulative summation of the electric field magnitude after various m round trips. These plots are shown for wedge angles of $\alpha = 0.03^0$, 0.05^0 and 0.09^0. For small wedge angles, the effect of the Gouy phase dominates creating similar plots to that shown in Figure 5-17(a) and Figure 5-17(b). At large number of round trips, the effect of the phase shift due to the non-constant path length change reverses the shift in the electric field magnitude. This is shown by the electric field minima shifting to shorter wavelengths. The electric field actually shifts to longer wavelengths, with an electric field minimum from shorter wavelengths shifting into the wavelength range corresponding to the reflectivity peak. This is similar to the effect on the electric field at the far edges of the beam as described for Figure 5-27 for a ring based aperture.

As the wedge angle increases, the path length change per round trip increases greater than that for small wedge angles as shown in Figure 6-9 and Figure 6-10 for a wedge angle of 0.03° and 0.05° respectively. This causes the reversal in the shift of the electric field in a reduced number of round trips, as shown by Figure 6-11(b) and Figure 6-11(c). The electric field maximums shown by the circles in Figure 6-11(b) and Figure 6-11(c), align closely as wedge angle increases forming the sub-resonant peaks in the ITF_λ. These sub-resonant peaks grow as the wedge angle increases until the cavity is no longer resonant.

6.4 Summary of ITF$_\lambda$s in a wedged FPI

The general trend of ITF$_\lambda$s for a wedged FPI illuminated with a Gaussian beam is that as the wedge angle increases, the asymmetry reduces to form a symmetric ITF$_\lambda$, and further increases in the wedge angle result in the reversal of asymmetry, with sub resonant features occurring. This is due to the alteration in the path length propagated by the beam in a wedged FPI. This path length change on each round trip results in a complex interplay between the Gouy phase, radial phase and the phase due to the additional path length on each round trip. This causes the electric field to shift direction as one component of phase is greater than the others. The phase shifts on each round trip are non-linear, leading to the asymmetric shaped ITF$_\lambda$s. For a certain wedge angle, there exists optimal beam radii that gives the best finesse and visibility. The smaller the wedge angle the greater the range of beam radii that can be used to obtain the highest finesse and visibility. As the wedge angle increases, the range of beam radii becomes narrow. The finesse and visibility both decrease overall with increasing wedge angle. Therefore when designing FPI sensors if the non-uniformity in the cavity thickness is of a certain wedge angle, then the choice of optimum beam radii will be limited. To know the cavity thickness non-uniformities in FPI sensors used for photoacoustic imaging, an experiment to measure the cavity thickness over the area of the FPI sensor is presented in the next two sections.

6.5 Experimental method for measuring surface change

This section presents an experimental technique for measuring cavity thickness non-uniformities. Section 6.6 presents the cavity thickness variation across the area of the FPI sensors. The purpose of undertaking this study is so that the effect of cavity thickness non-uniformity can be taken into account when designing optimised FPI sensors.

6.5.1 Measuring non-uniform cavity thicknesses

6.5.1.1 *Phase equivalence for different ITFs*

The cavity spacing across the surface of the FPI sensor was measured by an interferometric technique. The method consisted in measuring the change in the bias wavelength λ_{bias} of the reflectivity peak of the ITF_{λ}. This is because of a shift in the reflectivity peak as the cavity thickness is varied. The wavelength corresponding to the phase at the bias point of the reflectivity peak in the ITF_{λ} is then changed. The phase of a non-diverging beam at a particular wavelength is expressed as,

$$\phi = \frac{4\pi nl}{\lambda} \tag{6.8}$$

where λ is the wavelength, n is the refractive index and l is the physical cavity thickness. The phase of the opticalbeam at the bias wavelengths of two points on the FPI with cavity thickness l_0 and l_1 can be equated together,

$$\frac{4\pi nl_0}{\lambda_0} = \frac{4\pi nl_1}{\lambda_1} \tag{6.9}$$

where the bias wavelengths are λ_0 and λ_1 for the two points on the FPI sensor with cavity thickness l_0 and l_1 respectively. Rearranging Eqn. 6.9 in terms of l_1, the thickness of the FPI sensor is then expressed as,

$$l_1 = l_0 \frac{\lambda_1}{\lambda_0} \tag{6.10}$$

Therefore the ratio of the two bias wavelengths is used to infer the surface profile knowing the cavity thickness l_0. The cavity thickness l_0 is known by measuring the ITF_λ across two consecutive reflectivity peaks (dips) and finding the FSR_λ expressed in chapter 5 Eqn. 5.6. Figure 6-12 shows the ITF_λ for a 40 µm and 40.01 µm cavity thickness, with wavelengths λ_0 and λ_1 corresponding to the reflectance minima respectively. As the cavity thickness increases, the corresponding bias point shifts to longer wavelengths. Alternatively if the cavity thickness decreases, the bias point shifts to shorter wavelengths.

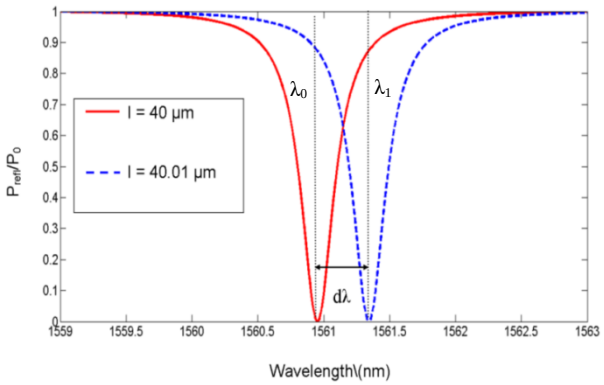

Figure 6-12 Graph showing the ITF_λ for a 40 µm and 40.01 µm cavity thickness, with the wavelength corresponding to the reflectance minima shifting as cavity thickness l changes

Therefore using Eqn. 6.10 and obtaining the bias point at each point on the interrogation area of the sensor, it is possible to infer the cavity thickness at individual points on the FPI sensor. This shows the cavity thickness variation across the area of the FPI sensor.

6.5.2 Experimental arrangement for measuring surface non-uniformity

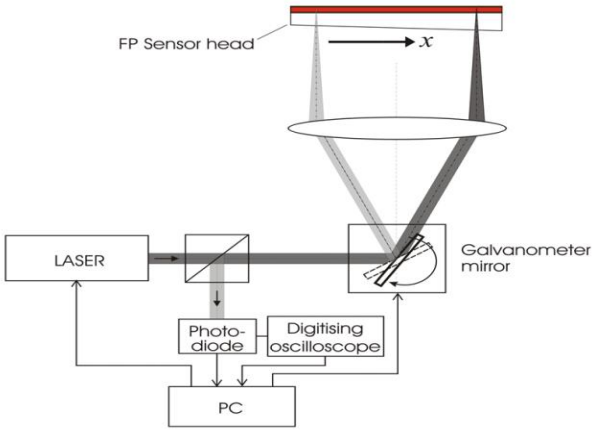

Figure 6-13 Experimental schematic for measuring the uniformity of the sensor by scanning the beam in the x and y directions by using two pairs of Galvanometer mirrors, where the beam is incident normal to the FPI sensor

Figure 6-13 shows a schematic of the experimental arrangement used to obtain measurements of cavity thickness variations. The experimental system is the same that is used to validate the planar model of a Gaussian beam illuminating a FPI. The experimental arrangement consisted of a laser (Santec TSL-510) with an output in the wavelength range of 1510-1620 nm. A focussed beam of 38 μm beam radius ω_0 was used. The beam is scanned across the *x*-*y* plane by using the galvanometers to vary the incident position of the beam on the focussing lens L1, which alters the position of the beam on the FPI sensor. A step size of 100 μm and a scan area of 20 by 20 mm was used in the experiments. The ITF_λ containing two reflectivity peaks at a single point on the FPI sensor was obtained to measure the FSR_λ [95]. Therefore the cavity thickness can be calculated. At all other scan point a measurement of just the single reflectivity peak of the ITF_λ was made. At each point, the wavelength corresponding to the maximum and minimum of the derivative is recorded. This along with the cavity thickness measured is used to calculate the cavity thickness l_1 at all other points, through the use of Eqn. 6.10. The method described in the previous section assumed a non-diverging beam, whereas in the experiment a Gaussian beam of 38 μm radius is used. Therefore the shape of the ITF_λ and FSR_λ may be slightly different to that of a non-diverging beam. The FSR_λ calculated using the Gaussian beam model for a 38 μm beam radius incident on FPIs with cavity thickness between 10 μm and 40 μm, and the Airy function had a difference of 0.001%. This is assumed a negligible difference when measuring the cavity thickness of the FPI sensors.

6.6 Non-uniformity of spacer layers in FPI sensors

6.6.1 Non-uniformity measurements of FPI sensors

This section presents the results of experimental scans of the FPI sensors. Fabry Perot Interferometer sensors of various cavity thicknesses ranging from 10 µm to 40 µm, and mirror reflectivities between 95% and 98% were measured. This is for the purpose of obtaining average non-uniformity in cavity thicknesses.

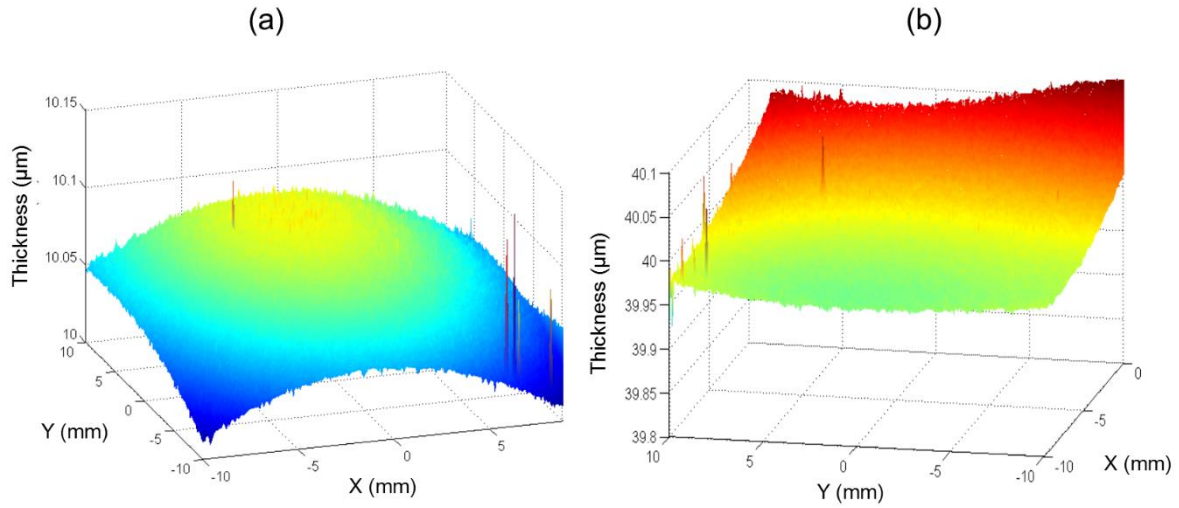

Figure 6-14 Surface profile FPI sensors with cavity thicknesses of (a) 10 µm, (b) 40 µm µm for mirror reflectivities of R=98%

Figure 6-14 shows cavity thickness variations in FPI sensors for 10 µm and 40 µm cavity thickness, although a greater number of sensors were measured. The FPI sensors in general have a dome like shape, with some showing quite a flat surface profile. The following work in this thesis presents the thickness non-uniformities in various sensors

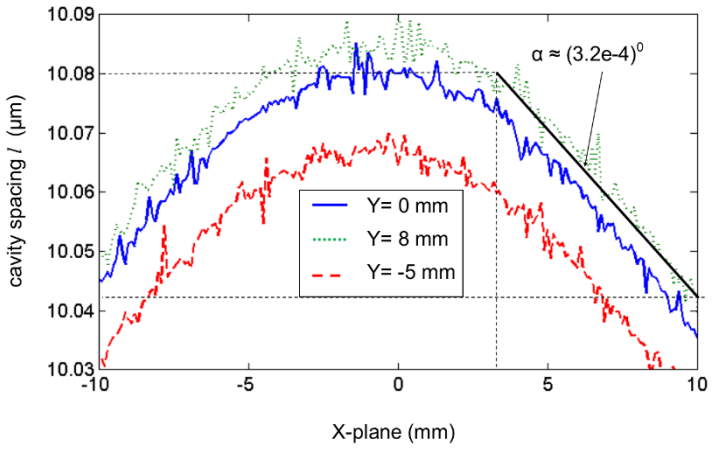

Figure 6-15 Cross sectional profile of surface along the x plane for various y positions for a 10 µm cavity thickness

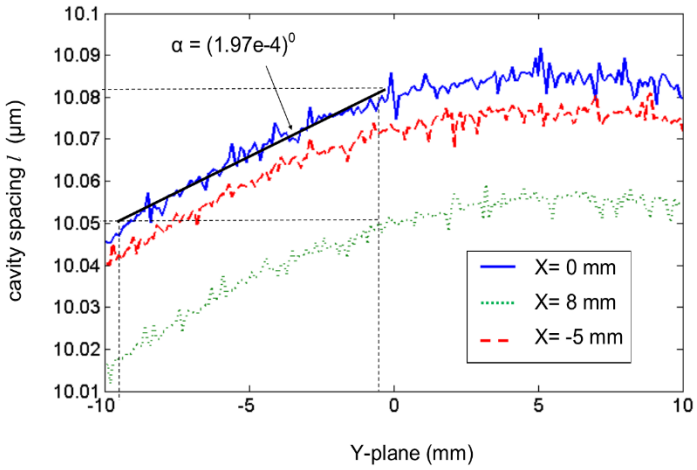

Figure 6-16 Cross sectional profile of surface along the y plane for various x positions for a 10 µm cavity thickness

Figure 6-15 and Figure 6-16 shows the cross sectional profiles along the *x* and *y* plane respectively, at various *x* and *y* positions. As the x plane moves from a positive *y* position to a negative *y* position, the overall cavity thickness decreases. This is because the general surface profile is a domed shape surface profile, as shown in Figure 6-14(a). Figure 6-16 shows that the cavity thickness is maximum at *x*=0, while at *x* = 8 mm and *x*= -5 mm the overall cavity thickness is less. The general surface non-uniformity can be approximated as linear, particularly so for the beam dimensions used in interrogating the FPI sensor which are less than 100 µm. The change in the cavity thickness is around 0.04 µm over a scale of millimetres, therefore for a beam radius on the scale of a few tens of microns, this can be assumed a constant cavity thickness variation. The wedge angle calculated is $(3.2\text{x}10^{-4})^{\circ}$ along the *x* plane and $(1.97\text{x}10^{-4})^{\circ}$ along the *y* plane. The small cavity thickness fluctuations across the profile is due to the noise affecting the choice of bias wavelength.

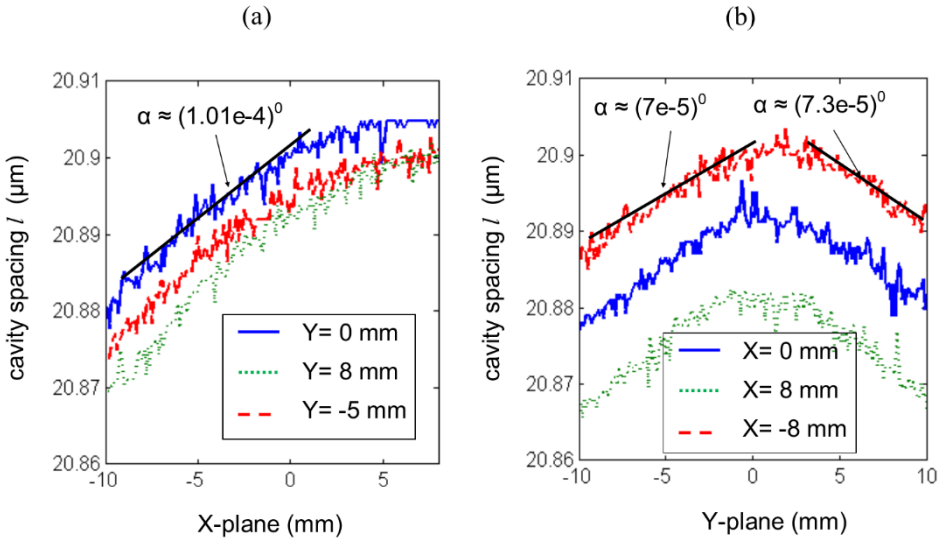

Figure 6-17 Cross sectional surface profiles along the (a) x-plane and (b) y-plane for a 20 μm thick cavity FPI

Figure 6-17 shows the surface profile in the *x* and *y* plane for a FPI with a 20 μm thick cavity. It has a similar profile to the 10 μm FPI sensor shown in Figure 6-15. The non-uniformity in the cavity spacing can be approximated as linear. The wedge angles calculated are around $(1.01 \times 10^{-4})^{\circ}$ along the *x* plane and around $(7 \times 10^{-5})^{\circ}$ along the *y* plane.

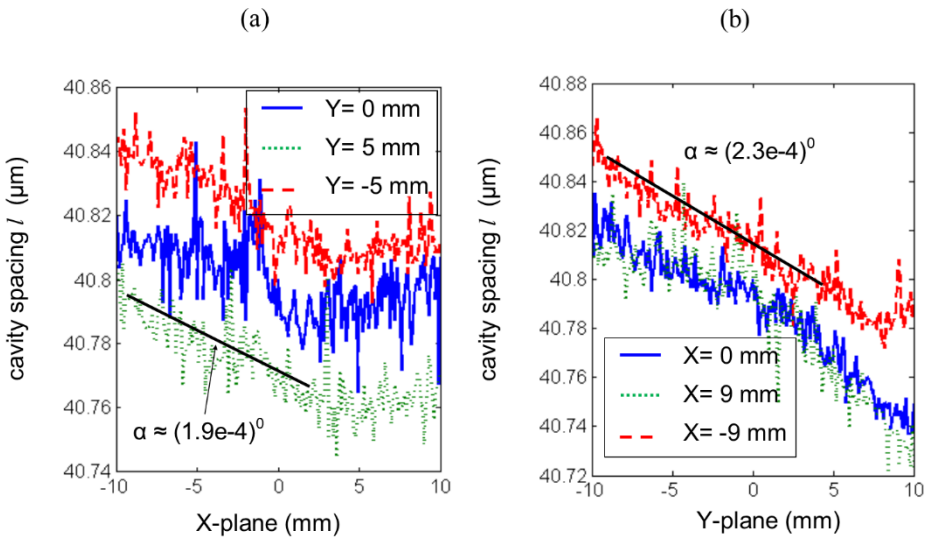

Figure 6-18 Cross sectional surface profiles along the (a) x-plane and (b) y-plane for a 40 µm thick cavity FPI

Figure 6-18 shows the surface profile along the x and y plane at various x and y positions for a FPI with a 40 µm thick cavity. Unlike the 10 µm and 20 µm thick cavity FPI sensors, the surface profile is not a dome shape. The wedge angles were calculated by taking a linear approximation and are found to be $(1.9\text{x}10^{-4})^{\circ}$ along the *x* plane and $(2.3\text{x}10^{-4})^{\circ}$ along the *y* plane.

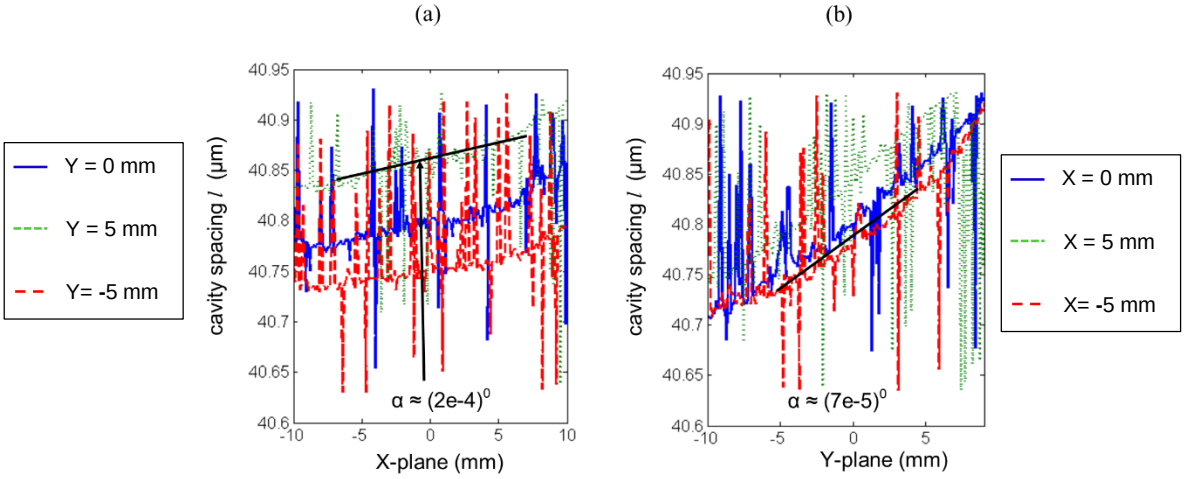

Figure 6-19 Cross sectional surface profiles along the (a) x-plane and (b) y-plane for a 40 µm thick cavity FPI with mirror reflectivities of R=98%

Figure 6-19 shows a surface profile along the *x* and *y* plane at various *x* and *y* positions for a FPI with a 40 µm thick cavity and mirror reflectivities of 98%. There are huge spikes in the surface non-uniformity for this surface profile. This is due the contamination by dust and dirt particles during the coating process, leading to failure points during the scan of the surface of

the FPI sensor. However, a general non-uniformity profile can still be inferred from the data. Taking a linear approximation along the *x* and *y* planes, wedge angles of $(2x10^{-4})^{\circ}$ and $(7x10^{-5})^{\circ}$ are calculated along the *x* and *y* axis respectively.

6.6.2 Effect of non-uniformity of FPI sensors

The non-uniformity measurements presented in section 6.6.1, showed the variation in the cavity thickness of FPI sensors used for PA imaging. This is useful to know the limitations imposed by cavity thickness non-uniformities when considering the optimised design of FPI sensors. For beam waists of a few microns, the non-uniformity can be approximated as a wedge, as the variation in cavity thickness of 0.1 μm occurs over a spatial dimension of millimetres. The non-uniformity variation was independent of the cavity thickness. The wedge angles presented were from FPI sensors in use for photoacoustic imaging. To gather a more informed view of the non-uniformity in cavity thickness, a larger sample of surface profiles is required. This is so that a mean wedge angle may be found and a variation in the wedge angle given by the standard deviation. Based on the experimental results obtained an average wedge angle of 0.00018°, with a variation of $\pm 0.00009^{\circ}$ for a sample of six FPI sensors with about 10 measurements over both the *x* and *y* plane of each sensor. Although as mentioned, the greater the number of samples measured the better informed the statistics become in returning an average wedge angle and variation.

Chapter 7 Defining metrics for characterising the performance of FPI sensors

This chapter presents the development of metrics to characterise the performance of FPI sensors, namely the sensitivity as well as the effect of system noise on the performance. The departure of the ITF_λ from that of a non-diverging beam results in the definition of optical sensitivity in chapter 2, sub-section 2.1.4.2 being no longer valid. As a result a new definition of optical sensitivity is needed. This is important as a measure of the performance of the FPI sensor, as well as determining the wavelength to bias the FPI sensor. This chapter defines the optical sensitivity, and how that leads to choosing the optimum wavelength to bias the sensor. In addition to the definition of the optical sensitivity, a noise analysis for a typical laser used for acquiring signals from the FPI sensor is presented. The purpose of this is to implement a metric to take into account the effect of system noise, such that the optimum parameters are chosen. This is done by analysing the contributions from various noise sources, such as the optoelectronic system used to detect the light from the FPI sensor, as well as the noise arising due to the laser. Section 7.1 details the definition of optical sensitivity and how one should choose the wavelength to bias the Fabry Perot Interferometer sensor. Section 7.2 is a noise analysis, which considers the various sources of noise which are encountered when using the Fabry Perot Interferometer sensor.

7.1 Defining the optical sensitivity for FPI sensors

This section examines the definition of optical sensitivity. Defining the optical sensitivity is important, as it aids in choosing the optimum wavelength to obtain the highest detected signal. The definition of optical phase sensitivity derived from the Airy function is no longer applicable due to the departure of the ITF_λ from that of a non-diverging beam. This is due to the phase characteristics of a Gaussian beam as presented in chapters 5 and 6.

7.1.1 Definition of optical sensitivity

7.1.1.1 *Definition of the optical phase sensitivity for a non-diverging beam*

The development of a model for Gaussian beams illuminating FPIs showed the shape of the ITF_λ depart from the ideal case of a non-diverging beam. Asymmetric ITF_λs with reduced visibility were shown when FPIs were illuminated by beam radii with a short Rayleigh range compared to the distance propagated per round trip. The optical sensitivity has so far been defined as the change in the reflected light per unit change in the phase ($dR/d\varphi$). This is not valid for Gaussian beams, due to the additional phase contributions by a Gaussian beam, described in Chapter 5. The total electric field that is reflected from the FPI for a Gaussian beam is,

$$E_{total} = \sum_{m=0}^{\infty} a_m E_0 e^{-i(2kml - \Theta_m + \frac{k\rho^2}{2R_m(2ml)})} \quad 7.1$$

where a_m is the amplitude coefficient and 2m*l* is the distance propagated on each round trip. E_0 is the incident electric field. Compared to the expression for the non-diverging beam which leads to the Airy function, Eqn. 7.1 does not form a geometric series, hence an analytical form can't be achieved. This is because of the additional phase components, such as the Gouy phase Θ_m and the radial phase which vary in a non-linear fashion with round trip number *m*. Therefore it is impossible to factor out m. As the phase description and shape of the ITF_λ departs from that of a non-diverging beam for Gaussian beams, the optimum wavelength is not according to the maximum of the derivative of ITF_φ.

7.1.1.2 *Alternative optical sensitivity definitions*

The wavelength at which to interrogate the FPI sensor would seem to be the wavelength corresponding to the maximum derivative of the wavelength ITF_λ ($\sim dR/d\lambda$).

For a non-diverging beam the relation between the derivatives of the phase ITF_φ and the wavelength ITF_λ is related as below,

$$\frac{dR}{d\lambda} = \frac{dR}{d\varphi}\frac{d\varphi}{d\lambda}$$
$$\frac{dR}{d\lambda} = \frac{dR}{d\varphi}\frac{4\pi nl}{\lambda^2} \qquad 7.2$$

For acoustic sensing the phase is being modulated by a change in the cavity thickness induced by a pressure change. Therefore the optimum wavelength is where the maximum change in dR for a given change in the cavity thickness (~dR/d*l*) occurs. For a non-diverging beam this is related to the derivative of the phase ITF_φ as,

$$\frac{dR}{dl} = \frac{dR}{d\varphi}\frac{d\varphi}{dl}$$
$$\frac{dR}{dl} = \frac{dR}{d\varphi}\frac{4\pi n}{\lambda} \qquad 7.3$$

Figure 7-1 shows the shift in the wavelength ITF_λ when the cavity thickness changes, due to the pressure amplitude of the acoustic wave.

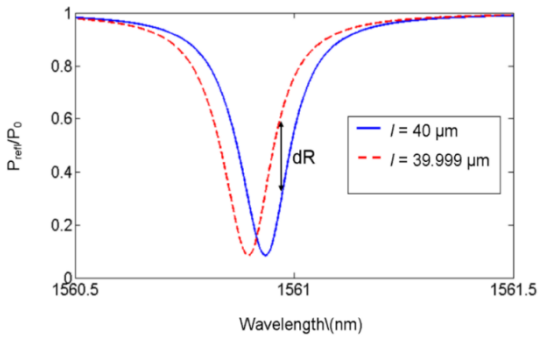

Figure 7-1 Graph of the reflectivity peak in the ITF_λ shifting as the cavity spacing changes by d*l* in a FPI with R=98%, *l* =40 µm, n=1.639 and illuminated with beam radius of ω_0 =40 µm

Taking the ratio of the two expressions dR/dλ and dR/dl in Eqn. 7.2 and Eqn. 7.3 respectively,

$$\frac{\frac{dR}{d\lambda}}{\frac{dR}{dl}} = \frac{\frac{dR}{d\varphi}\frac{4\pi nl}{\lambda^2}}{\frac{dR}{d\varphi}\frac{4\pi n}{\lambda}} \tag{7.4}$$

leads to the following explicit expression,

$$\frac{dl}{d\lambda} = \frac{l}{\lambda} = s \tag{7.5}$$

where s is a constant, and where a decrease in l results in a proportional decrease in λ, and vice versa. This shows that dR/dλ is related to dR/dl through a constant for a non-diverging beam. The following sections analyse the relationship between dR/dλ and dR/dl for Gaussian beams for the purpose of finding the optimum wavelength to bias the FPI sensor.

7.1.1.3 *Modulation of cavity thickness due to pressure change*

The cavity spacing of the FPI sensor changes when a pressure wave impinges on it. The pressure change causes the cavity spacer material to contract and expand, which in turn alters the phase and reflected intensity of the light beam. This causes the wavelength ITF_λ to shift towards shorter wavelengths when the spacer layer is contracting, and towards longer wavelengths when it is expanding. This section presents the change in the wavelength ITF_λ when the cavity contracts, and then shows how the cavity spacing ITF_l changes as the cavity spacing varies. The calculation for the thickness change Δl is given by rearranging the acoustic sensitivity expression in terms of Δl

$$\begin{aligned} \frac{\Delta l}{\Delta p} &= \frac{l}{E} \ \ (Acoustic\ sensitivity) \\ \Delta l &= \frac{l}{E}\Delta p\ (Thickness\ change) \end{aligned} \tag{7.6}$$

where E is the young's modulus, (for polymer FPI sensors in PA imaging the spacer layer is Parylene-C, E= 2.8 GPa), l is the cavity thickness of the FPI sensor, Δp is the change in pressure. The pressure amplitudes detected in typical photoacoustic experiments range from 0.1 kPa to 100 kPa. In the following analysis the pressure amplitude Δp used was 100 kPa.

7.1.1.4 *Effect of wavelength ITF$_\lambda$s under a pressure change*

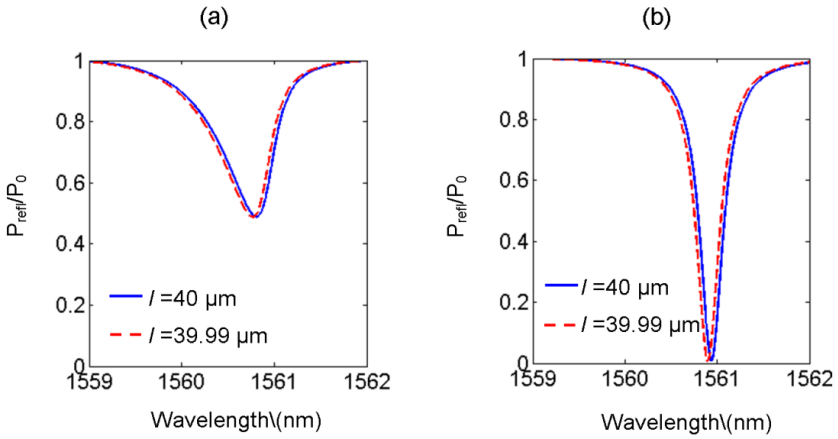

Figure 7-2 Graph of reflectivity peaks shifting as the cavity spacing changes by d*l* in a FPI with R=95%, *l*=40 μm, *n*=1.639 for beam radiuses of (a) ω_0 = 10 μm, and (b) ω_0 = 50 μm

Figure 7-2(a) shows the ITF$_\lambda$s for l = 40 μm and l = 39.99 μm for a 10 μm beam radius with mirror reflectivities of R=95%. Figure 7-2(b) show ITF$_\lambda$s for a beam radius of 50 μm. A pressure amplitude of 100 kPa produces a small shift of the ITF$_\lambda$ towards shorter wavelengths. This causes a change in the reflected light dR. For a sharper slope the change in dR will be larger compared to a shallower slope. The optimum wavelength which then produces the largest change dR would be the maximum or minimum of dR/dλ. It is more useful to analyse the change in the reflected light for l-space ITF$_l$, as a change in the cavity spacing produces a change in the reflected light for a wavelength λ. This shows us for a wavelength λ the cavity spacing at which the maximum change in dR occurs. By varying the wavelength until the maximum change in light for a small change in the cavity thickness is achieved. This shows the optimum wavelength to bias the FPI sensor, which is presented in the next section.

7.1.2 Optimum bias wavelengths according to the optical sensitivity definition

7.1.2.1 *Comparing wavelength ITF$_\lambda$s and cavity spacing ITF$_l$s*

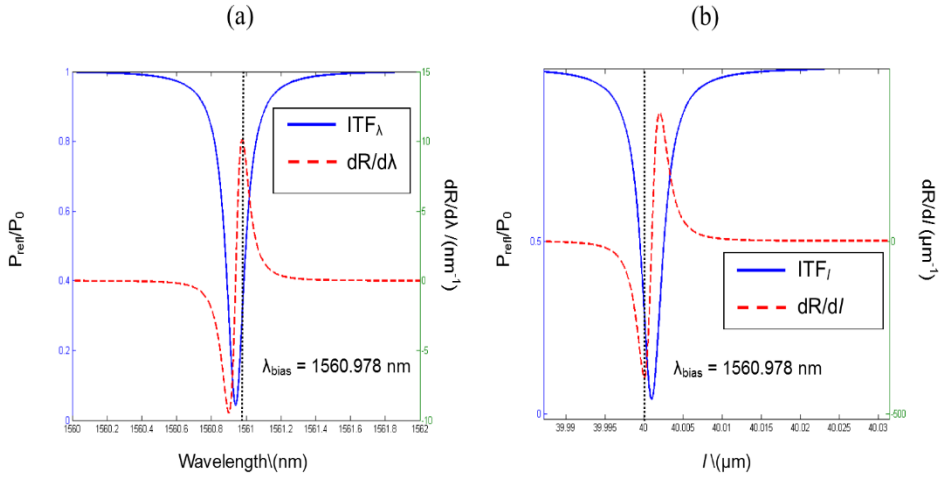

Figure 7-3 Graphs of (a) wavelength ITF$_\lambda$ and dR/dλ and inserting the wavelength corresponding to the maximum of dR/dλ (λ_{bias} = 1560.978 nm) into the simulation of (b) a *l*-space ITF$_l$, for a FPI with 40 μm cavity thickness, and mirror reflectivities of R=98%, with an incident beam radius of 50 μm

Figure 7-3(a) shows a wavelength ITF$_\lambda$ for a FPI with mirror reflectivities of R=98% and cavity thickness of 40 μm. The incident beam radius ω_0 is 50 μm. The bias wavelength of λ_{bias} = 1560.978 nm corresponds to the maximum of dR/dλ. The value of this wavelength is then inserted into the model to simulate the *l*-space ITF$_l$, as shown in Figure 7-3(b). The minimum of dR/d*l* is at the cavity thickness of 40 μm, when the wavelength is λ_{bias} = 1560.978 nm. If the wavelength corresponding to the minimum of dR/dλ is set the *l*-space ITF$_l$ would shift such that the maximum of dR/d*l* is at *l* = 40 μm. This analysis used a 50 μm beam radius which approximates to a non-diverging beam. Figure 7-4 shows the ITFs for a highly divergent beam, where the ITF shape becomes asymmetric due to the Gouy phase magnitude having an effect on the round trip phase.

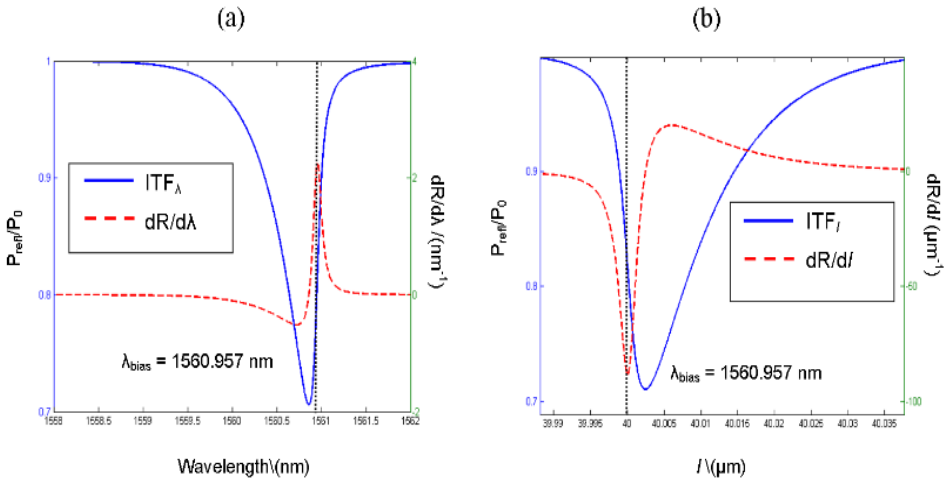

Figure 7-4 Graphs of (a) wavelength ITF$_\lambda$ and dR/dλ and inserting the wavelength corresponding to the maximum of dR/dλ (λ_{bias} = 1560.957 nm) into the simulation of (b) a *l*-space ITF$_l$, for a FPI with 40 μm cavity thickness, and mirror reflectivities of R=98%, with an incident beam radius of 10 μm

Figure 7-4(a) shows a wavelength ITF$_\lambda$ for a FPI with the same optical parameters as used in Figure 7-3, although the beam radius used is 10 μm. This is a highly diverging beam for the FPI parameters used, as it forms a highly asymmetric ITF$_\lambda$ with low visibility. The maximum of dR/dλ was found to be at a wavelength of λ_{bias} = 1560.957 nm. The bias wavelength λ_{bias} was then inserted into the model to simulate *l*-space ITF$_l$'s shown in Figure 7-4(b). The minimum of dR/d*l* corresponds to the cavity thickness of 40 μm, as that shown for a 50 μm beam radius in Figure 7-3(b). If the wavelength corresponding to the minimum of dR/dλ was used, then the *l*-space ITF$_l$ would shift such that the maximum of dR/d*l* is at l = 40 μm. This shows that choosing the wavelength corresponding to the maximum of dR/dλ results in the largest magnitude change in dR for a small modulation d*l*.

This is useful for choosing the wavelength corresponding to the greatest change in the reflected power as the pressure wave modulates the cavity thickness, and is similar to that for the analytical expression described by the Airy function.

7.1.2.2 *Relating dR/dl to dR/dλ*

The relationship between dR/d*l* and dR/dλ is presented in this section. For Gaussian beams, the phase cannot simply be stated as that for a non-diverging beam. For divergent beam radii, the ITF_λ are asymmetric and defining the bias wavelength according to dR/dφ would lead to choosing a wavelength that is not optimal. The current technique for signal acquisition in the FPI sensor relies on biasing at a wavelength which corresponds to the maximum slope of the wavelength ITF_λ. Therefore the wavelength stays constant, and it is the change in the cavity thickness which produces the change in the reflected light. It was shown in the previous section that the wavelength corresponding to the maximum of dR/dλ corresponds to the largest magnitude of dR/d*l*. It is important to analyse the relationship between dR/d*l* and dR/dλ. Figure 7-5 shows the relationship between dR/d*l* and dR/dλ.

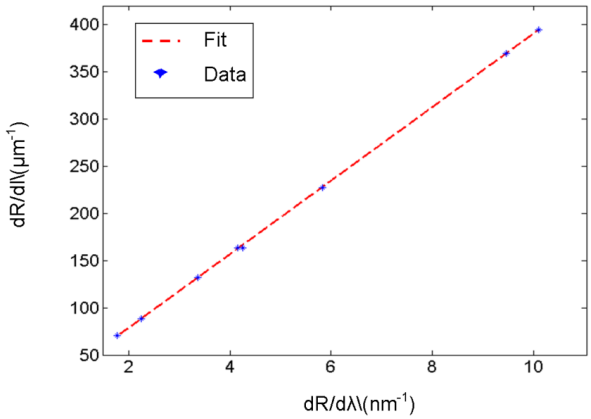

Figure 7-5 Graph of dR/d*l* vs.dR/dλ simulated for various optical parameters from highly divergent beam radii to large beam radii, various mirror reflectivities and cavity thicknesses were also simulated, showing a linear relationship between both optical sensitivity measures.

The relationship between dR/dλ and dR/d*l* is linear for decreasing beam radius. As the beam radius decreases, dR/d*l* decreases linearly with dR/dλ. These results were obtained by simulating various beam radii, from a small highly diverging beam to a larger beam radius. Also the results encompass various mirror reflectivities. The overall sensitivity S which was defined as the product of the optical phase sensitivity and the acoustic sensitivity,

$$S = \frac{dR}{d\varphi}\frac{d\varphi}{dp} \tag{7.7}$$

can be redefined in terms of the change in cavity thickness d*l*,

$$S = \frac{dR}{dl}\frac{dl}{dp} \tag{7.8}$$

where dφ has been directly replaced with d*l*. The linear relationship between dR/d*l* and dR/dλ can be used to express dR/d*l* in terms of dR/dλ.

$$\frac{dR}{dl} = s\frac{dR}{d\lambda} \tag{7.9}$$

Equation 7.9 defines a linear relationship between dR/d*l* and dR/dλ. The constant s (nm per μm^{-1}) is the ratio of the change in wavelength dλ per unit change in cavity thickness d*l*. The value of *s* is determined to be 38.947 (nm per μm) based on a 40 μm thick cavity. The physical meaning of *s* is how much the wavelength changes for a given change in the reflected light due to the cavity thickness modulation. Therefore the overall sensitivity can now be defined as,

$$S = s\frac{dR}{d\lambda}\frac{dl}{dp} \tag{7.10}$$

where dR/d*l* has been replaced with the relation defined in Eqn. 7.9. This definition of sensitivity reduces the need to define the sensitivity in terms of phase φ. The optical sensitivity defined as the change in reflected light per unit change in cavity thickness, and the acoustic sensitivity defined as the change in cavity spacing per unit of pressure are mutually independent. This is because the optical sensitivity relates to the slope of the ITF_λ and the acoustic sensitivity relates to the mechanical properties of the cavity spacer layer. To experimentally validate that dR/dλ provides the highest signal, experimentally obtained ultrasound signals from a FPI sensor at various wavelengths around the slope of the reflectivity peak is considered. The maximum signal would correspond to the bias wavelength. The following section details the experimental arrangement and results.

7.1.3 Experimental determination of optimum bias wavelength

7.1.3.1 *Experimental arrangement*

This section briefly describes the setup used to measure ultrasound signals at wavelengths near the bias wavelength. The setup used is similar to the scanner used in photoacoustic imaging. Figure 7-6 shows the experimental schematic.

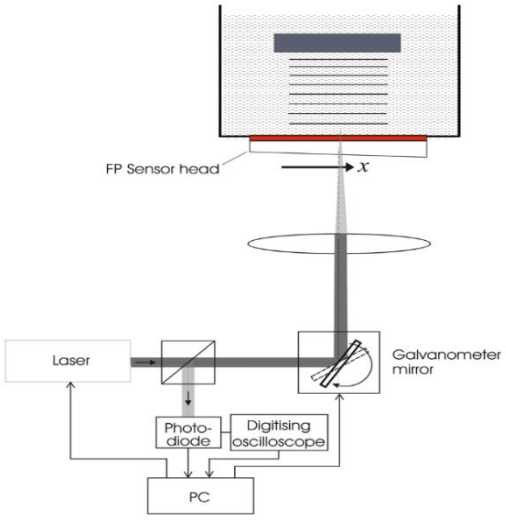

Figure 7-6 Experimental setup using a 3.5 MHZ planar traducer to generate pressures impinging on the FPI sensor to change the cavity thickness, in turn generating a signal

The FPI sensor was placed in contact with a water tank that housed a 3.5 MHz planar transducer. The peak pressure amplitude generated by the transducer was 50 kPa. The interrogation laser used was the Yenista Tunics T100s. The output power of the laser was set at 3 mW. A FPI sensor with a cavity thickness of l = 40 µm and mirror reflectivities of R=98% was used. The incident beam radius at the focus of the interrogation beam was varied. The bias wavelength according to dR/dλ was found by a LabView VI program. The wavelength was found by normalising and fitting a function to the experimental ITF_{λ}. The maximum of the derivative of the function corresponds to the bias wavelength. The wavelength was then set at ±0.01 nm of the wavelength corresponding to dR/dλ. The detected signal had a continuous average of 20 applied for the purpose of averaging out the noise, as well as having a stable peak to peak signal. The wave forms were then acquired four times, and the average signal amplitude of the four wave forms was found to improve the statistics. The bias wavelength was tracked as the continuous illumination of the FPI sensor would lead to self-heating causing an expansion in the cavity spacing. This would shift the bias wavelength to longer wavelengths. The time scale of this self-heating is much longer than the

time to acquire a signal, so the effect can be neglected. The time window for acquiring the noise and the signal was set at 10 µs, with a sampling interval of 4 ns.

7.1.3.2 *Noise Equivalent Pressure (NEP) measurement*

The Noise Equivalent Pressure (NEP) is the minimum detectable pressure, where the signal can be distinguished from the noise floor. The NEP is defined as the average peak to peak noise N, divided by the peak signal(voltage) generated per unit of pressure S_p,

$$NEP = \frac{N}{S_p} \tag{7.11}$$

7.1.3.3 *Experimental results for wavelength biasing*

The experimental results for choosing the optimum wavelength to bias the FPI sensor, is presented in this section. The results are presented for a FPI with mirror reflectivities of R=98%, and cavity thickness of 40 µm.

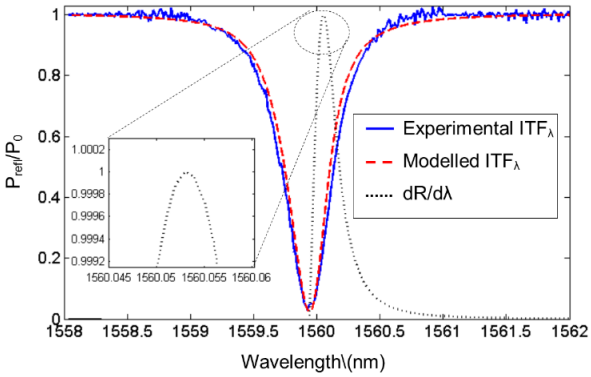

Figure 7-7 Graph of ITF$_\lambda$ reflectivity peak for R=98% with cavity spacing *l* = 40 µm and an incident beam radius of 35 µm. dR/dλ shows a bias wavelength λ_{bias} of 1560.054 nm

Figure 7-7 shows the ITF$_\lambda$ reflectivity peaks for a FPI with cavity thickness of 40 µm cavity thickness and mirror reflectivities of R=98%, and incident beam radii of ω_0 = 35 µm. The bias wavelength of dR/dλ was found to be λ_{bias} = 1560.054 nm by taking the derivative of the modelled ITF$_\lambda$.

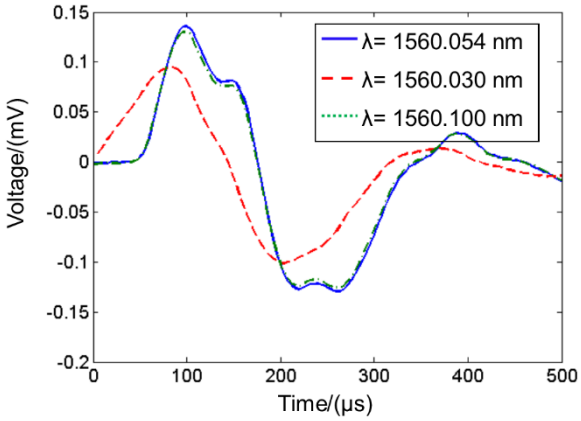

Figure 7-8 Ultrasound signal at various wavelengths near the bias wavelength of λ_{bias}=1560.054 nm with 3.5 MHz planar transducer, using a R=98% FPI sensor with *l* =40 μm, and beam radius of ω_0 = 35 μm

Figure 7-8 shows the signal waveform at each wavelength for a beam radius of 35 μm. The bias wavelength was λ_{bias} = 1560.054 nm, the signals for other wavelengths shown are λ = 1560.054 nm, and λ = 1560.100 nm.

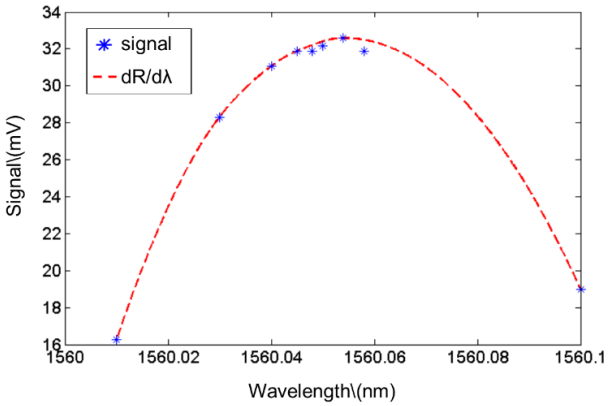

Figure 7-9 Graph of signal amplitudes for a FPI sensor with R=98% and cavity spacing of *l* = 40 μm with an incident beam radii of 35 μm

Figure 7-9 shows the signal amplitudes at various wavelengths around the bias wavelength of λ_{bias} = 1560.054 nm. The signal amplitude falls as the wavelength departs from the bias wavelength following a similar curve to dR/dλ. This suggests that biasing at the wavelength corresponding to the maximum of dR/dλ, or close to the bias wavelength will result in the largest signal amplitude.

7.2 Noise characteristics of telecomm C+L band (1510-1620nm) laser systems

This section details how the noise varies with the incident optical power on the photodiode, while the laser output remains constant. This section does not provide an extensive noise analysis of the experimental system, but the aim is to characterise how the noise sources vary with optical power and what are the limitations to the noise. This is useful in establishing metrics to optimise the design of Fabry Perot Interferometer sensors, as will be presented in chapter 8.

7.2.1 Noise variation with power

7.2.1.1 *Experimental arrangement for noise measurements*

This section details the experimental arrangement for analysing the noise performance of the system. The power on the photodiode is changed while the laser output power remains constant. Figure 7-10 shows the experimental schematic for making noise measurements.

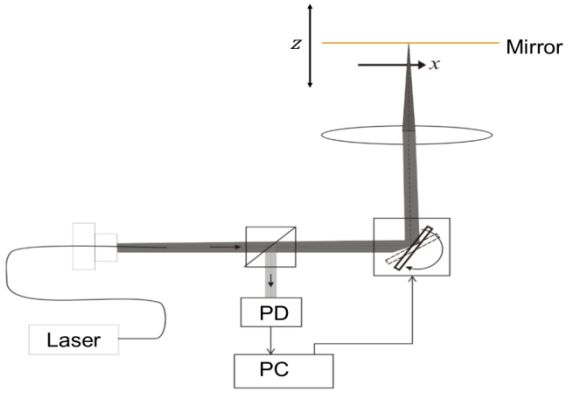

Figure 7-10 Experimental setup of system for measuring noise using a mirror to reflect the light back onto the photodiode (PD), and changing the power of the incident light detected by the photodiode.

The experimental arrangement used was the same as that used to validate the planar FPI model. The laser used was a Yenista Tunics T100S laser (1520-1620nm). The maximum ouput power of the laser was set to 9 mW, which is below its maximum oputput power of 10 mW. The wavelength was set to 1550 nm. The Fabry Perot etalon was replaced with a gold mirror, with the incident power reflected from the mirror back to the photodiode. The power of the beam incident on the photodiode was varied by adjusting the mirror along the optic axis, which effectively apertures the beam reflected from the mirror. This is analogous to the

reflected power from the etalon varying as the wavelength is changed. The power incident on the photodiode was less than 9 mW due to the aperturing of the reflected beam from the mirror. The noise was measured on the AC output from the transimpedance amplifier, in order to separate the high frequency signals from the low frequency. The cut-off frequency is 300 kHz. Figure 7-11 shows the circuit diagram for measuring the noise and acoustic signals. The output DC voltage V_{DC} is measured by connecting it directly to the scope.

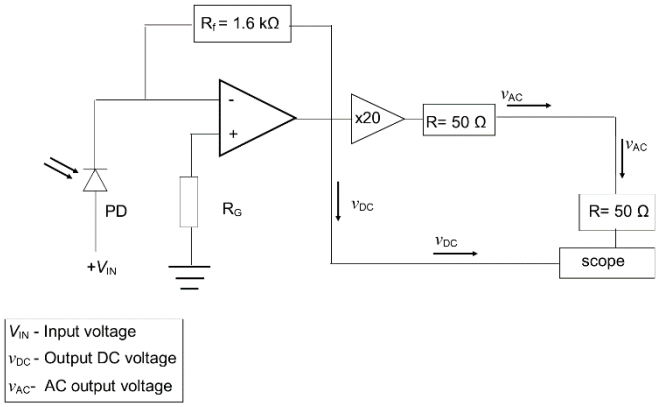

Figure 7-11 Circuit diagram showing the transimpedance amplifier for the measurement of output DC voltage and the high pass filter for the AC voltage on which the acoustic signal and noise is measured

There is a factor of 20 gain applied on the AC output v_{AC}, with an output termination impedance of 50 Ω to match the impedance of the wire. Therefore the AC output has a 50 Ω terminator when connected to the scope to impedance match to the output terminal of the gain and wire. This is to prevent reflections from the scope. The connection of two 50 Ω resistors in series results in the potential measured by the scope to be half the v_{AC}. The difference between the DC output and AC output has a factor of 10 difference. The DC output is connected directly to the scope, where the impedance is high (~1 MΩ). The transimpedance amplifier was used primarily for linear conversion of current to voltage, such that the voltage change is linear with power change.

7.2.1.2 *Laser specifications of the Yenista Tunics T100S*

Table 3 shows some of the specifications of the Yenista Tunics T100S laser, for comparing the noise measurements obtained in the experiment against the specifications provided.

Laser Parameter	Specification value
Output Power (Full Wavelength range)	>±10dBm
Wavelength stability	±5pm/h
Spectral Width (FWHM)	>400 kHz
Output stability power	±0.01dB/h
Relative Intensity Noise[2]	-145 dB/Hz
Wavelength resolution	1 pm

Table 3 Various specifications for Yenista Tunics T100s laser

7.2.1.3 *Analysis of various sources of noise*

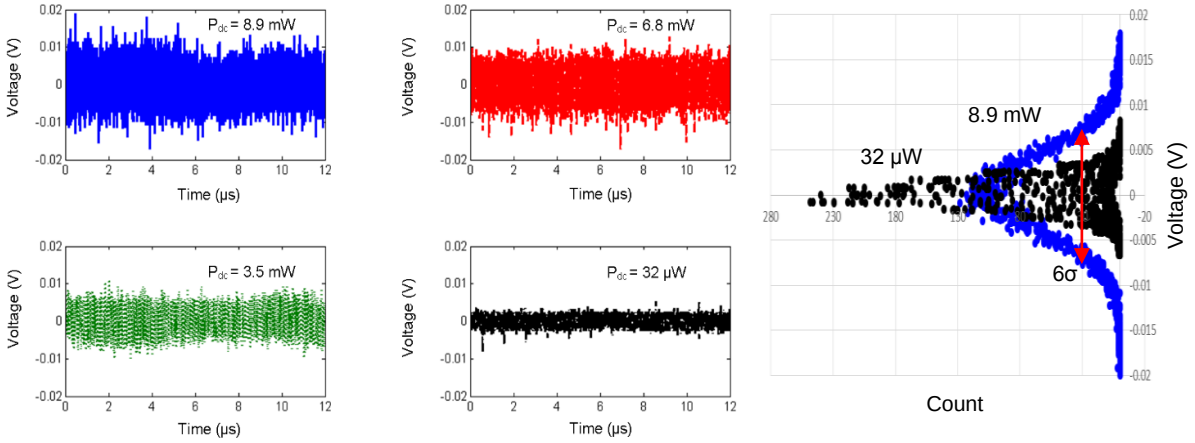

Figure 7-12 Noise segments in a 12 µs window, with 4 ns sampling time for various levels of power incident at the photodiode with the rigt hand side graph showing the Gaussian distribution of noise for 8.9 mW and 32 µW power

Figure 7-12 shows noise measurements at various power levels. The noise data at each power measurement was averaged over four 12 µs time windows to find the average standard devation, which is then multipled by six (6σ), such that 99.7% of the measured peak to peak noise voltage is encompassed [96] [97]. As can be seen in Figure 7-12, the noise reduces with

[2] For output power with 0 dBm, measured at 100 MHz

decreasing incident power on the photodiode. The right hand side of Figure 7-12 shows a Gaussian distribution of the noise amplitude for 8.9 mW and 32 μW power levels. As the power drops, the standard deviation gets smaller. The sources of noise in the experimental system, which is comprised of the photodiode and transimpedance amplifier, and the laser are as following:-

- Shot noise due to the dark current
- Thermal noise due to the feedback resistor
- Laser intensity noise (RIN)
- Shot noise due to the laser RIN
- Phase noise (when measuring the reflected light from the Fabry Perot Interferometer)

The shot noise due to the dark current of the photodiode is defined as,

$$v_d = \sqrt{2qI_d\Delta f}R_f \tag{7.12}$$

where I_d is the dark current, R_f is the resistance, q the electronic charge and Δf the electrical bandwidth. The dark current for an InGaAs detector is around 20 nA, and the electrical bandwidth is 125MHz, therefore the shot noise due to the dark current is 12.5 μV, which is a thousandth smaller than the other sources of noise.

The thermal noise (Johnson Nyquist noise) is the thermal agitation of the charge carriers in the device, and the thermal noise due to the feedback resistor is defined as,

$$v_{th,R_f} = \sqrt{4k_BTR_f\Delta f} \tag{7.13}$$

where T is the temperature and k_B is the Boltzmann constant. Taking the temperature at room termperature (T= 300 K), the thermal noise is calculated as 58 μV. In this analysis we have assumed these various sources of noise as the intrinsic noise of the transimpedance amplifier. The main purpose of the noise analysis is to observe how the noise sources due to the photocurrent vary as the power on the photodetector varies while the output power of the laser is constant. These sources of noise are grouped together because they were found to be much less than the noise components due to photocurrent, as shown in Figure 7-12. Therefore v_{op} is the contribution to the noise from the shot noise due to the dark current and thermal noise of the feedback resistor of the transimpedance amplifier, and is defined as,

$$v_{op} = \sqrt{{v_d}^2 + {v_{th,R_f}}^2} \tag{7.14}$$

The relation of the various sources to the measured noise voltage v_m is a sum of the various noise sources. Defining v_{int} as the noise due to the photocurrent, and the shot noise due to the photocurrent as v_{shot}, the measured noise v_m is defined as,

$$v_m = \sqrt{{v_{int}}^2 + {v_{op}}^2 + {v_{shot}}^2} \tag{7.15}$$

therefore knowing the total measured noise v_m, and calculating the shot noise v_{shot} due to the photocurrent, the noise contribution due to the laser intensity v_{int} can be known. The noise sources due to the photodiode and operational amplifier v_{op} is measured when the photodiode is unilluminated. The shot noise due to the photocurrent v_{shot} is defined as following,

$$v_{shot} = \sqrt{2qi_{DC}\Delta f}R \tag{7.16}$$

where q is the electron charge, i_{DC} is the photocurrent, Δf is the bandwidth, R is the resistance across the feedback resistor.

7.2.1.4 *Analysis of laser RIN and shot noise*

This section analyses how the laser RIN and corresponding shot noise due to the RIN varies with the optical power. The RIN is calculated by taking the logarithm to base 10 of the ratio of the root mean square of the noise v_m to the average DC voltage v_{DC}, taking into account the factor G and electrical bandwidth Δf=125 MHz.

$$RIN = 20\log_{10}\frac{v_m}{v_{DC}G_{ac}\sqrt{\Delta \mathrm{f}}} \qquad 7.17$$

Taking experimentally measured values of v_{DC} = 2.71 V, v_m = 17.205 mV, and G = 10, the RIN was calculated as -144.915 dB/Hz. This is in close agreement to the specified value of -145 dB/Hz.

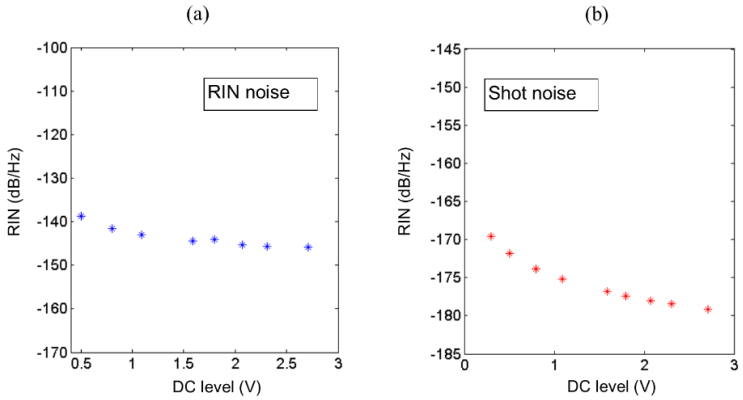

Figure 7-13 Graph of laser RIN vs. DC level and the shot noise due to laser RIN vs. DC level for a Yenista Tunics T100-S

Figure 7-13(a) shows the RIN as DC voltage increases, with Figure 7-13(b) showing the RIN for the shot noise due to the photocurrent. The value of the shot noise RIN decreases as the photocurrent increases (DC level). The laser RIN is constant for changing DC levels. The shot noise is always much less than the intensity noise. The RIN decreases by -3 dB at low DC levels, due to the dominance of the transimpedance amplifier noise. The above analysis has assumed a flat response of the RIN over the frequency range measured. To validate this assumption, the RIN as a function of frequency is analysed. This is done by applying a Fourier transform to the ratio of the measured intensity noise to the DC voltage. The time

domain noise is converted to the frequency domain obtaining an amplitude spectrum S(*f*) of the noise,

$$S(f) = FFT(\frac{v_{int}(t)}{V_{DC}G}) \quad 7.18$$

where $v_{int}(t)$ is the measured intensity noise voltage, and G is the gain on the AC output. The RIN was calculated by taking the time domain noise measurement for an incident power of 1 mW. Figure 7-14 shows the RIN value over a 100 MHz bandwidth, for the Yenista Tunics T100s.

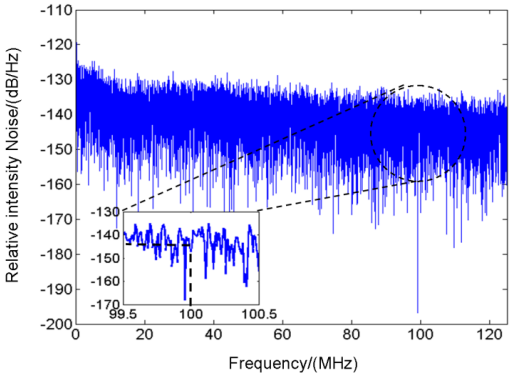

Figure 7-14 Power spectrum density of Yenista Tunics T100s measured at a power of 1 mW, and a wavelength of 1550 nm

The value of RIN at 100 MHz is close to the specified value of -145 dB/Hz, stated in Table 3. The RIN is flat over a 100 MHz bandwidth. Therefore the RIN can be assumed flat with frequency. The above noise measurements were made with a mirror, and have neglected the effects of the laser linewidth, which is an additional source of noise in making noise measurements involving resonant cavities like the Fabry Perot cavity. When illuminating a FPI the effect of the laser line width needs to be taken into account. For ITF_λs with a sharp slope in the reflectivity peak, the effect of the laser line width will be to increase the noise at the maximum slope of the reflectivity peaks in the ITF_λ. To observe the effects of the noise contribution due to the linewidth, a wavelength scan to measure the noise across a reflectivity peak is undertaken. This noise analysis is presented in the following subsection.

7.2.2 Noise variation in a Fabry Perot etalon

7.2.2.1 *Analysis of laser linewidth noise*

This section details how the various noise sources change when the wavelength is varied for a beam incident on a Fabry Perot etalon. The Fabry Perot etalon used in this experiment had mirror reflectivities R=98%, and cavity spacing of l = 200 μm composed of fused silica (n=1.44). The incident beam power on the etalon was set at 3 mW. The phase noise contribution v_{phase} is an extra source of noise inherent in the noise measurement when the beam is illuminating a Fabry Perot etalon. At sharp slopes of the reflectivity peak the linewidth of the laser affects the noise performance. The phase noise contribution is expressed as,

$$v_{phase} = \sqrt{{v_m}^2 - v_{int}(\lambda)^2 - {v_{op}}^2 - {v_{shot}}^2} \tag{7.19}$$

where the $v_{int}(\lambda)$ is scaled proportionally by a factor σ, defined as the ratio of the measured DC_λ over the DC_{max} at maximum reflection. DC_λ is the DC level at a particular wavelength λ, and DC_{max} is the DC level where the ITF_λ has a maximum reflection.

$$v_{int}(\lambda) = \sigma v_{int} \tag{7.20}$$

$$\sigma = \frac{DC_\lambda}{DC_{max}}$$

Eqn. 7.20 expresses how the $v_{int}(\lambda)$ is related to the intensity noise v_{int} at maximum reflection. Figure 7-15 shows noise segments when measured at various interrogation wavelengths in a 12 μs time window with 4 ns sampling intervals, for the etalon described above. As shown in Figure 7-15, the amplitude of the noise decreases with decreasing power incident on the photodiode, this is due to the drop in the reflected power from the etalon.

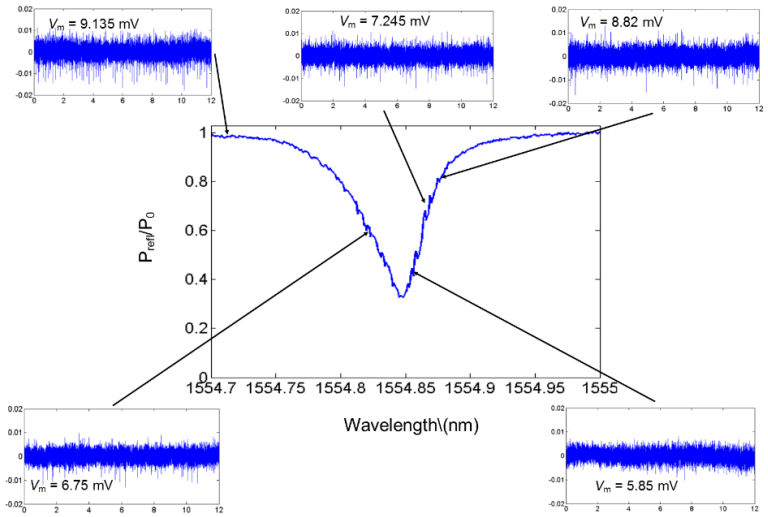

Figure 7-15 Noise segments at various wavelengths with output beam power of 3 mW for a wavelength ITF$_\lambda$ in a Fabry Perot etalon with R=98% and cavity thickness of 200 µm

Figure 7-16 shows the various noise components at each wavelength in the reflectivity peak of the ITF$_\lambda$.

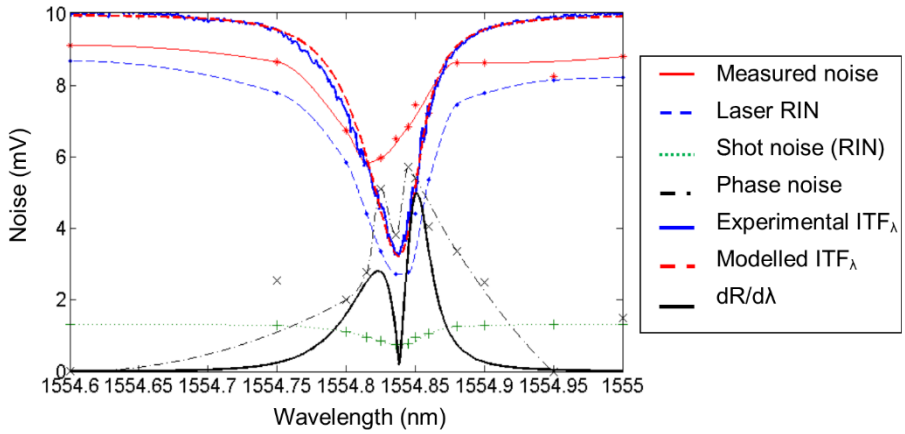

Figure 7-16 Graph of various noise source contributions when the beam is illuminating a etalon with R=98%, *l*=193.021 µm and n=1.44, and the wavelength is varied across a reflectivity peak of a ITF

The laser RIN noise decreases with decreasing reflected power (blue dashed line), as does the shot noise (green dotted line). The phase noise contribution v_{phase} increases when the slope of the reflectivity peak becomes steep. Therefore when interrogating the FPI sensor at the bias point, the noise is primarily limited by the phase noise v_{phase} and secondly by the laser RIN noise v_{int}. The effect of the shot noise due to the photocurrent compose a negligible proportion of the total measured noise. To reduce the RIN noise to the inherent noise of the experimental system, for a DC voltage of V_{DC} = 2.71 V, the specified RIN needs to -162 dB/Hz. This is lower by -17 dB/Hz than -145 dB/Hz. Another method of reduction of the RIN

noise is by using a photodiode to measure the RIN noise of the output beam and subtract it from the noise on the photodiode used to detect the reflected light from the FPI sensor. A cross correlation technique can be used to take into account any phase offset between the two noise measurements. This noise cancellation leads to the reduction of the RIN noise, although has not yet been implemented in the PA imaging setup. These improvements in the noise performance leads to the ability to measure smaller pressure amplitudes for a FPI with a certain optical sensitivity.

7.3 Summary

This chapter redefined the optical sensitivity and analysed the noise characteristics of experimental systems employing FPI sensors for ultrasound detection. The definition of optical sensitivity was presented in section 7.1. The maximum of $dR/d\lambda$ for the wavelength ITF_λ was shown to give the highest optical sensitivity through its linear relationship with dR/dl for a non-diverging and Gaussian beam. Section 7.2 showed the noise performance in a FPI, and it was found that the noise performance is limited by the phase noise and laser RIN noise. ITF_λs with high visibility would mean a reduced reflected power at the bias wavelength, resulting in lower noise. This noise analysis of how various sources of noise vary with reflected power is important in defining a metric for characterising the FPI sensor performance. This is so that the choice of optical parameters is optimum. It was shown that to get the RIN noise to match the noise performance of the experimental system noise, a laser with a RIN value of -162 dB/Hz is required. Alternative lasers that might prove suitable are NP photonics Rock laser series, with an output power of 25 mW, line width of <200 Hz and where the noise performance is shot noise limited. Another laser is the Santec TSL-510 which has a line width of 200 kHz and RIN of -145 dB/Hz. This laser is used in PA imaging due to its fast wavelength sweep speed. However when measuring the noise, it suffers from resonant noise peaks which are periodic, and are amplified as the output power is increased. The reduction in the noise is beneficial in improving the minimum detectable pressure (NEP) that can be achieved, and aids in the design of FPI sensors to achieve the best performance.

Chapter 8 Designing optimised Fabry Perot Interferometer sensors

The thesis has presented the implementation and experimental validation of a model simulating ITF_λs for a FPI illuminated by a Gaussian beam. An understanding of the shape of the ITF_λs particularly for divergent beams was presented in Chapter 5, and an understanding of how the shape of the ITF_λ is varied by a wedge angle was presented in Chapter 6. The results in chapters 5 and 6, as well as chapter 7 are a prerequisite for understanding the design and optimisation of the FPI sensor presented in this chapter. This chapter presents the metrics, which measure the performance of the FPI sensor. The value of the metric changes as the beam radii and mirror reflectivities are varied, leading to the choice of optical parameters required for an optimised FPI sensor. To put the design of FPI sensors into context, various examples of FPI sensors are considered. Also presented in this chapter in section 8.5 is the pressure linearity that can be achieved while retaining high optical sensitivity.

8.1 Characterising the FPI sensor performance for various optical parameters

8.1.1 Effect of beam divergence and mirror reflectivity on the ITF_λ

The current subsection presents the effect on the ITF_λ, as the beam radius is increased when illuminating FPIs with various mirror reflectivities. Figure 8-1 shows ITF_λs for an FPI with a cavity thickness of 40 μm and with mirror reflectivities of 90%, 95% and 98%. Figure 8-1(a) shows the ITF_λs for a 10 μm incident beam radius. As the mirror reflectivity increases the reflectivity peaks becomes narrower but the asymmetry increases. The asymmetry increases with mirror reflectivity because the initial round trips by the field in the cavity have a greater contribution to the resonance than that for lower mirror reflectivities. Therefore the effect of the Gouy phase on the shape of the ITF_λ becomes more considerable with higher mirror reflectivities. The visibility also reduces as the reflectance minima is higher.

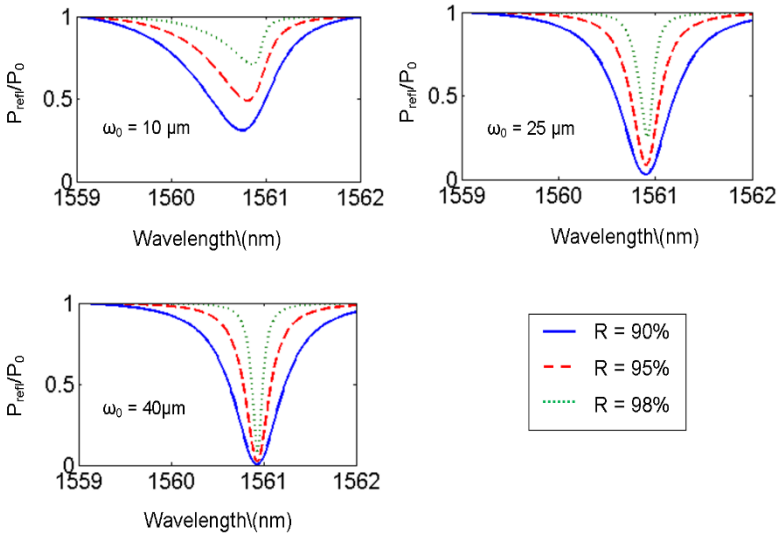

Figure 8-1 ITFλs for a FPI with cavity thickness of 40 μm, with R=90% (solid blue line), R=95% (medium dashed red line) and R=98% (short dashed green line) and beam radii of (a) 10 μm, (b) 25 μm and (c) 40 μm

As the beam radius increases to 25 μm, the visibility for R=90% is high and then decreases as the mirror reflectivity increases. The reflectivity peak also narrows as the mirror reflectivity increases. The trend is also the same for when the FPI is incident with a beam radius of 40 μm. The general trend in the ITFλs is characterised as follows:

- As the mirror reflectivity increases the reflectivity peak becomes sharper for all beam radii, although for small beam radii it also becomes asymmetric.
- The visibility reduces as the mirror reflectivity increases for all beam radii but the reduction in visibility is less for larger beam radii. This is because larger beam radii approximate to a non-diverging beam due to the larger Rayleigh range z_0.

It is assumed that increasing the mirror reflectivities would increase optical sensitivity. However diffraction effects would lead to ITFλs that depart from a non-diverging beam. This would limit the optical sensitivity and in some cases reduce the optical sensitivity as will be shown in section 8.3 for variations in mirror reflectivities. Therefore this chapter presents how one should choose the optimum beam radius and mirror reflectivities to obtain the highest optical sensitivity. Characterisation of the finesse and visibility variation with beam radius and mirror reflectivity is important in helping choose the required optical parameters. The next sub-section presents the finesse and visibility variation with beam radius and mirror reflectivity.

8.1.2 Finesse and visibility variation with beam radius

The relationship between finesse and visibility with beam radii (ω_0) is presented in this section. The finesse is defined in wavelength space as $F=FSR_\lambda/FWHM_\lambda$. The Free spectral range FSR_λ is the wavelength interval between two reflectance minima. The full width at half maximum ($FWHM_\lambda$) is the width in wavelength at half the height of the reflectivity peak. The visibility is a measure of the depth of the reflectivity peak. It is expressed as,

$$V = \frac{R_{max} - R_{min}}{R_{max} + R_{min}} \tag{8.1}$$

where R_{max} is the normalised reflectivity at maximum reflection and R_{min} is the normalised reflectivity at the reflectance minima.

8.1.2.1 *Finesse variation with beam radius*

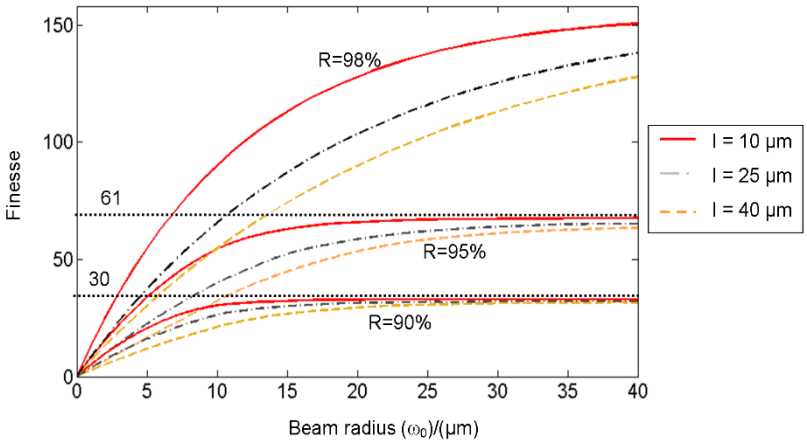

Figure 8-2 Graph of finesse versus beam radius (ω_0) for mirror reflectivities of 90%, 95% and 98% and for various cavity thicknesses

Figure 8-2 shows the finesse varying with the beam radius (ω_0) for mirror reflectivities of R=90% and R=95%. For small beam radii the finesse is low due to asymmetric ITF_λs, causing a broad Full Width at Half Maximum ($FWHM_\lambda$). As the beam radius increases, the finesse tends to a limiting value of finesse which is that for a non-diverging beam. This is the case for all mirror reflectivities, the finesse increases with increasing mirror reflectivities. As the cavity thickness increases the finesse decreases particularly at smaller beam radii. This is

because the distance propagated on a round trip is increased as cavity spacing is increased. This causes the beam to propagate into the far field causing the shape of the ITF_λ to be altered, hence the finesse to be reduced. Figure 8-2 shows that as the beam radius approaches zero the finesse approaches zero. As the beam radius tends to infinity, for a planar FPI the finesse tends to the limiting value of finesse F_0 which is that of a non-diverging beam. A function to describe the trend is useful for providing metrics such as the finesse, visibility rather than simulating ITFs for each optical parameter. This is advantageous in requiring rapid designs of optimised FPI sensors. Therefore a function which describes the modelled trend in Figure 8-2 is expressed as,

$$F(\omega_0) = F_0(1 - e^{-\alpha\omega_0}) \tag{8.2}$$

where F_0 is the reflectivity finesse due to a non-diverging beam and expressed as,

$$F_0 = \frac{\pi\sqrt{R}}{(1-R)} \tag{8.3}$$

And α corresponds to the inverse of the optimum beam radius $\omega_{0,opt}$ and is expressed as,

$$\alpha = \frac{1}{\omega_{0,opt}} \tag{8.4}$$

An explicit expression for the optimum radius can be obtained by equating the expression for the Rayleigh range to a proportion β of the total distance propagated.

$$z_0 = \beta 2 m_{max} l \tag{8.5}$$

This then leads to the following expression,

$$\omega_{0_{opt}} = \sqrt{\frac{1}{20}\frac{2m_{max}l\lambda}{\pi}} \qquad 8.6$$

where l is the cavity thickness, λ is the wavelength and m_{max} is the number of round trips until the electric field falls to a negligible value. The propagation factor β is 1/20 and arises to give the best fit between the explicit expression for the finesse stated in Eqn. 8.2 and the modelled finesse for mirror reflectivities between 90% to 98% and cavity spacings of 10 µm to 40 µm. The variation between the model and expression for these cavity spacings and mirror reflectivities was found to be an average of 8%, where the majority of the difference occurs at small beam radii. Eqn. 8.6 shows that increasing mirror reflectivities (increasing m_{max}), or the cavity thickness l, or both simultaneously the optimal beam radius increases. Taking values of l = 40 µm, m_{max} = 120 (R=95%) and λ = 1550 nm, the optimal beam radius was found to be 14 µm. If we take 10 µm as the cavity thickness, then the optimum beam radius is 8 µm. Taking the cavity thickness of 10 µm and 40 µm for R=90%, then the optimal beam radii are 5 µm and 10 µm respectively. The finesse is 63% of F_0 when the beam radius is equivalent to $\omega_{0,opt}$.

8.1.2.2 *Visibility variation with beam radius*

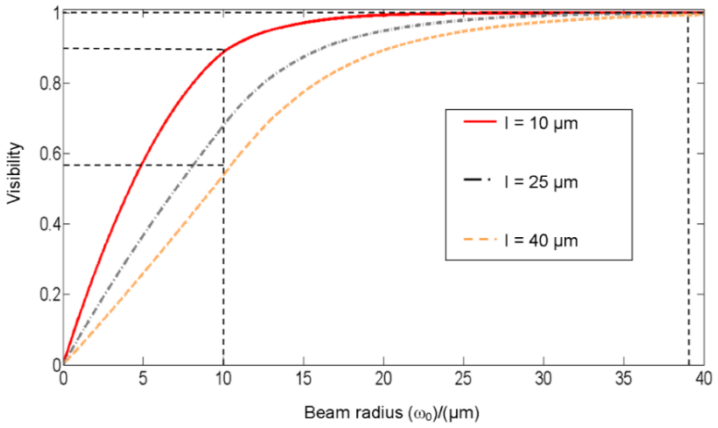

Figure 8-3 Visibility variation with beam radius for mirror reflectivity of 95%, for various cavity thicknesses

The reflectance minima in the ITF_λ, as shown in Figure 8-1 decreases as the beam radius decreases. The relation of visibility with beam radius is shown in Figure 8-3 for 95% mirror reflectivities, and cavity thicknesses of 10 µm, 25 µm and 40 µm. The trend of visibility with beam radius is similar to the trend of finesse with beam radius. As the cavity thickness increases, the visibility decreases particularly at small beam radii. The beam radius at which the visibility tends to the limiting value of 1 is higher for larger cavity thicknesses.

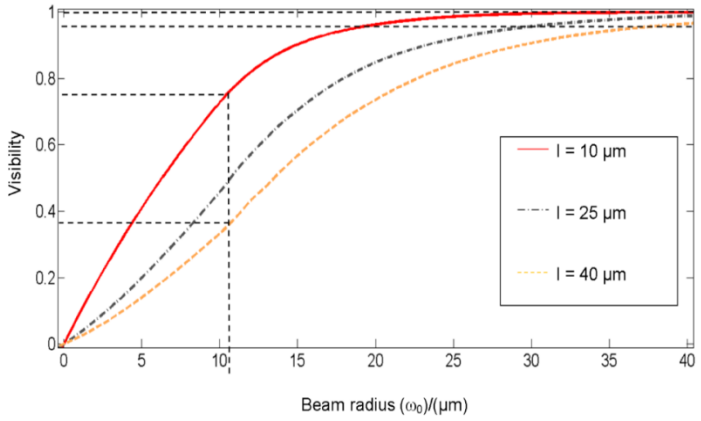

Figure 8-4 Visibility variation with beam radius for mirror reflectivity of 90%, for various cavity thicknesses

Figure 8-4 shows the visibility variation with beam radius for FPI mirror reflectivities of 90%, and cavity thicknesses of 10 µm, 25 µm and 40 µm. Comparing the visibility between R = 90% and R = 95%, the beam radii at which the visibility starts to approach 1 for R=90% is smaller. This shows a combination of high mirror reflectivity and small beam radii causes a greater reduction in visibility, consistent with the ITF_λs in Figure 8-1 .

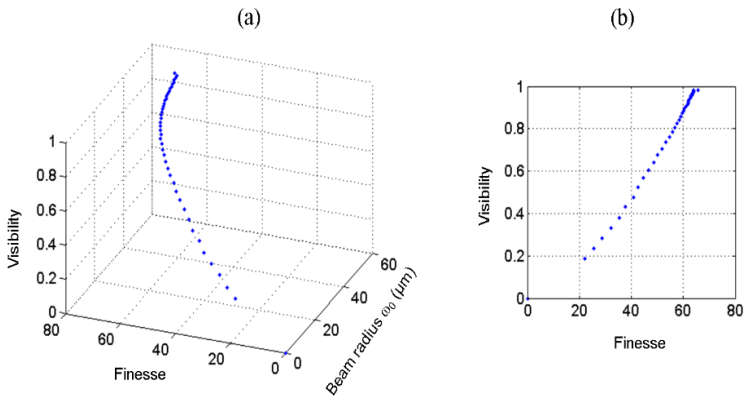

Figure 8-5 Graph showing (a)visibility and finesse varying with the beam radius from 10 µm to 50 µm for mirror reflectivities of 95% and (b) linear relationship between finesse and visibility as beam radius varies

Figure 8-5 shows the relationship between finesse and visibility as the beam radius increases from 10 μm to 50 μm for a planar FPI with mirror reflectivity of 95%. To a first approximation the relationship between finesse and visibility as beam radius increases is considered linear, as shown in Figure 8-5(b). This trend shows that as beam radius increases both finesse and visibility increase linearly. An expression for the visibility as a function of beam radius is expressed as,

$$V(\omega_0) = \varepsilon F_0(1 - e^{-\alpha\omega_0}) \qquad 8.7$$

where ε is a constant of proportionality linking finesse to visibility. Equation 8.7 is valid for mirror reflectivities between 90% and 98% and cavity spacing's of 10 μm to 50 μm, as a difference of less than 10% between the model and expression was found. Equation 8.2, Eqn. 8.7 along with Eqn. 8.6 is useful in choosing the optimum beam radius for when a FPI with specific mirror reflectivities and cavity thickness is designed.

8.1.2.3 *Optical sensitivity variation with beam radius*

Sections 8.1.2.1 and 8.1.2.2 showed the variation of finesse and visibility with beam radius respectively. For a planar FPI the slope of the reflectivity peak increases with increasing beam radius. Reducing the cavity thickness would reduce the slope. The finesse defined as the ratio of the FSR_λ to the $FWHM_\lambda$ can lead to the cavity thickness being small, increasing the FSR_λ hence increasing the finesse although the $FWHM_\lambda$ may be wide. Therefore it would suggest that the optical sensitivity is high although it has reduced. Therefore for measuring the performance of FPI, the magnitude of the maximum or minimum of the slope ~ $dR/d\lambda$ is required, as was shown in chapter 7.

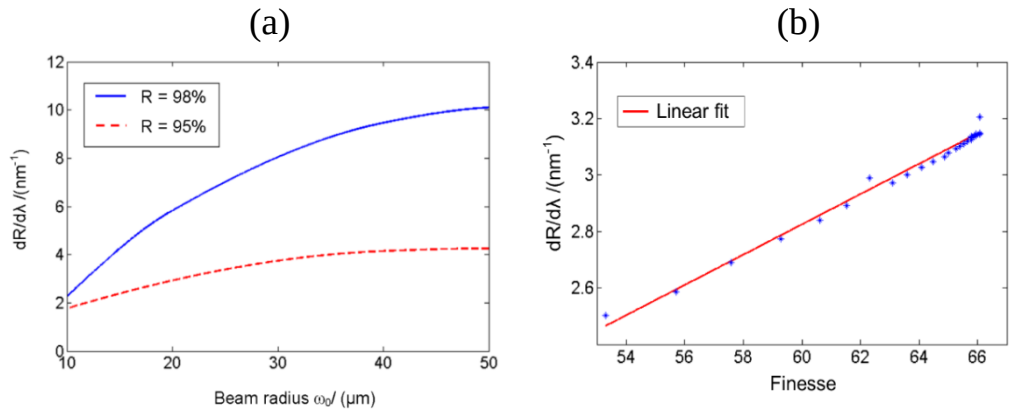

Figure 8-6 Graph of (a) dR/dλ variation with beam radius for R=95% and R-98% and (b) dR/dλ variation with finesse

Figure 8-6(a) shows the variation in dR/dλ as the beam radius is varied for a FPI with mirror reflectivities of 95% and 98%, and cavity thickness of 40 μm. The general trend is similar to that of finesse and visibility varying with beam radius. The slope becomes sharper as the beam radius and mirror reflectivities increase. This is consistent with the ITF$_\lambda$s in the opening section of this chapter. Figure 8-6(b) shows the variation of optical sensitivity dR/dλ with finesse for each beam radius, showing a linear trend. However this linear trend is valid only for planar FPIs, whereas in the wedge FPI the finesse and optical sensitivity are not linear with wedge angle. The slope dR/dλ shows how sensitive the change in reflected power is to a small modification in the phase characteristic of the beam. The following sections in this chapter will use dR/dλ as the measure of optical sensitivity, due to the use of the FPI as an optical sensor. Although in certain cases the finesse is a useful metric to define the optical sensitivity, as the finesse is proportional to the optical sensitivity. Therefore rather than calculating the optical sensitivity the finesse can be an alternative measure of the optical sensitivity.

8.2 Variation in optical sensitivity by spatial filtering

Figure 8-6 in the previous section showed optical sensitivity decreasing at small beam radii due to the shallow slope caused by the beam divergence. Chapter 5 showed how spatially filtering the reflected beam using a ring or disc based aperture changed the shape of the ITF_λ. This is advantageous if a small beam radii is needed to interrogate the FPI sensor with high optical sensitivity. The following sub-sections present the effect of different types of spatial filters on the optical sensitivity. The methods of spatial filtering considered are a disc aperture at the centre of the beam and off-centred ring apertures.

8.2.1 Spatial filtering by a disc aperture

This section analyses the effect of aperturing the reflected beam from a high finesse FPI illuminated by a highly divergent beam. Figure 8-7 shows the ITF_λs when aperturing the reflected beam from the FPI sensor by means of a disc at the centre of the beam. The mirror reflectivities of the FPI are R=98%, cavity spacing of l = 50 µm and an incident beam radius of 5 µm.

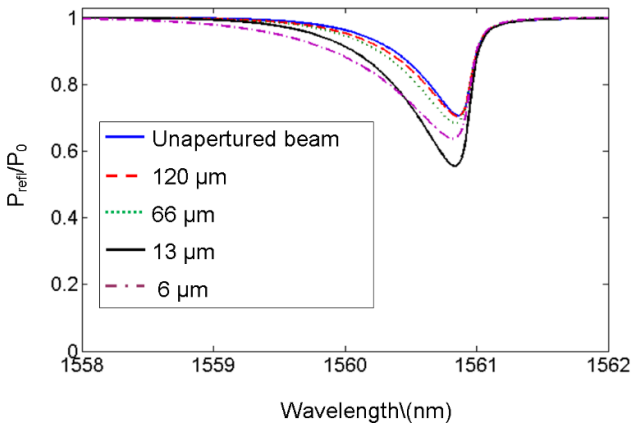

Figure 8-7 Effect on the ITF_λ when aperturing the reflected beam by various amounts, for a FPI with R=95%, l = 50 µm and incident beam radius of 5 µm

As the radius of the aperture gets smaller the ITF_λ becomes more asymmetric and the visibility increases. For a 13 µm disc radius the visibility is high and asymmetry reduced contrary to the general trend. For a 6 µm disc radius the asymmetry increases because only the intensity at the centre of the beam is taken into account, as the intensity at certain radii away from the centre is blocked by the aperture. This alters the shape of the reflectivity peak, as the contribution of the ITF_λs at certain radii from the centre are neglected. The ITF_λs at

certain distance from the centre of the beam were found to be more symmetric for highly divergent beams as was shown in Chapter 5. This was due to the radial phase counter acting the Gouy phase. Therefore the summation of ITF_λs at the centre and close to the centre up to ρ = 13 µm for this example, results in an ITF_λ that is symmetric and with higher visibility.

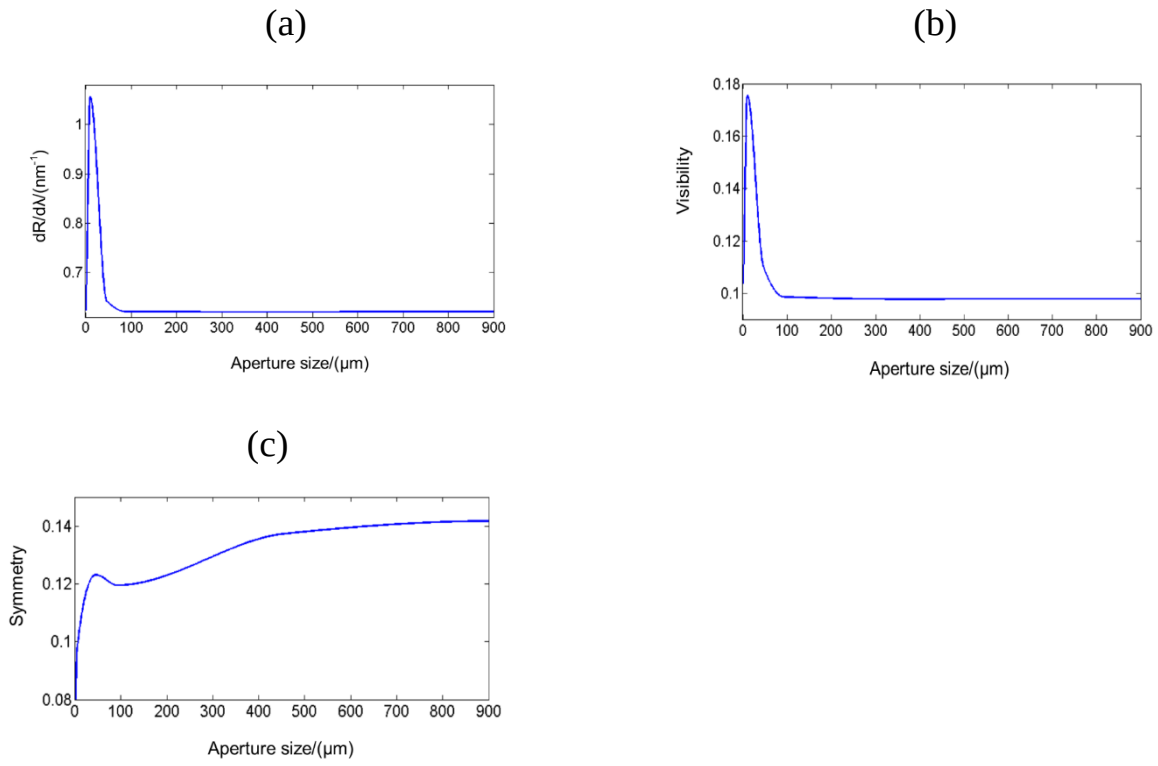

Figure 8-8 Graphs showing (a) normalised dR/dλ, (b)visibility and (c) symmetry varying with the aperture for a FPI with R=95%, *l* = 50 µm, and an incident beam radius of 5 µm

Figure 8-8(a) shows the variation of the dR/dλ for the ITF_λs shown in Figure 8-7. The slope is fairly uniform for aperture radii of 100 µm or greater. As the aperture size gets smaller dR/dλ increases to a maximum when the aperture radius is 15 µm and then decreases as it gets smaller. Figure 8-8(b) shows the visibility variation with aperture size. It has a similar trend to that of dR/dλ. The reason for the increasing asymmetry and visibility decreasing at extremely small aperture sizes (< 10 µm) is because the electric field with only the Gouy phase component affecting the phase is considered, as the radial phase is neglected. At around a 15 µm disc aperture, the electric fields close to the centre of the beam has the radial phase affecting the shape of the ITF_λ. The summation of these ITF_λs results in higher optical sensitivity and visibility shown in Figure 8-8(a) and Figure 8-8(b). The optimum aperture size is found to be around 15 µm. This is slightly larger than the beam radius. The trade-off is that the detected power is much lower which would reduce the signal to noise ratio (SNR),

although can be counter acted by increasing the power of the beam incident on the FPI. In this example when a 15 µm aperture radius is applied, the reflected power is 70% of the power incident on the FPI sensor. This suggests there is a possibility of applying a disc aperture to increase the optical sensitivity. Figure 8-8(c) shows the asymmetry variation with the aperture size. The asymmetry increases as the aperture size decreases. At around 40 µm there is a peak where the ITF_λ becomes slightly symmetric.

8.2.2 Spatial filtering by a ring based aperture

This section presents how the optical sensitivity varies as the reflected beam is spatially filtered by a ring based aperture. Chapter 5 showed how the ITF_λ became more symmetric as radii ρ increased from the centre of the beam, and was explained by the radial divergence component of the phase counter acting the Gouy phase.

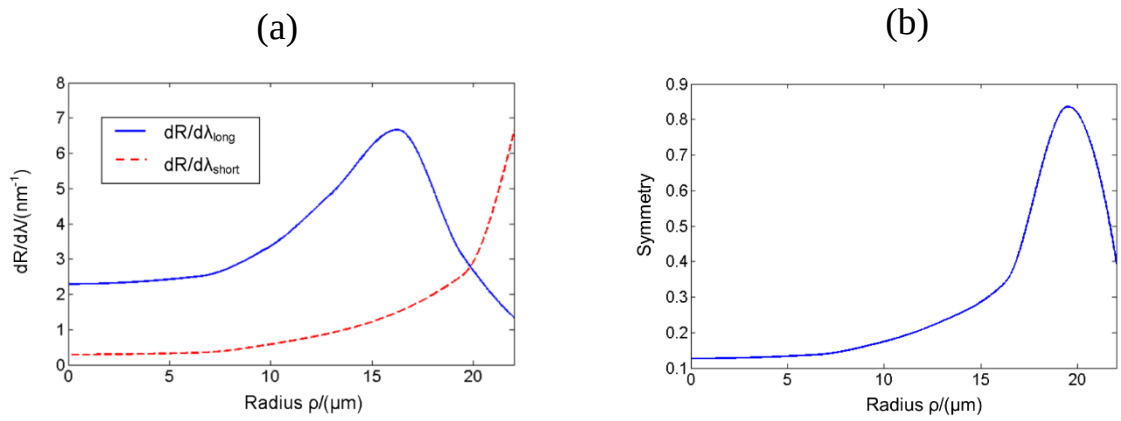

Figure 8-9 (a) Maximum and mimimum of dR/dλ and (b) symmetry of the reflectivity peak, for increasing radii ρ away from the centre of the beam, for a FPI with R=98%, l=40 µm and incident beam radius of 10 µm

Figure 8-9(a) shows how the slope of the reflectivity peak at short and long wavelengths vary with the radial position ρ, for a 10 µm beam radius and mirror reflectivities of 98% and cavity spacing of 40 µm. At long wavelengths the slope increases to a maximum at ρ=17 µm and then decreases. For short wavelengths, the slope has constant value at short radial distances from the centre, and after ρ=10 µm the slope increases. Therefore a ring radii ρ between 12 to 15 µm should be chosen to attain the highest optical sensitivity. The increase in dR/dλ for long wavelengths is a factor of 3 greater at ρ>15 µm, while for the short wavelengths the increase in the slope is a factor of 6. Figure 8-9(b) shows the variation in asymmetry as the distance ρ from the centre increases. The value of asymmetry gets closer to 1 at around ρ=19

μm, where the graphs for short and long wavelengths in the reflectivity peak intersect. At ρ>19 μm, the asymmetry increases as it has reversed. This is because the slope at short wavelengths is greater than that at longer wavelengths. This shows that spatially filtering off-centre increases the optical sensitivity, greater than what can be achieved by a disc based aperture at the centre. However the disadvantage is that at radii far from the centre, the power of the beam is much less. This could result in lower signal to noise ratio, but can be overcome by increasing the power of the incident beam to an appropriate level. In this example the reflected power detected is less than 20% of the incident power. A method of detecting the reflected beam with a ring based apertured is by expanding the reflected beam and using a Spatial Light Modulator (SLM) that forms a ring shaped beam which is then focussed and incident on the photo detector. The previous two sub-sections have shown possible ways of obtaining highest optical sensitivity for when high finesse FPIs require a small beam radii.

8.3 Choice of optimum mirror reflectivities for optimum FPI performance

The mirror reflectivities of both FPI mirrors has been assumed to be the same, in that $R_1=R_2$ where R_1 and R_2 are mirror reflectivities for mirror 1 and 2 respectively. Understanding the effect on the optical sensitivity as either of the mirror reflectivities are varied is important in order to identify the optimum mirror reflectivities that gives the highest optical sensitivity. In certain scenarios, the performance of the sensor is affected by the noise in regards to the noise equivalent pressure (N.E.P). Therefore the optimum mirror reflectivities to choose may be altered. This section therefore describes how to choose the optimum mirror reflectivities for a range of scenarios.

8.3.1 Optimum mirror reflectivities with a non-diverging beam

The optical sensitivity variation with mirror reflectivity for a non-diverging beam is presented in this section. Figure 8-10 shows the optical sensitivity variation for a 40 µm thick FPI sensor. The mirror reflectivities of R_1 is varied while R_2 is held fixed. R_2 is then changed, with R_1 consequently being varied and the process repeating for various R_2 values.

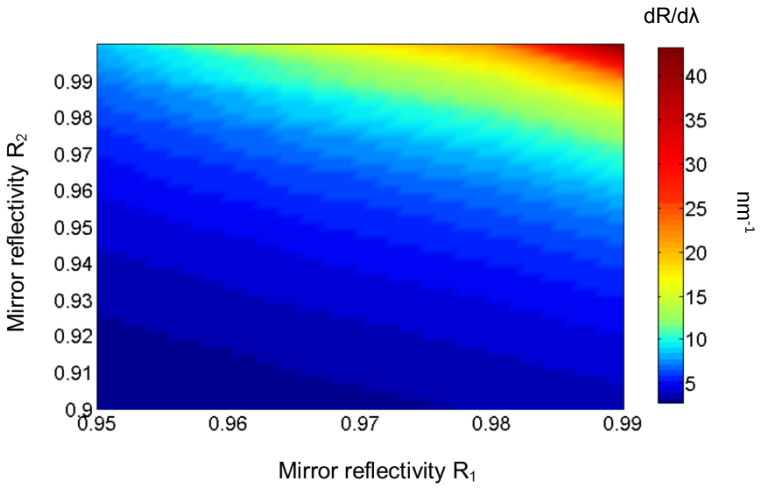

Figure 8-10 dR/dλ variation with mirror reflectivity R_1 and R_2, for and a non-diverging beam incident on a FPI with 40 µm cavity thickness

For a non-diverging beam the highest optical sensitivity is achieved when both R_1 and R_2 increases as shown in Figure 8-10. The optical sensitivity increases from 4 nm^{-1} to greater than 40 nm^{-1} as the mirror reflectivity of R_2 increases from 95% to 99.99%. This is the expected behaviour for a non-diverging beam as the reflectivity peak, hence the slope (dR/dλ)

becomes sharper as mirror reflectivity increases. In comparison a Gaussian beam would diverge as it propagates in high finesse FPIs leading to a departure in the ITF_{λ} from a non-diverging case. Therefore increasing the mirror reflectivities would be counterproductive when trying to achieve higher optical sensitivity. The next section discusses the choice of optimum mirror reflectivities when Gaussian beams illuminate FPIs.

8.3.2 Optimum mirror reflectivities for Gaussian beams

The optimum mirror reflectivities for a Gaussian beam are different to that of a non-diverging beam. This is because increasing the mirror reflectivities would mean the beam has undergone a greater number of round trips, leading the beam to diverge as it propagates in the FPI. The visibility would also be reduced, which now plays a part in the design of the FPI sensor. A low visibility would mean the normalised reflected power R_{DC} at the wavelength corresponding to the maximum of $dR/d\lambda$ is high. A higher reflected power would mean a higher noise floor due to the contributions of the laser intensity noise and shot noise, which in turn would lead to a high N.E.P. A figure of merit needs to be formulated which takes into account the effect of visibility. The next sub-section describes a metric which takes into account the effect of noise when choosing the optimum mirror reflectivities.

8.3.2.1 *Metric to choose the optimum mirror reflectivities*

This section presents a metric to choose the optimum mirror reflectivity, by considering both optical sensitivity and visibility. For a Gaussian beam the visibility would decrease as the beam becomes more divergent. This has the effect of increasing the power reflected R_{DC} hence the noise at the bias wavelength (λ_{bias}), corresponding to the maximum of the slope ($dR/d\lambda$). This would lead to a higher N.E.P. Therefore a metric for optimised mirror reflectivities is proposed, which combines the sharpness of the slope ($dR/d\lambda$) and the visibility V. The product of the two parameters will help in choosing the optimum mirror reflectivities. Equation 8.8 expresses the figure for optimised mirrors (F.O.M),

$$F.O.M = \frac{dR}{d\lambda}V \tag{8.8}$$

The largest value of Eqn. 8.8 would show the mirror reflectivities where the optical sensitivity and visibility are optimum to give the best performance. This figure of merit applies if the noise varies with R_{DC} linearly. The intensity noise in chapter 7, section 7.2 showed a linear variation with reflected power. It is assumed that the normalised reflectivity R_{DC} varies linearly with the visibility.

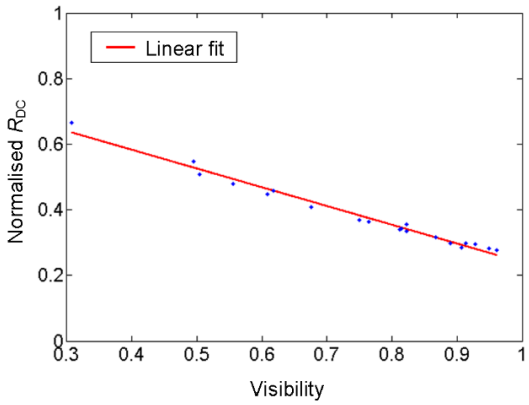

Figure 8-11 Linear relationship between visibility and R_{DC}

Figure 8-11 shows that as visibility increases the normalised reflectivity R_{DC} at the bias wavelength decreases linearly. Therefore the choice of visibility as a measure of the reflected power can be assumed. If the noise is constant irrespective of the reflected power, then the optical sensitivity (dR/dλ) is the overall performance measure of the sensor. However if the noise variation is significant with the detected power variations then the F.O.M is the measure to use to choose the optimum mirror reflectivities.

A caveat is that the F.O.M is not a measure for defining the performance of the FPI sensor. Rather the F.O.M feeds back into the design of FPI sensors by selecting mirror reflectivities that give the highest optical sensitivity, while having a high visibility.

8.3.2.2 *Effect of beam radius on optical sensitivity variations with mirror reflectivities*

This subsection presents the effect on optical sensitivity for various beam radii as the mirror reflectivities are varied. Figure 8-12(a) shows the variation in dR/dλ while varying R_1 and having R_2 held at 98%. Figure 8-12(b) shows the visibility variation with R_1.

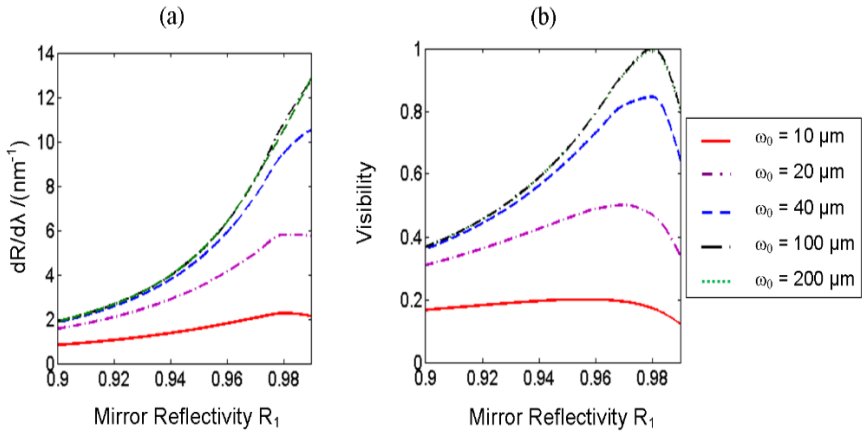

Figure 8-12 (a) dR/dλ variation with reflectivity R_1 of mirror 1, and R_2 is 98% for a FPI with cavity thickness of 40 μm and various incident beam radii, (b) visibility variation with R_1

The overall optical sensitivity increases as the beam radius increases. The increase in the optical sensitivity for 100 μm and 200 μm is small at low R_1 mirror reflectivities as the optical sensitivity tends to the limiting value. For all beam radii the optical sensitivity increases as R_1 increases. For the 10 μm and 20 μm beam radius the optical sensitivity falls after R_1 is 98%, as the slope of the ITF_λ reflectivity peak becomes shallower. For larger beam radii the optimum mirror reflectivity can be pushed up to R=99% to obtain higher optical sensitivities. The increase in optical sensitivity in going from 10 μm to 40 μm is a factor of 6. However if the choice of mirror reflectivity accounted for the effect of noise from the experimental system, then the F.O.M leads to the choice in optimum mirror reflectivities. Therefore the variation in the maximum visibility attainable shows the change in maximum visibility being 0.8 in going from a 10 μm beam radius to a 100 μm beam radius. This follows from the relationship shown in Figure 8-3 and Figure 8-4. The visibility increases as R_1 increases and then decreases after R_1 is greater than 97% ~98%. Therefore going to higher mirror reflectivities of 99% for all beam radii would decrease the visibility leading to an increase in the reflected power R_{DC}. Figure 8-13 shows the variation of the F.O.M.

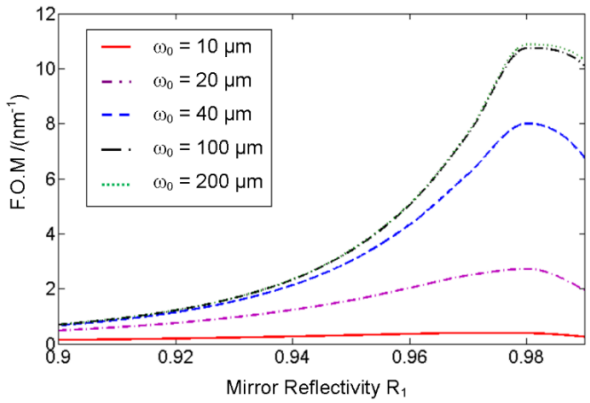

Figure 8-13 F.O.M variation with variation in reflectivity R_1 of mirror 1, while R_2 is 98% for a FPI with cavity thickness of 40 μm and various incident beam radii

As the beam radius increases the F.O.M increases to a maximum around R_1=98%. At mirror reflectivities higher than this the F.O.M decreases due to the visibility decreasing. Therefore the optimum mirror reflectivities based on F.O.M are between 97.8% and 98% when R_2 is held at 98%. This sub section has shown that increasing the beam radius and increasing mirror reflectivity results in higher optical sensitivity, visibility and F.O.M. However the variation in the optical sensitivity, F.O.M when both mirror reflectivities are varied needs to be analysed. This then leads to the optimum choice of mirror reflectivities. The next sub section presents the optimum choice of both mirror reflectivities.

8.3.2.3 *Optical sensitivity, visibility and F.O.M variation with mirror reflectivities*

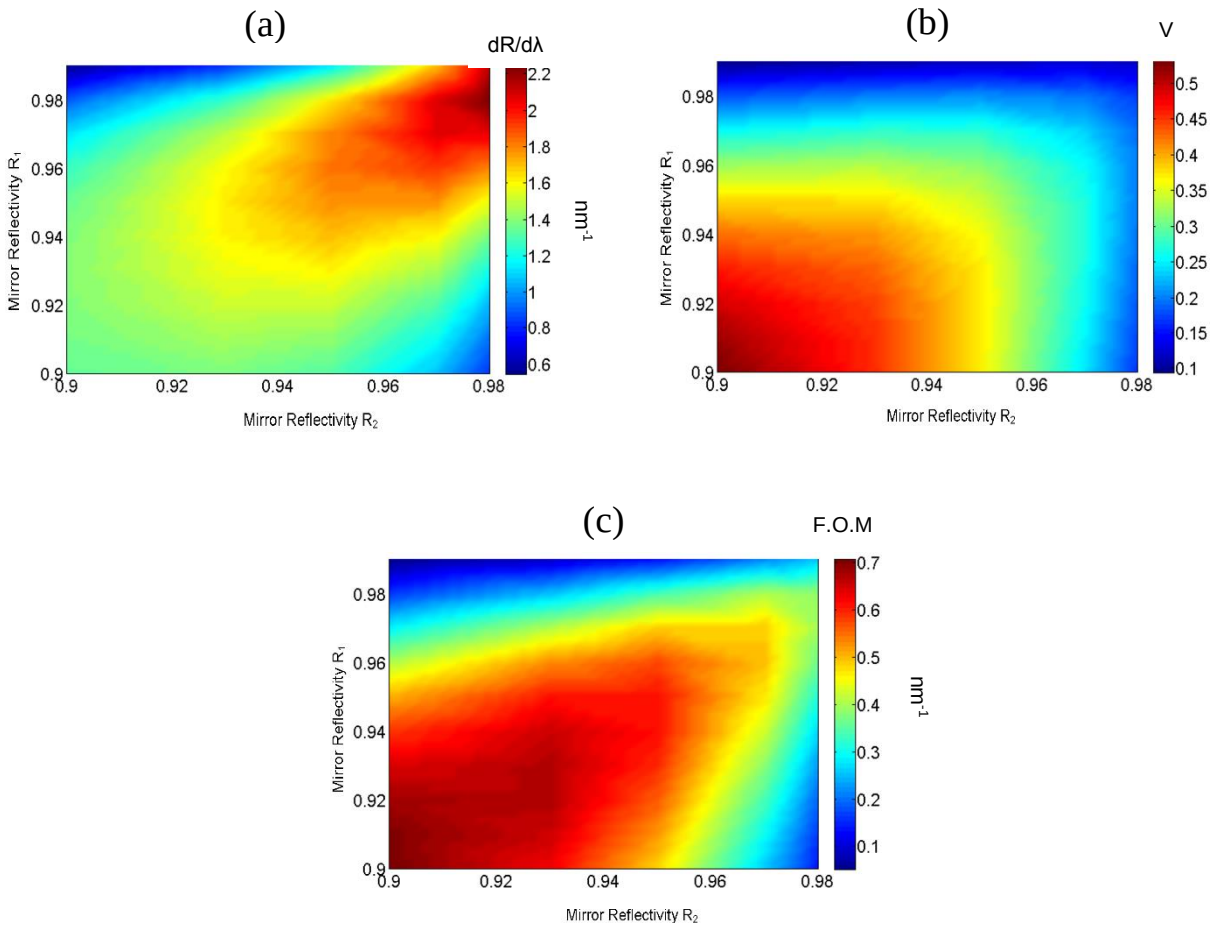

Figure 8-14 Variation in (a) optical sensitivity, (b) visibility and (c) F.OM when both mirror reflectivities R1 and R2 are varied for a 10 um beam radius with FPI cavity thickness of 40 um

Figure 8-14(a) shows the optical sensitivity variation for a 10 μm beam radius as both mirror reflectivities R_1 and R_2 are varied. Figure 8-14(b) shows the visibility variation and Figure 8-14(c) shows the F.O.M. In general the optical sensitivity increases as both mirror reflectivities increase. Compared to a non-diverging beam shown in Figure 8-10 the optical sensitivity is highest when both mirror reflectivities are in the region of 97% ~ 98%. Any increase in either mirror reflectivity reduces the optical sensitivity. The visibility is high when the mirror reflectivities are 90%~ 94% as shown in Figure 8-15(b). The F.O.M which optimises the choice of mirror reflectivities by taking into account the noise variation, shows that the optimum mirror reflectivities should be 95%. The choice for these mirror reflectivities is based on the analyses that the optical sensitivity is 1.8 nm^{-1} and the visibility is 0.35. These mirror reflectivities provide optimum optical sensitivity and visibility.

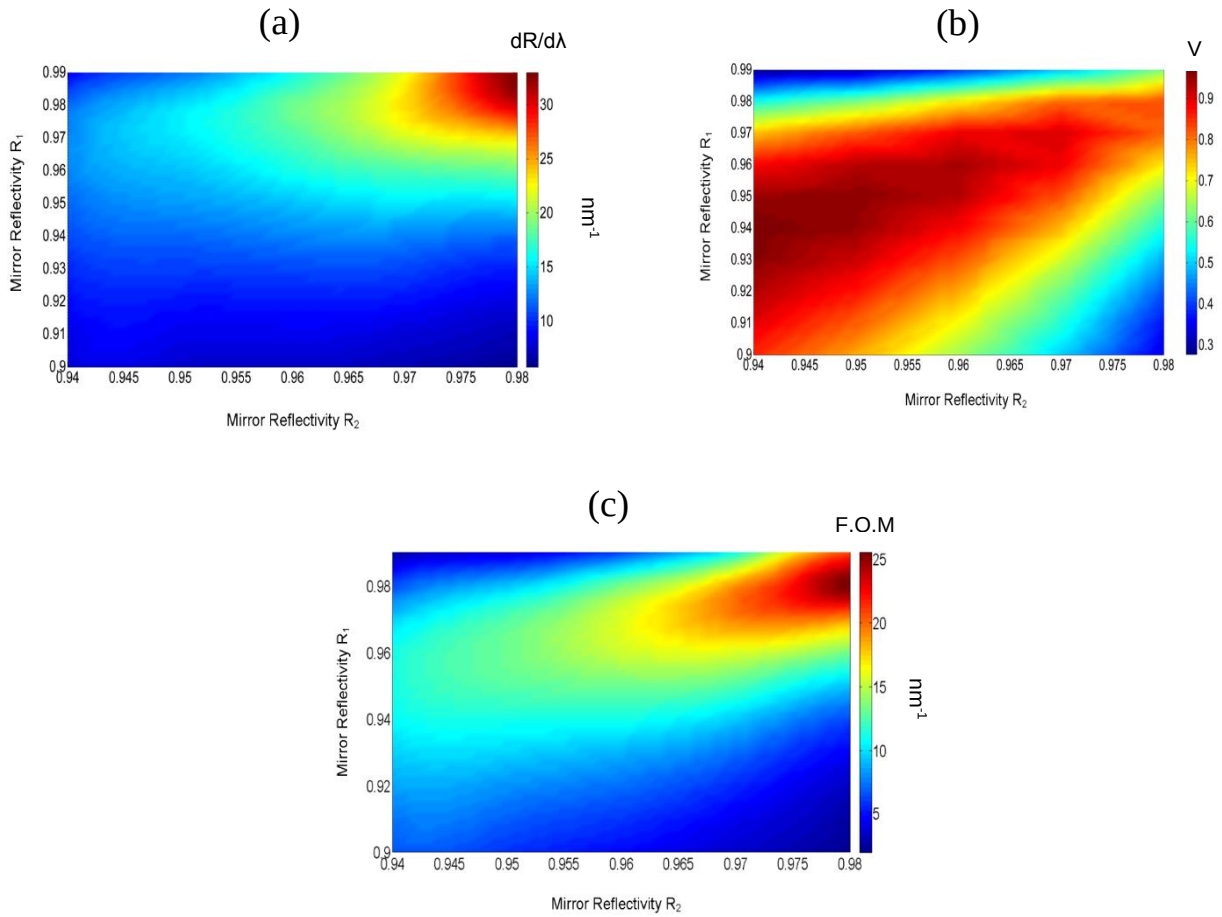

Figure 8-15 Variation in (a) optical sensitivity, (b) visibility and (c) F.OM when both mirror reflectivities R_1 and R_2 are varied for a 40 µm beam radius with FPI cavity thickness of 40 µm

Figure 8-15(a) shows the variation in optical sensitivity for a 40 µm beam radius. Figure 8-15(b) shows the visibility and Figure 8-15(c) the F.O.M as both mirror reflectivities are varied. The optical sensitivity at all mirror reflectivities is greater than that for the 10 µm beam radius. The 10 µm beam radius has a maximum of 2.3 nm^{-1}, while the 40 µm beam radius has maximum optical sensitivity of 35 nm^{-1}. The optimum mirror reflectivities are 98% when based on optical sensitivity. The visibility is much higher compared to the 10 µm beam radius, even at lower mirror reflectivities. The visibility is low when one mirror reflectivity is between ~90% and 93%, and the other mirror between 97% and 99% as shown in Figure 8-15(b). The choice of optimum mirror reflectivities when F.O.M is considered is 98% where the F.O.M is 27 nm^{-1}, while for the 10 µm beam radius the F.O.M is 0.4 at 98%. The F.O.M value for the 10 µm beam radius at optimum mirror reflectivities of 95% is 0.6. Therefore to the choice of optimum mirror reflectivities to obtain high optical sensitivity or F.O.M will depend on the beam radius.

8.3.2.4 *Effect of mirror reflectivity uncertainties*

The effect of the uncertainties in the mirror reflectivities must also be considered when choosing mirror reflectivities. These changes in the mirror reflectivity arise as a result of the manufacturing process. This subsection therefore studies the effect of mirror uncertainties. The uncertainties in the mirror reflectivities as quoted by the coating manufacturer (SLS Optics) is 1%. Referring to the 2D plots in Figure 8-14 and Figure 8-15 for a 10 μm and 40 μm beam radius respectively, the effect of a 1% change in the mirror reflectivities will have a greater effect at higher mirror reflectivities. For a 10 μm beam radius at high mirror reflectivities (97%~98%), the change in optical sensitivity is 9%, whereas for a 40 μm beam radius it is 31%. The mirror reflectivities to choose when to reduce the percentage change in the optical sensitivity needs to be different to that for when high optical sensitivity or F.O.M is required. Therefore the mirror reflectivities to choose would be in the region of 93% to 95% for both beam radii. The change in the optical sensitivity is 7% and 20% for a 10 μm and 40 μm beam radius respectively. However if the noise is to be considered then for a 10 μm beam radius the mirror reflectivities corresponding to the highest F.O.M covers a large mirror reflectivity range of 90% ~ 94%. For a 40 μm beam radius the optimum mirror reflectivities are when R_1 is in the range 94% to 96%, and R_2 is between 94% and 95% to give a percentage change of 22% in the F.O.M.

8.3.3 Optimum mirror reflectivities for spatially filtered ITFλs and non-linear noise response

8.3.3.1 *Optimum mirror reflectivities for spatial filtering of the beam*

The choice in mirror reflectivities so far has concentrated on a unapertured beam. It was shown in section 8.2 that an aperture of various sizes and geometry increased the optical sensitivity for a divergent beam incident on a high finesse FPI. The choice of optimum mirror reflectivities therefore may be different to the unapertured case mentioned previously. This subsection shows what the optimum mirror reflectivities would be when the beam is apertured with a disc aperture at the centre and by a ring aperture off-centre.

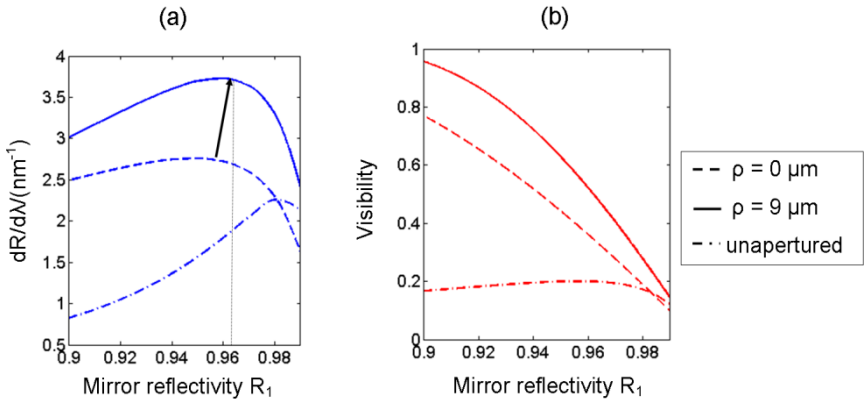

Figure 8-16 Variation in (a) dR/dλ vs. R_1 and (b) visibility vs. R_1 when the reflected beam is apertured at the centre with a disc radius of 14 μm and off centre with a ring aperture with ρ = 9 μm and a 2 μm ring width as well as an unapertured beam, with R_2 held at 98%, for an incident beam radius of 10 μm and a cavity thickness of 40 μm

Figure 8-16 shows the variation in optical sensitivity and visibility for a 10 μm beam radius, as R_1 is varied while R_2 is held at 98%. For an apertured beam at the centre, as the mirror reflectivity R_1 is increased the optical sensitivity increases to a maximum at R_1=95%, compared to R_1 = 98% for an unapertured beam. The maximum optical sensitivity increase when apertured by a disc shows an increase of ~0.5 nm^{-1} compared to an unapertured beam. The optical sensitivity for a ring aperture is highest when R_1 = 96.3%, with the optical sensitivity increase being almost 1.5 nm^{-1} compared to a unapertured beam. The visibility decreases with increasing R_1 for when the beam is apertured by a disc and a ring aperture. The visibility for a ring aperture is higher compared to when the beam is apertured at the centre. If the effect of noise is to be taken into account, the choice of optimum mirror reflectivity will be different.

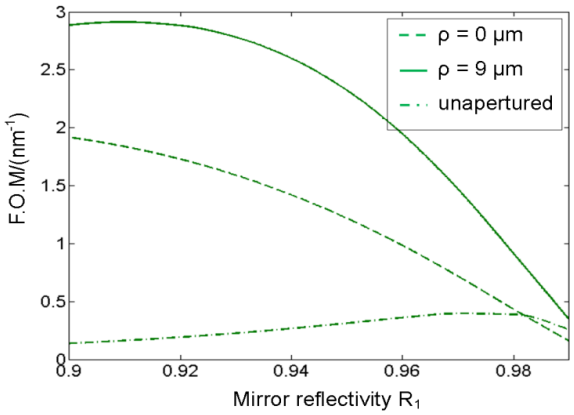

Figure 8-17 Variation in F.O.M when the reflected beam is spatially filtered at the centre with a disc radius of 14 μm and off centre at ρ = 9 μm with a 2 μm ring width as well as an unapertured beam, with R_2 held at 98%, for an incident beam radius of 10 μm and a cavity thickness of 40 μm

Figure 8-17 shows the variation in the F.O.M shown by the dashed lines, for a 10 μm beam radius for the different aperturing cases. The F.O.M for both cases decreases as R_1 increases, compared to the unapertured case. The optimum mirror reflectivity then seems to be R_1=90% and R_2=98% for when the beam is apertured at the centre. This is because the visibility is higher at lower mirror reflectivities for an apertured beam. For a ring based apertured, the optimum mirror reflectivities are R_1 = 91% and R_2 = 98% and then decreases as R_1 increases. If the ring radius was to increase, then the optimum mirror reflectivities would be higher as the ITF_λ is more symmetric. Both R_1 and R_2 can be varied to see the optimum mirror reflectivities as that shown in Figure 8-14, as this example had R_2 held at 98%. The F.O.M increases by 1.5 nm^{-1} from when the beam is unapertured to when it is apertured by a disc. This change in the F.O.M increases to 2.5 nm^{-1} when apertured by a ring aperture. Therefore a disc aperture which detects 70% of the detected light has to have mirror reflectivities which are R_1 = 90% compared to R_1 = 98% for a unapertured case. For a ring aperture R_1 has to be 92% to achieve a high F.O.M.

8.3.3.2 *Non-linear increase in noise with DC level*

The F.O.M has been assumed as the product of the visibility with the optical sensitivity. This has assumed that the effect of the noise varies linearly with the visibility, as was shown in chapter 7 in Figure 7-13 and Figure 7-16. However if the noise is dominated by shot noise, then the variation of the noise with the reflected power has a square root dependence. The variation in the noise as a function of the visibility is then multiplied with the optical sensitivity to provide the choice of optimum mirror reflectivities. This section shows the optimum mirror reflectivities for a case when there is a non-linear change in noise with R_{DC}.

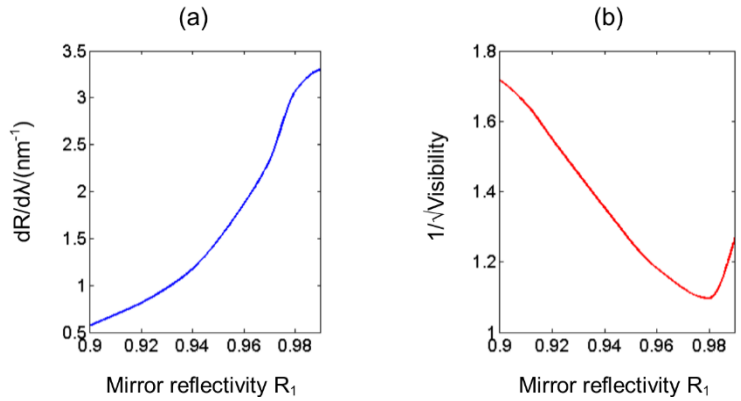

Figure 8-18 Graph of optical sensitivity vs. mirror reflectivity R_1 and (b) 1 over square root of the DC level vs. mirror reflectivity R_1 for a 20 µm beam radius with a cavity thickness of 40 µm and R_2 = 98%

Figure 8-18(a) shows the variation in optical sensitivity as R_1 changes and R_2 is held at 98% for a 20 µm beam as shown in Figure 8-12. Figure 8-18(b) shows the variation of 1/√V. At high visibilities R_{DC} will be low and at low visibilities R_{DC} will be high. The factor 1/√V decreases to a minimum at R_1 = 98% as the mirror reflectivity increases. This is because the visibility increases as R_1 increases therefore R_{DC} will be low hence reducing the shot noise.

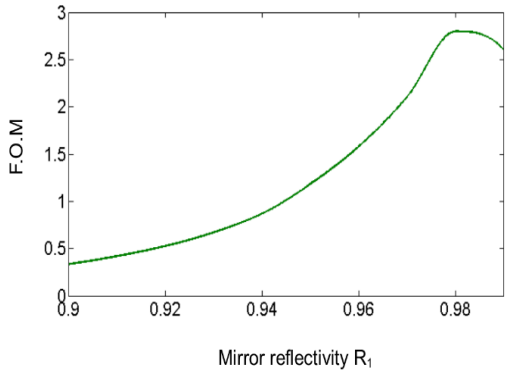

Figure 8-19 Variation in F.O.M when the variation in noise with DC level is non-linear

Figure 8-19 shows the F.O.M when the noise varies non-linearly with visibility. As R_1 increases the F.O.M increases to a maximum of R_1=97.8%. Therefore the optimum mirror reflectivity is R_1=97.8% when R_2=98%. This is similar to the case for when the noise varied linearly with the visibility. The optimum mirror reflectivities can be found by varying both R_1 and R_2 for various beam radii.

8.3.4 Choosing the optimum mirror reflectivities

Section 8.3 has shown the choice of optimum mirror reflectivities and how they change for various parameters, such as beam radius, applying an aperture on the reflected beam as well as a non-linear variation in the noise with reflected power. The choice of optimum reflectivity is dependent on beam radius, where the optical sensitivity for all mirror reflectivities increase with beam radius. At small beam radii the optimum mirror reflectivities are 98% while for large beam radii the mirror reflectivities can be greater than 98%. The difference in the maximum optical sensitivity is a factor of 15. If the choice of optimum mirror reflectivities is based on F.O.M then for a 10 μm beam radius the optimum mirror reflectivities are 95%, while for larger beam radii it is in the region of 97% to 98%. These choice of optimum mirror reflectivities are also affected by aperturing the beam. The optical sensitivity provided by aperturing the beam is greater than when the beam is unapertured, as was shown in section 8.2. It was shown for R_2 held at 98% that R_1 has to be 95% to obtain the highest optical sensitivity for a disc based aperture. The choice of optimum R_1 for R_2 at 98% based on F.O.M is in the region of 90% to 91%. Therefore the various parameters chosen such as beam radius and various setups implemented such as disc aperturing will have an effect on the optical sensitivity as well as the choice of mirror reflectivities.

8.4 Designing optimum FPI sensors

To design optimised FPI sensors, the various design considerations presented in this chapter thus far need to be given in context. It was shown in section 8.1.2 how to choose the optimum beam radius for a FPI with specific mirror reflectivities and cavity thickness. The choice of mirror reflectivities when considering different beam radii and different types of aperturing was presented in section 8.3. This section combines the individual design considerations, such that the sensor can be optimised.

8.4.1 Designing FPI sensors for various applications

8.4.1.1 *FPI sensor with highest optical sensitivity*

To design a FPI with the highest optical sensitivity, with no restrictions on the beam radius or cavity spacing is a simple case. The beam radius can be as large as possible so that it can approximate to a non-diverging beam. The mirror reflectivities can then be increased to obtain the highest possible optical sensitivity, similar to the case of a non-diverging beam. The optical sensitivity that can be achieved is greater than 45 nm^{-1}. These parameters can be chosen assuming that the FPI is planar, whereas in reality there will be some non-uniformities in the cavity spacing, as was shown in chapter 6, section 6.6 for FPI sensors. For the beam radii used in typical PA imaging which are in the range of 10 μm to 40 μm, the non-uniformities determined experimentally would not affect the optical sensitivity, however increasing the beam radius and mirror reflectivities the limiting factor to optical sensitivity is the surface non-uniformity. This is discussed in subsection 8.4.2.

8.4.1.2 *Combination of optical and acoustic sensitivity*

If a FPI sensor requires acoustic properties such as high directivity and wide acoustic bandwidth, then requirements will have to be placed on the cavity thickness and beam radius. The choice of optimum beam radius is dependent on the expression in Eqn. 8.6 for a specific cavity thickness and mirror reflectivity. If the cavity spacing of the FPI was 40 μm then reducing the cavity spacing is beneficial in having a uniform frequency response at higher frequencies of (~100 MHz).

Defining the acoustic sensitivity as,

$$S_A = \frac{dl}{dp} = \frac{l}{E} \qquad 8.9$$

where *l* is the cavity spacing and E is the Young's modulus. Therefore in going from a cavity spacing of 40 μm to that of 10 μm would reduce the acoustic sensitivity by 75%. The gain in the optical sensitivity for specific mirror reflectivities and beam radius must increase by 75%. Reducing cavity thickness would also lead to the beam propagation being reduced hence reducing the divergent effect of the beam as the distance travelled on each round trip is less. For a FPI with mirror reflectivities of 95% and beam radius of 10 μm, in going from a 40 μm cavity spacer to a 10 μm cavity spacer the optical sensitivity decreases by 49%. When the mirror reflectivities are 98% the optical sensitivity decreases by 34%. The reduction in optical sensitivity is less for higher mirror reflectivities. The cavity thickness decreases both optical sensitivity and acoustic sensitivity such that the overall sensitivity decreases. The drop in optical sensitivity in going from a 40 μm to a 10 μm cavity spacer is because the phase accumulation per round transit is lower by 75%. Therefore the periodicity of the electric field magnitude as a function of wavelength per round transit is reduced. This is equivalent to low finesse FPI sensors. If a FPI sensor with a thin cavity spacing (l<10 μm) is required for a large acoustic bandwidth, then to obtain high optical sensitivity the beam radius has to be slightly larger than the optimum beam radius for mirror reflectivities of 98%. The beam radius required to interrogate the FPI sensor would be 40 μm giving an optical sensitivity of 3.5 nm^{-1}, and an acoustic sensitivity of 3.44 μm per GPa. If however the cavity spacing was 40 μm with an interrogation beam radius of 40 μm then the optical sensitivity would be 11.7413 nm^{-1} with an acoustic sensitivity of 13.7931 μm per GPa. Therefore the advantage of reducing the cavity spacing to increase the bandwidth is at the expense of the sensitivity, which is reduced by a factor of ~14 in going from a cavity spacing of 40 μm to 10 μm.

8.4.1.3 *Fibre optic hydrophone FPI sensors*

Subsection 8.2.1 showed the effect on optical sensitivity when the reflected beam is apertured. A particular example of where the reflected beam from the FPI is apertured is a fibre optic hydrophone (F.O.H). This is where the FPI sensor is deposited on the tip of an optical fibre. The reflected beam from the FPI is apertured with a known disc radius of 5 µm which is the radius of the fibre core (for a single mode fibre). Therefore optimising the design of the FPI sensor for fibre optic hydrophones is discussed in this subsection. Currently the cavity spacing is set at 10 µm to achieve a large acoustic bandwidth. The beam radius is fixed at 5 µm due to the radius of the fibre core.

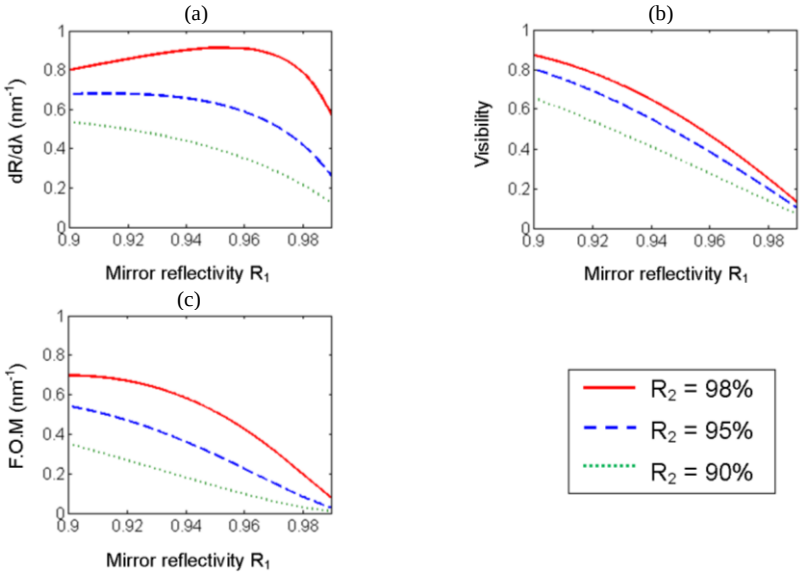

Figure 8-20 (a) dR/dλ, (b) visibility and (c) F.O.M as R_1 is varied for various R_2 values for a FPI with 10 µm cavity thickness with a 5 µm beam radius incident apertured with a 5 µm disc

Figure 8-20(a) shows the optical sensitivity as R_1 and R_2 is varied for a fibre optic hydrophone. The optimum mirror reflectivities are R_1 = 97% and R_2 = 98%. However if the F.O.M is used, the optimum mirror reflectivities are then R_1 = 90% while R_2 = 98% as shown in Figure 8-20(c). This is because of the reduced visibility at higher mirror reflectivities. The effect of the spatial filtering increases the optical sensitivity at the sharper slope of the ITF_λ reflectivity peak but also increases the asymmetry. At the shallow slope of the reflectivity peak the optical sensitivity is less but has the potential to have greater pressure linearity. This is studied in more depth in section 8.5.

8.4.1.4 *Designing FPI sensors for fibre coupled experimental systems*

A disc based aperture was considered in section 8.2 to improve optical sensitivity. In PA imaging setups the reflected light from the FPI sensor is coupled back into the single mode fibre used to deliver the interrogation source. The reflected light is separated from the incident light by an optical fibre circulator. To model this type of system, the reflected light in the model is apertured by considering a Gaussian amplitude weighting. The reflected light from the etalon is coupled back such that 80% of the incident power is received.

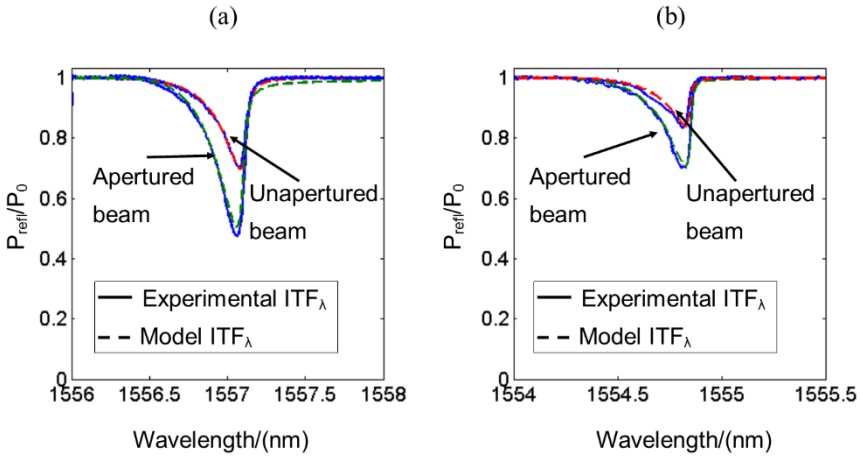

Figure 8-21 Experimental ITF_λs for an apertured and an unapertured beam for a beam radius of 17 µm incident on a etalon with (a) R=95% and (b) R=98%

Figure 8-21(a) presents ITF_λs between an unapertured and a fibre coupled aperture for an incident beam radius of 17 µm and FPI with mirror reflectivities of 95% and cavity thickness of 190 µm. For a unapertured ITF_λ the visibility is low and asymmetric, while the apertured ITF_λ has greater visibility and an altered shape. There is good agreement between model and experiment. To get a good fit between the experimental and modelled ITF_λ when the beam is fibre coupled involved offsetting the etalon from the focus by z = -175 ± 10 µm in the model. The Rayleigh range of the beam radius is 605 µm, therefore the offset is within the Rayleigh range. The shape of the modelled ITF_λs beyond the offset in the model do not give a good fit with the experiment. A reason for this is that when the etalon is adjusted along the optic axis to be in the focus, the highest detected intensity is achieved when the etalon is off-focus and close to the lens. This is because the light reflected of the first mirror of the etalon and from the etalon cavity are focussed by the various optical components to couple back into the fibre. As a consequence, the highest amount of light is detected when the focus of the beam is in the etalon cavity. Figure 8-21(b) shows the ITF_λs for an etalon with mirror reflectivities of 98%. For the fibre based aperture the etalon was set to the focus to give the best fit to the

experiment. It was found that that offsetting the FPI by z= -50 µm did not produce any considerable change in the ITF_λ. This is because the percentage of light entering into the etalon cavity and being reflected back to the fibre does not have a strong interference with the light reflected of the first mirror of the etalon. The first mirror of the etalon can be approximated to be close to a perfectly reflecting mirror. Further studies of the effect of fibre coupling in regards to the positioning of the FPI along the optic axis needs to be investigated. This can then be used to feedback into the design of FPI sensors. Therefore when designing optimal FPI sensors one must also consider the experimental arrangement and the effect it will have on the ITF_λs based on the aperturing and focussing effects. This will also have an effect on the choice of optimum mirror reflectivities.

8.4.2 Effect of surface non-uniformity on optical sensitivity for FPI sensors

The design of FPI sensors has so far considered beam radii encountered in optical FPI sensors employed for PA imaging. The typical beam radii used in experimental arrangements range from 10 µm to 40 µm, and cavity thicknesses of 10 µm to 50 µm. Figure 8-22 shows the variation in the optical sensitivity (dR/dλ) with beam radius for wedged FPIs.

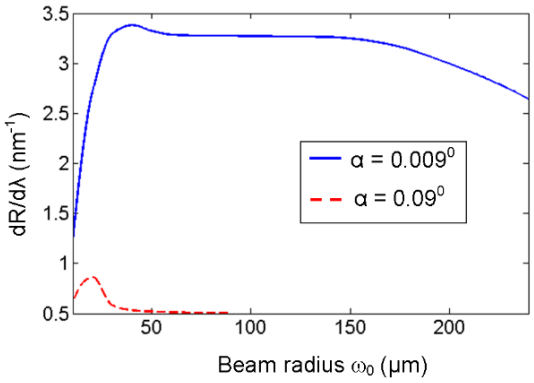

Figure 8-22 dR/dλ variation with beam radius for wedged FPIs with a wedge angle of 0.009^0 and 0.09^0

For a wedge angle of 0.009^0 the optical sensitivity increases to a maximum at a beam radius of 40 µm. Further increases in the beam radius result in a gradual decrease in the optical sensitivity. As the wedge angle increases to 0.09^0 the overall optical sensitivity decreases, with a reduction in optical sensitivity of almost a factor of 3. The optimum beam radius is 20 µm when the wedge angle is 0.09^0. In the design consideration the FPI has been assumed as perfectly planar, as the variation in cavity thickness is nanometres over an area of millimetres. Therefore for the beam radii used in PA imaging, the effect of surface non-uniformity is negligible. For extremely large beam radii, such as 200 µm or greater the effect of the experimentally determined wedge angles along with high mirror reflectivities could be considerably detrimental to the optical sensitivity.

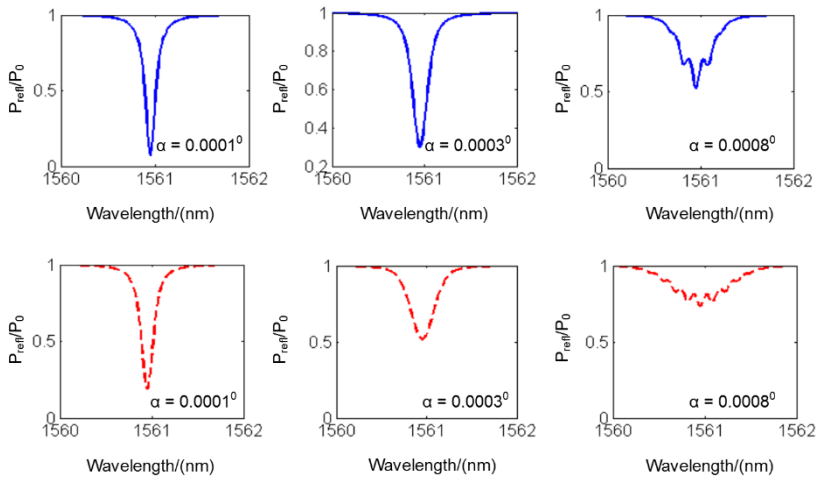

Figure 8-23 ITF$_\lambda$s for a FPI with R=98% and *l* = 40 µm with various wedge angles, for incident beam radius ω_0 of 500 µm in solid blue and 1000 µm in dashed red

Figure 8-23 shows ITF$_\lambda$s for two different beam radii of 500 µm (solid blue) and 1000 µm (dashed red) for a FPI with mirror reflectivities of 98%, cavity spacing of 40 µm and wedge angles which are similar to those determined experimentally. A maximum beam radius of 1000 µm was considered, as an increase in the beam radius beyond this would mean that the approximation of the surface non-uniformity as a wedge would no longer apply. This is because the variation in the wedge angle is linear over the scale of millimetres. Figure 8-23 shows that as wedge angle increases the ITF$_\lambda$s becomes broader, along with the appearance of sub resonant behaviour at large wedge angles. The ITF$_\lambda$ for the beam radius of 500 µm does not vary for small wedge angles.

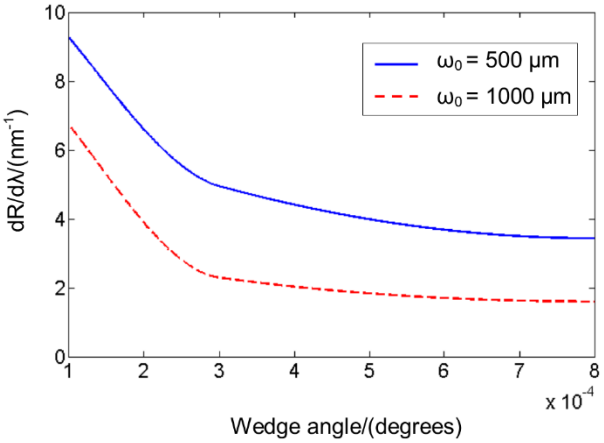

Figure 8-24 dR/dλ variation with wedge angle for beam radii of 500 µm and 1000 µm for a FPI with R=98% and cavity thickness of 40 µm

Figure 8-24 shows the variation in the optical sensitivity as the wedge angle varies for the ITF$_\lambda$s presented in Figure 8-23. The optical sensitivity decreases with wedge angle for both beam radii. The optical sensitivity is overall higher for the 500 µm beam radius compared to that for the 1000 µm beam radius. This suggests that using a beam radius that is 500 µm or less will give higher optical sensitivity for average non-uniformities that are typical of those found in FPI sensors with high mirror reflectivities.

8.5 Pressure linearity of FPI sensors

Certain applications require a large pressure range to be measured, this requires an understanding of how pressure linearity is related to the slope of the ITF_λ. This section presents how the pressure linearity is calculated and how one can increase the linearity. Higher pressure linearity is required in ultrasound metrology and medical applications such as high frequency ultrasound (HIFU) for monitoring the ultrasound dose delivered to patients in clinical scenarios.

8.5.1 Calculating the maximum linear pressure amplitude

Another practical design consideration of the FPI sensor is to increase the pressure range over which the change in the reflected light detected dR is linear with the change in pressure d*p*. For a specific optical sensitivity dR/d*l*, the linear range is where the change in the optical sensitivity falls to 90% of the maximum. The choice of 90% is arbitrary, and can be lower or higher than this, although the magnitude of the reflected light R should be linear with the change in the pressure amplitude *p*. The expression for obtaining the pressure range d*p* in which the change in reflected light R is linear is obtained from the acoustic sensitivity expression,

$$A_s = \frac{dl}{dp} = \frac{l}{E}$$
$$dp = \frac{Edl}{2} \qquad 8.10$$

where E is the Young's modulus of the material forming the cavity spacing, *l* is the cavity thickness and d*p* is the peak to peak linear amplitude pressure range. The factor of 1/2 arises so that the pressure range is only taken for the peak pressure range and not the peak to peak. The pressure amplitude d*p* increases with increasing d*l* for a specific Young's modulus E, and cavity thickness *l*, as expressed in Eqn. 8.10.

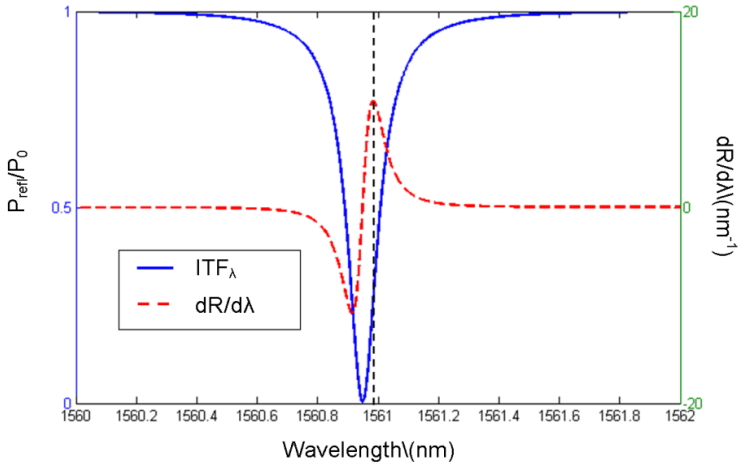

Figure 8-25 ITF$_\lambda$ for a 100 µm beam radius with mirror reflectivities of R=98%, and dR/dλ, for a cavity thickness of 40 µm

Figure 8-25 shows the ITF$_\lambda$ for a 100 µm beam radius with mirror reflectivities of R=98%, and refractive index n=1.639. The wavelengths corresponding to the maximum and minimum derivatives are 1560.987 nm and 1560.891 nm respectively. The corresponding ITF$_l$ in *l*-space is shown in Figure 8-26, which is a close up of the region where the minimum of dR/d*l* occurs. The sampling interval for d*l* was 0.0001 µm. The maximum of dR/d*l* occurs when the cavity spacing is 40 µm.

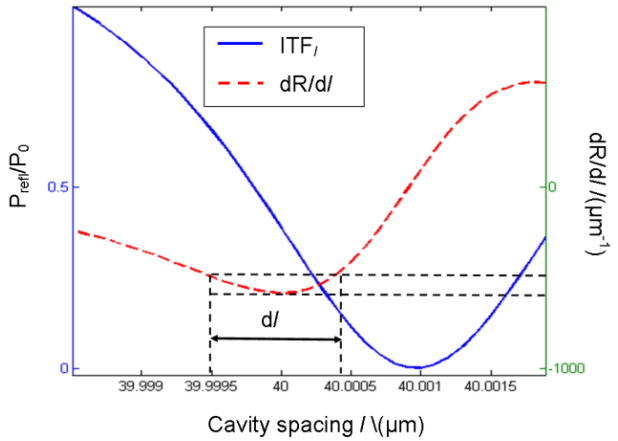

Figure 8-26 ITF$_l$ and dR/d*l* for a 100 µm beam radius and mirror reflectivities of R=98%, at a wavelength of 1560.987 nm

The maximum sensitivity dR/d*l* is 398.91 µm^{-1}, the 90% value of this maximum is 359.159 µm^{-1}. The range d*l* as shown in shown in Figure 8-27 corresponds to the peak to peak range over which the reflected light R is linear with *l* the cavity spacing.

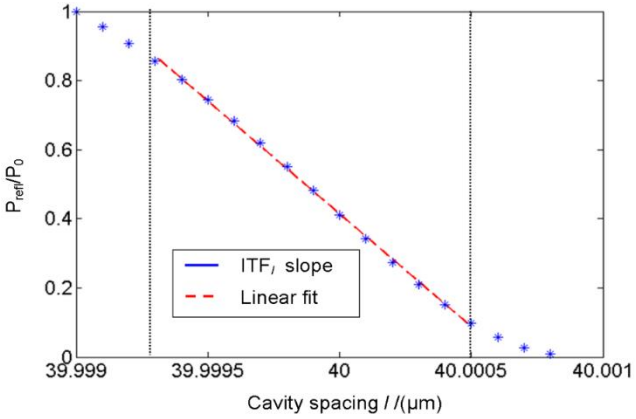

Figure 8-27 Linear fit to the ITF$_l$ slope around the maximum of the slope for wavelength λ = 1560.987 nm, and mirror reflectivities of R=98% with a beam radius of 100 μm

Figure 8-27 shows a linear fit to the slope of the ITF$_l$ for a 100 μm beam radius, and mirror reflectivities of R=98%. Taking dl as 0.0012 μm, the cavity thickness l as 40 μm, and the Young's modulus E as 2.9 GPa, and using Eqn. 8.10, the maximum pressure amplitude is 43.5 kPa.

8.5.2 Pressure linearity in asymmetric ITF$_\lambda$s

For an ITF$_l$ with a sharp slope hence large optical sensitivity, the maximum pressure amplitude will be small. To increase the maximum pressure amplitude, a larger linear range dl is needed. A possible way of achieving this is to induce asymmetry in the ITF$_l$, by illuminating the FPI with a highly divergent beam. The disadvantage in this method, is that the optical sensitivity is reduced. The asymmetry can be increased further by spatially filtering the reflected beam with a disc based aperture. This results in a larger pressure range that can be detected as well as slightly increased optical sensitivity.

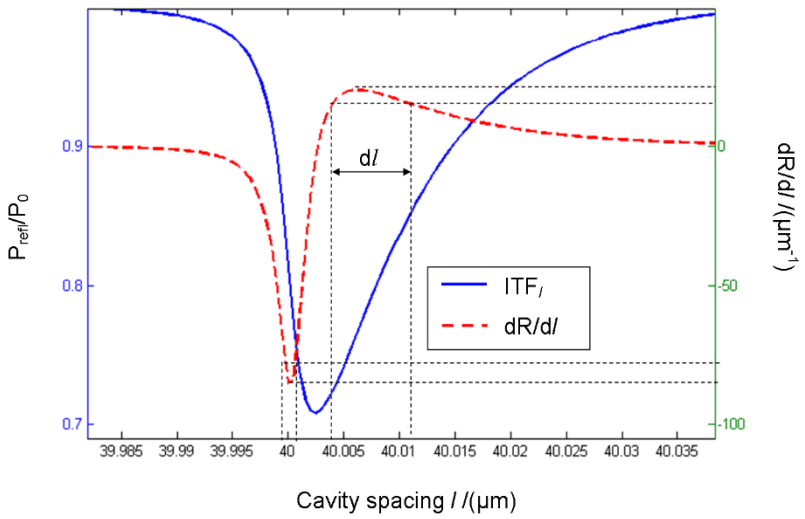

Figure 8-28 ITF$_l$ in *l*-space for a FPI with R=98%, and incident beam radius of 10 μm, at a wavelength of 1560.957 nm

Figure 8-28 shows the ITF$_l$ at bias wavelength of 1560.97 nm, for a FPI with R=98%, and cavity thickness of 40 μm with an incident beam radius of 10 μm. The linear range dl over which the optical sensitivity has fallen to 90% of the minimum is much greater, due to the shallower slope, particularly at longer cavity thicknesses where the slope of the reflectivity peak is shallower.

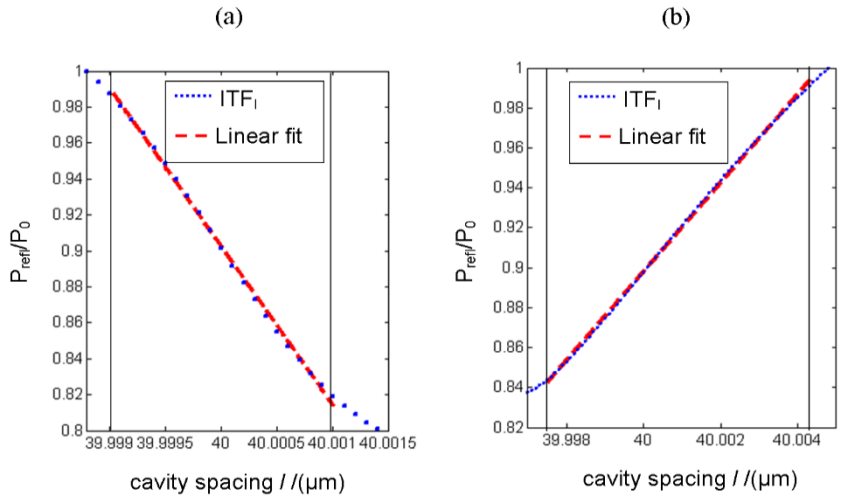

Figure 8-29 Linear fit to the slope of ITF$_l$ around the maximum of the gradient for the two bias wavelengths of (a)1560.957 nm and (b)1560.69 nm for a FPI with R=98%, and beam radius of 10 um

Figure 8-29 show a linear fit to the slope for the ITF$_l$ in Figure 8-28, for the two bias wavelengths of 1560.957 nm and 1560.78 nm, which correspond to the maximum and minimum of dR/dλ. The shorter wavelength shifts the ITF$_l$ such that maximum derivate dR/dl corresponds to l = 40 μm. Taking E=2.9 GPa, l = 40 μm and the linear range dl as 0.002 μm for λ = 1560.975 nm and 0.0062 μm at λ = 1560.78 nm, the maximum pressure amplitudes dp at both wavelengths are 72.5 kPa and 224.75 kPa respectively. An increase in pressure linearity of 150 kPa is achievable. This shows the asymmetric ITF$_l$ can be beneficial in obtaining higher maximum pressure amplitudes, if the optical sensitivity is not a major concern. However if optical sensitivity along with the minimum detectable pressure – NEP is a consideration, then a solution is to spatially filter the reflected beam, to increase the asymmetry. The optical sensitivity is higher than when the beam is unapertured. The visibility also increases such that the effect of the intensity noise and shot noise reduces.

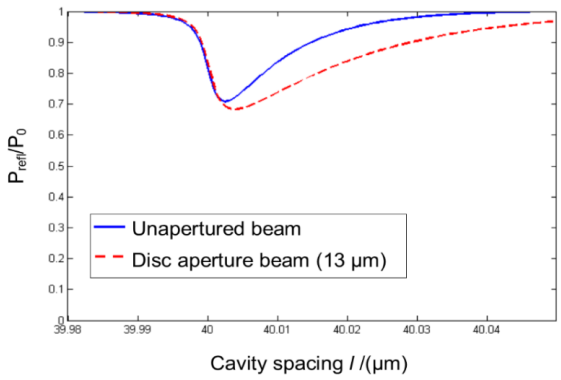

Figure 8-30 Graph of ITF$_l$s for a FPI with R=98%, and cavity thickness of 40 μm, with an incident beam radius of 10 μm, at a wavelength of 1560.957 nm for a apertured and unapertured beam

Figure 8-30 shows the ITF_ls for a unapertured beam and an apertured beam consisting of a 13 µm disc. The apertured beam has greater asymmetry, but increased optical sensitivity on the sharper slope. At shallow slopes the unapertured beam has the greatest optical sensitivity, compared to the apertured beam. The wavelength corresponding to the bias at short wavelengths in the reflectivity peak of the wavelength ITF_λ is 1560.58 nm for the apertured beam, and 1560.69 nm for the unapertured beam. The linear region d*l* is calculated as 0.0092 µm for the apertured beam. As shown in Figure 8-29(b) the maximum linear pressure amplitude was 224.75 kPa for the unapertured beam. The maximum pressure amplitude for an apertured beam is 333.5 kPa. This shows an increase of over a 100 kPa when spatially filtered.

8.5.3 Designing FPIs with high pressure linearity

Section 8.5 has shown the how the pressure linearity can be calculated, and the usefulness of asymmetric ITF_λs in increasing the maximum pressure amplitude that can be measured, although there is a trade-off with optical sensitivity. This can be slightly overcome with spatial filtering. Therefore, if one designs a FPI sensor which is highly sensitive for specific optical parameters, then if the beam is made more divergent and spatially filtered, it can increase the maximum pressure amplitude it detects. This shows the dynamic applications of FPI sensors, where one can achieve high sensitivity but can also increase the pressure amplitude it detects. For the same FPI sensor illuminating with a larger beam radii improves the optical sensitivity when the pressure linearity is not a consideration.

8.5.4 Relating linearity of d*l* to dλ

Equation 8.10 which expressed d*p* in terms of d*l* can appropriately be described in terms of the wavelength range dλ. Taking the constant *s*' as,

$$s' = \frac{d\lambda}{dl} \tag{8.11}$$

and rearranging in terms of dλ, and equating it into Eqn. 8.10, leads to the expression for d*p* as,

$$dp = \frac{Ed\lambda}{2ls'} \tag{8.12}$$

This shows that as the wavelength range dλ increases the pressure range increases, due to the proportional relationship. The constant s' is also present in Eqn. 8.12 due to the conversion from d*l* to dλ. Therefore for wavelength ITF$_\lambda$s being used to design practical FPI sensors, the wavelength range dλ can be used to calculate pressure linearity without the need for simulating cavity thickness ITF$_l$s.

8.6 Developing the model as a design software tool

The model presented in Chapter 4 and used in modelling the FPI sensor has been experimentally validated. It has shown the optical sensitivity for various optical parameters, such as mirror reflectivities and beam radii. This has shown it to be a predictive tool in designing planar FPI sensors used in photoacoustics for ultrasound detection, but can also have a use where the FPI is used in other applications, such as spectral filters and in laser line width control.

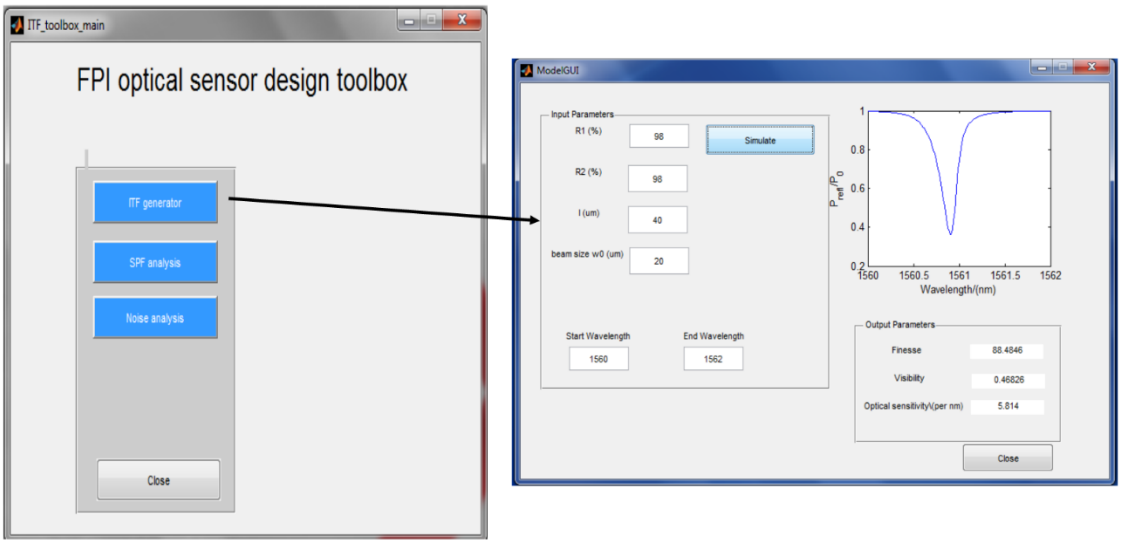

Figure 8-31 Screenshot of User Interface (UI) for FPI sensor software

Figure 8-31 shows screenshots of a software created for designing FPI sensors. The model is coded in Matlab, and the software can be run as a standalone package using Matlab Compiler Runtime (MCX). The main panel is shown in the left of the figure, with various options to call a sub routine that opens another panel. An option is to generate an ITF_λ for a given set of parameters such as mirror reflectivity, cavity thickness, beam radius and wavelength range. This in turn generates a plot of the ITF_λ and returns the value of finesse, visibility and the optical sensitivity. These values are also written to a data file (.dat) in the folder directory where the software files are located. Other options on the main panel are the analysis of the optical sensitivity, finesse, visibility and asymmetry for a spatially filtered beam, where the user can choose the type of spatial filter such as a disc based aperture or ring based aperture. The other option is to choose the optimum mirror reflectivities based on the noise variation with the visibility. Although the initial deployment of the software only considers a Gaussian beam, further developments in the model to propagate Gaussian beams of higher order

modes, or non-Gaussian beams can be incorporated to improve the use and application of the software package.

8.7 Design summary

A performance indicator of FPI sensors is its optical sensitivity. This chapter has presented how to choose optical parameters to optimise the FPI sensors. This was done by showing the effect of beam radius on the finesse, visibility and optical sensitivity for FPIs with various mirror reflectivities. Also described was how to obtain higher optical sensitivities with highly divergent beam radii by aperturing the detected beam, as well as discussing the trade-offs such as the loss of power. This was followed by a discussion on the choice of mirror reflectivities to obtain high optical sensitivity, as well as incorporating the effects of uncertainties in mirror reflectivities and the noise performance. Various FPI sensor examples were considered to show how to optimally design FPI sensors for certain cases. Section 8.5 described the effect of the slope on the pressure linearity, and it was found that an asymmetric ITF_λ, with the beam being apertured by a disc to increase asymmetry gives the highest pressure amplitude that can be detected. The disadvantage of obtaining high pressure linearity is the reduction in optical sensitivity. The optical sensitivity decreases by 75%, from using a beam radius of 50 μm to a 10 μm beam radius for a FPI with R=98%. The visibility also decreases, leading to the noise being affected by the intensity and shot noise, while the effect of the phase noise is less as the slope of the ITF_λ is shallower. The maximum pressure linearity that can be achieved is a useful measure of the performance of the FPI sensor along with the optical sensitivity.

Chapter 9 Modelling alternative Fabry Perot type resonators

The aim of this chapter was to model and design alternative FPI sensors for ultrasound detection. This is based on the understanding of the characteristics of Gaussian beam behaviour in a planar and wedged FPI, and the effect it has on the ITF_λ shapes. This helped in the design of planar FPI sensors by choosing the optimum beam radius and mirror reflectivities to attain the highest performance of the FPI sensor. This chapter applies the understanding of the effects of Gaussian beams in Fabry Perot Interferometers to alternative forms of FPI type resonators. The two types of Fabry Perot Interferometers considered are a FPI at the tip of a fibre GRIN (graded index) lens, and a FPI with a hemi-spherical geometry.

9.1 FPIs at the tip of fibre GRIN lenses

The FPI at the tip of fibre GRIN lenses is presented in this section. It has a potential use in photoacoustic imaging, where the excitation light can be focussed to a certain spot size and focal length. This is particularly useful in optical resolution photoacoustic microscopy (OR-PAM), where the excitation light is focussed into the tissue to target specific chromophores. However the interrogation beam delivered through the same fibre and focussed by the GRIN lens would result in the beam being off-focus when incident with the first mirror. This could affect the shape of the ITF_λ. An understanding of the phase characteristics when the beam is incident on the FPI off-focus helps in the tolerance and design of the GRIN lens with a FPI to achieve high optical sensitivity. Figure 9-1 shows a diagram of a setup of a FPI at the tip of a GRIN lens on a fibre.

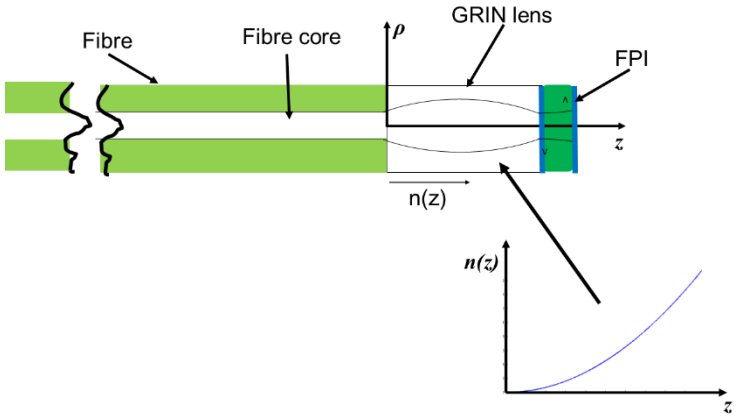

Figure 9-1 Diagram of a GRIN lens at the tip of a fibre with a FPI deposited at the distal end of the lens

To understand how the FPI being off focus will affect the ITF_λ, it is useful to consider the effect of various phase components of Gaussian beams as the beam propagates in the FPI.

9.1.1 Phase analysis of Gaussian beams along the optic axis

This section presents how the phase and wavelength ITF_λ vary as the FPI is moved along the optic axis, to understand the effect of fibre GRIN lenses. The Gouy phase as it propagates along the optic axis, shows that at a certain distance the magnitude of the Gouy phase is constant, as shown in Figure 9-2 for a 10 µm beam radius.

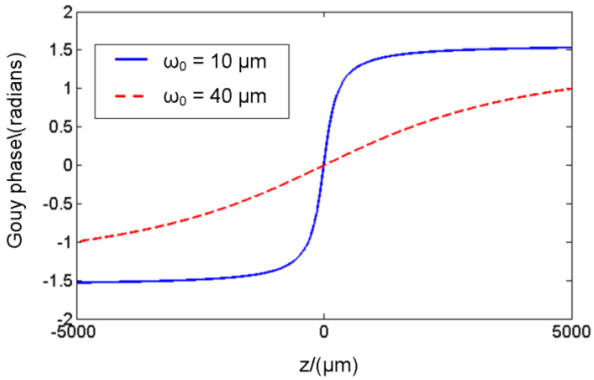

Figure 9-2 Graph of Gouy phase variation vs. distance propagated z, for a 10 µm and 40 µm beam radius

For a larger beam radius of 40 µm, the distance at which the magnitude of the Gouy phase is constant with z, is much larger. This is because of the larger Rayleigh range z_0 and the lower divergence. The Gouy phase is defined as,

$$\Theta = \tan^{-1}\left(\frac{z}{z_0}\right) \qquad 9.1$$

The Gouy phase is negative when the beam propagates towards the beam waist (negative z), and positive as it propagates away from the beam waist (positive z). Therefore if one puts the FPI at a point far in the negative z, such that the beam is being focussed towards the beam waist, then the Gouy phase would act as a constant phase shift, rather than one which evolves with distance to create an asymmetric reflectivity peak. The effect of constant Gouy phase is also true when the FPI is at a point in the far field, for when the beam is diverging away from the beam waist. The effect of the phase contribution due to the radial phase divergence must also be considered.

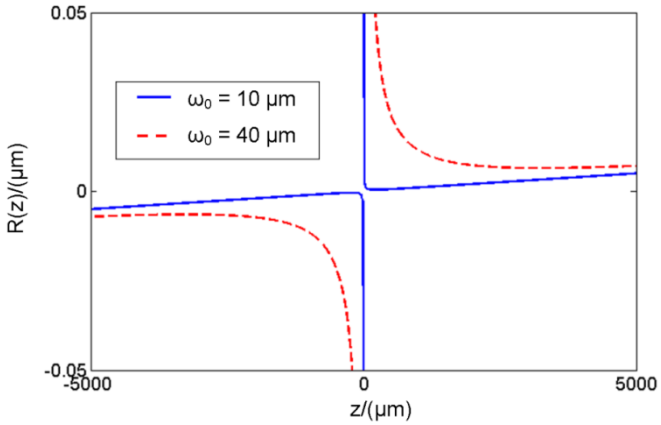

Figure 9-3 Radius of curvature of the wave front along the optic axis for a beam radius of 10 μm and 40 μm

Figure 9-3 presents the variation in the radius of curvature of the wave front along the optic axis. The radius of curvature R(z) is a function of z and z_0, and defined as

$$R(z) = z(1 + \frac{{z_0}^2}{z^2}) \qquad 9.2$$

The radius of curvature R(z) tends to infinity close to the focus at $z = 0$, and decreases to a minimum at the Rayleigh range ($z = z_0$). The radius of curvature increases in a linear fashion away from the beam waist for the 10 μm beam waist, as shown in Figure 9-3. The radius of

curvature for the 40 μm beam waist starts increasing linearly at a greater distance because of the larger Rayleigh range. When the FPI is placed at a point in the far field at negative *z*, the radial phase component is now negative and the Gouy phase will be positive. This will create asymmetry in the negative *z* for ITF$_\lambda$s at a radii ρ due to the non-constant radial phase.

9.1.2 Model and experimental arrangement of FPIs being off focus

9.1.2.1 *Model setup for an off-focus FPI*

This section presents the setup of a model for comparing the effects of an off-focus FPI with those in the experiments. The model was setup by adjusting the Gouy phase and radius of curvature phase expression in the model by inserting an offset distance z_{offset}. The field reflected of the first mirror of the FPI was defined as,

$$E_f = r_1 \frac{\omega_0}{\omega(z_{offset})} e^{-\frac{\rho^2}{{\omega_0}^2}} E_0 \tag{9.3}$$

where the ratio of the beam waist ω_0, to the beam radius at z_{offset}, $\omega(z_{offset})$ will reduce the incident amplitude of the beam at the first mirror of the FPI, compared to when the beam waist is incident on the FPI. The Gouy phase as the beam propagates on each round trip in the FPI is expressed as,

$$\Theta_m = tan^{-1}\left(\frac{z_{offset} + 2ml}{z_0}\right) \tag{9.4}$$

and the radius of curvature on each round trip is expressed as,

$$R_m(z_m) = z_m\left(1 + \frac{{z_0}^2}{{z_m}^2}\right) \tag{9.5}$$

$$z_m = 2ml + z_{offset}$$

where z_m is the point at which the electric field of the beam is sampled along the optic axis. These phase terms are inserted into the model setup in Chapter 4 for a planar FPI for when it is offset from the beam waist. The effect of the phase terms of a Gaussian beam would be to alter the shape of the ITF_λ, due to the way the phase terms vary at different positions along the optic axis.

9.1.2.2 *Experimental arrangement for off-focus FPI*

The experimental arrangement for investigating the ITF_λ along the optic axis used the same setup as that to experimentally validate the planar FPI model presented in Chapter 5, when the FPI is at the focus of the beam. The FPI is adjusted along the optic axis by a mechanical translation stage connected to the mount housing the Fabry Perot etalon. The Fabry Perot etalon with mirror reflectivities of R=98% was used, with a cavity thickness of 193 μm composed of fused silica (n=1.44). The reflected beam from the etalon was fibre coupled back into the same fibre used as the source for the incident beam. The fibre coupling efficiency was estimated to be 80%, which needed to be taken into account in the model by aperturing the beam such that around 80% of the incident power of the beam is taken into account.

9.1.3 Modelled and experimental results of off-focus FPIs

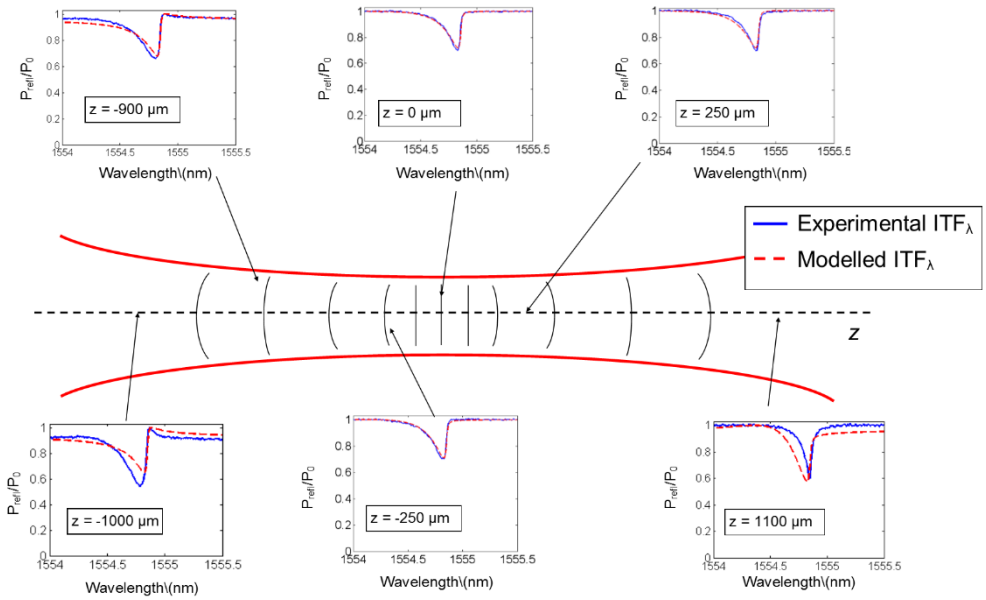

Figure 9-4 Plots of modelled and experimental ITF$_\lambda$ along the optic axis for a FPI with R=98% and cavity thickness of 193 µm, and an incident beam radius of 17 µm

Figure 9-4 shows wavelength ITF$_\lambda$s at various points along the optic axis in both the positive and negative positions from the beam waist for a beam radius of 17 µm, and a FPI with mirror reflectivities of R=98% and cavity thickness of 193 µm. The modelled and experimental ITF$_\lambda$ at the beam waist agree well. At positions less than ±900 µm, the fit between the experiment and model agree, although beyond that the fit agrees less well.

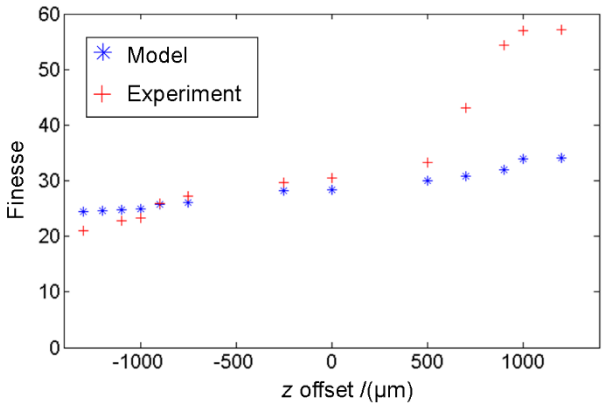

Figure 9-5 Comparison of finesse for experimental and modelled ITFλs when placing the FPI at various positions along the optic axis of the beam with beam waist of ω_0 = 17 µm

Figure 9-5 shows the comparison of finesse between the experiment and model, when the FPI is placed at various positions along the optic axis. The value of finesse between model and experiment follow the same trend at negative z position, of decreasing finesse from the beam waist. At negative z positions the reflectivity peak of the experimental ITF_λ becomes more asymmetric as the position increases away from the beam waist. This is because the beam is being focussed towards the beam waist. As the beam is being apertured, the beam radius on each round trip is getting smaller hence the radial phase component at the edges of the beam are moving into the detection region. The radial phase component is negative, hence acts the same as the Gouy phase to create asymmetry in the ITF_λ. In the positive z positions, the experimental finesse increases, as does the modelled finesse. The modelled finesse is lower than the experimental finesse. This is due to the reflectivity peak of the experimental ITF_λ becoming symmetric as shown in Figure 9-4. The Gouy phase starts to reach an asymptote to the value of $\pi/2$ at these distances. This suggests the beam has reached the far field and is similar to a non-diverging beam. This is suggests the model needs to be adjusted in the far field to replicate experimental ITF_λs.The Rayleigh range z_0 of the 17 µm beam radius is calculated as 585.17 µm, and where the cavity thickness is 193 µm. Also the phase contributions away from the centre of the beam are neglected due to the aperturing of the beam.

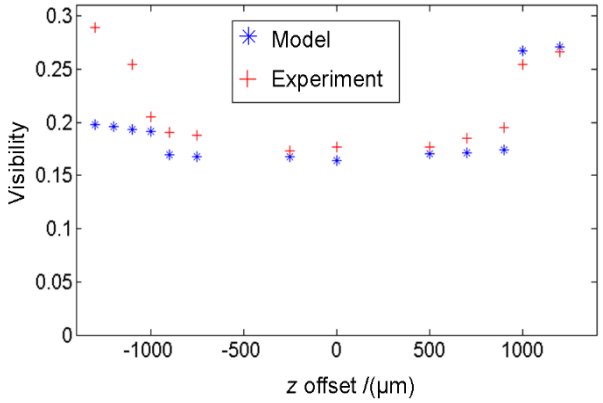

Figure 9-6 Comparison of visibility for experimental and modelled ITFλs when placing the FPI at various positions along the optic axis of the beam with beam waist of ω_0 = 17 µm

Figure 9-6 shows the visibility between experiment and model, when the FPI is placed at various positions along the optic axis. As the FPI moves from the negative z far field towards the focus, the modelled and experimental visibility decreases. The experimental and modelled visibility then increases again as the FPI moves away from the focus towards positive z positions. This is because of the ITF_λ becoming symmetric as the beam moves towards the far

field at positive z positions. The experimental visibility is much higher at the extreme far fields. This is probably due to an increase in the effective aperture inserted in the model to aperture the reflected beam. In addition the power of the beam incident on the etalon is very low, due to the Gaussian beam amplitude variation along the optic axis.

The general trend between the finesse and visibility is followed by both model and experiment. However to get a good fit between model and experiment, the offset entered in the model is altered from that measured experimentally. When the beam is being focussed towards the focal waist, the offset uncertainty in the model is greater by about 100 to 200 μm, and when the beam is propagating away from the focus the offset uncertainty in the model is slightly less by about 50 to 70 μm. This is possibly due to the small changes in the ITF_{λ} when the etalon is within the Rayleigh range of the beam. Another point to consider is that the aperturing of the beam is kept constant such that 80% of the incident beam is considered, whereas in practice the amount of power coupled back to the fibre may have a substantial change as the FPI is moved off-focus. An improvement to this experiment can be made by using a calibrated motorised translation stage with micrometre precision rather than a mechanical translation stage. A knowledge of the fibre coupling variation at various points off-focus can then be used to feedback into the model.

9.2 Hemi-spherical Fabry Perot Interferometer

9.2.1 Geometry of Fabry Perot Interferometer

This section describes the brief work undertaken on hemi-spherical type Fabry Perot resonators [98]. The geometry of these resonators is that one of the mirrors has a dome type structure, which is approximated as a hemi-spherical type resonator. The second mirror which is in a domed shape structure, acts like a lens to focus the light back to the first mirror. As a consequence it leads to high finesse cavities when small incident beam radii are used. The advantage of this type resonators is to confine the Gaussian beam divergence to overcome the limitations due to a planar FPI [99] [100]. For a FPI sensor, it can be used to utilise high optical sensitivities with small beam radii such as at the tip of optical fibres [41]. These kind of resonator structures can be created by high pressure injection of liquid polymers onto a substrate [101]. This allows a 2D array of hemi-spherical resonators to be manufactured.

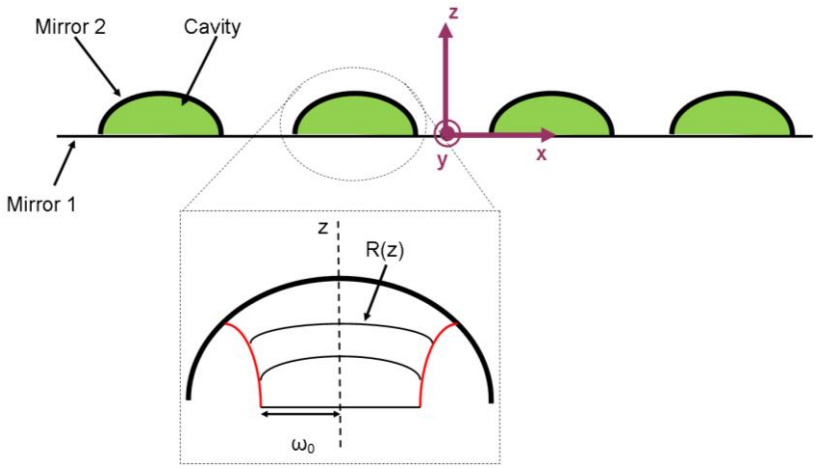

Figure 9-7 Diagram of array of hemi-spherical Fabry Perot resonators, with a blow up of a beam propagating towards mirror 2 in the resonator

Figure 9-7 shows an array of hemi-spherical Fabry Perot resonators, with an enlargement showing a wave front of the beam propagating in the resonator structure when the radius of curvature of the beam wave front matches that of the dome. The electric fields would be at normal incidence to the curve mirror and hence reflect back traversing the same path. The resonator structures are placed equally apart along the x and y directions, where y is going into the plane of the paper shown on the diagram. The curvature of the second mirror is spherical, and if it matches the curvature of wave front of the beam, then the electric fields traverse the same path back to mirror 1. This is the case for subsequent round trips, such that

the radial divergence of the beam is confined by the geometry of the resonator [102]. Figure 9-8 shows an image taken under a microscope of the Fabry Perot type resonators.

9.2.2 Calculation of optimum beam radius

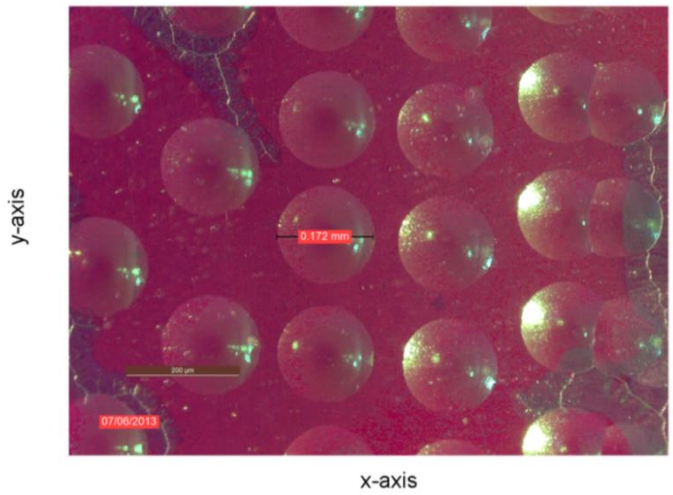

Figure 9-8 Array of high finesse domed hemi-spherical Fabry Perot Interferometers, with the picture taken under a microscope

Figure 9-8 shows an image taken under the microscope of the hemi-spherical FPI resonators by myself. The diameters of the domes are fairly uniform. Therefore knowing the diameter D of the dome and the height *h* at the centre of the dome, the radius of curvature R_d of the dome can be found. From this the optimum beam radius to interrogate the resonator can be calculated. The relationship between the radius of curvature of the dome R_d, and the radius *a* of the base of the dome and height *h* is expressed as,

$$R_d = \frac{h^2 + a^2}{2h} \tag{9.6}$$

Eqn. 9.6 is derived from the expression for the radius of curvature of a spherical cap. This is because the dome is being approximated as a spherical cap of a sphere. A full derivation of the expression is found in Appendix C. The minimum radius of curvature would be twice the Rayleigh range. This is because of the relationship of z with R, expressed in Eqn. 9.2. When $z = z_0$, the radius of curvature will be $2z_0$. The height of the dome would have to be the Rayleigh range z_0.

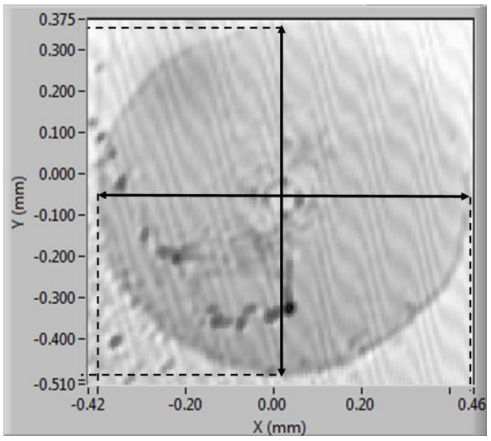

Figure 9-9 Reflected intensity of a domed FPI, as the beam is scanned in the x-y plane

Figure 9-9 shows a 2D scan in the x-y plane of a domed FPI resonator, with an incident beam radius ω_0 of 17 µm. The 2D scan is performed by scanning the beam across the plane of the FPI sensor, by use of the galvanometers. An area of 900 µm by 900 µm is scanned, where the spatial resolution is around 22 µm. The diameter of the dome is estimated to be 880 µm. The wavelength at each position is then varied over a set wavelength range, and the reflected intensity data recorded from which a wavelength ITF_λ is reconstructed. This helps in finding the location of the centre of the dome, as this is where the highest optical sensitivity is achieved. In the dome shown in Figure 9-9, this was found to be at positions x=+0.002 mm and y= -0.550 mm.

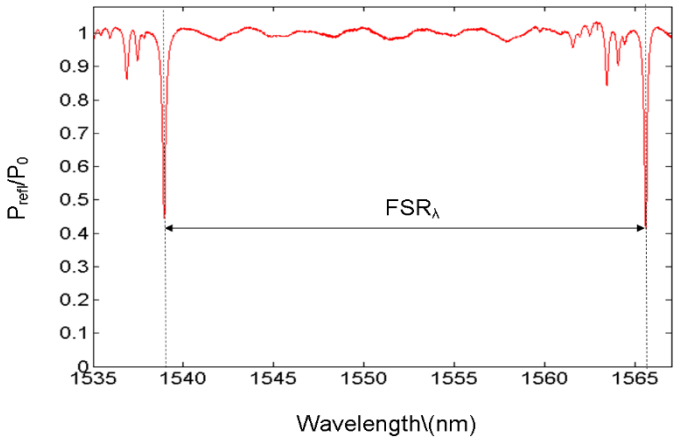

Figure 9-10 ITF_λ of a domed FPI for a beam radius of 17 µm

Figure 9-10 shows the ITF_λ for the dome shown in Figure 9-9. The Free Spectral Range FSR_λ is found by scanning across a wavelength range that encompasses two reflectivity peaks. The height of the dome *h* is found by rearranging the expression for the FSR_λ, in terms of *l*,

$$l = \frac{\lambda^2}{2nFSR_\lambda} \tag{9.7}$$

For the ITF_λ in Figure 9-10 the FSR_λ is 29 nm and the refractive index n is 1.5. The height of the dome *h* at the centre is calculated as 30.6 µm. The radius of curvature of the dome R_d can then be found by inserting the value of *h* and the dome radius *a*, which is 440 µm, into Eqn. 9.6. The value of the radius of curvature R_d is found to be 3178.69 µm. From the radius of curvature, the optimum beam radius to interrogate the Fabry Perot resonator can be found. Using the expression for radius of curvature in Eqn. 9.2,

$$R(h) = h(1 + \frac{{z_0}^2}{h^2}) \tag{9.8}$$

where *h* is the height of the dome, and substituting the expression for the Rayleigh range, expressed below into Eqn. 9.8,

$$z_0 = \frac{\pi {\omega_0}^2}{\lambda} \tag{9.9}$$

and rearranging Eqn. 9.8 in terms of the beam radius, leads to the expression for calculating the optimum beam radius,

$$\omega_0 = \sqrt[4]{\frac{\lambda^2}{\pi^2}(R_d h - h^2)} \tag{9.10}$$

For the radius of curvature found for the dome in Figure 9-9, along with the height *h* of the dome, the optimum beam radius was found to be 12 µm. Alternatively, the relationship between the radius of curvature and beam radius is expressed as,

$$R_d(h,\omega_0) = h + \frac{\pi^2 {\omega_0}^4}{\lambda^2 h} \qquad 9.11$$

The radius of curvature of the dome, for a specific height *h* increases as the fourth power of the beam radius ω_0. Conversely the beam radius required for a radius of curvature of the dome R_d, increases as the quadratic root of the radius of curvature.

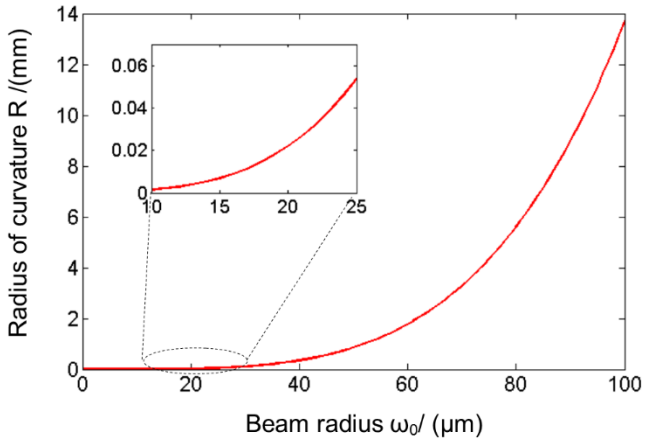

Figure 9-11 Radius of curvature R variation with beam radius ω_0, for a height *h* of 30.6 µm

Figure 9-11 shows the radius of curvature variation with beam radius ω_0, as expressed in Eqn. 9.11, for a specific dome height *h*. For large beam radii, the increase in the radius of curvature R is large for a small change $d\omega_0$ in the beam radius. At small beam radii, the increase in R is smaller. The derivative of Eqn. 9.11, with respect to the beam radius ω_0 is expressed as,

$$\frac{dR}{d\omega_0} = \frac{4\pi^2 {\omega_0}^3}{\lambda^2 h} \qquad 9.12$$

The change in radius of curvature dR per unit change in beam radius $d\omega_0$ has a dependence on ω_0^3. Figure 9-12 shows the variation in $dR/d\omega_0$ with beam radius ω_0. This is important in choosing the optimum beam radius that provides the smallest change in the radius of curvature of the wave front with a small change in beam radius ω_0.

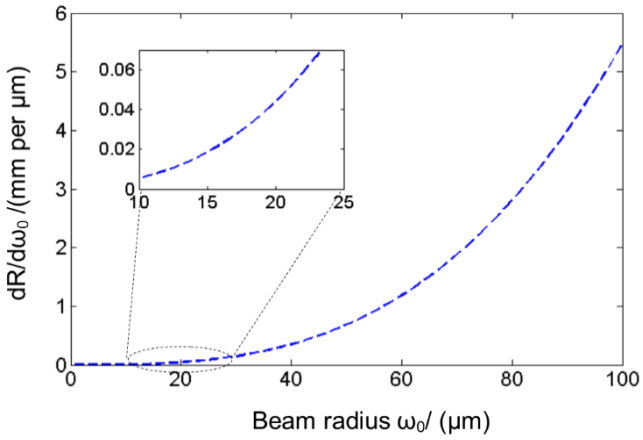

Figure 9-12 $dR/d\omega_0$ variation with beam radius ω_0, for a dome height of 30.6 μm

This analysis has shown that for small beam radii, the radius of curvature of the dome is small and that the variation in the radius of curvature with beam radius is also small, compared to that at large beam radii. This therefore shows that designing the Fabry Perot resonators to have a small radius of curvature is optimum, as a mismatch between the radius of curvature of the beam wave front R_w and the dome R_d, will be insignificant due to the approximately shallow increase in the radius of curvature with beam radius. At large beam radii, a small change in the beam radius causes the mismatch between R_w and R_d to be significant. This relationship of R as a function of ω_0 is indicative of the finesse variation with beam radius. The finesse is highest when R_w matches R_d. However at small beam radii, the finesse deviation will be small due to the shallow increase in the radius of curvature R with the beam radius ω_0. The optimum beam radius for a domed radius is expressed as,

$$\omega_{0_{opt}} = \sqrt[4]{\frac{\lambda^2}{\pi^2}(R_d h - h^2)} \qquad 9.13$$

Which is found by rearranging Eqn. 9.11. If the radius of curvature of the dome was much greater than the wave fronts of the beam, then the FPI can be approximated as a planar FPI.

Therefore the optimum beam radius expression reduces to the expression for that of a planar FPI,

$$\omega_{0_{opt}} = \sqrt{\frac{1}{20}\frac{2m_{max}l\lambda}{\pi}} \qquad 9.14$$

which arises because the radius of curvature parameter is neglected due to the approximation of the resonator as a planar FPI. Therefore the optimum beam radius is when the Rayleigh range is equivalent to a factor of the total distance propagated by the beam in the cavity. An analysis by Favero. F was undertaken for spherical and spheroidal FPI cavities on the tip of optical fibres [103], such a study with a Gaussian beams illuminating hemi-spherical cavities has not been undertaken.The analysis concentrated on the relation between the radius of curvature of the spheres to the optical sensitivity when the FPI undergoes a strain.

9.3 Future directions for modelling high finesse FPI type resonators

This chapter has shown the effect on the shape of the ITF_λ, when moving a high finesse FPI away from the focus of the beam, and how the asymmetry and visibility change when the FPI is moved along the optic axis of the beam. Also shown was an alternative Fabry Perot type resonator which had a domed shape geometry. The purpose of this was the ability to use small beam radii while retaining a high Q cavity by confining the beam divergence. Both of these FPI designs show promising application as optical sensors for detecting ultrasound, especially the domed resonator due to the geometry of the resonator acting as a lens to focus the light. A simple relationship between the radius of curvature and the beam radius was shown. It was found that the optimal radius of curvature corresponded to small beam radii. For extremely large radius of curvatures the optimum beam radius becomes that of a planar FPI. Although a study on how the shape of the ITF_λ, and the finesse variation with beam radius was not presented but can be inferred from the relationship between R and ω_0. A way to study this relationship explicitly is to use a ray tracing software package such as FRED (Photon Engineering) to setup a domed resonator cavity, and measuring how the reflected light varies as a function of wavelength to give the ITF_λ. From this the finesse variation with beam radius can also be attained. As a validation of the ray tracing software the ITF_λ output

from the software can be compared with the ITF_{λ} output from the Matlab model. If the ITF_{λ}s are the same, this would show that the ray tracing software is modelling the propagation and phase characteristics of a Gaussian beam in a planar and wedged FPI correctly. This also shows an additional tool provided by the planar FPI model, for the purpose as a validation tool for modelling more geometrically complex FPI structures.

Chapter 10 Conclusions

This chapter summarises and concludes the work undertaken in this thesis of modelling optical Fabry Perot Interferometer sensor in various configurations for ultrasound detection.

10.1 Achievements

This thesis set out to design FPI sensors for improved performance in photoacoustic imaging and the wider medical ultrasound field. This has been achieved by undertaking the main tasks described below:-

- The implementation of a numerical model simulating Gaussian beams illuminating FPIs
- Experimental validation of the model to check that the model replicates the physical situation encountered in experiments.
- Applying the model to design optimised FPI sensors for high sensitivity and high pressure linearity

This work can hopefully be used to design improve FPI sensors and implement them in various photoacoustic imaging modalities, with faster image acquisition times by combining it with compressed sensing techniques [104] and acoustic reflectors [105]. The improved optical sensitivity would help detect smaller pressure amplitudes to aid in resolving anatomical features imaged with compressed sensing techniques, which otherwise might have been missed with conventional detectors, as well as detecting pressure amplitudes which may have been multiply reflected by acoustic reflectors reducing the pressure amplitude when detected. Photoacoustic imaging systems for clinical imaging of various anatomical features [106], [107], [108], as well as integration with other optical imaging modalities such as fluorescence imaging requires a optically transparent and highly sensitive and robust sensor [109]. It can also hopefully be integrated with thermo-acoustic imaging setups such that highly sensitive FPI sensors can detect low frequency wave acoustic waves arriving from deeper in biomedical tissue (~few centimetres).

10.2 Novel features

The novel features arising as a result of this work are highlighted below:-

- An understanding of how the shape of ITF_λs are influenced by the non-linear phase variation in FPIs. This leads to asymmetric ITF_λs for divergent beam radii, where the shape of the ITF_λ is also altered by the shape of the geometric aperture
- The introduction of a wedge on the FPI resulting in the asymmetry reversing, in that the shallow slope is at long wavelengths and sharp slope at short wavelengths for a wavelength ITF_λ along with the explanation of these shapes using the E-field decomposition method. This was also used to explain the sub-resonant peaks at large wedge angles.
- Experimental determination of non-uniformities in polymer FPI sensors for PA imaging. These were found to be negligible for the range of beam radii used (few tens of microns).
- A set of metrics such as optical sensitivity and the F.O.M, were used in order to choose the optical parameters such as the specific beam radius and mirror reflectivities for optimised FPI sensors.
- A understanding of how the ITF_λ shapes vary when the FPI is not incident at the beam waist but at various points along the optic axis

The FPI sensors were optimised for various case studies presented in chapter 8, section 8.4. These achievements have led to the possibility of designing FPI sensors with improved optical sensitivity. Also for the same FPI sensor it is possible to achieve high pressure linearity by inducing asymmetry in the ITF_λ.

10.3 Conclusions

10.3.1 Understanding of ITF$_\lambda$ shapes

The modelling results have led to new understanding of how the shape of the wavelength ITF$_\lambda$ as well as ITFs in general are affected by non-uniform phase variation with propagation distance. This was explicitly shown by an E-field decomposition method. This understanding has helped in designing optimum FPI sensors, but can also help in designing FPIs in general.

The asymmetric ITF$_\lambda$ was caused by the non-linear Gouy phase reducing the propagation phase on each round trip. This caused a shift in the electric field on each round trip forming an asymmetric ITF$_\lambda$. Aperturing the reflected beam with a ring geometry resulted in less asymmetric ITF$_\lambda$s for a divergent beam. This was due to the radial phase counteracting the effect of the Gouy phase. The addition of a wedge on the FPI due to the thickness non-uniformities caused additional path lengths to be propagated by the beam on each round trip. This created an additional source of variation in the phase, which along with the radial phase reversed the shift in electric field magnitude.

This understanding in the shape of the ITFs is important for a wide range of applications which the Fabry Perot Interferometer finds itself in, particularly in applications where control of the ITF$_\lambda$ is crucial. Applications where this may be useful is in using the FPI as a spectral filter, WDMs in telecommunications or in laser line width to control the power spectrum.

10.3.2 Optical Fabry Perot Interferometer sensor design

The understanding of the shape of the ITF$_\lambda$s led to designing FPI sensors with high optical sensitivity by choosing the optimum beam radius, aperture geometry and mirror reflectivities. It was shown that a factor of 2 increase in optical sensitivity is gained when applying a disc aperture where the detected light is 70% of the incident light for an incident beam radius of 5 μm. If a ring aperture is applied then an increase in optical sensitivity of a factor of 2 is achieved when biased at the long wavelength of the maximum of $dR/d\lambda$. A factor of 6 increase in optical sensitivity is achieved when biasing at the shorter wavelength of the reflectivity peak ($dR/d\lambda_{min}$) of the ITF$_\lambda$. This is due to the optical sensitivity being low initially due to the asymmetry.

The optimum mirror reflectivities were found to vary with beam radii, the type of aperturing employed and the effects of noise variation. The optimum mirror reflectivities based on optical sensitivity would be 98% for a unapertured beam. However for an apertured beam R_1 would be between 90% and 94% based on the aperture geometry, with R_2 being 98%. The optimum mirror reflectivities will change if based according to the metric F.O.M.

The FPI if designed with high mirror reflectivities can provide both high optical sensitivity, but also can provide high pressure linearity by varying the beam radius. When the FPI is illuminated with a divergent beam which is apertured by a disc, it would lead to a highly asymmetric ITF_λ. This has the advantage of providing high pressure linearity when the bias wavelength corresponds to the shallow slope. However biasing at the longer wavelength of the reflectivity peak would increase the optical sensitivity but reduce the pressure linearity. If high optical sensitivity is required, then the FPI can be illuminated with larger beam radii.

The asymmetric ITF_λ proves to be useful in obtaining high optical sensitivity while also obtaining high pressure linearity.

10.4 Future directions

The future avenues of work arising from this thesis is discussed in this section. The main context in this thesis has been optimising FPI sensor performance. The beam in all situations has been assumed to be a Gaussian beam of a single mode optical fibre (TE_{00}). Chapter 9 explored the effects of the planar FPI being set off-focus, as well as FPIs with alternate geometries. It was shown that a combination of aperturing and offsetting the FPI from the focus altered the propagation of the beam such that the ITF_λ has a sharper slope. Another way to counteract the limitations in planar FPIs is to alter the geometry of the FPI sensor. A hemi-spherical dome was studied to show the optimum beam radius and radius of curvature for the FPI type resonator. It was shown that a small radius of curvature of the dome is optimum. This is due to the smaller change in the radius of curvature at small beam radii, compared to larger changes at larger beam radii. This is due to the radius of curvature increasing to the power of four with beam radius.

Other future work can involve modelling FPI sensors illuminated with high order modes of Gaussian beams. A possible solution to overcome limitations due to Gaussian beams is to use Bessel beams. The advantage of Bessel beams is that they appear to be non-diverging with a

longer diffraction free range than Gaussian beams. The diffraction free range of Bessel beams is of order of a couple of millimetres. Also the central spot size of the Bessel beam can be made as small as the wavelength. Bessel beams were first theoretically formulated by Durnin [110]. A Fabry Perot device has been used to generate Bessel beams [111], whereas the use of Bessel beams to interrogate FPI sensors is absent from the literature. Therefore future work may lead in the direction of setting up experimental systems to use Bessel beams to interrogate with small beam radius without the effect of diffraction found in conventional Gaussian beams. Bessel beams have found applications in optical tweezers for moving atoms and molecules in solid structures [112], [113], as well as in biophotonics [114].

Appendix A Explicit code for planar and wedged model

Explicit code for the model of a planar FPI illuminated by a Gaussian beam:-

```
function [ Transf ] = transfer1(R1,R2,l,w0,lambda_vec,m_max)

%--------------------------------------------------------------------------
% Plots transfer function of a guassian beam illumination
%--------------------------------------------------------------------------

%--------------------------------------------------------------------------
% Plots Intensity vs. phase/wavelength for a particular wavelength range,
% taking into account Gaussian beam propagation and integration over final
% beam size. Model returns the intensity vs. wavelength for particular
parameters.
%
%R1-power reflection coefficient of mirror 1
%R2-power reflection coefficient of mirror 2
%l-thickness of polymer spacer
%lambda_vec-wavelength range

%--------------------------------------------------------------------------
%Initialising variables.

%Refractive index

n=1.639;


%Amplitude coefficients for mirror 1
r1f=sqrt(R1);
r1b=-r1f;
t1f=sqrt(1-R1);
t1b=sqrt(1-(r1b^2));

Af=0;

%Amplitude coefficients for mirror 2
r2f=sqrt(R2);
r2b=-r2f;


% FORM RADIUS AND LAMBDA ARRAYS
%m_max = 700;

%Rayleigh range vector
z0_vec=(n*pi*w0^2)./lambda_vec;

wm_max=max(w0.*sqrt(1+((2.*m_max.*l)./z0_vec).^2));


%radius over which we will integrate final reflected intensity
```

```
rad_vec = (0:0.0025:1).*wm_max;



%radius over which we will integrate incident beam intensity
r_vec=(0:0.0025:1).*w0;

%radial sampling size
dr = rad_vec(2) - rad_vec(1);
dr1=r_vec(2) - r_vec(1)

%arrays with all values of radius and lambda
[rad,lambda] = meshgrid(rad_vec,lambda_vec);
[r,lambda1]=meshgrid(r_vec,lambda_vec);

%Rayleigh range in cavity spacer and surrounding medium (air)
z0=(n*pi*w0^2)./lambda;
z01=(pi*w0^2)./lambda1;

% k-values
k0=2.*pi./(lambda);
k=2.*pi.*n./(lambda1);

% ------------------------
% Analytical solution for collimated beam
%
%Coefficient of Finesse and Airy Function
%F=4*r1f*r2f/((1-r1f*r2f)^2);
%phi_vec=(4.*pi.*n.*l)./lambda;
%Airy=F.*(sin(phi_vec./2).^2)./(1+F.*(sin(phi_vec./2).^2));
% ------------------------

%Reflected field from first mirror
E0=r1f.*exp(-(rad.^2)./(w0.^2));%.*exp(1i*(k0.*(rad.^2)./4.*z01));



%Incident electric field
E01=exp(-(r.^2)./(w0.^2));%.*exp(1i*(k0.*(r.^2)./4.*z01));



%intialise Em and m
Em=0;
m=0;

%Loop over the sampling of electric field m times until m_max

while(m<m_max)

    m=m+1;

    %Distance propagated by beam in cavity
    z=2*m*l;
    %Spot size of beam after round trip in cavity
    %wm=w0.*sqrt(1+(z./z0).^2);
    %Radius of curvature
    %Rz=z.*(1+(z0./z).^2);

    %Amplitude coefficients
```

```
    %am=t1f*t1b*(r2b^m)*(r1b^(m-1));

    Em=Em+t1f*t1b*(r2b^m)*(r1b^(m-
1)).*(w0./(w0.*sqrt(1+(z./z0).^2))).*exp(-
(rad.^2)./((w0.*sqrt(1+(z./z0).^2)).^2)).*exp(-1i*(-
k.*z+atan(z./z0))).*exp(-1i*(-k.*(rad.^2)./(2*(z.*(1+(z0./z).^2)))));

    %mth Electric field
    %E=psi1.*am;

    %Summed electric field
    %Em=Em+E;

end


%Total Electric field
Et=Em+E0;


%Intensity calculation
Iout=sum(Et.*conj(Et).*(2*pi).*rad.*dr,2);


%Incident intensity calculation
Iin=sum((E01).*conj(E01).*(2.*pi.*r).*dr,2);

% Tranfer function implementation.
Transf=(Iout./Iin);
Transf=Transf./max(Transf);


%plot Interferometer Transfer Function
figure;
plot(lambda_vec*1e9,Transf);


end
```

The explicit code for a model of a Gaussian beam illuminating a wedged FPI.

```
function [ Transf3 ] = wedgegauss1(R1,R2,l,w0,lambda,m_max)

%-------------------------------------------------------------------------
%The calculation of Transfer function for a wedged Fabry Perot
%Interferometer where each wavelength produces a reflected power ratio.
%-------------------------------------------------------------------------
%R1-power reflection coefficient of mirror 1
%R2-power reflection coefficient of mirror 2
%l-thickness of polymer spacer
%lambda_vec-wavelength range



%% Initiliasing variables

n=1.639; %refractive index of medium in cavity

%Amplitude coefficients for mirror 1
r1f=sqrt(R1); %Amplitude reflection coefficient of front of first mirror
r1b=-r1f; %Amplitude reflection coefficient of back of first mirror

t1f=sqrt(1-R1); %Amplitude transmission coefficient through front of first
mirror
t1b=sqrt(1-(r1b^2));  %Amplitude transmission coefficient through back of
first mirror

%Amplitude coefficients for mirror 2
r2f=sqrt(R2); %Amplitude reflection coefficient of second mirror internally
r2b=-r2f; %Amplitude reflection coefficient of second mirror externally



%Wedge angle of FPI in radians
alpha=0.0009*(pi/180); %Angle of wedge in radians

%Distance from apex fo wedge to the centre of the beam x0
x0=l/tan(alpha); %Distance from edge where thickness becomes zero.

%% Initiliasing relations between variables

x_vec=(-100:1:100)'*1e-3; %x-vector on x-coordinate plane
y_vec=(-100:1:100)'*1e-3; %y-vector on y-coordinate plane

[x,y]=meshgrid(x_vec,y_vec); %meshgrid of x and y vectors
r=sqrt(x.^2+y.^2); %radius expression for x-y plane.

z0=((w0^2)*pi)/lambda; %Rayleigh range corresponding to w0(beam size) and
lambda(wavelength)

k0=(2*pi)/lambda; %free space wavevector
k=(2*pi*n)/lambda; %wavevectro in cavity medium

% Incident electric field and electric field reflected of first mirror
```

```
E01=exp(-(r.^2)./w0^2).*exp((1i.*k0.*r.^2)./(4*z0)); %phase and amplitude
of initial incident beam
E0=E01.*r1f; %Electric field reflected of first field

m=0; %initialise number of round trips
Em=0; %Initialise summed mth round trip el




%% Summation of reflected field trips in cavity

while(m<m_max)

   m=m+1; %looping number of round trips
   %z=abs((x-x0).*sin(2*m*alpha));
   z=((x+x0).*sin(2*m*alpha)); %relationship for z(distance
travelled/propagated by beam) in new plane
   xn=(x+x0).*cos(2*m*alpha)-x0; %local x-plane transformation of radius of
beam
   %x=xn; %transformation of coordinates
   r=sqrt(xn.^2+y.^2); %radius alteration due to plane of mirror being
wedged

   wz=w0.*sqrt(1+(z./z0).^2); %beam size after distance z
   Rz=z.*(1+((z0^2)./(z.^2))); %Radius of curvature of beam

   am=t1f*t1b*(r1b^(m-1))*(r2b^m); %Amplitude coefficient for mth  round
trip
   psi=(w0./wz).*exp(-
(r.^2)./(wz.^2)).*exp(1i.*(k.*(r.^2))./(2.*Rz)).*exp(-1i.*(-
k.*z*+atan(z./z0))); %Amplitude and phase profile for mth reflected
gaussian beam

   E=am.*psi;%Electric field for mth relfected field from cavity




end

%% Total Field and Intensity summed to give power

E_total=E0+Em; %Total reflected field from front surface.
I=E_total.*conj(E_total);%Intensity at each x and y point


%Summing over area of FPI to obtain total reflected power

Pr=sum(I,2); %summming rows of Intensity matrix
Pr=sum(Pr,1); %summing over column of Intensity array

I0= E01.*conj(E01); %Incident intensity of Electric field



I01=sum(I0,2); %summming rows
```

```
I01=sum(I01,1); %summing over column


Transf3=Pr/I01; %Ratio of reflected power

End
```

References

1. H.Kuttruff, *Acoustics: An Introduction* (Taylor & Francis, 2004).

2. P. C. Beard, F. Perennes, and T. N. Mills, "Transduction mechanisms of the Fabry-Perot polymer film sensing concept for wideband ultrasound detection," IEEE Trans. Ultrason. Ferroelectr. Freq. Control **46**, 1575–1582 (1999).

3. P. Beard and T. Mills, "Extrinsic optical-fiber ultrasound sensor using a thin polymer film as a low-finesse Fabry-Perot interferometer," Appl. Opt. **35**, 663–675 (1996).

4. B. T. Khuri-Yakub and O. Oralkan, "Capacitive micromachined ultrasonic transducers for medical imaging and therapy.," J. Micromech. Microeng. **21**, 54004–54014 (2011).

5. A. Bhuyan, J. W. Choe, B. C. Lee, I. O. Wygant, A. Nikoozadeh, Ö. Oralkan, and B. T. Khuri-Yakub, "Integrated circuits for volumetric ultrasound imaging with 2-D CMUT arrays.," IEEE Trans. Biomed. Circuits Syst. **7**, 796–804 (2013).

6. S. Vaithilingam, T.-J. Ma, Y. Furukawa, I. O. Wygant, X. Zhuang, A. De La Zerda, O. Oralkan, A. Kamaya, S. S. Gambhir, R. B. Jeffrey, and B. T. Khuri-Yakub, "Three-dimensional photoacoustic imaging using a two-dimensional CMUT array.," IEEE Trans. Ultrason. Ferroelectr. Freq. Control **56**, 2411–2419 (2009).

7. H. Peng, Y. Su, Z. Ye, and B. Zhou, "A novel fiber Bragg grating sensor for weak pressure measurement based on the Stokes parameter," Opt. Fiber Technol. **18**, 485–489 (2012).

8. K. Peters, "Polymer optical fiber sensors—a review," Smart Mater. Struct. **20**, 1–17 (2011).

9. J.-O. Gaudron, F. Surre, T. Sun, and K. T. V. Grattan, "Long Period Grating-based optical fibre sensor for the underwater detection of acoustic waves," Sensors Actuators A Phys. **201**, 289–293 (2013).

10. J.-R. Lee, S.-S. Lee, and D.-J. Yoon, "Simultaneous multipoint acoustic emission sensing using fibre acoustic wave grating sensors with identical spectrum," J. Opt. A Pure Appl. Opt. **10**, 1–9 (2008).

11. G. Thursby, D. C. Betz, B. Culshaw, and W. J. Staszewski, "Versatile fiber Bragg grating arrays for strain mapping and ultrasound Lamb wave detection," in *SPIE Proceedings*, A. Wang, C. S. Baldwin, and A. A. Kazemi, eds. (2006), Vol. 6379, pp. 63790F–1 – 63790F–12.

12. G. Wild and S. Hinckley, "Spatial Performance of Acousto-Ultrasonic Fiber Bragg Grating Sensor," IEEE Sens. J. **10**, 805–806 (2010).

13. M. Mieloszyk, M. Krawczuk, A. Zak, and W. Ostachowicz, "An adaptive wing for a small-aircraft application with a configuration of fibre Bragg grating sensors," Smart Mater. Struct. **19**, 1–12 (2010).

14. G. Wild, G. Allwood, and S. Hinckley, "Distributed sensing, communications, and power in optical Fibre Smart Sensor networks for structural health monitoring," in *2010 Sixth International Conference on Intelligent Sensors, Sensor Networks and Information Processing* (Ieee, 2010), pp. 139–144.

15. B. Culshaw, "Fibre Optic Sensors in Smart Structures: Achievements, Challenges and Prospects," in *SPIE Proceedings*, W. Ecke, K. J. Peters, and T. E. Matikas, eds. (2011), Vol. 7982, pp. 798202 –1 – 798202–9.

16. M. Majumder, T. K. Gangopadhyay, A. K. Chakraborty, K. Dasgupta, and D. K. Bhattacharya, "Fibre Bragg gratings in structural health monitoring—Present status and applications," Sensors Actuators A Phys. **147**, 150–164 (2008).

17. S. T. Lau, S. Y. Liu, H. Y. Tam, and H. L. W. Chan, "Characterization of a Fibre Grating Laser-Based Hydrophone for Detection of High Frequency Medical Ultrasound: A Comparison with PVDF Membrane Hydrophone," Ferroelectrics **333**, 115–120 (2006).

18. N. E. Fisher, J. Surowiec, D. J. Webb, D. a Jackson, L. R. Gavrilov, J. W. Hand, L. Zhang, and I. Bennion, "In-fibre Bragg gratings for ultrasonic medical applications," Meas. Sci. Technol. **8**, 1050–1054 (1997).

19. J. Surowiec, N. E. Fisher, D. J. Webb, D. A. Jackson, L. Gavrilovt, J. W. Hand, L. Zhangz, I. Benniont, and H. Atm, "A Novel Miniature Optical Fibre Probe For MHz Frequency Ultrasound," in *IEEE Ultrasonics Symposium* (1996), pp. 1051–1054.

20. D. H. Wang, P. G. Jia, Z. G. Ma, L. F. Xie, and Q. B. Liang, "Tip-sensitive fibre-optic Bragg grating ultrasonic hydrophone for measuring high-intensity focused ultrasound fields," Electron. Lett. **50**, 649–650 (2014).

21. L. Z. and I. B. NE Fisher, DJ Webb, CN Pannell, DA Jacksona, LR Gavrilov , JW Handb, "Medical ultrasound detection using fiber Bragg gratings," in *SPIE Proceedings …* (1999), Vol. 3541, pp. 27–32.

22. P. Roriz, L. Carvalho, O. Frazão, J. L. Santos, and J. A. Simões, "From conventional sensors to fibre optic sensors for strain and force measurements in biomechanics applications: a review.," J. Biomech. **47**, 1251–61 (2014).

23. B. Lee, "Review of the present status of optical fiber sensors," Opt. Fiber Technol. **9**, 57–79 (2003).

24. Q. Sun, N. Chen, Y. Ding, Z. Chen, and T. Wang, "Optical Fiber Extrinsic Fabry-Perot Interferometer Sensors for Ultrasound Detection," in *SPIE Proceedings*, X. Li, Q. Luo, V. Ntziachristos, and Y. Yasuno, eds. (2009), Vol. 7634, pp. 763410–1 – 763410–7.

25. E. Hansis, T. Cubel, J.-H. Choi, J. R. Guest, and G. Raithel, "Simple pressure-tuned Fabry–Pérot interferometer," Rev. Sci. Instrum. **76**, 033105–1 – 033105–3 (2005).

26. S. Liu, Y. Wang, C. Liao, G. Wang, Z. Li, Q. Wang, J. Zhou, K. Yang, X. Zhong, J. Zhao, and J. Tang, "High-sensitivity strain sensor based on in-fiber improved Fabry-Perot interferometer.," Opt. Lett. **39**, 2121–2124 (2014).

27. E. Zhang, J. Laufer, and P. Beard, "Backward-mode multiwavelength photoacoustic scanner using a planar Fabry-Perot polymer film ultrasound sensor for high-resolution three-dimensional imaging of biological tissues.," Appl. Opt. **47**, 561–577 (2008).

28. C. Sheaff and S. Ashkenazi, "Polyimide-etalon all-optical ultrasound transducer for high frequency applications," in *Proceedings of SPIE*, A. A. Oraevsky and L. V. Wang, eds. (2014), Vol. 8943, pp. 8943M–1 – 8943M–8.

29. K.-S. Kim, Y. Mizuno, and K. Nakamura, "Fiber-optic ultrasonic hydrophone using short Fabry-Perot cavity with multilayer reflectors deposited on small stub.," Ultrasonics **54**, 1047–1051 (2014).

30. S. Rajagopal, B. Zeqiri, and P. Gélat, "Calibration of miniature medical ultrasonic hydrophones for frequencies in the range 100 to 500 kHz using an ultrasonically absorbing waveguide.," IEEE Trans. Ultrason. Ferroelectr. Freq. Control **61**, 765–768 (2014).

31. P. C. Beard, F. Perennes, and T. N. Mills, "Transduction mechanisms of the Fabry-Perot polymer film sensing concept for wideband ultrasound detection.," IEEE Trans. Ultrason. Ferroelectr. Freq. Control **46**, 1575–1582 (1999).

32. B. E. Treeby, B. T. Cox, E. Z. Zhang, S. K. Patch, and P. C. Beard, "Measurement of broadband temperature-dependent ultrasonic attenuation and dispersion using photoacoustics.," IEEE Trans. Ultrason. Ferroelectr. Freq. Control **56**, 1666–1676 (2009).

33. B. T. Cox and P. C. Beard, "The frequency-dependent directivity of a planar fabry-perot polymer film ultrasound sensor.," IEEE Trans. Ultrason. Ferroelectr. Freq. Control **54**, 394–404 (2007).

34. B. J. Slagmolen, M. B. Gray, K. G. Baigent, and D. E. McClelland, "Phase-sensitive reflection technique for characterization of a fabry-perot interferometer.," Appl. Opt. **39**, 3638–3643 (2000).

35. D. Guo, R. Lin, and W. Wang, "Gaussian-optics-based optical modeling and characterization of a Fabry-Perot microcavity for sensing applications," JOSA A **22**, 1577–1588 (2005).

36. P. R. Wilkinson and J. R. Pratt, "Analytical model for low finesse , external cavity , fiber Fabry – Perot interferometers including multiple reflections and angular misalignment," Appl. Opt. **50**, 4671–4680 (2011).

37. A. G. Bell, "On the production and reproduction of sound by light," Am. J. Sci. **20**, 305–324 (1880).

38. W. F. Cheong, S. A. Prahl, and A. J. Welch, "A review of the optical properties of biological tissues," IEEE J. Quantum Electron. **26**, 2166–2185 (1990).

39. P. Beard, "Biomedical Photoacoustic Imaging," Interface Focus **1**, 602–31 (2011).

40. B. T. Cox, S. R. Arridge, and P. C. Beard, "Estimating chromophore distributions from multiwavelength photoacoustic images.," J. Opt. Soc. Am. A. Opt. Image Sci. Vis. **26**, 443–455 (2009).

41. R. A. Kruger, "Photoacoustic ultrasound," Med. Phys. **21**, 127–131 (1994).

42. J. Laufer, D. Delpy, C. Elwell, and P. Beard, "Quantitative spatially resolved measurement of tissue chromophore concentrations using photoacoustic spectroscopy : application to the measurement of blood oxygenation and haemoglobin concentration," Phys. Med. Biol. **52**, 141–168 (2007).

43. T. Tarvainen, B. T. Cox, J. P. Kaipio, and S. R. Arridge, "Reconstructing absorption and scattering distributions in quantitative photoacoustic tomography," Inverse Probl. **28**, (2012).

44. C. Li and L. V Wang, "Photoacoustic tomography and sensing in biomedicine," Phys. Med. Biol. **54**, R59–97 (2009).

45. D. Yang, L. Zeng, C. Pan, X. Zhao, and X. Ji, "Noninvasive photoacoustic detecting intraocular foreign bodies with an annular transducer array," Opt. Express **21**, 984–991 (2013).

46. J. Xia and L. V Wang, "Small-animal whole-body photoacoustic tomography: a review.," IEEE Trans. Biomed. Eng. **61**, 1380–1389 (2014).

47. J. C. Ranasinghesagara, Y. Jiang, and R. J. Zemp, "Reflection-mode multiple-illumination photoacoustic sensing to estimate optical properties," Photoacoustics **2**, 33–38 (2014).

48. B. T. Cox and P. C. Beard, "Exact photoacoustic image reconstruction using a planar sensor array and image sources," in *Proceedings of SPIE* (Spie, 2007), Vol. 6437, p. 64371H–64371H–5.

49. C. H. Farny, R. G. Holt, and R. a Roy, "Temporal and spatial detection of HIFU-induced inertial and hot-vapor cavitation with a diagnostic ultrasound system.," Ultrasound Med. Biol. **35**, 603–615 (2009).

50. M. Gyöngy and C.-C. Coussios, "Passive spatial mapping of inertial cavitation during HIFU exposure.," IEEE Trans. Biomed. Eng. **57**, 48–56 (2010).

51. J. Serrone, H. Kocaeli, T. Douglas Mast, M. T. Burgess, and M. Zuccarello, "The potential applications of high-intensity focused ultrasound (HIFU) in vascular neurosurgery.," J. Clin. Neurosci. **19**, 214–221 (2012).

52. J. Haller, K.-V. Jenderka, G. Durando, and A. Shaw, "A comparative evaluation of three hydrophones and a numerical model in high intensity focused ultrasound fields.," J. Acoust. Soc. Am. **131**, 1121–1130 (2012).

53. Y. M. and Y. Matsuura, "All-optical photoacoustic imaging system using fiber ultrasound probe and hollow optical fiber bundle," Opt. Express **21**, 22023–22033 (2013).

54. H. Cui, J. Staley, and X. Yang, "Integration of photoacoustic imaging and high-intensity focused ultrasound.," J. Biomed. Opt. **15**, 021312–1 – 021312–4 (2010).

55. M. Alhamami, M. C. Kolios, and J. Tavakkoli, "Photoacoustic detection and optical spectroscopy of high-intensity focused ultrasound-induced thermal lesions in biologic tissue.," Med. Phys. **41**, 053502–1 – 053502–13 (2014).

56. B. Zeqiri, "Metrology for ultrasonic applications.," Prog. Biophys. Mol. Biol. **93**, 138–52 (2007).

57. P. J. Kaczkowski, M. R. Bailey, V. A. Khokhlova, and O. A. Sapozhnikov, "Quantitative Schlieren imaging of continuous and pulsed high-intensity ultrasonic fields using narrow band spatial filters.," J. Acoust. Soc. Am. **128**, 2280–2280 (2010).

58. C. I. Zanelli and S. M. Howard, "Schlieren metrology for high frequency medical ultrasound.," Ultrasonics **44**, 105–107 (2006).

59. J. Laufer, P. Johnson, E. Zhang, B. Treeby, B. Cox, B. Pedley, and P. Beard, "In vivo preclinical photoacoustic imaging of tumor vasculature development and therapy," J. Biomed. Opt. **17**, 056016–1 – 056016–8 (2012).

60. E. Z. Zhang, B. Povazay, J. Laufer, A. Alex, B. Hofer, B. Pedley, C. Glittenberg, B. Treeby, B. Cox, P. Beard, and W. Drexler, "Multimodal photoacoustic and optical coherence tomography scanner using an all optical detection scheme for 3D morphological skin imaging.," Biomed. Opt. Express **2**, 2202–2215 (2011).

61. M. A. Roggenbuck, R. D. Walker, J. W. Catenacci, and S. K. Patch, "Volumetric thermoacoustic imaging over large fields of view.," Ultrason. Imaging **35**, 57–67 (2013).

62. M. Pramanik, G. Ku, C. Li, and L. V. Wang, "Design and evaluation of a novel breast cancer detection system combining both thermoacoustic (TA) and photoacoustic (PA) tomography," Med. Phys. **35**, 2218–2223 (2008).

63. H. Ke, T. N. Erpelding, L. Jankovic, C. Liu, and L. V. Wang, "Performance characterization of an integrated ultrasound, photoacoustic, and thermoacoustic imaging system," J. Biomed. Opt. **17**, 056010–1 – 056010–6 (2012).

64. P. Morris, "A Fabry-Perot fibre-optic hydrophone for the characterisation of ultrasound fields," University of London (2008).

65. O. I. Szentesi and E. A. Noga, "Parylene C Films for Optical Waveguides," Appl. Opt. **13**, 2458–2459 (1974).

66. H. T. Kim, T. Koo, and C. Park, "Parylene-C thin films deposited on polymer substrates using a modified chemical vapor condensation method," Korean J. Chem. Eng. **27**, 748–751 (2010).

67. J. Yao and L. V. Wang, "Breakthroughs in Photonics 2013: Photoacoustic Tomography in Biomedicine," IEEE Photonics J. **6**, 0701006–1 – 0701006–6 (2014).

68. T. Gangopadhyay, "Prospects for Fibre Bragg Gratings and Fabry-Perot Interferometers in fibre-optic vibration sensing," Sensors Actuators A Phys. **113**, 20–38 (2004).

69. H. J. Konle, C. O. Paschereit, and I. Röhle, "A fiber-optical microphone based on a Fabry–Perot interferometer applied for thermo-acoustic measurements," Meas. Sci. Technol. **21**, 015302 (2010).

70. P. Morris, A. Hurrell, A. Shaw, E. Zhang, and P. Beard, "A Fabry-Perot fiber-optic ultrasonic hydrophone for the simultaneous measurement of temperature and acoustic pressure," J. Acoust. Soc. Am. **125**, 3611–3622 (2009).

71. P. Morris, A. Hurrell, A. Shaw, E. Zhang, and P. Beard, "A Fabry-Perot fiber-optic ultrasonic hydrophone for the simultaneous measurement of temperature and acoustic pressure.," J. Acoust. Soc. Am. **125**, 3611–22 (2009).

72. W. Tsai and C. Lin, "A novel structure for the intrinsic Fabry-Perot fiber-optic temperature sensor," J. Light. Technol. **19**, 682–686 (2001).

73. D. Su, X. Qiao, Q. Rong, H. Sun, J. Zhang, Z. Bai, Y. Du, D. Feng, Y. Wang, M. Hu, and Z. Feng, "A fiber Fabry–Perot interferometer based on a PVA coating for humidity measurement," Opt. Commun. **311**, 107–110 (2013).

74. H. Y. Choi, K. S. Park, S. J. Park, U.-C. Paek, B. H. Lee, and E. S. Choi, "Miniature fiber-optic high temperature sensor based on a hybrid structured Fabry-Perot interferometer.," Opt. Lett. **33**, 2455–2457 (2008).

75. T. Wei, Y. Han, Y. Li, H.-L. Tsai, and H. Xiao, "Temperature-insensitive miniaturized fiber inline Fabry-Perot interferometer for highly sensitive refractive index measurement," Opt. Express **16**, 5764 (2008).

76. T. Zhang, Z. Gong, R. Giorno, and L. Que, "A nanostructured Fabry-Perot interferometer.," Opt. Express **18**, 20282–8 (2010).

77. J. Yin, T. Liu, J. Jiang, K. Liu, S. Wang, F. Wu, and Z. Ding, "Wavelength-division-multiplexing method of polarized low-coherence interferometry for fiber Fabry–Perot interferometric sensors," Opt. Lett. **38**, 3751–3753 (2013).

78. S. R. Mallinson, "Wavelength-selective filters for single-mode fiber WDM systems using Fabry-Perot interferometers.," Appl. Opt. **26**, 430–436 (1987).

79. D. G. Peterson and A. Yariv, "Interferometry and laser control with solid Fabry-Perot etalons.," Appl. Opt. **5**, 985–991 (1966).

80. H.-J. Pan, P. Ruan, H.-W. Wang, and F. Li, "Confocal Fabry-Perot interferometer for frequency stabilization of laser," Laser Phys. **21**, 336–339 (2011).

81. N. N. Elkin and a. P. Napartovich, "Numerical study of the stability of single-mode lasing in a Fabry–Perot resonator with an active medium," Appl. Math. Model. **18**, 513–521 (1994).

82. T. Błachowicz, R. Bukowski, and Z. Kleszczewski, "Fabry–Perot interferometer in Brillouin scattering experiments," Rev. Sci. Instrum. **67**, 4057–4060 (1996).

83. J. M. Vaughan, *The Fabry-Perot Interferometer. History, Theory, Practice and Applications* (IOP Publishing, 1989).

84. F. L. Pedrotti and L. M. Pedrotti, *Introduction to Optics (2rd Edition)* (Pearson Education Limited, 2006), p. Chapter 27.

85. H. Abu-Safia, R. Al-Tahtamouni, I. Abu-Aljarayesh, and N. A. Yusuf, "Transmission of a Gaussian beam through a Fabry-Perot interferometer," Appl. Opt. **33**, 3805 (1994).

86. J. Y. Lee, J. W. Hahn, and H.-W. Lee, "Spatiospectral transmission of a plane-mirror Fabry-Perot interferometer with nonuniform finite-size diffraction beam illuminations.," (May 2002).

87. T. Lanternier, J. Cotteverte, A. Le Floch, and F. Bretenaker, "Jones matrices of a quarter-wave plate for Gaussian beams," Appl. Opt. **34**, 6806–6818 (1995).

88. S. Feng and H. G. Winful, "Physical origin of the Gouy phase shift," Opt. Lett. **26**, 485–487 (2001).

89. R. (University O. U. Abbas, "Resonator equation relating Fresnel number, finesse, and number of beam transits," Appl. Opt. **20**, 3469–3470 (1981).

90. G. Xia, Z. Wu, M. Liu, and Y. Pan, "Transmitted characteristics for a Gaussian beam passing through a misaligned Fabry-Perot interferometer," Opt. - Int. J. Light Electron Opt. **114**, 521–524 (2003).

91. M. Liu, X. Chao, and Z. Ye, "Transmitting intensity distribution after a Gaussian beam incidenting nonnormally on a wedged Fabry–Perot cavity," Opt. - Int. J. Light Electron Opt. **119**, 661–665 (2008).

92. Y. H. Meyer, "Fringe shape with an interferential wedge," J. Opt. Soc. Am. **71**, 1255–1263 (1981).

93. J. M. Green, "Fabry-Perot etalons - limitations to “ single-shot” linewidth measurements at longer wavelengths," J. Phys. E **13**, 1302–1304 (1980).

94. P. La Penna, "Transmittivity profile of high finesse plane parallel Fabry–Perot cavities illuminated by Gaussian beams," Opt. Commun. **162**, 267–279 (1999).

95. B. J. Slagmolen, M. B. Gray, K. G. Baigent, and D. E. McClelland, "Phase-sensitive reflection technique for characterization of a fabry-perot interferometer.," Appl. Opt. **39**, 3638–3643 (2000).

96. P. R. Bevington and D. K. Robinson, "Instrumental and statistical uncertainties," in *Data Reduction and Error Analysis for the Physical Sciences*, 3rd ed. (McGraw-Hill, 2003), pp. 36–39.

97. D. G. Altman and J. M. Bland, "Standard deviations and standard errors," Br. Med. J. **331**, 903 (2005).

98. J. Li, A. Taylor, I. Papakonstantinou, E. Zhang, and P. Beard, "Highly sensitive optical microresonator sensors for photoacoustic imaging," in *Proceedings of SPIE*, A. A. Oraevsky and L. V. Wang, eds. (2014), Vol. 8943, pp. 89430C–1 – 89430C–10.

99. A. Griffith, J. Cardenas, C. B. Poitras, and M. Lipson, "High quality factor and high confinement silicon resonators using etchless process," Opt. Express **20**, 21341–21345 (2012).

100. T. Kobayashi, "Experimental studies of completely closed optical cavities enclosed with total-internal-reflection walls.," Opt. Express **20**, 16033–8 (2012).

101. D. Xie, H. Zhang, X. Shu, and J. Xiao, "Fabrication of polymer micro-lens array with pneumatically diaphragm-driven drop-on-demand inkjet technology.," Opt. Express **20**, 15186–95 (2012).

102. J. . S. a. Collins, "Analysis of Optical Resonators Involving Focusing Elements," Appl. Opt. **3**, 1263 (1964).

103. F. C. Favero, L. Araujo, G. Bouwmans, V. Finazzi, J. Villatoro, and V. Pruneri, "Spheroidal Fabry-Perot microcavities in optical fibers for high-sensitivity sensing," Opt. Express **20**, 7112–7118 (2012).

104. N. Huynh, E. Zhang, M. Betcke, S. Arridge, P. Beard, and B. Cox, "Patterned interrogation scheme for compressed sensing photoacoustic imaging using a Fabry Perot planar sensor," in *Proceedings of SPIE*, A. A. Oraevsky and L. V. Wang, eds. (2014), Vol. 8943, pp. 894327–1 – 894327–5.

105. R. Ellwood, E. Z. Zhang, P. C. Beard, and B. T. Cox, "The use of acoustic reflectors to enlarge the effective area of planar sensor arrays," in *Proceedings of SPIE*, A. A. Oraevsky and L. V. Wang, eds. (2014), Vol. 8943, pp. 89436A–1 – 89436A–9.

106. J. M. Mari, S. West, P. C. Beard, and A. E. Desjardins, "Multispectral photoacoustic imaging of nerves with a clinical ultrasound system," in *Proceedings of SPIE*, A. A. Oraevsky and L. V. Wang, eds. (2014), Vol. 8943, pp. 89430W–1 – 89430W–7.

107. C. Kim, C. Favazza, and L. V Wang, "In vivo photoacoustic tomography of chemicals: high-resolution functional and molecular optical imaging at new depths.," Chem. Rev. **110**, 2756–2782 (2010).

108. X. Wang, J. B. Fowlkes, J. M. Cannata, C. Hu, L. Paul, and P. L. Carson, "Photoacoustic Imaging with a Commercial Ultrasound System and a Custom Probe," Ultrasound Med. Biol. **37**, 484–492 (2012).

109. J. James, V. M. Murukeshan, and L. S. Woh, "Integrated photoacoustic, ultrasound and fluorescence platform for diagnostic medical imaging-proof of concept study with a tissue mimicking phantom," Biomed. Opt. Express **5**, 2135–2144 (2014).

110. J. Durnin, "Exact solutions for nondiffracting beams. I. The scalar theory," J. Opt. Soc. Am. A **3**, 651–654 (1987).

111. A. J. Cox and D. C. Dibble, "Nondiffracting beam from a spatially filtered Fabry-Perot resonator," J. Opt. Soc. Am. A **9**, 282–286 (1992).

112. D. McGloin and K. Dholakia, "Bessel beams: Diffraction in a new light," Contemp. Phys. **46**, 15–28 (2005).

113. K. Dholakia and T. Čižmár, "Shaping the future of manipulation," Nat. Photonics **5**, 335–342 (2011).

114. T. Čižmár and K. Dholakia, "Shaping the light transmission through a multimode optical fibre: complex transformation analysis and applications in biophotonics," Opt. Express **19**, 18871–18884 (2011).